Electrochemical Analysis and Development of Novel Electrode Materials for High-Temperature Electrolysis

Elektrochemische Analyse und Entwicklung neuartiger Elektrodenmaterialien für die Hochtemperaturelektrolyse

Von der Fakultät für Mathematik, Informatik und Naturwissenschaften der RWTH Aachen University zur Erlangung des akademischen Grades einer Doktorin der Ingenieurwissenschaften genehmigte Dissertation

vorgelegt von

Stephanie Elisabeth Wolf, M.Sc.

aus

Köln

Berichter: Univ.-Prof. Dr. rer. nat. Rüdiger-Albert Eichel

Univ.-Prof. Dr.-Ing. Matthias Wessling

Univ.-Prof. Dr. rer. nat. Joachim Mayer

Tag der mündlichen Prüfung: 10.01.2025

Eidesstattliche Erklärung

Ich, Stephanie Elisabeth Wolf, erkläre hiermit, dass diese Dissertation und die darin dargelegten Inhalte meine eigenen sind und selbstständig, als Ergebnis meiner eigenen originären Forschung, generiert wurden.

Hiermit erkläre ich an Eides statt:

1. Diese Arbeit wurde vollständig oder größtenteils in der Phase als Doktorand dieser Fakultät und Universität angefertigt;
2. Sofern irgendein Bestandteil dieser Dissertation zuvor für einen akademischen Abschluss oder eine andere Qualifikation an dieser oder einer anderen Institution verwendet wurde, wurde dies klar angezeigt;
3. Wann immer andere eigene Veröffentlichungen oder Veröffentlichungen Dritter herangezogen wurden, wurden diese klar benannt;
4. Wenn aus anderen eigenen Veröffentlichungen oder Veröffentlichungen Dritter zitiert wurde, wurde stets die Quelle hierfür angegeben. Diese Dissertation ist vollständig meine eigene Arbeit, mit der Ausnahme solcher Zitate;
5. Alle wesentlichen Quellen von Unterstützung wurden benannt;
6. Wann immer ein Teil dieser Dissertation auf der Zusammenarbeit mit anderen basiert, wurde dies von mir klar gekennzeichnet;
7. Ein Teil oder Teile dieser Arbeit wurden zuvor veröffentlicht[1–6].
   Eine Auflistung findet sich auf Seite 121.

Acknowledgments

This thesis was written between October 2020 and March 2024 as a result of an exciting and educational journey that I undertook at the Institute of Energy Technologies - Fundamental Electrochemistry (IET-1) under the supervision of Prof. Dr. Rüdiger-A. Eichel, Dr. L. G. J. (Bert) de Haart, Dr. Izaak C. (Ico) Vinke, and Dr. Vaibhav Vibhu.

I would like to express my deepest appreciation to Prof. Rüdiger-A. Eichel for the opportunity to earn a doctoral degree in a highly interdisciplinary working environment with a wide range of scientific and technical opportunities in international collaborations and industry-oriented projects. In particular, I would like to highlight the constructive and inspiring scientific discussions as well as the opportunity to spend time abroad. Furthermore, I would like to express my deepest appreciation to Prof. Matthias Wessling, for his time and effort in acting as the second examiner for this thesis.

I want to extend special thanks to Dr. Bert de Haart and Dr. Ico Vinke. The scientific discussions in our weekly impedance meetings led by Ico have largely influenced and guided this work. He consistently dedicated time to address our questions on electrolysis, electrochemical processes, and impedance spectroscopy. His expertise has made my work more productive and successful. I would also like to thank Bert for his many suggestions, guidance, joint publications, and constant feedback, despite his considerable responsibilities as Deputy Director of IET-1.

My deepest gratitude goes to my direct supervisor, Dr. Vaibhav Vibhu, whose competent guidance, teachings, and professional support have significantly contributed to my scientific and personal growth. His expertise and knowledge have been invaluable throughout this research journey, characterized by constructive scientific discussions, productive feedback, and encouragement. I thank you for your time in the lab, your corrections of papers, presentations, and posters, and your support for my exploration of the scientific community outside of Germany. You encouraged me to look beyond my dissertation topic and always consider additional perspectives. I will remember you for your great scientific curiosity and work ethic.

I would not have undertaken this journey without the support of Dr. Lucy Nohl, who guided me with great dedication during my internship in the High-Temperature Electrochemistry Group of IET-1 in 2019 and during my subsequent master's thesis. Her invaluable contribution and feedback to my experimental work during my master and doctoral studies greatly facilitated my professional and personal growth. Whenever I needed a new perspective, whenever I faced a challenging task, she supported me with inspiring words or challenged me with tricky scientific questions.

Whether it was making new discoveries or exploring a new city, I thoroughly enjoyed the time we spent together.

I had the pleasure of collaborating with the group of Hon.-Prof. Dr.-Ing. Norbert H. Menzler (IMD-2, FZJ), which gave me the invaluable experience of publishing and organizing across groups and institutes. High-temperature XRD studies and Rietveld refinements were performed by and evaluated with Mirko Ziegner (IMD-2, FZJ). The XPS measurements have been commissioned from and evaluated with Dr. Heinrich Hartmann (ZEA-3, FZJ). High-resolution SEM-EDX, HAADF-STEM, and HR-TEM images were performed and evaluated in collaboration with Pritam K. Chakraborty, and Dr. Shibabrata Basak (IET-1, FZJ). I also wish to thank Dr. Jean-Marc Bassat, Dr. Jacinthe Gamon, and Romuald Frugier from the Institut de Chimie de la Matière Condensée de Bordeaux, who imparted their knowledge and perspectives to me on the topic of oxygen exchange experiments and for hosting me in their laboratory from September to November 2023.

I would also like to thank my wonderful colleagues Dr. Markus Nohl, Jan Uecker, Ifeanyichukwu Unachukwu, Tanja Brambach, Claudia Tropartz, and Niklas Eyckeler. Our regular exchange of ideas, their helpful scientific input, the stress-free business trips together, as well as the relaxing talks over a cup of coffee or lunch have enriched the atmosphere during my time at the Institute and led to new insights and discoveries. I would like to extend my sincere thanks to my students Eric Tröster, Niklas Eyckeler, Carla L. Coll, and Finn Dröge, who have completed their bachelor thesis under my supervision. Their hard work and good teamwork led to a lot of interesting experimental results, which are part of this thesis, and to new research ideas for future projects. I would also like to thank Dr. Ansgar Kretzschmar, Victor Selmert, Beatrice Wolff, Elisabeth Richter, Igor Graf von Westarp, and Dr. Sven Jovanovic. Their moral support and words of encouragement, as well as our joint free-time activities, helped a lot to balance the scientific work.

I would like to express my deep gratitude to my family. Their unconditional support, their understanding of my time-consuming research work and their always open ears have strengthened me and made this journey possible. A special thank you goes to Mathias Kiesel. Your unwavering support was the driving force behind my success. Thank you for standing by my side, being my rock, and cheering me on every step of the way.

Overall, I would like to thank each and every one of you for your help and support. Without all of you, this scientific journey would have been less successful and fulfilling. Thank you for your trust, advice, and our journey together.

Kurzfassung

Diese Arbeit konzentriert sich auf die Analyse der Leistungsfähigkeit und des Degradationsverhaltens von Ni-Cermet- und Ni-freien Perowskitmaterialien für die Brenngaselektrode unter Wasserdampf-, CO_2 und Ko-Elektrolysebedingungen. Die Alterungstests von kommerziellen Festoxidzellen mit einer Ni-8YSZ-Brennstoffelektrode wurden bei einer konstanter Stromdichte von $-1 \quad A \cdot cm^{-2}$ für 1000 h durchgeführt. Die anschließende Mikrostrukturanalyse zeigte Nickelpartikel-Migration und Agglomeration an der Grenzfläche zwischen der Aktiv- und Trägerschicht. Diese wesentlichen mikrostrukturellen Veränderungen führten zu einer erhöhten Zellspannung im Laufe der Alterungstests unter Wasserdampfelektrolysebedingungen.

Da der Hauptdegradationsprozess von Ni-Cermet-Elektroden als Ni-Verarmung identifiziert worden war, wurden Ni-freie $Sr_2FeMoO_{6-\delta}$-Elektrodenmaterialien synthetisiert und getestet. Elektronenmikroskopische Messungen zeigten, dass Nanopartikel in Wasserstoffatmosphäre aus der Perowskitmatrix herausgelöst werden und sich eine neue Perowskit-Metall-Heterogrenzfläche bildet, die die reaktive Oberfläche vergrößert. Die Leitfähigkeitsuntersuchung ergab, dass $Sr_2FeMoO_{6-\delta}$-basierte Materialien höhere Leitfähigkeiten in reduzierenden Atmosphären aufweisen als andere Perowskitmaterialien, die als Alternative zu Ni-Cermet-Elektroden in Betracht gezogen werden. Die Materialien $Sr_2FeMoO_{6-\delta}$ (SFM) and $Sr_2FeMoO_{6-\delta}$-GDC (SFM-GDC) wurden elektrochemisch untersucht und erreichten höhere Stromdichten bei 1.5 V als Ni-8YSZ in der Wasserdampf- und Ko-Elektrolyse, jedoch geringere Stromdichten als Ni-GDC. Der Langzeittest unter Wasserdampfelektrolysebedingungen zeigte eine deutlich höhere Degradation für SFM im Vergleich zu SFM-GDC, deren Ursache auf mikrostrukturelle Veränderungen der SFM-Elektrode zurückgeführt werden konnte.

Der Einfluss der Dotierung wurde durch die Synthese des Doppelperowskits $Sr_2FeMo_{0.65}M_{0.35}O_{6-\delta}$ mit M = Ti, Co, Cu, Mn und Ni untersucht. Die B-Site-Dotierung zeigte eine Zunahme der Leitfähigkeit in oxidierender und reduzierender Atmosphäre bis zu 152 $S \cdot cm^{-1}$ für $Sr_2FeMo_{0.65}Cu_{0.35}O_{6-\delta}$-GDC aufgrund der Herauslösung bimetallischer Fe-Cu-Nanopartikel.Die höchste Stromdichte aller untersuchten Materialien, verglichen mit Ni-GDC und Ni-8YSZ, wurde festgestellt für $Sr_2FeMo_{0.65}Ni_{0.35}O_{6-\delta}$ (SFM-Ni). Nach 500 h unter Wasserdampfelektrolysebedingungen zeigte die SFM-Ni Mikrostruktur jedoch eine Partikelagglomeration und Elektrodenverdichtung. Um den Einfluss des Brenngases zu untersuchen, wurden SFM-basierte Elektrodenmaterialien zur CO_2 Elektrolyse in einer Atmosphäre von 80% CO_2 + 20% CO getestet. Die höchste Stromdichte und eine sehr gute Langzeitstabilität über 1000 h zeigte erneut das Material $Sr_2FeMo_{0.65}Ni_{0.35}O_{6-\delta}$.

Abstract

This work focuses on the analysis of the performance and degradation behavior of Ni-cermet and Ni-free perovskite materials for the fuel gas electrode under steam, CO_2, and co-electrolysis conditions. Degradation tests of commercial solid oxide cells with a Ni-8YSZ fuel electrode were carried under a constant current density of $-1\ A \cdot cm^{-2}$ for 1000 h. Subsequent microstructural analysis showed nickel particle migration and agglomeration at the interface between the active and support layer. These significant microstructural changes led to an increased cell potential during the degradation tests under steam electrolysis conditions.

As the main degradation process of Ni-cermet electrodes was identified as Ni depletion, Ni-free $Sr_2FeMoO_{6-\delta}$ electrode materials were synthesized and tested. Electron microscopy measurements showed that nanoparticles are dissolved from the SFM perovskite matrix in a hydrogen atmosphere, forming a new perovskite-metal heterointerface that increases the reactive surface area. Conductivity studies showed that $Sr_2FeMoO_{6-\delta}$-based materials exhibit higher conductivities in reducing atmospheres than other perovskite materials considered as alternatives to Ni-cermet electrodes. The materials $Sr_2FeMoO_{6-\delta}$ (SFM) and $Sr_2FeMoO_{6-\delta}$-GDC (SFM-GDC) were electrochemically investigated and achieved higher current densities at 1.5 V than Ni-8YSZ in steam and co-electrolysis, but lower current densities than Ni-GDC. Long-term testing under steam electrolysis conditions showed significantly higher degradation for SFM compared to SFM-GDC, which was attributed to microstructural changes in the SFM electrode.

The effect of doping was investigated by synthesizing the double perovskite $Sr_2FeMo_{0.65}M_{0.35}O_{6-\delta}$ with M = Ti, Co, Cu, Mn, and Ni. B-site doping showed an increased conductivity in oxidizing and reducing atmospheres up to $152\ S \cdot cm^{-1}$ for $Sr_2FeMo_{0.65}Cu_{0.35}O_{6-\delta}$-GDC due to the exsolution of bimetallic Fe-Cu nanoparticles. The highest current density of all materials studied, compared to Ni-GDC and Ni-8YSZ, was found for $Sr_2FeMo_{0.65}Ni_{0.35}O_{6-\delta}$ (SFM-Ni). After 500 h under steam electrolysis conditions, however, the SFM-Ni microstructure showed particle agglomeration and electrode densification. To investigate the effect of the fuel gas, SFM-based electrode materials were tested for CO_2 electrolysis in an atmosphere of 80% CO_2 + 20% CO. The highest current density and very good long-term stability over 1000 h was shown by the $Sr_2FeMo_{0.65}Ni_{0.35}O_{6-\delta}$.

Contents

List of Abbreviations and Symbols

Abbreviations

SOECs	Solid Oxide Electrolysis Cells
SOE	Solid Oxide Electrolysis
SOFCs	Solid Oxide Fuel Cells
SOC	Solid Oxide Cell
FESCs	Fuel Electrode-Supported Cells
ESCs	Electrolyte-Supported Cells
HER	Hydrogen Evolution Reaction
OER	Oxygen Evolution Reaction
ORR	Oxygen Reduction Reaction
TPB	Triple Phase Boundary
DPB	Double Phase Boundary
EIS	Electrochemical Impedance Spectroscopy
CPE	Constant Phase Element
SSR	Sum of Square Residuals
OCV	Open Circuit Voltage
ASR	Area Specific Resistance
AC	Alternating Current
DC	Direct Current
ECM	Equivalent Circuit Model
DRT	Distribution of Relaxation Times Analysis
CNLS	Complex Nonlinear-Least-Square
MIECs	Mixed Ionic and Electronic Conductors
YSZ	Yttria-Stabilized Zirconia
GDC	Gadolinium-Doped Ceria
SFMNi	$Sr_2FeMo_{0.65}Ni_{0.35}O_{6-\delta}$
SFMTi	$Sr_2FeMo_{0.65}Ti_{0.35}O_{6-\delta}$
SFMMn	$Sr_2FeMo_{0.65}Mn_{0.35}O_{6-\delta}$

SFMCo	$Sr_2FeMo_{0.65}Co_{0.35}O_{6-\delta}$
SFMCu	$Sr_2FeMo_{0.65}Cu_{0.35}O_{6-\delta}$
LSM	Lanthanum Strontium Manganite
TEC	Thermal Expansion Coefficient
EDX	Energy-Dispersive X-Ray Spectroscopy
XRD	X-Ray Diffraction
TEM	Transmission Electron Microscopy
XPS	X-Ray Photoelectron Spectroscopy
HAADF	High-Angle Annular Dark-Field Imaging
HRTEM	High-Resolution Transmission Electron Microscopy
TGA	Thermo Gravimetric Analysis
SEM	Scanning Electron Microscopy
MFCs	Mass Flow Controllers

Symbols

ΔH	Enthalpy Change	$kJ \cdot mol^{-1}$
ΔG	Gibbs Free Energy Change	$kJ \cdot mol^{-1}$
ΔS	Entropy Change	$kJ \cdot K^{-1}$
T	Temperature	K / °C
F	Faraday's Constant	$C \cdot mol^{-1}$
N	Number of Transferred Electrons	-
E_{tn}	Thermoneutral Voltage	V
σ	Conductivity	$S \cdot cm^{-1}$
I	Current	A
i	Current Density	$A \cdot cm^{-2}$
i_0	Exchange Current Density	$A \cdot cm^{-2}$
D^*	Oxygen Diffusion Coefficient	$cm^2 \cdot s^{-1}$

k^*	Surface Exchange Coefficient	$\mathrm{cm} \cdot \mathrm{s}^{-1}$
$\Re$	Universal Gas Constant	$\mathrm{J} \cdot \mathrm{mol}^{-1}\mathrm{K}^{-1}$
p	Partial Pressure	Pa
E_{cell}	Standard Cell Potential	V
E_{Nernst}	Nernst Potential	V
E^0	Standard Cell Potential	V
η	Concentration Overpotential	V
α_{i}	Charge-Transfer Coefficient of the Anodic or Cathodic Process	-
R_Ω	Area Specific Ohmic Resistance	$\Omega \cdot \mathrm{cm}^2$
R_{P}	Area Specific Polarization Resistance	$\Omega \cdot \mathrm{cm}^2$
D	Diffusion Coefficient	$\mathrm{m} \cdot \mathrm{s}^{-1}$
D^{eff}	Effective Diffusion Coefficient	$\mathrm{m} \cdot \mathrm{s}^{-1}$
i_{L}	Limiting Current Density	$\mathrm{A} \cdot \mathrm{cm}^{-2}$
c_{R}	Reactant Concentration	
c^*_{R} / c^0_{R}	Reactant Concentration in Bulk Gas Phase	
f	Frequency	Hz
f_1	Decay Rate to Products	-
J	Reaction rate	$\mathrm{mol} \cdot \mathrm{s}^{-1}$
$\mathfrak{L}$	Thickness	μm
t	Time	min
j	Imaginary number	
ω	Angular Frequency	s^{-1}
ϕ	Phase angle	rad
V	Voltage	V

L	Inductance	H
C	Capacitance	F
Z^*	Complex Impedance	Ω
Z^*_{k}	Complex Impedance for Circuit Element k, with k = R, L, C or CPE	Ω
Z''	Imaginary Part of the Complex Impedance	Ω
Z'	Real Part of the Complex Impedance	Ω
m_{CPE}	CPE Fit Parameter	
d	Diameter	m

1. Motivation

The detrimental impact of fossil-fuel-based energy carriers on the global climate has led to an increased interest in carbon-neutral energy technologies such as wind, solar, and biomass to renewably generate power. To facilitate the large-scale integration of renewables, enable efficient global energy logistics and locally support the balancing of the power grid, temporarily unused electrical power can be converted through electrochemical reduction of steam (H_2O), carbon dioxide and hydrocarbons to hydrogen (H_2) and carbon monoxide (CO). These gases can be used as a sustainable feedstock for the chemical industry (power-to-X, power-to-fuel, power-to-chemicals, power-to-heat). Green hydrogen produced by renewably generated power sources is considered essential for a sustainable transition of the energy system as a coupling element for different sectors due to its versatile application possibilities. The highly efficient electrochemical production of H_2 and CO is possible in a traditional oxide ion-conducting electrolysis cell[7].

Solid Oxide Electrolysis Cells (SOECs) are typically operated at elevated temperatures above 600 °C, which results in lower ohmic losses compared to alkaline and proton exchange membrane electrolyzers as well as advantageous kinetics and thermodynamics. In comparison, the energy efficiency of up to 100% and the use of inexpensive catalyst materials make SOEC systems more cost-effective as well[8]. In contrast to solid oxide cells in fuel cell mode, the SOEC stack designs still exhibit higher degradation rates, depending on the respective operating conditions applied, for example, current density. Long-term system durability is a key challenge to the increased economic competitiveness and more widespread industrial implementation of SOEC technology in the future. Foremost, the reliable long-term performance of an SOEC stack system requires all components to be thermally stable. However, state-of-the-art systems have shown several lifetime issues related to single-stack components. The main challenge for the long-term and large-scale deployment of SOEC technology is the electrode durability. One of the most critical factors determining the stability and performance of solid oxide electrolysis cells is the electrode/electrolyte interface evolution. The typical changes that are considered detrimental to the cell performance include microstructural changes, interfacial reactions, micropore formation, and element segregation/diffusion as well as subsequent deterioration of the electrode surface functionality[5].

Previous studies on the degradation behavior of the state-of-the-art Ni Yttria-Stabilized Zirconia (YSZ) cermet (Ni-8YSZ) fuel electrode have shown two predominant degradation mechanisms during electrolysis that lead to microstructural

changes: coarsening/agglomeration of the Ni particles, and the migration of Ni from the electrode/electrolyte interface[9–12]. Ni serves as both a catalyst and an electron conductor in the electrode, but it also exhibits high mobility with high steam partial pressure and in the temperature range of 650 - 950 °C. Changes in local Ni concentrations or the dislocation of Ni particles within the electrode layer, therefore, have a strong influence on the electrode performance.

Ni-free perovskite fuel electrodes with mixed ionic and electronic conductive properties are considered an alternative to Ni-cermet fuel electrodes due to their high catalytic activity, good conductivity, high chemical and thermal stability, as well as higher reactive surface area. Among the considered perovskite materials are $La_{0.4}Sr_{0.4}TiO_{3-\delta}$ (LST)[13], $La_{0.75}Sr_{0.25}Cr_{0.5}Mn_{0.5}O_{3-\delta}$ (LSCM)[14], $Sr_2FeNbO_{6-\delta}$ (SFN)[15], as well as $Sr_2FeMoO_{6-\delta}$ (SFM)[16–18]. SFM has been considered especially due to its excellent redox-stability, good catalytic performance, and reported long-term stability in fuel cell mode for symmetrical cells[19–21]. However, the long-term stability for SFM as fuel electrode material in humidified electrolysis for H_2 and synthesis gas production has not been investigated yet.

This thesis therefore focuses on the investigation of alternative Ni-free double perovskites $Sr_2Fe_{2-x}Mo_{x-y}M_yO_{6-\delta}$ for the application as fuel electrode material in steam, co- and CO_2 electrolysis. The strontium iron molybdenum fuel electrode with the formula $Sr_2FeMoO_{6-\delta}$ as well as the composite electrode $Sr_2FeMoO_{6-\delta}$-$Ce_{0.8}Gd_{0.2}O_{1.9}$ were prepared and electrochemically tested in the range of 750 °C to 900 °C. The physicochemical properties of the materials were characterized using in-situ techniques to determine the thermal expansion behavior, the total conductivity in oxidizing and reducing atmospheres, as well as the chemical processes during the steam (H_2O), CO_2 and co-electrolysis reactions. Long-term SOEC operation was investigated at $-0.3\ A \cdot cm^{-2}$ and 900 °C with 50% H_2O + 50% H_2 (steam electrolysis) fuel gas composition. To increase the performance, the synthesized materials were doped on the B-site and the double perovskite $Sr_2FeMo_{0.65}M_{0.35}O_{6-\delta}$ was analyzed in terms of performance and long-term durability up to 500 h in steam electrolysis. Furthermore, the performance and durability of the synthesized SFM materials were tested in CO_2 electrolysis conditions (80% CO_2 + 20% CO) and compare to state-of-the-art Ni cermet electrodes.

2. Solid Oxide Electrolysis Cells

The following chapter describes the working principles of Solid Oxide Electrolysis Cells (SOECs), including all cell components, their state-of-the-art materials in current industrial use and the main stability issues leading to degradation and cell performance loss. Parts of this chapter have been published under the CC BY 3.0 (http://creativecommons.org/licenses/by/3.0/)[5] with graphical support given by S. B. C. Lehmann.

2.1 Working Principles

Solid Oxide Electrolysis (SOE) is operated in ceramic cells with a solid oxide electrolyte and electrodes made of metals or metal oxides (cermets). The solid oxide electrolyte necessitates elevated operating temperatures between 650 °C to 900 °C, to achieve high ionic conductivity. Figure 2.1 shows the schematic working principles during electrolysis operation. The reactive sites of the electrolysis reaction at the negatively charged fuel electrode are located at the Triple Phase Boundary (TPB), which is the interface between the electron-conducting electrode, the gas phase, and the ion-conducting electrolyte. Here, the gaseous reactants pass over the electrode and are reduced due to the external power supply to give gaseous products. Oxygen ions are generated, which migrate through the electrolyte to the positively charged oxygen electrode, where they are oxidized to oxygen (O_2).

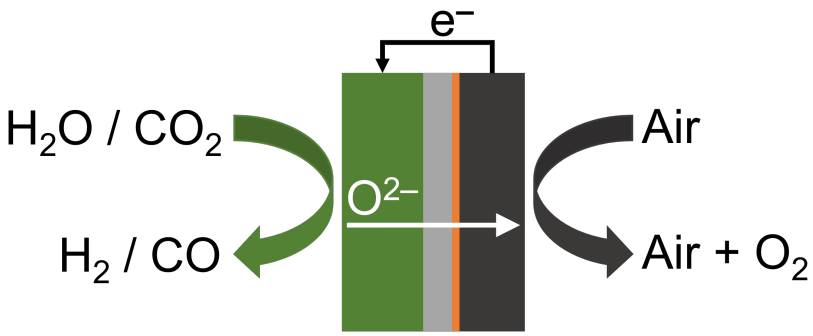

Figure 2.1: Working principle of high-temperature electrolysis in a solid oxide cell.

The Solid Oxide Electrolysis Cells (SOECs) can be operated with a wide range of inlet fuels such as steam (H_2O) or carbon dioxide (CO_2), which will determine the composition of the gaseous product. During steam electrolysis, H_2O is reduced at the fuel electrode to hydrogen (H_2) and oxygen ions (Equation 2.1). The oxygen ions pass through the ion-conducting electrolyte to the oxygen electrode, where they are further oxidized to molecular oxygen (Equation 2.2). The total redox reaction

is made of both half-cell reactions given in Equation 2.1.

$$2\ H_2O + 4\ e^- \longrightarrow 2\ H_2 + 2\ O^{2-} \tag{2.1}$$

$$2\ O^{2-} \longrightarrow 4\ e^- + O_2 \tag{2.2}$$

$$2\ H_2O \longrightarrow 2\ H_2 + O_2 \tag{2.3}$$

Analogous, CO_2 is reduced to carbon monoxide (CO) and oxygen ions in the same chemical reaction mechanism in CO_2 electrolysis as given in Equations 2.4 to 2.6.

$$2\ CO_2 + 4\ e^- \longrightarrow 2\ CO + 2\ O^{2-} \tag{2.4}$$

$$2\ O^{2-} \longrightarrow 4\ e^- + O^{2-} \tag{2.5}$$

$$2\ CO_2 \longrightarrow 2\ CO + O_2 \tag{2.6}$$

The simultaneous conversion of steam and carbon dioxide is a distinguished advantage of high-temperature solid oxide electrolysis and is called co-electrolysis. A gas mixture CO_2 and H_2O is reduced to a mixture of CO and H_2, called syngas.

$$CO_2 + H_2O \longrightarrow CO + H_2 + O_2 \tag{2.7}$$

This gas mixture is essential for today's chemical industry[22–24]. A unique advantage of SOECs is that different ratios of H_2:CO can be set in SOE depending on the reaction conditions during the co-electrolysis process specifically tailored for downstream processes like a Fischer-Tropsch process. The operating conditions impact the process equilibrium of the (reverse) water gas shift reaction ((R)WGS) (Equation 2.8). This results in varied gas mixtures of H_2O, CO_2, CO, and H_2 in the product gas stream.

$$CO_2 + H_2 \leftrightarrow H_2O + CO \tag{2.8}$$

2.2 Thermodynamics

The high-temperature electrolysis of H_2O and CO_2 requires the supply of energy, given by the change in enthalpy $\Delta H(T)$, in form of electrical energy and thermal energy (Equation 2.9). The electrical energy demand for the electrolysis is given by the Gibbs free energy change $\Delta G(T)$ and the supply-demand of thermal energy or heat is determined by the product of reaction temperature and entropy change $T\Delta S(T)$.

$$\Delta H(T) = \Delta G(T) + T \cdot \Delta S(T) \tag{2.9}$$

The equilibrium voltage of the electrolysis $E_{\mathrm{eq}}(T)$ cell necessary for the endother-

mic chemical reaction ($\Delta H(T) > 0$) at standard pressure (1 bar) is defined by the change in Gibbs free energy as shown in Equation 2.10, where F is Faraday's constant (96485 C·mol^{-1}) and n gives the number of transferred electrons per reaction.

$$E_{\mathrm{eq}}(T) = \frac{\Delta G(T)}{nF} \tag{2.10}$$

The thermoneutral voltage E_{tn} gives the minimum potential that is required for the electrolysis process in case the thermal energy demand is compensated with electricity. A cell polarized at E_{tn} produces the necessary power to satisfy the thermal energy demand $T\Delta S(T)$ and the electrolysis system's external thermo-management only has to compensate for the heat loss to the surrounding environment. The extent of heating or cooling of the system depends on the insulation: Cooling is necessary for $E_{\mathrm{cell}} > E_{\mathrm{tn}}$, while heating is required in the case of $E_{\mathrm{eq}} < E_{\mathrm{cell}} < E_{\mathrm{tn}}$.

$$E_{\mathrm{tn}} = \frac{\Delta H}{nF} \tag{2.11}$$

The development of the reaction enthalpy ΔH and the Gibbs free energy change ΔG over temperature is illustrated in Figure 2.2 for the electrolysis of H_2O and CO_2 from room temperature up to the operating temperature range at standard pressure (1 bar). The minimum potential necessary for both reactions is given by ΔG and decreases in case of H_2O and CO_2 electrolysis. An exception is the phase change from liquid water to steam at 100 °C. The reaction enthalpy ΔH, on the other hand, remains nearly constant in the range of operation temperatures for SOECs between 650 °C to 900 °C. In consequence, the entropy term ($T\Delta S(T)$) in Equation 2.9 increases and a larger amount of the enthalpy can be supplied with external heat, as the electrical energy demand decreases. These thermodynamics make high-temperature electrolysis in solid oxide cells the most efficient technology with electrical efficiencies reported around 80 - 90%[26].

In co-electrolysis, the Gibbs free energy change for H_2O and CO_2 reduction around 827 °C becomes significant. Above 827 °C, the Gibbs free energy for the CO_2 reduction decreases and is thereby lower than for H_2O reduction. This results in an equilibrium shift of the ((R)WGS) towards the production of CO.

2.3 Solid Oxide Cell Configurations

SOECs are predominantly tested in a planar configuration to ease the manufacturability, e.g. for production methods like screen-printing and tape casting, thereby increasing their cost-effectiveness in addition to cell stack upscaling. The cells' support is the thickest layer, which determines the overall cell properties like the Area

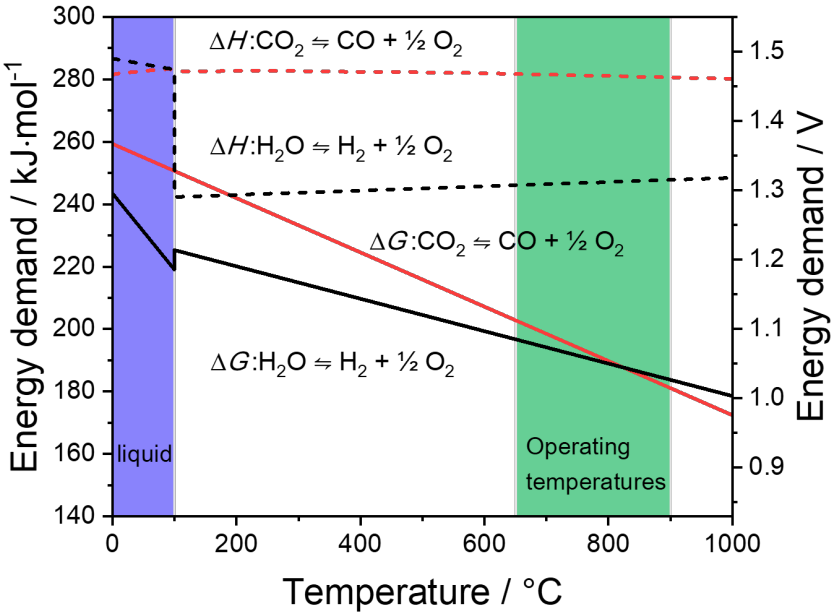

Figure 2.2: Schematic energy demand for H_2O and CO_2 electrolysis based on thermodynamics[25].

Specific Resistance (ASR), the contribution of the electrochemical processes to the cells' resistance, the optimum operating temperature range, and the mechanical cell properties. The two different support types mainly manufactured in the industry are shown in Figure 2.3 and include Fuel Electrode-Supported Cells (FESCs), as well as Electrolyte-Supported Cells (ESCs). Regardless of cell design, each cell requires a thick mechanical support layer, which ensures good handleability during processing and absorbs the thermal stresses that may result from Solid Oxide Cell (SOC) operation.

Electrolyte-supported cells have a thick electrolyte layer of 90 - 250 µm in between electrodes with a thickness of 15 - 20 µm[9,27–29]. Compared to electrode-supported cells, ESCs exhibit higher mechanical stability and better redox behavior [9,28,29]. The ionic resistivity of the thick electrolyte support layer partially stabilized zirconia is the main contributor to the cells' total resistance, which leads to lower power densities and necessitates high operating temperatures over 850 °C. These high operating temperatures require good thermal insulation and expensive thermostable materials[28,30,31]. In fuel electrode-supported cells, the mechanical support is given by a thick porous electrode layer of around 250 - 400 µm, on which an active fuel electrode layer of ∼5 - 20 µm is deposited. The electrolyte layer can be significantly thinner (2 - 10 µm)[27] than for ESCs, which leads to a decrease in ohmic resistance and allows lower operating temperatures of 650 °C to 800 °C. The main resistance contribution originates from the electrode transport

processes. Electrode-supported cells exhibit higher power densities, but also lower redox-stability important for redox-cycling[29,32].

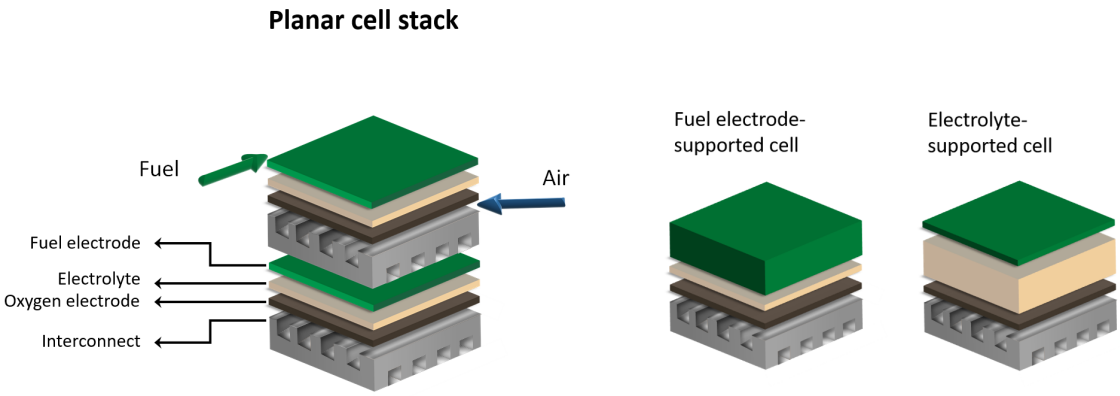

Figure 2.3: Scheme of the planar cell design and two different cell support types reported in current literature: Fuel electrode-supported cells, and electrolyte-supported cells. Reproduced scheme from[5], which is licensed under CC BY 3.0 (http://creativecommons.org/licenses/by/3.0/), © 2023 by the authors.

2.4 Solid Oxide Cell Materials

2.4.1 Electrolyte

The ion-conducting electrolyte separates the fuel and oxygen electrode and consequently must be stable in both reducing and oxidizing atmospheres. Thickness, material properties, and operating temperature impact the performance of the cell as well as the electrolyte itself. High ionic conductivity ($>0.1\ S \cdot cm^{-1}$)[33] and negligible electronic conductivity at operating temperatures are essential to lower ohmic resistance and avoid current leakages. High operating temperatures increase the ionic conductivity of the materials and promote thermally activated electrochemical processes. For electrolyte-supported cells, the electrolyte material governs the thermal expansion of the full multi-layer cell, thus preventing delamination of other layers, such as the electrodes, caused by a thermal expansion mismatch[34,35].

The state-of-the-art electrolyte material for electrolyte- and fuel electrode-supported cells (ESCs, FESCs) is Yttria-Stabilized Zirconia (YSZ), which has good oxygen ionic conductivity between 700 °C - 900 °C, good mechanical properties and excellent chemical stability over a wide range of oxygen partial pressures and operating temperatures[36–39]. The direct substitution with 8 - 10 mol% yttria stabilizes the cubic fluorite structure of ZrO_2 and creates large oxygen vacancy concentrations

through charge balance. 8 mol% YSZ (8YSZ) exhibits the highest conductivity of $0.14\,\mathrm{S}\cdot\mathrm{cm}^{-1}$ at 1000 °C and is still the material of choice for fuel electrode-supported as well as electrolyte-supported cells[40]. Other divalent and trivalent dopants e.g. Sc^{3+} have been used to stabilize ZrO_2, their ion radius greatly impacting the ionic conductivity.

Fluorite-type doped ceria is a material with higher ionic conductivity than stabilized zirconia at medium operating temperatures from 600 °C to 800 °C and reaches its maximum conductivity around 15 mol% of dopant e.g. Gd, Sm, or Y. Doped ceria electrolytes exhibit undesirable electrical conductivity and possible mechanical instability in a reducing environment as a result of Ce^{4+} reduction to Ce^{3+}[34,41]. Therefore, Gadolinium-Doped Ceria (GDC) electrolytes are mostly used at lower operating temperatures (∼600 °C) to avoid electronic leakage at elevated temperatures. In this case, an additional very thin YSZ electron blocking layer is applied to circumvent electron leakage[5,42].

2.4.2 Fuel Electrode

The fuel electrode exhibits excellent catalytic activity for the Hydrogen Evolution Reaction (HER) and high chemical stability in an reducing atmosphere without microstructural changes and formation of insulating phases with the electrolyte material. The thermomechanical expansion properties should be similar to those of the electrolyte (10 - $12{\cdot}10^{-6}$ $°C^{-1}$) to avoid thermal stresses upon heating or cooling. High electric and ionic conductivities over 10^3 $\mathrm{S}\cdot\mathrm{cm}^{-1}$ and 10^{-3} $\mathrm{S}\cdot\mathrm{cm}^{-1}$, respectively, are required for good ion transport, and a high conversion rate, which results in low ohmic cell resistance. The most important property of the fuel electrode, however, is its long-term chemical stability over a wide range of pO_2, including reducing atmospheres in H_2 and CO, oxidizing conditions with high partial pressures of H_2O and CO_2, as well as different carrier gases (N_2, Ar) and the sintering process typically conducted in air during cell fabrication.

The state-of-the-art fuel electrode material is Ni cermet, which was previously developed for Solid Oxide Fuel Cells (SOFCs). This electrode type uses a mixture of Ni (electron-conductor) and electrolyte material (ion-conductor) e.g. 8YSZ or GDC to match the electrolyte's thermal expansion behavior. The reactant molecules are reduced at the TPB, where gaseous reactants, electronic, and ionic conductor meet. Subsequently, the oxide ions migrate through the ion-conducting electrolyte to the oxygen electrode.

Ni-8YSZ Cermet Electrodes

The most commonly used fuel electrode is made of Ni-8YSZ cermet, although recent research interest considers gadolinium-doped ceria (Ni-GDC) electrodes as well. During the fabrication process, NiO-8YSZ electrodes are produced and the NiO is reduced in-operando to Ni, thereby forming the Ni cermet electrode. The performance of the cermet electrode depends strongly on the Ni content, electrode microstructure (e.g. particle size, particle distribution) and the percolation networks. High amounts of Ni grant the cermet electrode a very good electrical conductivity, but also impact the electrode's Thermal Expansion Coefficient (TEC) detrimentally, by increasing the thermomechanical mismatch with the electrolyte material[43]. The ratio of Ni and 8YSZ particles has a strong impact on the electric conductivity and the optimal Ni content was found to be between 30 - 40 vol% with an electric conductivity of >1300 $S \cdot cm^{-1}$ at 680 °C[44]. By increasing the 8YSZ particle size, percolation can be achieved at a smaller volumetric ratio. The connectivity of the Ni particles is essential for stable electrode performance and is directly linked to the electrode's porosity. 30% to 35% of reduced Ni is necessary and translates to around 40 vol% NiO. Commercial fuel electrode-supported SOCs show low cell area specific resistances at open-circuit voltage of less than 140 $m\Omega \cdot cm^2$ (800 °C, 50 % H_2 + 50% H_2O)[2].

Ni cermet fuel electrodes exhibit higher degradation rates in SOECs operation especially at higher current densities, in comparison to their use in fuel cell mode despite their excellent initial performance for high-temperature electrolysis[9,11,45–50]. The fuel electrode degradation was observed to be the main degradation process in SOECs and is dependent on the microstructure and operating parameters, such as, polarization/overpotential, current density, gas humidity, temperature, and the local redox potential of the respective gas composition[9–11,46,51]. During cell manufacturing, the sintering temperature impacts cell microstructure and performance. Possible detriment processes depending on the temperature are particle agglomeration and growth as well as cation interdiffusion between electrode and electrolyte[52]. The main degradation mechanisms that occur during long-term electrolysis are Ni migration from the electrolyte/fuel gas electrode interface and Ni particles coarsening (Ni agglomeration).

The Ni particles agglomeration occurs without influence of operating mode and polarization and is credited to an Ostwald ripening process at high gas humidity[9–11]. The average particle size increases with a decrease in catalytic area, as larger particles grow at the cost of smaller sized particles to minimize the systems surface free energy. Higher steam partial pressure on small particles results in a concentration

gradient and, thus, mass transport from the smaller particles through the gas phase or surface diffusion. An alternative mechanism describes the Ni particle coarsening as a result of high particle mobility and subsequent $Ni(OH)_x$ formation. As Ni particle diameter increases, the Ni particle percolation networks is reduced. This leads to a rapid decrease in electrical conductivity and catalytic activity as the TPB length and of the porosity at the electrode/electrolyte interface are reduced[9,51,53]. Ni particles migration from the TPB toward the electrode substrate, leads to Ni loss in the active layer near the electrolyte, a decreased electrical conductivity and catalytic activity as well as reduced TPB length and electrode porosity in the active layer. The electrode's porosity, the catalytic TPB length, and the number of percolating Ni particles are reduced with higher current densities[9,46]. Different hypotheses are currently discussed in literature to explain the Ni particle migration during electrolysis and the underlying mechanisms[9–12,51].

Mogensen et al.[51] suggested that the Ni particle migration is electrical potential driven and leads to temperature dependent surface diffusion of $Ni(OH)_x$ species (<800 °C) and gas phase diffusion of Ni hydroxides (≥ 900 °C). They identified the main parameters affecting migration as the local overpotential of the Ni particles, the local pH_2O, and the activity of the $Ni(OH)_x$ species. In the case of strong negative polarization (SOE) at temperatures between 800 - 900 °C, the strong cathodic overpotential leads to a contact loss between 8YSZ and the polarized Ni particles. This leads to decreased electrical conductivity and catalytic activity as well as a reduced TPB length and porosity at the electrode/electrolyte interface. The Ni particles move down the electrochemical and/or pO_2 potential gradients toward relative negative potential against the H_2O gradient (pO_2)[10,51]. Consequently, the TPB region moves further away from the electrolyte, which results in a higher ohmic cell resistance[9,54,55]. Additionally, percolation between Ni particles is reduced and the electronically insolated Ni particles obtain the pO_2 potential of the local gas composition[51]. The local pH_2O around the particles increases, as more H_2O molecules migrate towards the electrolyte without hydrogen evolution taking place at polarized Ni particles in the TPB. This leads to a local pH_2O minimum around the Ni particles of the new TPB. $Ni(OH)_x$ species activity is proportional to the potential and the lowest potential is at the lowest pH_2O at the new TPB. Therefore, the Ni particle migrate to and precipitate near the new active TPB.

Different authors are in agreement that the locally prevailing polarization is a significant contributor to the Ni migration and agglomeration process[9–12]. Sun et al.[12] found that the degradation rate increases with increasing cathodic/negative polarization of the fuel electrode. According to his hypothesis, the polarization

increases the tendency of Ni particles to separate from 8YSZ and subsequent migrate to less polarized electrode regions. The underlying mechanism is a demixing process of the electrode, causing vacancy accumulation and Ni particle dissolution from the composite electrode. The Ni migration is explained by the authors through gaseous $Ni(OH)_x$ species influenced by the steam partial pressure[5].

Strontium Iron Molybdenum Oxide – $Sr_2Fe_{2-x}Mo_xO_{6-\delta}$

Perovskite-based alternative fuel electrode materials with mixed ionic and electronic properties (Mixed Ionic and Electronic Conductors (MIECs)) have gathered interest due to their high catalytic activity, high chemical and thermal stability, as well as their high electric and ionic conductivity. In contrast to Ni cermet electrodes, they facilitate the HER throughout their entirely electrochemically active electrode surface (Double Phase Boundary (DPB)) in addition to the TPB. Thus, MIECs allow for large surface exchange rate constants (Figure 2.4)[5]. To prevent Ni-related degradation mechanism on the fuel electrode side, Ni-free perovskite materials with mixed ionic and electronic conductive properties are considered. The considered MIEC fuel electrode materials include $La_{0.75}Sr_{0.25}Cr_{0.5}Mn_{0.5}O_{3-\delta}$ (LSCM)[14], $Sr_2FeNbO_{6-\delta}$ (SFN)[15], $La_{0.4}Sr_{0.4}TiO_{3-\delta}$ (LST)[13], $(PrBa)_{0.95}(Fe_{0.9}Mo_{0.1})_2O_{5+\delta}$ (PBFM)[56] as well as $Sr_2FeMoO_{6-\delta}$ (SFM). Among the considered MIEC materials the double perovskite $Sr_2Fe_{2-x}Mo_xO_{6-\delta}$ ($0.5 \leq x \leq 1.5$), has gathered widespread interest due to its excellent redox-stability, good catalytic performance, and reported long-term stability in fuel cell mode for symmetrical cell tests[4,5,16,19,57–60].

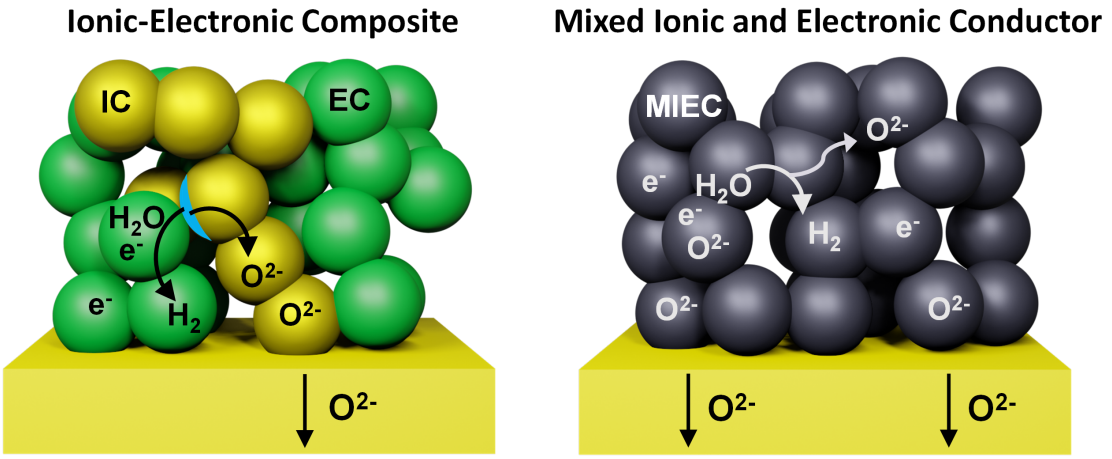

Figure 2.4: Scheme of steam reduction and hydrogen evolution reaction occurring at the TPBs in an ionic-electronic composite as well as at the DPBs in mixed ionic and electronic conductor materials for the fuel electrode.

The Mo-doped $SrFeO_{3-\delta}$ has shown high sensitivity of the B-site cation order

on physical properties such as electrical conductivity, oxygen defect formation, and catalytic activity by the incorporation of high-valence Mo ions, which influence the oxidation state of iron in the perovskite[61–63]. With increasing Mo dopant concentration in the brownmillerite structure $SrFeO_{3-\delta}$ in oxidizing atmosphere, the activation energy for oxygen transport decreases[64,65]. At higher Mo doping ($0.5 \leq x \leq 1.5$), the structure crystallizes as a double perovskite $Sr_2Fe_{2-x}Mo_xO_{6-\delta}$[66–68]. In this B-cation ordered double perovskite, the B-site is occupied with alternating Fe and Mo ions, which results in each FeO_6 octahedron being surrounded by six corner-sharing MoO_6 octahedra as illustrated in Figure 2.5[66–68]. The two different transition metal (TM) cations, found at the B-site, govern material properties like electrical conductivity, thereby offering higher flexibility compared to ABO_3 perovskites. The ferromagnetic $Sr_2FeMoO_{6-\delta}$, in contrast, can only be synthesized under reducing conditions due to the lack of Mo solubility in oxidizing atmosphere, which leads to the formation of $SrMoO_4$[69,70]. The high ionic conductivity of 0.13 $S \cdot cm^{-1}$ observed for the p-type conducting double perovskite $Sr_2Fe_{1.5}Mo_{0.5}O_{6-\delta}$ originates from weak Fe-O bonds[21]. Upon removal of the neutral oxygen atom, an extra charge delivered to the lattice is fully delocalized, thus forms a high concentration of oxygen vacancies[71]. The total conductivity of $Sr_2Fe_{1.5}Mo_{0.5}O_{6-\delta}$ measured at 800 °C was 32 $S \cdot cm^{-1}$ in H_2 and 14.90 $S \cdot cm^{-1}$ in air at 750 °C[72,73]. In an atmosphere of 50% CO_2 + 50% CO at 750 °C, SFM shows an electrical conductivity of 19 $S \cdot cm^{-1}$[16]. These results show that the conductivity of SFM is higher than those of other ceramics such as $La_{0.75}Sr_{0.2}Cr_{0.5}Mn_{0.5}O_{3+\delta}$ (LSCM) or $La_{0.2}Sr_{0.8}Ti_{0.9}Mn_{0.1}O_{3+\delta}$ (LSTO)[5].

2.4.3 Oxygen Electrode

The oxygen electrode requirements are similar to the fuel electrode with an emphasis on high chemical stability in an oxidizing environment without the formation of insulating phases with the electrolyte. The catalytic activity, electrode kinetics, and transport properties of the oxygen electrode are expressed through the oxygen diffusion coefficient D^*, the surface exchange k^*, the exchange current density i_0 and further influenced by microstructural parameters such as electrode porosity ϵ, tortuosity τ, and oxygen surface concentration C_0, grain size (distribution) and electrode thickness ("active penetration depth"). Perovskite materials have replaced noble metal electrodes in the last decades as they meet these characteristics, are less expensive and highly compatible with the electrolyte materials[5].

Oxygen-deficient Perovskites $ABO_{3-\delta}$

The simple perovskite structure ABO_3 crystallizes in an ideal cubic structure. The larger A-site cations, typically rare-earth, alkaline-earth, or alkaline ions with a low

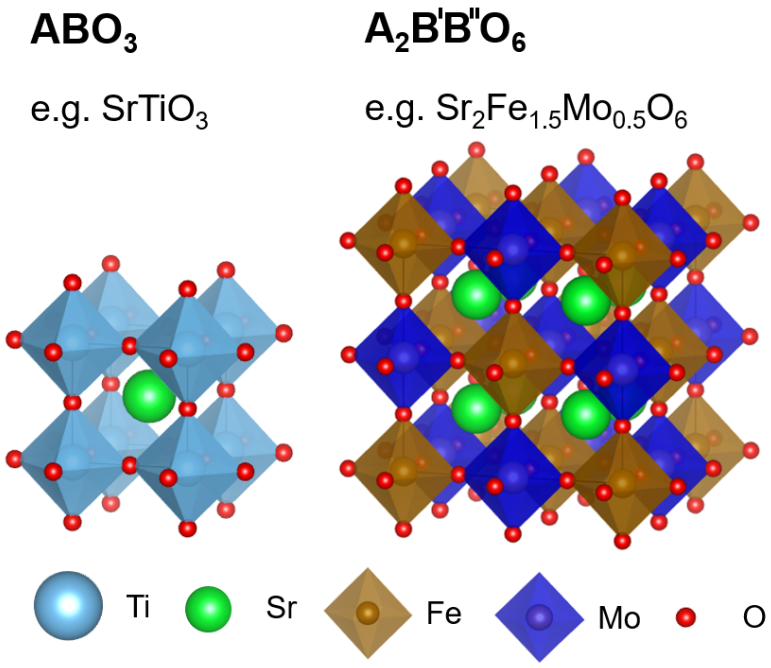

Figure 2.5: Crystal structure of fuel electrode materials for the simple $SrTiO_3$ perovskite and the double perovskite $Sr_2FeMoO_{6-\delta}$. The crystal structures were produced with VESTA©[74].

charge, are coordinated by twelve oxygen ions at the cubes' corners. The smaller B-cations of transition metal sites in the cubic center and are coordinated octahedrally by the anions. Lanthanum Strontium Manganite (LSM) $La_{1-x}Sr_xMnO_{3-\delta}$ is known for its high structural stability, which increases with the A-cation radius. The partial substitution of the trivalent rare-earth La^{3+} cation with the divalent Sr^{2+} cation induces p-type conductivity through the formation of an electric hole at the B-site. This makes LSM a pure electronic conductor with high electrical conductivity σ_e, which increases with higher Sr doping up to a conductivity of 200 - 490 $S \cdot cm^{-1}$ for $La_{0.5}Sr_{0.5}MnO_{3-\delta}$ at 1000 °C[75–77]. The ionic conductivity σ_i remains low at around $5.93{\cdot}10^{-7}$ $S \cdot cm^{-1}$[78].

Today's state-of-the-art oxygen electrode materials are the mixed-ionic and electronic conductors cobalt-based lanthanum strontium (ferrite) oxides $La_{1-x}Sr_xCoO_{3-\delta}$ (LSC) and $La_{1-x}Sr_xCo_{1-y}Fe_yO_{3-\delta}$ (LSCF). They have shown higher catalytic activity as well as structural and performance stability under long-term SOEC operation conditions in comparison to LSM. The electronic conductivity of LSC(F) (200 - 1200 $S \cdot cm^{-1}$) is higher compared to LSM (200 $S \cdot cm^{-1}$)[79]. The ionic conductivity and the transport properties surpass LSM as well with $8.0{\cdot}10^{-3}$ $S \cdot cm^{-1}$ at 800 °C[80]. The ionic conductivity is directly linked to the ratio of Co:Fe and increases for a higher amount of Co. This leads to an ionic conductivity of 0.22 $S \cdot cm^{-1}$ at 800 °C

for $La_{0.6}Sr_{0.4}CoO_{3-\delta}$ and an electronic conductivity around 1585 $S \cdot cm^{-1}$[79,80]. Compared to LSM, the cobalt-based lanthanum strontium (ferrite) oxides have shown higher oxygen surface exchange and higher oxygen self-diffusion coefficients[5].

Degradation processes at the oxygen electrode occurring during the electrolysis reaction have been related to the difference in oxygen activity and catalytic activity for the Oxygen Evolution Reaction (OER) in comparison to the Oxygen Reduction Reaction (ORR) in SOFC mode[81]. In the electrolysis reaction, a larger pO_2 gradient across the electrode/electrolyte interface promotes oxygen bubble formation at the interface and subsequent degradation phenomena such as micropore formation and electrode delamination. Cell performance loss under electrolysis conditions has been attributed also to interfacial reactions, and element segregation/diffusion. The electrode's surface functionality deteriorates due to cation segregation, formation of an insulating layer and obstruction of oxygen and charge transfer reactions. The segregation of volatile Sr species is well known to occur in operation of LSC(F)-based electrodes and has been linked to the decrease of surface stability, structural distortion, the ion mobility as well as operating conditions (temperature, polarization)[82–85].

To prevent the formation of an insulating $SrZrO_3$ layer with the 8YSZ electrolyte, cobaltite-based electrodes are used in combination with a ceria-based barrier layer in-between electrode and zirconia-based electrolyte[86,87]. However, Sr segregation and $SrZrO_3$ growth at the 8YSZ/GDC interface has been reported for LSCF electrodes. The cause could be Sr cation diffusion through grain boundaries or pores of the GDC layer[5,84].

3. Electrochemical Methods

3.1 Current-Voltage Characteristics

The performance of high-temperature solid oxide cells (SOCs) is measured by current-voltage characteristics, also called iV-curves, which relate the voltage of an electrochemical system to a given current density load or the reverse. The measurements can be performed potentiostatically as well as galvanostatically with a potentiostat/ galvanostat system. Solid oxide cells with increased performance exhibit a higher current density at a given voltage in comparison to lower-performing cells. A prerequisite for the measurement of iV characteristics is the thermal and chemical system equilibrium. In potentiostatic iV-curve measurements, direct voltage is applied to the system and swept between two voltage limits. The corresponding current output is recorded as a function of time. The time-dependent development of the scan rate is pre-set, wherefore, subsequently the voltage can also be plotted against the observed current, yielding a so-called iV-curve plot. The total cell resistance, also called Area Specific Resistance (ASR) is a measure for cells' conversion efficiency normalized by the cell area A. The parameter can be determined from the iV curve based on the ratio of potential E and current I, which equals the system resistance (Equation 3.1).

$$ASR = A \cdot \frac{E}{I} \tag{3.1}$$

3.1.1 Electrochemical Potential and Losses

The Nernst potential E_{Nernst} of an solid oxide electrolysis cell, also called theoretical reversible potential E_{th} or Open Circuit Voltage (OCV), is determined from the Nernst Equation (3.2) and relates to the sum of standard cell potential E^0 and the chemical activity of the reactive species for an equilibrium reaction, where T is the temperature, F is the Faraday constant and $\Re$ is the universal gas constant. For an ideal gas at 1 bar the activities can be replaced by the partial pressures of the redox species[88–91].

$$E_{\text{Nernst}} = E^0 + \frac{\Re T}{2F} \ln\left(\frac{p\text{H}_2 \cdot p\text{O}_2{}^{\frac{1}{2}}}{p\text{H}_2\text{O}}\right) \tag{3.2}$$

The standard potential E^0 is given by the standard Gibbs free energy change at steady-state conditions of the electrolysis reaction (Equation 3.3).

$$E^0 = \frac{\Delta G}{2F} \tag{3.3}$$

The actual cell potential is higher in electrolysis mode than the cells' theoretical potential (Nernst) due to irreversible electrochemical losses (overpotentials). These overpotentials η_{i} result from slow reaction kinetics (activation overpotential η_{act} e.g. charge transfer), internal ionic and electronic resistivity (ohmic overpotential η_{ohm}) and mass transport limitations at the electrode surface (concentration overpotential η_{conc}). Therefore the actual potential is given by the sum of the reversible potential and all overpotentials shown in Equation 3.4[88–91].

$$E_{\mathrm{cell}} = E_{\mathrm{Nernst}} + \underbrace{\eta_{\mathrm{act}} + \eta_{\mathrm{ohm}} + \eta_{\mathrm{conc}}}_{\eta_{\mathrm{i}}} \tag{3.4}$$

Activation overpotential

To convert reactants to products, an activation barrier ($\Delta G^{\check{\mathrm{E}}}$) in form of an increase in free energy has to be overcome in a chemical reaction. The reaction rate J depends on the probability of available activated species participating in the reaction and their conversion to product species. Equation 3.5 gives the reaction rate J_1 of the reactant to product formation (forward reaction) in dependence of the reactant surface concentration c_{R}^* and the product formation rate f_1. Activated species can be converted to product, but also revert back to reactant[88–91].

$$J_1 = c_{\mathrm{R}}^* f e^{\left(\frac{-\Delta G^{\check{\mathrm{E}}}}{\Re T}\right)} \tag{3.5}$$

The overall reaction rate is given by the difference between forward and reverse reaction rates. This expression can then be translated to the activation barriers and gives Equation 3.6.

$$\Delta G = \Delta G_1^{\check{\mathrm{E}}} - \Delta G_2^{\check{\mathrm{E}}} \tag{3.6}$$

The total reaction rate J is related to the current density i by the relation $i = nFJ$, wherefore the current densities for the forward and reverse reaction can be described as follows[88–91]:

$$i_1 = nFc_{\mathrm{R}}^* f_1 e^{\left(\frac{-\Delta G_1^{\check{\mathrm{E}}}}{\Re T}\right)} \tag{3.7}$$

$$i_2 = nFc_{\mathrm{P}}^* f_2 e^{\left(\frac{-(\Delta G_1^{\check{\mathrm{E}}} - \Delta G)}{\Re T}\right)} \tag{3.8}$$

At the thermodynamic equilibrium of $i_1 = i_2$, the current densities of both reactions, forward and reverse, are balanced and the net reaction rate and therefore

the total net current density is zero. For a reaction taking place in equilibrium, the characteristic current density is called exchange current density i_0. Away from the equilibrium, the cell potential influences the free energy of the charged species, which thus affects the activation barrier of the reaction. If the Galvani potential (activation barrier) of the forward creation is reduced by η, the barrier of reverse reaction is increased. This describes that the activation overpotential η_{act} is a measure of electrode activity and its magnitude depends on the reaction kinetics at the electrolyte-electrode interface. The activation overpotential can be observed in current-voltage characteristics at low currents[88–91]. The Butler-Volmer Equation given in Equation 3.9 for the net current density i states the exponential relation between overpotential η_{act} for both electrodes and current density i, in case the reversible reaction is limited by electron charge transfer. The symmetry of the activation barrier is given by the transfer coefficient α and is always between 0 and 1, wherefore $\alpha_{\text{fuel electrode,forward}} = 1 - \alpha_{\text{fuel electrode,reverse}}$[88–91].

The activation overpotential is named as such to recognize the additional overpotential that is needed to overcome the activation barrier of the electrochemical reaction. Even though the equation is only applicable to single-electron transfer reactions, it is considered a good approximation for more complex multi-step electrochemical reactions involving multiple transferred electrons[88–91].

$$i = i_0 \left\{ \exp\left(\frac{\alpha n F \eta_{\text{act}}}{\Re T}\right) - \exp\left(\frac{-(1-\alpha) n F \eta_{\text{act}}}{\Re T}\right) \right\} \tag{3.9}$$

To improve the reaction kinetics, the exchange current density has to be increased. Equation 3.7 showcases the relevant parameters c_R^*, $\Delta G_1^{\check{\text{E}}}$ and T may be varied , while n, F, f_1 and $\Re$ remain constant. Increasing the reactant concentration c_R^* well as the operation of the solid oxide cell stack at elevated pressures, thus increasing the reactant gas concentration, can improve the reaction kinetics. A significant way to increase i_0 is the improvement of the electrode's catalytic activity, which thereby lowers the activation barrier $\Delta G_1^{\check{\text{E}}}$. An increase in operating temperature will also increase the thermal activity thus the reaction rate and i_0. The magnitude of available reaction sites at the electrode surface will improve the reaction kinetics[88–91].

The Butler-Volmer Equation can be simplified for very small or very large η_{act}. In case of very small activation overpotential ($i \ll i_0$), Equation 3.9 can be linearized using a Taylor series expansion and limited to a linear proportionality between current density and overpotential for small deviations from the equilibrium. This way, i_0 can be obtained from plotting i versus η_{act} at low η_{act} values. However, such

measurements are impacted by additional losses (ohmic, mass transport)[88–91].

$$i = i_0 \frac{nF\eta_{\text{act}}}{\Re T} \tag{3.10}$$

For large activation overpotentials ($i \gg i_0$), the forward reaction dominates, the second equation term become negligible and the Butler-Volmer Equation is shortened to the Tafel-Equation (3.11). The exchange current density i_0 and the transfer α coefficient can be determined by fitting η_{act} versus $\ln i$ (Equation 3.12).

$$i = i_0 e^{\left(\frac{\alpha n F \eta_{\text{act}}}{\Re T}\right)} \tag{3.11}$$

$$\eta_{\text{act}} = -\frac{\Re T}{\alpha n F} \ln i_0 + \frac{\Re T}{\alpha n F} \ln i \tag{3.12}$$

Ohmic overpotential

In the electrochemical system, the charges are migrating from one electrode, where they are produced, to the other electrode where they are consumed. This charge transport is predominantly driven by a potential gradient called conduction[88–91].

$$\eta_{\text{ohm}} = iR_{\text{ohmic}} = i\left(R_{\text{electrodes}} + R_{\text{electrolyte}}\right) = i\left(R_{\text{elec}} + R_{\text{ionic}}\right) \tag{3.13}$$

The potential, that is used to drive the conduction process is known as ohmic overpotential, named after Ohm's law of conduction. R_Ω is the ohmic resistance of the solid oxide cell and takes into account the intrinsic ohmic resistances from the electrolyte and the electrodes, however, is pre-dominated by the electrolyte (ionic) resistance.

Concentration overpotential

In solid oxide cells, the electrodes are supplied with a gas stream constant of constant volume flow and composition of reactants along the active electrode layer, while product species desorb from the electrode to the bulk gas phase. The species concentration in the electrode active layer impacts the cell's performance. This concentration gradient between the electrode bulk and surface of the reactant and product species is caused by mass transport limitations (diffusion). At the electrode surface, as the gas velocity approaches zero, a diffusion-dominated layer is observed, where mass transport limitations are pre-dominant. As the rapid catalytic reaction continues i.e. charge transfer, product species accumulate and the reactant concentration at the TPB sites depletes relative to the bulk concentration. This leads to an increase in the reversible cell potential (Nernst losses). At a critical current,

named limiting current density i_{L}, the reactant species is converted immediately and the reactant concentration depletes at the electrode surface (Equation 3.14). The bulk concentration c_{R}^{0}, the effective diffusivity D^{eff} and the electrode (diffusion layer) thickness $\mathfrak{L}$ can be altered to increase the limiting current density by the electrode structure, the diffusion layer thickness, ensuring even reactant distribution and enhanced diffusivity[88–91].

$$i_{\mathrm{L}} = nFD^{\mathrm{eff}}\frac{c_{\mathrm{R}}^{0}}{\mathfrak{L}} \tag{3.14}$$

The voltage loss η_{conc} results from the reactant depletion at the TPB sites, which affects both the kinetic reaction rate and the Nernst potential, given by Equation 3.15.

$$\eta_{\mathrm{conc}} = \frac{\Re T}{nF}\left(1+\frac{1}{\alpha}\right)\ln\frac{i_{\mathrm{L}}}{i_{\mathrm{L}}-i} \tag{3.15}$$

3.2 Electrochemical Impedance Spectroscopy

Electrochemical Impedance Spectroscopy (EIS) is a method to characterize frequency-dependent properties of an electrochemical system, i.e. the complex impedance, by applying a small sinusoidal excitation signal (perturbation) (alternating (AC) voltage or current) to an electrochemical system in equilibrium with an amplitude at frequency f and measuring the sinusoidal response (current or potential). Equation 3.16 describes the time-dependent excitation signal $V(t)$ with sine wave amplitude V_0 and the phase of the waveform ωt. t is the time and $\omega = 2\pi f$ the angular frequency, so the magnitude of signal oscillations per time[92–95].

$$V(t) = V_0 \cdot \sin(\omega t) \tag{3.16}$$

$$V(t)^* = V_0 e^{j(\omega t)} \tag{3.17}$$

In linear or pseudo-linear systems, the current response $I(t)$ (3.18) has the same measurement frequency f, but shows a varied amplitude I_0 in dependence of the system impedance and is shifted in phase ϕ compared to the input signal[92–95].

$$I(t) = I_0 \sin(\omega t + \phi) \tag{3.18}$$

$$I(t)^* = I_0 e^{j(\omega t+\phi)} \tag{3.19}$$

$$Z^*(\omega) = \frac{V_0 e^{j(\omega t)}}{I_0 e^{j(\omega t+\phi)}} = |Z_0|e^{j\phi} = |Z_0|(\cos\phi + j\sin(\phi)) = Z^{'} + jZ^{''} \tag{3.20}$$

The frequency-dependent complex impedance Z^* can be expressed by Equation 3.20 analogous to Ohm's Law and consists of a frequency-dependent real resistance

$Z^{'}$ and an imaginary part $Z^{''}$ with the complex unit $j = \sqrt{-1} = e^{\frac{j\pi}{2}}$ including Euler's relationship $\left(e^{j\phi} = \cos\phi + j\sin(\phi)\right)$. At a chosen radial frequency ω, the phase angle ϕ can be determined as the ratio between imaginary and real impedance, as given in Equation 3.21[92–95].

$$\phi = \arctan\left(\frac{Z^{''}}{Z^{'}}\right) \tag{3.21}$$

The impedance data measured over a wide range of frequencies are visualized in the Nyquist plot (Figure 3.1), in which the negative imaginary impedance $-Z^{''}$ is plotted on the ordinate versus the real impedance part $Z^{'}$ abscissa. Both axes are scaled equivalent, as they are parts of one complex impedance Z^{*}. Additionally, the phase angle ϕ gives the angle between the impedance vector $|Z^{*}|$, magnitude of the impedance, and the abscissa in this depiction. The characteristic frequency is given by the arc's summit and allows the determination of the time constant $\tau = \frac{1}{\omega} = \frac{1}{2\pi f}$. The frequency-independent ohmic resistance R_{Ω} of the electrochemical system in the Nyquist plot is given by the high-frequency intercept with abscissa. The total impedance, also called ASR, is determined by the low-frequency abscissa intercept and is composed of the all resistive effects caused by electrochemical processes (polarization resistance, R_{P}) in addition to the ohmic resistance[92,93].

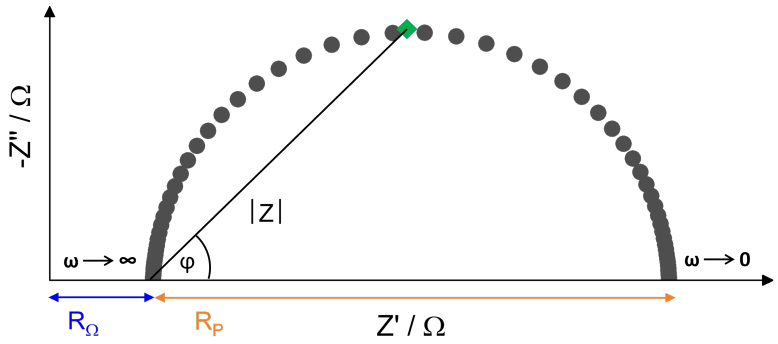

Figure 3.1: Nyquist plot representation.

3.2.1 Distribution of Relaxation Times Analysis

Electrochemical impedance spectroscopy data are typically analyzed by fitting the impedance spectra with an equivalent circuit model. However, the data quality can impact the analysis and the model decision can be complex. The Distribution of Relaxation Times Analysis (DRT) is an invaluable method to analyze and interpret

the impedance data as well as support the equivalent circuit model-based analysis. In the DRT analysis, the characteristic distribution is determined by fitting the experimental data against an ohmic resistor (R_∞) at high frequencies ($f \to \infty$) and an infinite sum of parallel resistors and capacitors in series as given by Equation 3.22[96] with $\gamma(\tau)$, as the distribution of relaxation times function. Through the DRT method, the electrochemical data are transformed from the frequency f to the time domain τ. The resulting DRT spectrum exhibits peaks at time constants that represent physical processes in the spectrum.

$$Z_{\mathrm{DRT}}(f) = R_\infty + \int_{-\infty}^{\infty} \frac{\gamma(\ln\tau)}{1 + j2\pi f\tau} d\ln\tau \tag{3.22}$$

$$\gamma(\ln\tau) = \tau\gamma(\tau) \tag{3.23}$$

In the DRT analysis, the DRT function is matched to the experimental data through the deviation between model prediction and measured data is minimized to determine the best fit. To achieve this goal, the least square errors of real and imaginary impedance data are used. However, the optimization of this problem is generally called ill-posed (Equation 3.23), i.e. a regularization (parameter) is needed to solve this problem in a physically meaningful way[96,97]. The Tikhonov regularization[98–100] is used to smooth the distribution function between neighboring time constants. The regularization magnitude impacts the data interpretation, as too high values lessen oscillations, which can reduce physically significant information (overfitting). On the other hand, besides narrower peaks, a low regularization increases probability of oscillations and satellite peaks (underfitting). The optimal regularization parameter λ is chosen such that the Sum of Square Residuals (SSR) between the initial and reproduced spectra is minimized[96,101].

3.2.2 Equivalent Circuit Modelling

The reactions in the electrochemical system are based on the transfer of charged species in reactions like charge transfer at the electrode surface, surface desorption and adsorption processes, as well as mass transfer processes (solid-state bulk diffusion, surface diffusion). The deconvolution of these processes from impedance data necessitates an Equivalent Circuit Model (ECM). The constructed circuit model should represent the physical understanding of the characterized system and account for electrode and electrolyte resistances, the capacitance and wire current-enduced inductivity. The most common passive circuit elements, which are used in series

or parallel to compose an ECM are resistors, inductors and capacitors as shown in Figure 3.2. The main challenge in the construction of an ECM is that more than one equivalent model can represent the same data set.

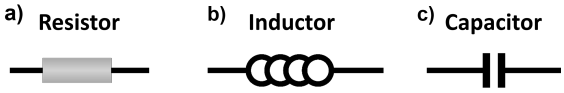

Figure 3.2: Schematic depiction of the passive element components for the model of an electrical circuit: (a) Resistor, (b) Inductor, and (c) Capacitor[92].

Resistor

The relation between potential and current for a resistor in the circuit is given by Ohm's Law in Equations 3.24 and 3.25. It concludes that the current flow $I(t)$ is directly proportional to the potential $V(t)$ across the resistor and inversely related to the resistance R_Ω. The imaginary part of the impedance of an ohmic resistor is consequently zero and is thus located on the Z' axis[93,102].

$$V(t) = R_\Omega I(t) \tag{3.24}$$

$$Z^*_\mathrm{R} = R_\Omega \tag{3.25}$$

Inductor

The relation of difference in potential and current for an inductor is given in Equation 3.26 with the inductance L. The impedance response relates directly to the frequency ω, which results in a $+90°$ phase-shifted of current passing through the inductor. An ideal inductor exhibits zero ohmic resistivity, which results in an parallel system response to Z''[93,102].

$$V(t) = L\frac{dI(t)}{dt} \tag{3.26}$$

$$Z^*_\mathrm{L} = j\omega L \tag{3.27}$$

Capacitor and Constant Phase Element

The capacitor accumulates electrical charges q, which equals the product of storing capacitance C and applied potential V. The current $I(t)$ flowing through the system is related to the charge. The capacitor's purely imaginary impedance Z^*_C is inversely proportional to angular frequency ω and capacitance, accounting for the $-90°$ phase shift between current and potential.

$$I(t) = C\frac{dV(t)}{dt} \tag{3.28}$$

$$Z^*_{\mathrm{C}} = \frac{1}{j\omega C} \tag{3.29}$$

More complex circuit models are made of passive elements in series or parallel. For elements connected in series, the impedance can be calculated from the sum of potential difference for all elements (Equation 3.30). The total impedance for passive elements in parallel, is given by the additive of the inverse impedance, the admittance (Equation 3.31).

$$Z^* = \sum_{\mathrm{k}} Z^*_{\mathrm{k}} \tag{3.30}$$

$$Z^* = \left(\sum_{\mathrm{k}} \frac{1}{Z^*_{\mathrm{k}}}\right)^{-1} \tag{3.31}$$

The impedance of electrode/electrolyte interfaces exhibit often a frequency dispersion that is described by using the Constant Phase Element (CPE) in an equivalent circuit model. This time-constant or frequency dispersion was related to a distribution of capacitance, whose origins discussed in literature encompass heterogeneous electrode surface[103,104], electrode porosity[105–107], inhomogeneities of layer properties[108] and non-uniform potential/current distribution[109–111]. The impedance Z^*_{CPE} in Equation 3.32 is related to parameter Q_0 for capacitive dispersion, angular frequency and the CPE exponent m_{CPE}. Depending on this fitting parameter, the CPE is considered to represent varied circuit elements[108,112,113]. In this work, the impedance data are modeled by a series of RQ elements. An RQ element is a parallel connection of a resistor and a CPE with the impedance Z^*_{RQ} (Equation 3.33).

When $m_{\mathrm{CPE}} = 1$, the CPE's capacitance is equivalent to an ideal capacitor's, and the RQ element equals an RC element, thus following the shape of a perfect semicircle in the complex plane (Figure 3.3). Surface heterogeneity and distributed time constants of charge-transfer reactions have been related to $m\mathrm{CPE} \neq 1$. In other cases, deviations $m_{\mathrm{CPE}} = 0$ and $m_{\mathrm{CPE}} = -1$ are related to resistor and inductor elements[114,115].

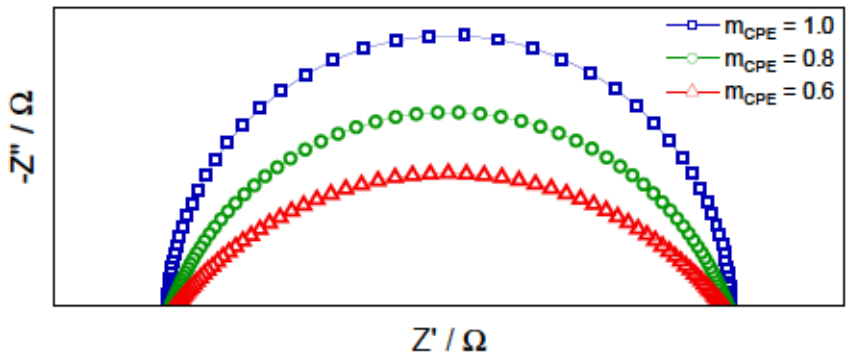

Figure 3.3: Nyquist plot representation of an RQ element for different values of m_{CPE}.

$$Z^*_{\mathrm{CPE}} = \frac{1}{Q_0(j\omega)^{m_{\mathrm{CPE}}}} \tag{3.32}$$

$$Z^*_{\mathrm{RQ}} = \frac{R}{1 + R \cdot Q_0 \cdot (j\omega)^{m_{\mathrm{CPE}}}} \tag{3.33}$$

4. Experimental

4.1 Material Synthesis and Analysis

Powder Preparation

The $Sr_2Fe_{2-x}Mo_xO_{6-\delta}$-based electrode materials were prepared using a solid state synthesis route. The precursor powders $SrCO_3$ (Aldrich chem, 99%), Fe_2O_3 (Alfa Aesar, 99%) and MoO_3 (Alfa Aesar, 99%) were pre-fired overnight at 900 °C to remove water content due to their hygroscopic character. According to the stoichiometry, the precursors were weighted and ball milled for 4 h at 250 rpm using isopropanol (VWR, 99.8%) and zirconia balls. After drying overnight at 80 °C, the powders were annealed at 1100 - 1200 °C for 8 h in air. The obtained powders were milled again with zirconia balls in isopropanol for 8 h to obtain a mean particle size of around 1 µm. For the $Sr_2Fe_{2-x}Mo_xO_{6-\delta}$-GDC composite electrode, commercial $Ce_{0.8}Gd_{0.2}O_{1.9}$ (GDC) powder (SOFCMAN, 99.5%) was used and weighted in a 70:30 ratio together with reduced SFM, ground in acetone, and dried overnight. The powder mixture was ball-milled at 1200 rpm for 10 min. The doped composition $Sr_2FeMo_{0.65}Ni_{0.35}O_{6-\delta}$ was prepared using a solid state route with the added precursor NiO (Alfa Aesar, 99%). A modified Pechini method was used to prepare the $La_{0.58}Sr_{0.4}Co_{0.2}Fe_{0.8}O_{3-\delta}$ (LSCF) powder[116].

X-Ray Diffraction Analysis (XRD)

The powder samples were first investigated by X-Ray Diffraction (XRD) at room temperature to check the phase purity of the sample using a PANanalytical X'pert MPD diffractometer (Almelo, Netherlands) with Cu-Kα incident radiation. Each diffractogram was fitted by profile matching with the Fullprof software and Rietveld refinements were carried out.

High-Temperature X-Ray Diffraction Analysis (HT-XRD)

The experiments were conducted with an Empyrean diffractometer (Malvern Panalytical, Almelo, The Netherlands) with Cu-Kα incident radiation. In ambient air, the powdered sample was heated from 25 °C to 900 °C with 5 °C $\cdot$ min^{-1}. In 100 °C steps, diffractograms were taken from 10 ° to 100 °. After cooling to room temperature, the atmosphere was changed to Ar-4% H_2 (1.5 bar, 2 ml$\cdot$min^{-1}). The sample was heated at 2 °C $\cdot$ min^{-1} from to 25 °C to 900 °C and kept for 7 h. During the

qualitative phase analysis, the positions and intensities of the Bragg reflections in the measured diffractogram are compared with reference patterns in different databases using a search/match procedure (HighScore Plus v.4.8, Malvern Panalytical).

Scanning Electron Microscopy (SEM)

The microstructure of the as-prepared and reduced $Sr_2FeMoO_{6-\delta}$ cells and powders was characterized by using a Scanning Electron Microscope (Quanta FEG 650, FEI equipped with an Energy-Dispersive X-Ray Spectroscopy (EDX) detector, USA) at 10 - 20 kV.

Transmission Electron Microscopy (TEM)

High-Resolution Transmission Electron Microscopy (HRTEM) images were captured using an aberration corrected Thermo Fischer Titan TEM at 300 kV. Elemental distribution mapping was carried out using a Hitachi HF5000, provided by Hitachi High-Technologies, Japan, and equipped with Energy-Dispersive X-Ray Spectroscopy (EDX) from Oxford Instruments.

In-situ Transmission Electron Microscopy (In-situ TEM)

The in-situ transmission electron microscopy (TEM) sample was prepared by depositing a suspension of as-prepared $Sr_2FeMoO_{6-\delta}$ particles in ethanol onto MEMS-based heating chips named "Climate" from DENS solutions via drop-casting. The chip assembly was integrated into the DENS solutions in-situ gas-flow and heating holder, and subsequently, the holder underwent plasma treatment. Following a successful leak test, the prepared holder was introduced into the TEM chamber. The Gas Supply System (GSS) from DENS solutions was utilized to facilitate the flow of gases through the nano-reactor cell of the in-situ holder. In-situ hydrogen reduction of as-prepared $Sr_2FeMoO_{6-\delta}$ was conducted in a Thermo Fischer Titan transmission electron microscope with aberration-correction at 300 kV. To eliminate any carbon impurities, the sample underwent decontamination within the nano-reactor for approximately 30 min, achieved by introducing Ar gas at a pressure of 0.95 bar (approximately 1 bar) and at 300 °C. Subsequent to the decontamination process, a gas mixture consisting of Ar-3% H_2 was circulated through the nano-reactor cell of the MEMS chip at a pressure of 0.95 bar (approximately 1 bar) at a temperature of 800 °C and with a flow rate maintained at 1 ml·min^{-1}. The in-situ movies were captured using the Gatan OneView Camera at a recording rate of 3 - 4 frames per second, with a resolution of 2K x 2K pixels.

Thermo Gravimetric Analysis (TGA)

The thermal gravimetric experiments were carried out in a TGA-5500 thermobalance (TA Instruments®, New Castle, USA). Approximately 100 mg of the sample was heated three times from 50 °C up to 1000 °C with 5 °C $\cdot$ min^{-1} in a continuous air flow of 25 ml $\cdot$ min^{-1}, then, the sample was cooled down to 50 °C. The purge atmosphere was changed to Ar-4% H_2. The samples was heated up with 2 °C $\cdot$ min^{-1} from 50 °C up to 1000 °C until constant weight was achieved.

Thermal Expansion Analysis

All specimens were prepared from milled powder precursors by uniaxial pressing at 4 MPa into a rectangular shape (4×4×12 mm) and sintering at 1050 - 1350 °C. The sintered samples were used to measure the longitudinal expansion as a function of temperature to determine the Thermal Expansion Coefficient (TEC). The dilatometry experiments were carried out with a push-rod dilatometer DIL 402 C from NETZSCH-Gerätebau GmbH (Selb, Germany), and calibrated with a 12 mm long aluminum oxide reference. Each sample was heated with 120 °C $\cdot$ h^{-1} to 1000 °C. The temperature was kept constant for 1 h to regulate the specimens' dimensional stability. Finally, the sample was cooled with 120 °C $\cdot$ h^{-1} to 25 °C. The linear thermal expansion coefficient was calculated from the change in length as a function of temperature over a defined temperature range according to:

$$TEC(T) = \frac{1}{L_0} \cdot \frac{\mathrm{d}L}{\mathrm{d}T} \tag{4.1}$$

where L_0 is the initial sample length at 30 °C, dL is the change in sample length and dT is the change in temperature.

X-Ray Photoelectron Spectroscopy (XPS)

Prior to the experiments the samples were heated up to 900 °C with 1 C·min^{-1} in N_2. At 900 °C, the atmosphere was set to 100 % H_2 for 72 h. Afterwards, the samples were cooled down to 25 °C (1 C·min^{-1}). XPS analyses were carried out by using a Phi5000 VersaProbeII (ULVAC-Phi Inc., USA) instrument. All spectra were collected using monochromatic Al $K\alpha$ irradiation at 50 W and an X-ray beam size of 200 µm at 15 keV. Survey scans were recorded with 0.8 eV steps (100 ms/step) and 187.5 eV analyzer pass energy. The high-resolution analyses (10 - 30 eV wide range) were carried out with 0.1 eV step and 23.5 eV analyzer pass energy. Data from all insulating materials have been charge corrected (referenced) using the main signal of the carbon 1s spectrum (hydrocarbon, C-C, moiety) assigned to occur at

285.0 eV. Core peaks were analyzed using a nonlinear Shirley-type background.

Conductivity Measurements

Analogous to thermal expansion experiments, rectangular bar samples with dimensions around 12x4x4 mm were prepared and sintered at 1050 - 1350 °C. The samples were installed into a ProboStat™ (NORECS AS, Oslo, Norway) placed in an automated test-rig (EBZ GmbH, Dresden, Germany) as shown in Figure 4.1. The four-point measurements were conducted by connecting the samples with two Pt current collectors and the voltage could be assessed between two Pt wires connected to the samples. The bar sample was fixed using a spring-loaded tripod. The furnace was heated to the initial operating temperature of 900 °C with a heating rate of 1 °C·min^{-1} in 9 l · h^{-1} air flow. The conductivity measurement was performed by using an Iviumstat™ (Ivium Technologies B.V., Eindhoven, Netherlands) from +0.100 V to −0.100 V with a rate of 5.0 mV·s^{-1}. The conductivity's temperature-

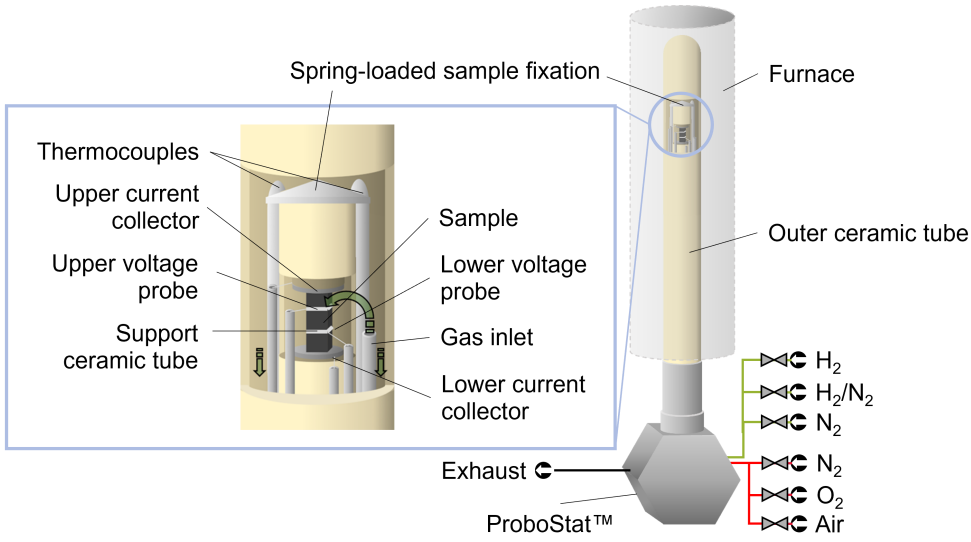

Figure 4.1: Schematic depiction of the ProboStat™ setup used for the conductivity measurements[117].

dependency in air was measured from 900 °C to 500 °C in steps of 50 °C. The gas atmosphere was changed to 9 l · h^{-1} 100 % H_2 from 900 °C to 650 °C in steps of 50 °C. The temperature limit of 650 °C was set for safety reasons. The electrical conductivity σ_e is defined as the reciprocal of electrical resistivity ρ and was calculated from the sample length l, the cross-section area A, as well as the total resistance R according to Equation 4.2.

$$\sigma_e = \frac{1}{\rho} = R\frac{l}{A} \tag{4.2}$$

4.2 Electrochemical Characterization

Electrolyte-Supported Single Cell Preparation

The electrolyte-supported button cells composed of SFM(-GDC)/GDC/8YSZ/GDC/LSCF were prepared by screen-printing (EKRA screen printing Technologies) the different cell layers onto commercially available 8YSZ electrolyte supports from Kerafol® GmbH (Eschenbach in der Oberpfalz, Germany) with a thickness of 250 µm and a diameter of 20 mm. Slurries of the layer materials were produced by mixing the powders with a solution of α-terpineol and 3% ethyl-cellulose in a 1:1 weight ratio. To homogenize the slurry viscosity and the mean particle site, they were mixed in a planetary vacuum mixer (THINKY Mixer ARV-310, California, USA) and roll milled for about 30 min.

The Gadolinium-Doped Ceria (GDC) barrier layers (thickness $\sim$ 5 µm, diameter d = 18 mm) were printed and then sintered at 1350 °C for 2 h in air. The SFMx-GDC fuel electrode (thickness $\sim$ 25 µm, d = 12 mm) was sintered at 1150 °C for 2 h and the LSCF oxygen electrode (thickness $\sim$ 25 - 30 µm, d = 10 mm) at 1080 °C for 3 h in air. To ensure acceptable cell contact with the Au current collector, a 5 µm thick Au contact layer (Heraeus GmbH, Hanau, Germany) was added on top of the fuel electrode and sintered at 900 °C for 2 h. The final single button cell configuration has an effective area of 0.79 cm^2.

Fuel Electrode-Supported Single Cells

The investigation of state-of-the-art Ni-8YSZ electrodes was conducted with commercially available fuel electrode-supported single cells by the company Elcogen® (thickness $\sim$ 315 $\pm$ 35 µm, d = 2 cm). The NiO-8YSZ fuel electrode consisted of a 10 µm thick active layer deposited on 300 $\pm$ 30 µm NiO-8YSZ support. The thin 8YSZ electrolyte (thickness $\sim$ 5 µm) and the GDC barrier layer (thickness $\sim$ 2 µm) are in-between to the 10 µm thin oxygen electrode layer made of $La_{0.6}Sr_{0.4}CoO_{3-\delta}$ (d = 1 cm).

Measurement Setup

The measurement setup is schematically depicted in Figure 4.2. The single button cells were installed in a two-electrode four probe conductivity & impedance spectroscopy Probostat setup (Norwegian Electro Ceramics®, NORECS, Oslo, Norway) [34]. On the oxygen electrode side, the cell was contacted with a Pt current collector. In dependence of the contact layer and electrode materials, the fuel electrode was contacted with Pt-Ni mesh in case of NiO electrodes and Au mesh for Au contact

layers. The total gas flow along fuel and oxygen electrode side was kept at $9\,\mathrm{l}\cdot\mathrm{h}^{-1}$ to even the pressure distribution on the cell. To control the gas flow, Mass Flow Controllers (MFCs) by the company Bronhorst Nord® (Kamen, Germany) were used. A gold seal gasket was used to separate the gas flows. The setup was placed in a furnace from the company Carbolite Gero® (Neuhausen, Germany) as described previously[2,3] and heated with a rate of $2\,^{\circ}\mathrm{C}\cdot\mathrm{min}^{-1}$ to reduce the risk of thermomechanical stress on cell materials. Prior to any measurements, the fuel electrode was reduced at 900 °C as aforementioned[2,3] and kept in reducing conditions thereafter to prevent e.g. Ni reoxidation. In addition the deviations between the obtained Open Circuit Voltage (OCV) values and theoretical calculations were determined to detect minimal gas leakages during testing. The gas flow on the fuel side (CO_2, CO, H_2) was led through a water bath before being directed to the fuel gas chamber for humidification. Based on the temperature dependence of the water vapor pressure, the steam concentration was adjusted. On the oxygen electrode side, the air gas supply channel was in direct contact with the current collector to provide a radial gas flow. Fuel and air gas outlets were led directly into the air ventilation and the steam was condensed.

Electrochemical Characterization

The Alternating Current (AC)- and Direct Current (DC)-measurements were recorded with a four-electrode Potentiostat/Galvanostat Vertex.5A setup (Ivium Technologies®, Eindhoven, The Netherlands). The impedance spectra were potentiostatically measured in the frequency range from 110 kHz down to 0.11 Hz with an amplitude of 50 mA taking 127 measurement points in 21 frequencies per decades. For temperature and gas mixture variation measurements, the impedance spectra were taken at OCV from 900 °C to 750 °C in steps of 25 °C. The investigated gas mixtures included steam electrolysis (50% H_2O + 50% H_2), CO_2 electrolysis (80% CO_2 + 20% CO) and co-electrolysis (40% CO_2 + 40% H_2O + 20% H_2). The polarization variation measurements entailed the recording of impedance spectra in the range of 0.7 V (Fuel Cell Mode) to 1.4 V (Electrolysis Mode). The current-voltage characteristics (iV curves) were measured in potentiostatic mode to investigate the cell performance at a scan rate of $10\,\mathrm{mV}\cdot\mathrm{s}^{-1}$ from OCV to 0.6 V to 1.5 V and back to OCV. The long-term stability tests were performed in steam and CO_2 electrolysis conditions at 900 °C with a constant current load of $-0.3\,\mathrm{A}\cdot\mathrm{cm}^{-2}$ and $-0.5\,\mathrm{A}\cdot\mathrm{cm}^{-2}$ for 500 h and 1000 h. Before and after the degradation test, current-voltage characteristics and impedance spectra at OCV and with varied polarization were taken. The degradation rate was determined from the change in cell voltage over time. The complex impedance diagrams were evaluated using an Equivalent

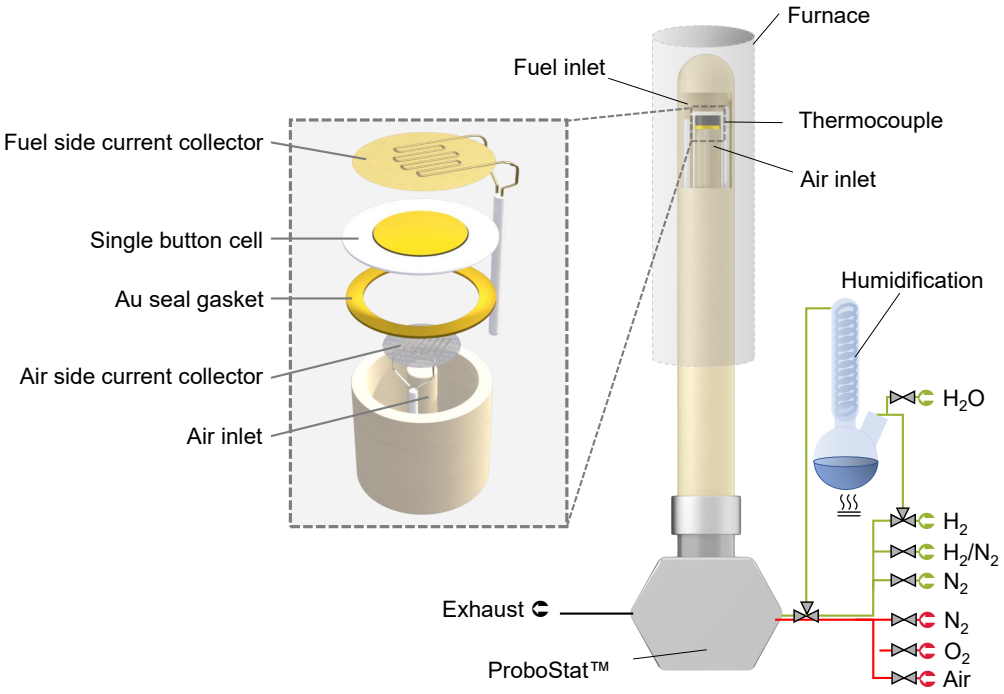

Figure 4.2: Schematic depiction of the ProboStat® setup used for the electrochemical testing of single button cells[117,118].

Circuit Model (ECM) with the help of the RelaxIS® software version 3.0.21.17. The number of time constants and elements in the ECM, the Distribution of Relaxation Times Analysis (DRT) spectra were analyzed prepared with a feasible λ value as described previously[119]. In order to perform the fitting of the complex nonlinear least squares problem, the implemented Levenberg-Marquardt algorithm was chosen to derive the local minima from the given starting parameters. Thereafter, the Nelder-Mead-Simplex algorithm was used to to iteratively improve the derived parameter. The evaluation of the fit quality was analyzed by comparison of the calculated and the experimental impedance data. The relative residuals as well as the X^2 error were evaluated to indicate a reasonable ECM. From the evaluated impedance measurement data, the Area Specific Resistance (ASR), the ohmic resistance R_Ω, and the polarization resistance R_P were derived.

5. Results

5.1 State-Of-The-Art Ni-8YSZ as Fuel Electrode

The following results show an analysis of temperature and gas atmosphere influence on the degradation phenomenon during the long-term electrolysis operation of solid oxide cells. The experiments were performed with fuel electrode-supported single cells composed of an $La_{0.6}Sr_{0.4}CoO_3$ (LSC) oxygen electrode with a Gadolinium-Doped Ceria (GDC) interlayer, an 8YSZ electrolyte and a NiO-8YSZ fuel electrode. The commercial Elcogen single cells were operated for 1000 h in varied measurement conditions in collaboration with Eric Tröster during his bachelor thesis[120]. Intermittent Alternating Current (AC)- and Direct Current (DC)-measurements were performed to characterize the single cells and to determine the responsible electrode processes for the degradation during long-term operation. An increased degradation rate is observed at 800 °C compared to 750 °C under steam electrolysis conditions. Moreover, a lower degradation rate is noticed under co-electrolysis operation in comparison to steam electrolysis operation. The post-test analyses using Scanning Electron Microscopy (SEM), Energy-Dispersive X-Ray Spectroscopy (EDX) and X-Ray Diffraction (XRD) were carried out in order to determine structural changes and the degradation mechanisms during the electrolysis operation. Parts of the results have been published under the CC BY 4.0 (http://creativecommons.org/licenses/by/4.0/)[2].

5.1.1 Durability Characterization

The galvanostatic degradation tests were performed with a gas composition of 50% H_2O + 50% H_2 for steam electrolysis at 800 °C and 750 °C and with 40% H_2O + 40% CO_2 + 20% H_2 at 800 °C for co-electrolysis under a constant current density of $-1\ A \cdot cm^{-2}$. The variation of cell voltage and the degradation rate as a function of operating time for steam and co-electrolysis are illustrated in Figures 5.1a and 5.1b.

The degradation of the operated cells is shown by an increase in the cell voltage throughout the electrolysis measurements up to 1000 h. In dependence of the varied measurement conditions (temperature, gas composition), the degradation rates vary in severity. Overall, all voltage curves follow the trend of initial moderate voltage increase, followed by a severe increase in cell voltage. Toward the end of the long-term measurements, a third period is observed, during which the degradation rate decreases.

Under steam electrolysis conditions at 800 °C, the cell voltage increases only

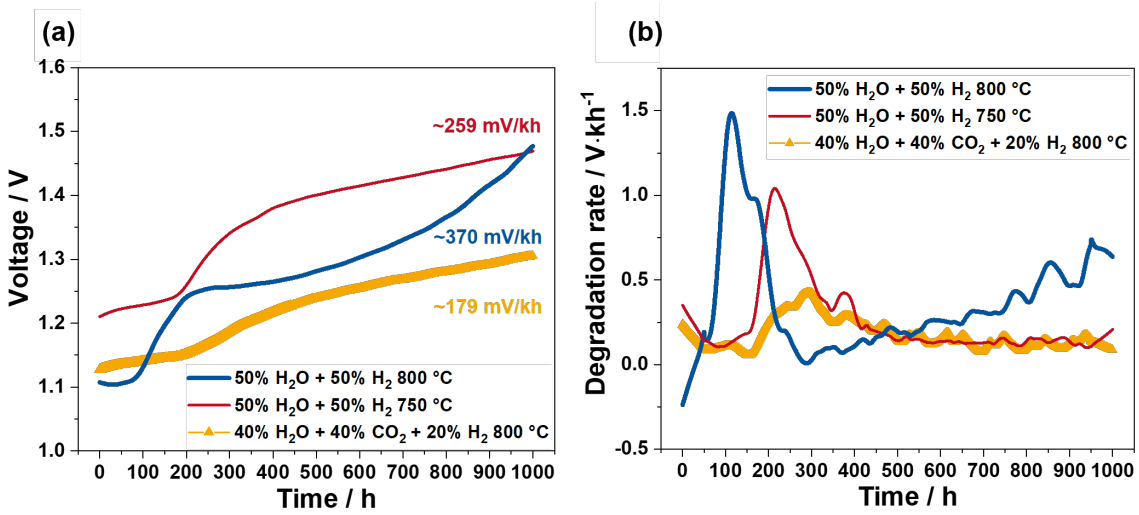

Figure 5.1: (a) Cell voltage development under galvanostatic degradation test and (b) degradation rate as a function of time. Reproduced from[2] published under the CC BY 4.0 (http://creativecommons.org/licenses/by/4.0/).

slightly from start-up to 82 h. This is followed by a severe cell voltage increase up to 193 h, during which the cell voltage increases by 132 mV. Starting at around 193 h, the voltage development displays progressive degradation until the measurement end at 1000 h with an overall increase of 33 $\cdot kh^{-1}$ (370 mV) in the cell voltage after 1000 h (Table 5.1).

The degradation test at 750 °C under steam electrolysis conditions shows higher initial cell voltage as expected due to higher ohmic and polarization resistances. At the lower operating temperature, the initial degradation period lasted up to around 174 h. In comparison to the measurement at 800 °C, the sharp increase in cell voltage lasted longer, up to 404 h. In the following hours, the test at 750 °C exhibited a continuous voltage increase. The absolute voltage increase over the measurement time averages to 22 $\cdot kh^{-1}$ of the initial cell voltage per 1000 h (Table 5.1). The total voltage increase at 800 °C was around 1.4 times higher than that of cell operated at 750 °C. The results emphasize that operation temperature has a direct impact on cell degradation. Since the humidity and current density were kept constant for both tests, therefore the large degradation rate at 800 °C arises from the temperature effect. The observed degradation rate is higher than the one reported in the literature by Trini et al. with 8.3 $\cdot kh^{-1}$ under the same measurement conditions (800 °C, -1 A $\cdot$ cm^{-2}, H_2 / H_2O (50/50))[11]. In another work, Schefold et al. performed long-term steam electrolysis test up to 23,000 h at 850 °C with -0.9 A $\cdot$ cm^{-2} current density using electrolyte supported single cell comprising scandia/ceria doped zirconia electrolyte (6Sc1CeSZ), GDC barrier layer, a LSCF

oxygen electrode, and a Ni-GDC fuel electrode. They reported significantly lower degradation rate of 0.57 $\cdot kh^{-1}$ as well[121,122]. The observed lower degradation rate can be due to different cell components used in their work.

In comparison to steam electrolysis, under co-electrolysis conditions at 800 °C, a moderate cell voltage increase of 21 mV could be observed in the first 184 h, followed by an increase of 80 mV up to 442 h. From this point onward, the voltage increased continuously. The long-term test resulted in an overall increase of 159 mV, which correspond to 16 $\cdot kh^{-1}$ from the initial cell voltage after 1000 h (Table 5.1). The degradation rate maxima in Figure 5.1b illustrate the impact of gas composition and operating temperature on the degradation development. A maximum degradation rate of 1490 $mV \cdot kh^{-1}$ for steam electrolysis at 800 °C is observed after 114 h. At 750 °C operating temperature, a lower maximum degradation rate of 1040 $mV \cdot kh^{-1}$ for steam electrolysis is observed after 214 h. For co-electrolysis, the maximum degradation decreases down to 430 $mV \cdot kh^{-1}$ and is reached after around 295 h. The development of the maximum degradation rate over time underlines that elevated temperatures are detrimental to the cells' stability[123]. The variation of fuel gas composition i.e. 40% H_2O + 40% CO_2 + 20% H_2 for co-electrolysis results in lower degradation rate than the variation of operating temperature during steam electrolysis from 800 °C down to 750 °C.

5.1.2 Electrochemical Characterization

The cell performance was analyzed as a function of operation time by AC- and DC-measurements. The initial performance under steam and co-electrolysis conditions is compared in Figure 5.2. The initial current density of the three measurements varied significantly, as expected from the differing measurement conditions. At 800 °C, the iV curves for steam and co-electrolysis reached about the same maximum current density of $-1.77\ A \cdot cm^{-2}$ and $-1.72\ A \cdot cm^{-2}$, respectively at 1.4 V. With decreasing the operating temperature to 750 °C, only $-1.52\ A \cdot cm^{-2}$ is reached in

Table 5.1: Overview of the absolute voltage increase after 1000 h degradation test depending on measurement conditions.

Conditions	$\boldsymbol{T}$ **/ °C**	$\boldsymbol{\Delta V}$ **/ mV**	$\boldsymbol{\Delta E}$ **/ % · h^{-1}**
50% H_2O + 50% H_2	800	370	33
50% H_2O + 50% H_2	750	259	22
40% H_2O + 40% CO_2 + 20% H_2	800	179	16

steam electrolysis atmosphere at the same voltage limit. However, the performance lowered significantly after 1000 h of electrolysis operation, as shown in Figure 5.2. The maximum current density at 800 °C decreased by $-1.03\ \mathrm{A \cdot cm^{-2}}$ for steam electrolysis and $-0.59\ \mathrm{A \cdot cm^{-2}}$ in co-electrolysis conditions. At 750 °C operating temperature in an atmosphere of 50% H_2O + 50% H_2, the current density decreased by $-0.89\ \mathrm{A \cdot cm^{-2}}$, which is less severe compared to the observed loss at 800 °C.

The comparison of the percentage decrease in performance from the initial values at 800 °C for steam (58 %) and co-electrolysis (34 %) emphasizes the crucial impact of the feed gas on cell performance over time. Long-term galvanostatic test results at $-0.75\ \mathrm{A \cdot cm^{-2}}$ at 750 °C by Rao et al.[124] under co-electrolysis conditions showed a higher performance loss of around 50 %. The authors used a different gas composition of 65% H_2O + 25% CO_2 + 10% H_2 i.e. with a higher steam content, which may cause the higher performance loss. After the degradation tests at 800 °C, the iV curves for co-electrolysis and steam electrolysis display a hysteresis. For steam electrolysis this hysteresis is more pronounced, wherefore the hysteresis' origin cannot be linked to the CO in co-electrolysis as suggested by Aicart[125] or low steam content[126].

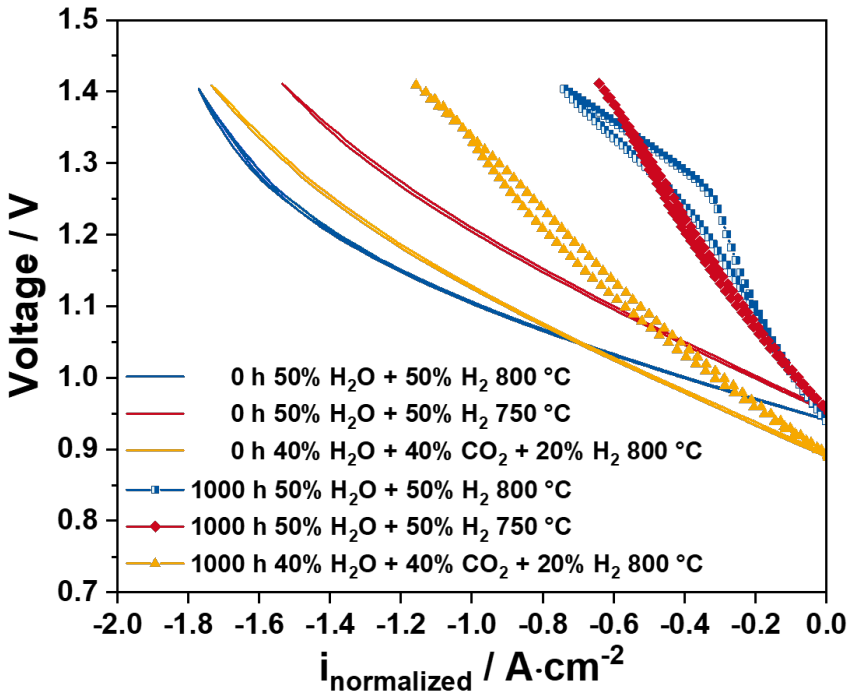

Figure 5.2: Comparison of current-voltage characteristics measured before and after the degradation measurement of 1000 h at constant load of $-1\ \mathrm{A \cdot cm^{-2}}$ for steam and co-electrolysis. Reproduced from[2] published under the CC BY 4.0 (http://creativecommons.org/licenses/by/4.0/).

5.1.2.1 Equivalent Circuit Model Evaluation

During the the long-term measurement at $-1\ \mathrm{A \cdot cm^{-2}}$, intermittent impedance spectra were taken at Open Circuit Voltage (OCV) in steps of 96 h from 0 h to 1000 h. The impedance spectra are depicted in Figure 5.3 as a function of time for steam electrolysis at 800 °C (Figure 5.3a), steam electrolysis at 750 °C (5.3b), and co-electrolysis at 800 °C (Figure 5.3c) to illustrate the resistance evolution over time. Foremost, despite the different measurement conditions, both ohmic resistance (R_Ω) and polarization resistance (R_P) increase for all three measurements. In the case of steam electrolysis at 800 °C (Figure 5.3a), R_Ω remains invariant during the first 288 h of testing. Subsequently, it begins to increase gradually. In contrast, the polarization resistance R_P starts increasing after 96 h. The differences of R_Ω and R_P before and after the durability tests are listed in Table A.1 in the Appendix. The impedance spectra in Figure 5.3a illustrate that the mid-frequency part of the impedance spectrum is influenced the most, followed by the high-frequency part. A similar evolution of R_Ω and R_P, as well as comparable impedance trends, are observed for steam electrolysis at 750 °C (Figure 5.3b). The evolution of EIS spectra for co-electrolysis (Figure 5.3c) on the other hand shows a significantly different trend in contrast to steam electrolysis. The increase in R_Ω under co-electrolysis conditions is the lowest compared to the steam electrolysis conditions (Table A.1), irrespective of the elevated operating temperature. However, R_P shows a gradual increase throughout the measurement up to 1000 h. In total, the increase of impedance is significantly lower for co-electrolysis compared to steam electrolysis. All impedance spectra displayed in Figure 5.3c show no evident change in the low-frequency region. This suggests, that the physical process observed in the low-frequency range is not influenced by cell degradation tests up to 1000 h.

For an in-depth process resistance analysis, the impedance spectra were fitted by an Equivalent Circuit Model (ECM). To find the number of appropriate elements for the model, the number of time constants were investigated by Distribution of Relaxation Times Analysis (DRT). The investigation of several impedance spectra using DRT led to the conclusion that an ECM with four RQ elements, as depicted in Figure 5.4a, is best suited to fit the measured impedance spectra, considering the DRT spectra (Figure 5.4b) exhibit four time constants. In addition, the ECM contains an inductance element to include the inductive effects resulting from the cable configuration in the experimental setup[127], which are often observed in the high-frequency region of the Nyquist plot, and play an important role in high frequency data evaluation. The serial resistor represents the ohmic resistance R_Ω of the system resulting from the ionic resistance (charged species), electronic resis-

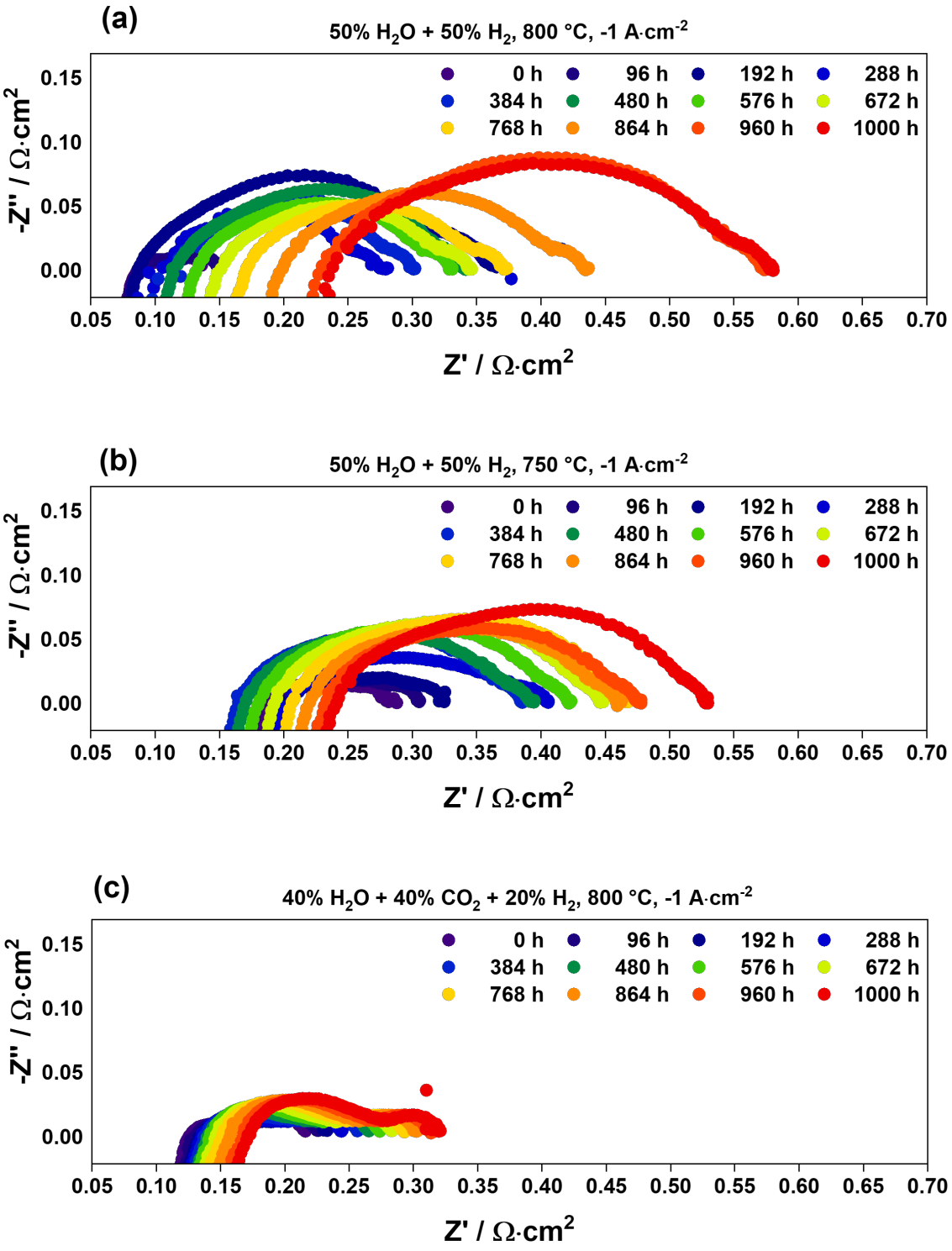

Figure 5.3: Comparison of Nyquist plots at OCV for a single cell composed of Ni-8YSZ/8YSZ/GDC/LSC. The durability tests were conducted under constant $-1\ \mathrm{A \cdot cm^{-2}}$ up to 1000 h with 9 $\mathrm{l \cdot h^{-1}}$ inlet fuel consisting of (a) 50% H_2O + 50% H_2 at 800 °C, (b) 50% H_2O + 50% H_2 at 750 °C, and (c) 40% H_2O + 40% CO_2 + 20% H_2 at 800 °C. Reproduced from[2] published under the CC BY 4.0 (http://creativecommons.org/licenses/by/4.0/).

tance (electron transport) and contact resistances. The fit quality, after using the Levenberg-Marquardt and the Nelder-Mead-Simplex algorithms to solve the complex nonlinear least square problem, was analyzed by comparison of experimental and calculated data from the fit. Figure 5.4c shows good agreement between these two and is also supported by the good qualitative agreement of the relative residuals shown in Figure 5.4d as well as the low X^2 error of 10^{-7} between the fitted and experimental data, indicating a reasonable ECM[127].

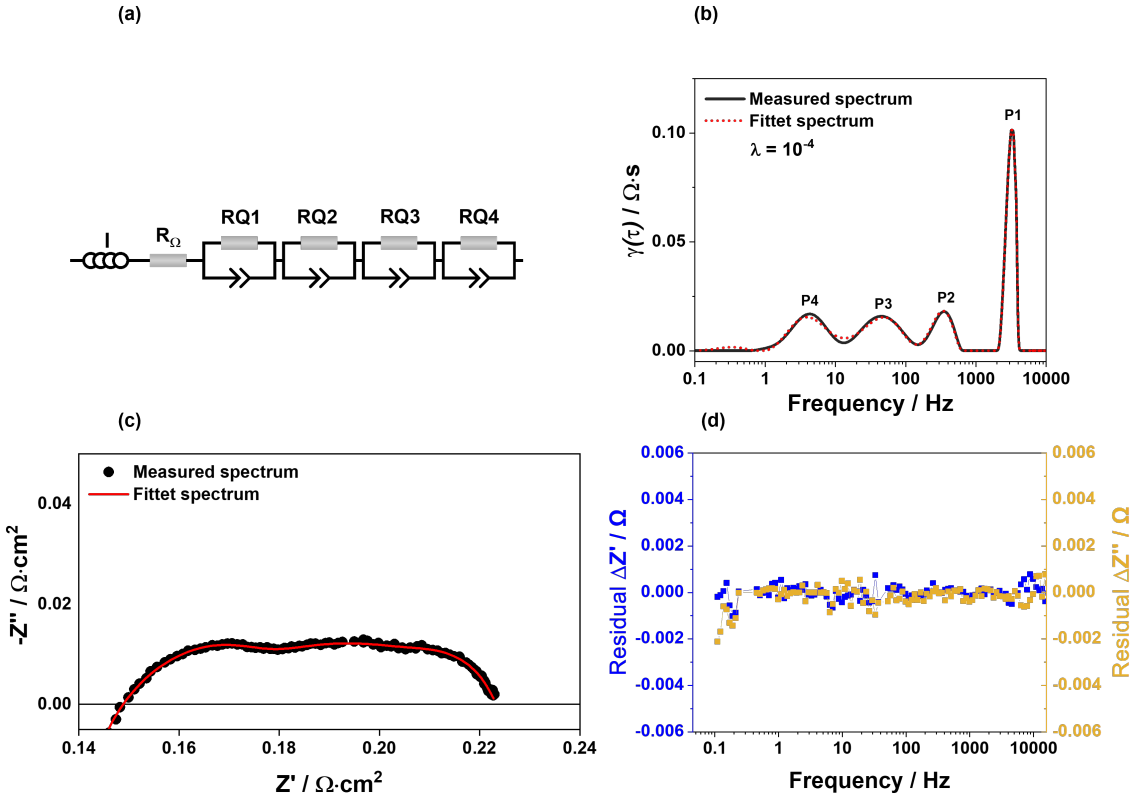

Figure 5.4: (a) Equivalent circuit model (ECM) of the experimental impedance data used for complex non-linear curve fit. (b) Distribution of relaxation times (DRT) of experimental and fitted impedance data for the Ni-8YSZ/8YSZ/GDC/LSC cell at 750 °C in 50% H_2O + 50% H_2 recorded at OCV. (c) Nyquist plot of the experimental data and the corresponding fit. (d) The residual of the fitted data to verify the quality of the CNLS fit.

To further understand the degradation behavior in dependence of measurement conditions, the Area Specific Resistance (ASR) was calculated from the impedance measurements and plotted in Figure 5.5 as a function of measurement time. Regardless of the difference in the initial ASR values, both cells operated under steam electrolysis conditions showed similar degradation behavior. After an initial degradation period, a sharp increase in the ASR was observed. The initial area-specific resistance of 175 $m\Omega \cdot cm^2$ at 800 °C increased to 730 $m\Omega \cdot cm^2$ after the 1000 h durability test.

This corresponds to an average ASR degradation rate of 555 $m\Omega \cdot cm^2kh^{-1}$. Decreasing the measurement temperature to 750 °C led to a lower average degradation rate of 387 $m\Omega \cdot cm^2kh^{-1}$. In contrast to results obtained in steam electrolysis, the ASR evolved linearly in co-electrolysis conditions over time, with an average degradation rate of 134 $m\Omega \cdot cm^2kh^{-1}$. This indicates different degradation mechanisms occurring in the cells dependent on the fuel gas compositions. Therefore, electrochemical impedance analysis was performed in regular intervals during long-term testing to determine the dominating degradation process depending on the gas atmosphere.

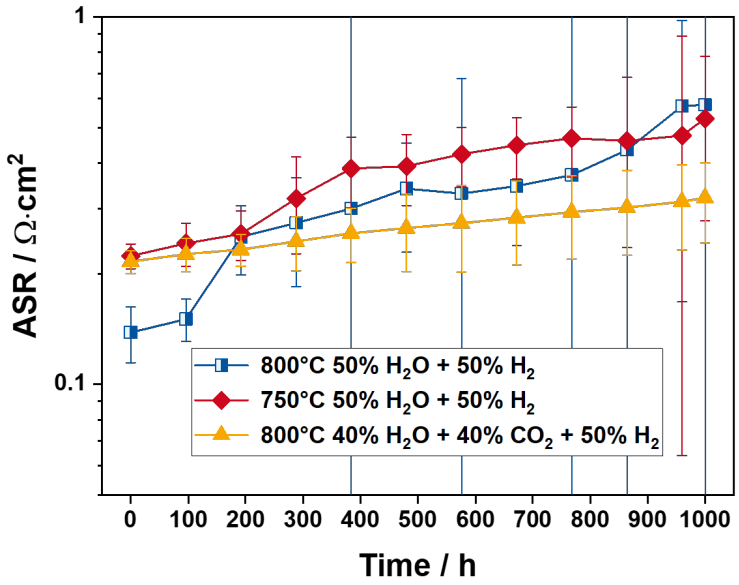

Figure 5.5: Comparison of the total area-specific resistance over time during 1000 measurement conducted under constant $-1\ A \cdot cm^{-2}$ with $9\ l \cdot h^{-1}$ inlet fuel consisting of 50% H_2O + 50% H_2 at 800 °C, 50% H_2O + 50% H_2 at 750 °C, and 40% H_2O + 40% CO_2 + 20% H_2 at 800 °C. Reproduced from[2] published under the CC BY 4.0 (http://creativecommons.org/licenses/by/4.0/).

The ASR evolution was broken down into the time-dependent R_Ω and R_P development for the three different measurement conditions, as shown in Figure 5.6. In the initial degradation period for steam electrolysis at 800 °C, the R_Ω remained constant within the error range (Figure 5.6a). However, the R_P showed a different behavior; i.e., it increased sharply between 96 h to 192 h, similar to that of ASR (c.f. Figure 5.5). In the third degradation period, R_P increased continuously up to 1000 h. At an operating temperature of 750 °C, R_Ω showed almost a linear increase throughout up to 1000 h. The R_P started to increase at around 200 h and exhibited a steep increase during the second degradation period from 200–384 h (Figure 5.6b). Thereafter, a continuous increase in R_P was observed. For co-electrolysis measurements, the R_Ω showed a linear increase throughout up to 1000 h (Figure 5.6). However, the

increase was less steep compared to that with steam electrolysis at 750 °C. The variation of R_P showed a linear behavior up to 1000 h, but interestingly, a lower increase in the total R_P was observed for co-electrolysis (61.2 $m\Omega \cdot cm^2 kh^{-1}$) compared to steam electrolysis at 750 °C (217 $m\Omega \cdot cm^2 kh^{-1}$) and 800 °C (303 $m\Omega \cdot cm^2 kh^{-1}$). This trend suggests that the cell degradation was more influenced by the R_P in comparison to the R_Ω and can be directly linked to the operating temperature and gas composition.

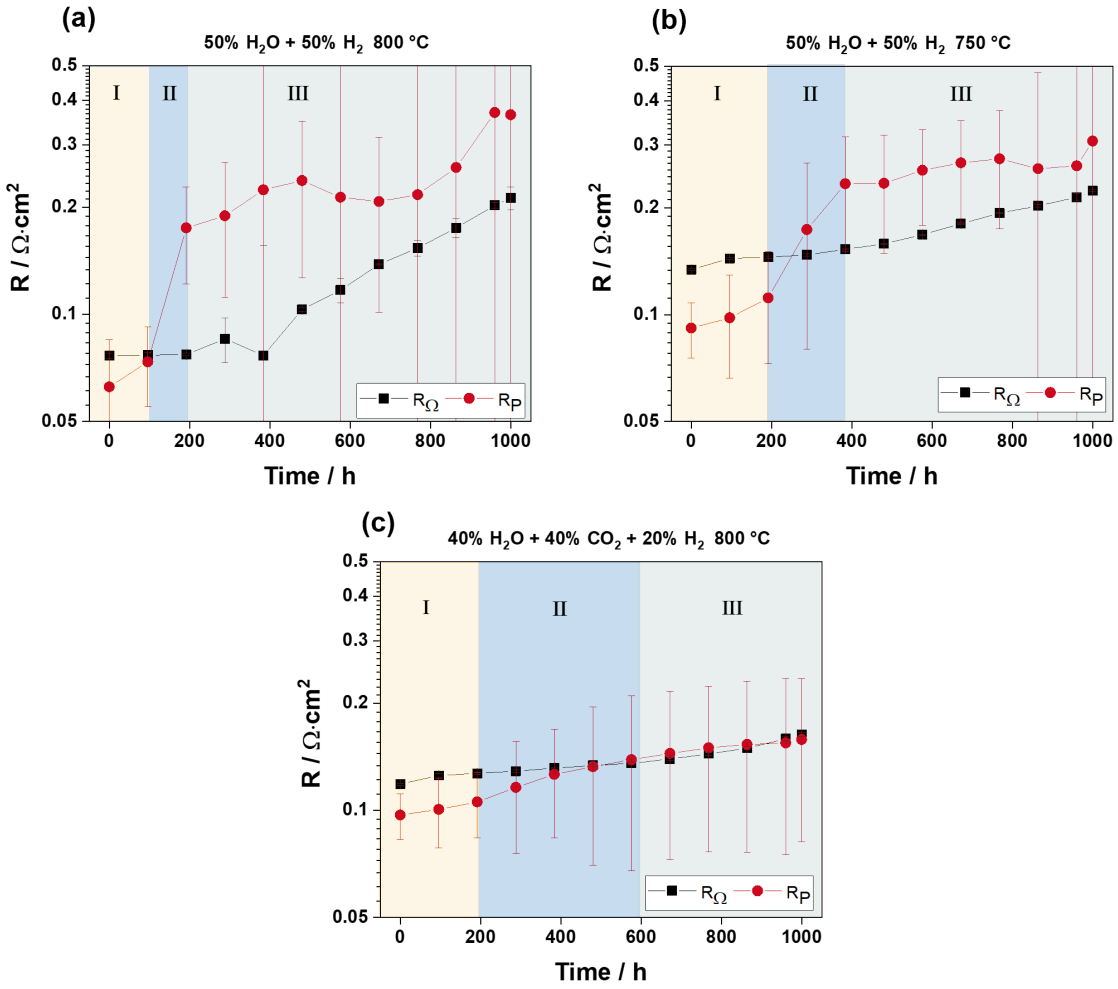

Figure 5.6: Comparison of the total area-specific resistance over time during 1000 measurement conducted under constant $-1\ A \cdot cm^{-2}$ with $9\ l \cdot h^{-1}$ inlet fuel consisting of (a) 50% H_2O + 50% H_2 at 800 °C, (b) 50% H_2O + 50% H_2 at 750 °C, and (c) 40% H_2O + 40% CO_2 + 20% H_2 at 800 °C. Reproduced from[2] published under the CC BY 4.0 (http://creativecommons.org/licenses/by/4.0/).

5.1.2.2 Process Resistance Analysis

Following the ASR and EIS evolution analysis over time, the polarization resistances R_P was investigated in more detail to determine the dominant degradation process.

The variation of individual resistances for steam electrolysis at 800 °C and 750 °C (Figure 5.7a and Figure 5.7b) shows the same trend. The R_{RQ3} shows the largest increase with time among all the four resistances. Therefore, this process is the main cause of the increase in total R_{P}. The processes modeled by R_{RQ1} and R_{RQ2} show a lower increase in comparison to the R_{RQ3}. In contrast, R_{RQ4} has no impact on the R_{P} increase. For the co-electrolysis measurement, a different behavior is observed (Figure 5.7c). The processes R_{RQ1}, R_{RQ2}, and R_{RQ3} are mainly affected, however, R_{RQ1} shows a relatively higher increase compared to the steam electrolysis. The lower increase in the resistance of R_{RQ1}, R_{RQ2} and R_{RQ3} in co-electrolysis suggests the electrode processes linked to these resistances are less influenced under co-electrolysis operation conditions. The R_{RQ4} displays no change over time for co-electrolysis similar to that of steam electrolysis.

This low-frequency process R_{RQ4} (7.9 - 1.9 Hz) has been investigated previously through temperature as well as fuel gas variation and is associated with gas diffusion processes at the fuel electrode due to its negligible activation energy of 9.2 $\mathrm{kJ \cdot mol^{-1}}$[126] and dependency on the fuel gas content[127]. Similarly, Leonide et al.[128] have also suggested that the gas diffusion processes occur with low thermal activation in this frequency range. The DRT analysis of electrochemical durability tests with a Ni-8YSZ supported single cell by Trini et al.[11] at 800 °C and -1 $\mathrm{A \cdot cm^{-2}}$ suggest the same development for a physical process around 10 Hz.

The process resistances R_{RQ1} (18.6 - 5.1 kHz) and R_{RQ2} (3.0 - 1.1 kHz) for steam and co-electrolysis in Table A.2, show an impact on cell degradation over the measurement time and are characterized by distinct thermal activation. R_{RQ1} displays negligible dependency on the fuel concentration, while the process resistance R_{RQ2} is distinguished by distinct dependency on the steam and hydrogen partial pressures[3,126]. In fuel cell mode, these two coupled high-frequency processes were previously reported to be assigned to a charge transfer at the triple-phase boundary at the fuel side and the oxygen transport in the 8YSZ electrolyte, according to Sonn et al.[129]. Trini et al.[11] supported this assignment of the high-frequency processes to the TPBs of the Ni/8YSZ fuel electrode, therefore these processes are related to the microstructure of the fuel electrode. This relation to the fuel electrode suggests that the resistance increase over time is connected to microstructural changes in this region. In consequence, these could cause a loss of conductivity in the fuel electrode.

The process given by R_{RQ3} (457 - 85Hz) is mainly contributing to the increase in the polarization resistance over time and exhibits Arrhenius behavior[126]. The resistance curves of R_{RQ3} in Figure 5.7a and Figure 5.7b show distinct temperature influence over time. Under steam electrolysis conditions at 800 °C, the resistance

R_{RQ3} increases by around 210 $m\Omega \cdot cm^2$, which is higher compared to the cell at 750 °C (153 $m\Omega \cdot cm^2$). In co-electrolysis conditions, R_{RQ3} increases by 27 $m\Omega \cdot cm^2$. This suggests that the degradation process related to this resistance is temperature-dependent as well as fuel gas dependent. The process RQ3 has been observed to be dependent on oxygen partial pressure as well as steam partial pressure[3,127]. The process part dependent on oxygen partial pressure related to RQ3 is the electrochemical process at the TPBs of the LSC/GDC electrode and an oxygen electrode transport process[127]. The steam partial pressure influence of RQ3 is related to fuel electrode transport processes. In earlier studies, the overlap of these two influences has been observed[127,128]. The impact of fuel side transport losses were shown to dominate the processes between 100 Hz to 500 Hz[127]. A similar behavior is observed in our case suggests that the affected fuel side plays a dominant role in the degradation mechanisms over time.

5.1.3 Microstructural Post-Test Analysis

To further understand the degradation behavior, as-prepared and operated single cells were investigated through in-depth SEM-EDX of the fuel and oxygen electrode layers. The changes in the electrode microstructure as well as the adhesion between different layers were investigated after 1000 h and compared with the as-reduced cell. Figure 5.8a and Figure 5.8b show the cross-section of the cell before and after the long-term test, where the bulk of LSC oxygen electrode, LSC/GDC interface, GDC/8YSZ interface, the bulk of 8YSZ electrolyte and Ni-8YSZ fuel electrode are visible. No severe damage in the bulk of the LSC oxygen electrode, GDC layer, 8YSZ electrolyte, or Ni-8YSZ fuel electrode is observed. However, the delamination of the LSC oxygen electrode at the LSC/GDC interface is visible for the single-cell operated under long-term electrolysis conditions (Figure 5.8b, Figure 5.8d). Such delamination is attributed to the evolution of oxygen gas bubbles, which penetrate pores of the electrolyte/electrode layer and build up a high oxygen gradient under anodic polarization[130,131]. The oxygen electrode delamination results in an irreversible increase in ohmic resistance of the cell[132], which was observed in the increase of R_Ω in Figure 5.6. This delamination can also lead to a large increase in the resistance (as observed for R_{RQ3}) by hindering the charge and oxide ion transport at the TPBs of the LSC/GDC.

Mostly, the delamination of the oxygen electrode is reported for LSM-based air-electrodes[129–134], however, it is also observed for LSCF oxygen electrodes by Kim and Choi for electrolyte supported cells without a GDC barrier layer after SOEC operation at 800 °C and -0.8 $A \cdot cm^{-2}$ for 50 h[135]. The performance stability of single cells in electrolysis mode is enhanced with a GDC barrier layer. For instance, a cell

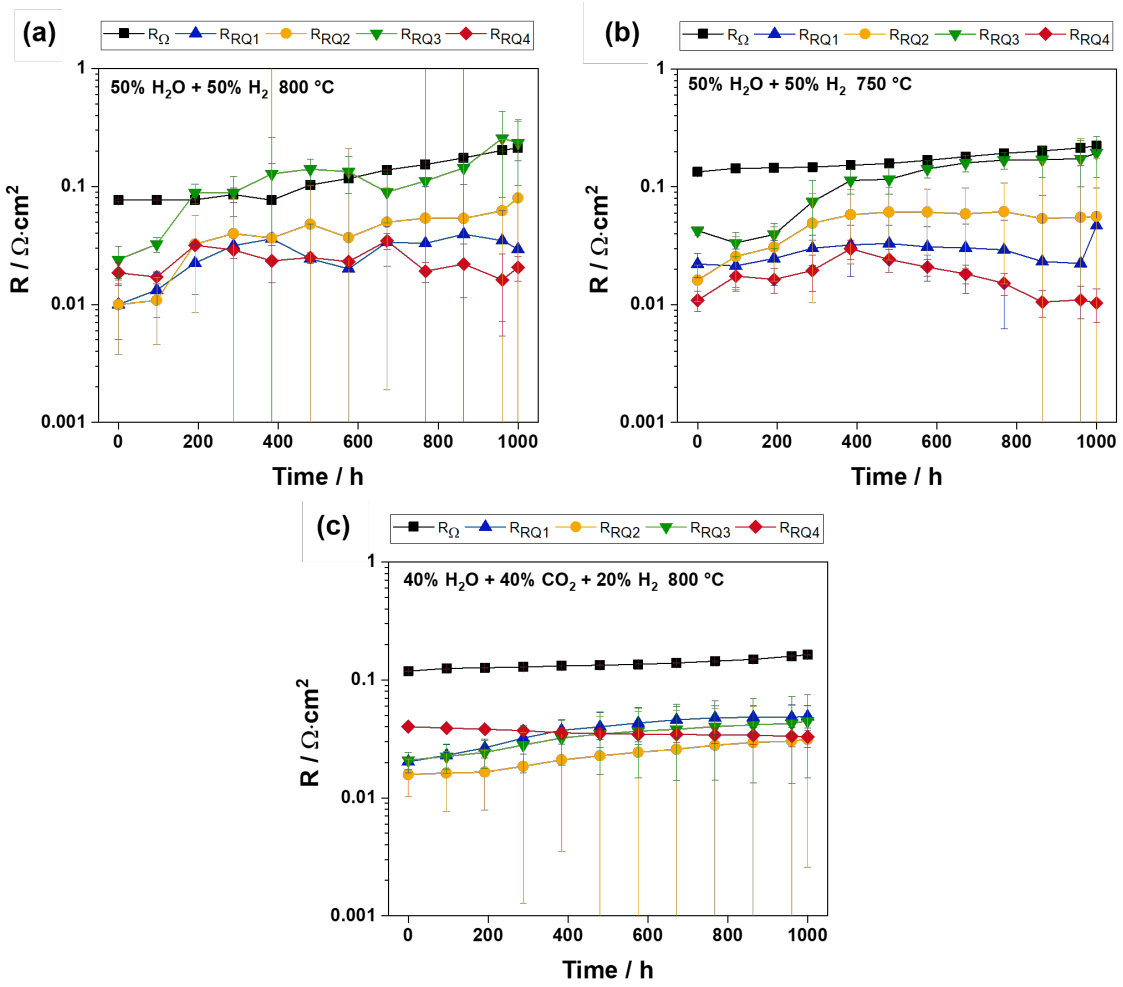

Figure 5.7: Individual resistance analysis for EIS spectra at OCV from 0 h to 1000 h with 9 $l \cdot h^{-1}$ inlet fuel consisting of (a) 50% H_2O + 50% H_2 at 800 °C, (b) 50% H_2O + 50% H_2 at 750 °C, and (c) 40% H_2O + 40% CO_2 + 20% H_2 at 800 °C. Reproduced from[2] published under the CC BY 4.0 (http://creativecommons.org/licenses/by/4.0/).

with LSCF oxygen electrode and GDC barrier layer showed a stable behavior and no delamination at 800 °C under electrolysis conditions up to 100 h with a current density of -0.8 A $\cdot$ cm^{-2}[135,136]. In long-term tests up to 2000 h, the delamination of an LSC electrode was observed under steam electrolysis conditions despite the addition of a GDC inter-barrier layer[137]. For the long-term test with a co-electrolysis gas mixture (800 °C) as well as steam electrolysis (750 °C), the LSC oxygen electrode showed no delamination as seen in supplementary information Figure A.1.

The SEM-EDX analysis results of the oxygen electrode for the reduced cell and the tested cell after 1000 h at 800 °C steam electrolysis showed no strontium diffusion/segregation through the GDC barrier layer from the LSC electrode to the electrolyte/GDC interface as shown in (Figure 5.9), which is contrary to the LSCF

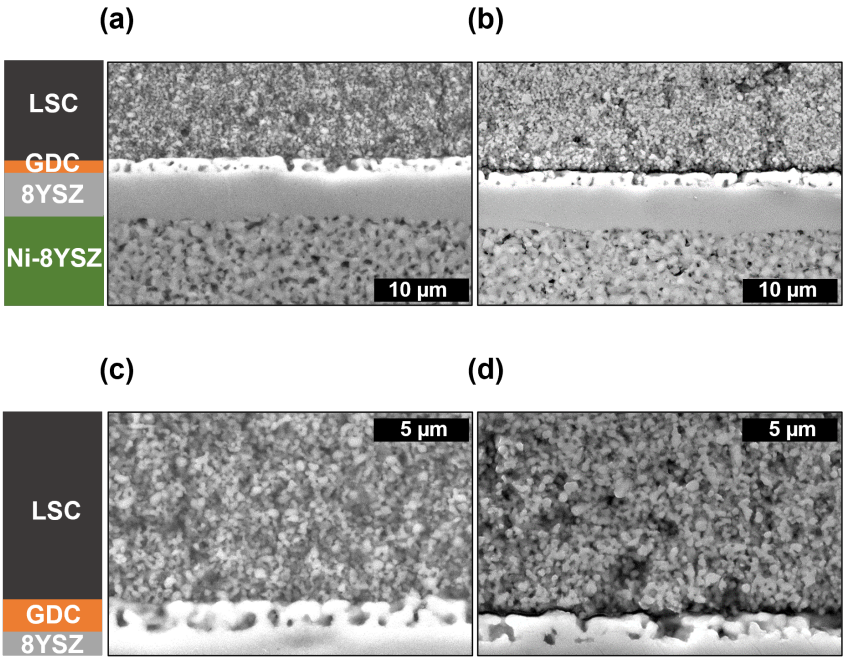

Figure 5.8: SEM-images of the single cell cross-sections (a, c) before and (b, d) after 1000 h durability test under constant current load of -1 A $\cdot$ cm^{-2} at 800 °C with 50% H_2O + 50% H_2. The SEM images in (c) and (d) are focused on the oxygen electrode. Reproduced from[2] published under the CC BY 4.0 (http://creativecommons.org/licenses/by/4.0/).

oxygen electrode[138]. Besides Sr, the ion distribution of Co, La, Ce and Zr were well distributed and located in the phase equivalent to the reference cell as well.

The fuel electrode/electrolyte interface and the bulk of the fuel electrode before and after the long-term durability test at 800 °C for steam electrolysis are depicted in Figure 5.10. The SEM images show an increase in pore size and higher pore fraction close to the electrolyte/electrode interface, after the long-term electrolysis test. The distribution of Ni in the active, as well as the support layer, is uneven after 1000 h under steam electrolysis conditions in comparison to the reference cell. The Ni migrated from the active layer and Ni particle agglomeration can be observed in the support layer at the interface to the active layer. Large Ni particle agglomerations evolved also around 20 µm from the electrolyte result in Ni starvation near the electrode/electrolyte interface, leaving only Zr and Y behind. The depletion of Ni from the electrolyte interface and subsequent agglomeration decreases the cell performance due to a significant loss in the local density of active sites at the TPB.

As seen earlier, the high-frequency processes (RQ1, RQ2), as well as the dual affected transport process RQ3, contributed to the increase of R_P. It can be confirmed that the increase is mainly due to the change in the electrode microstructure

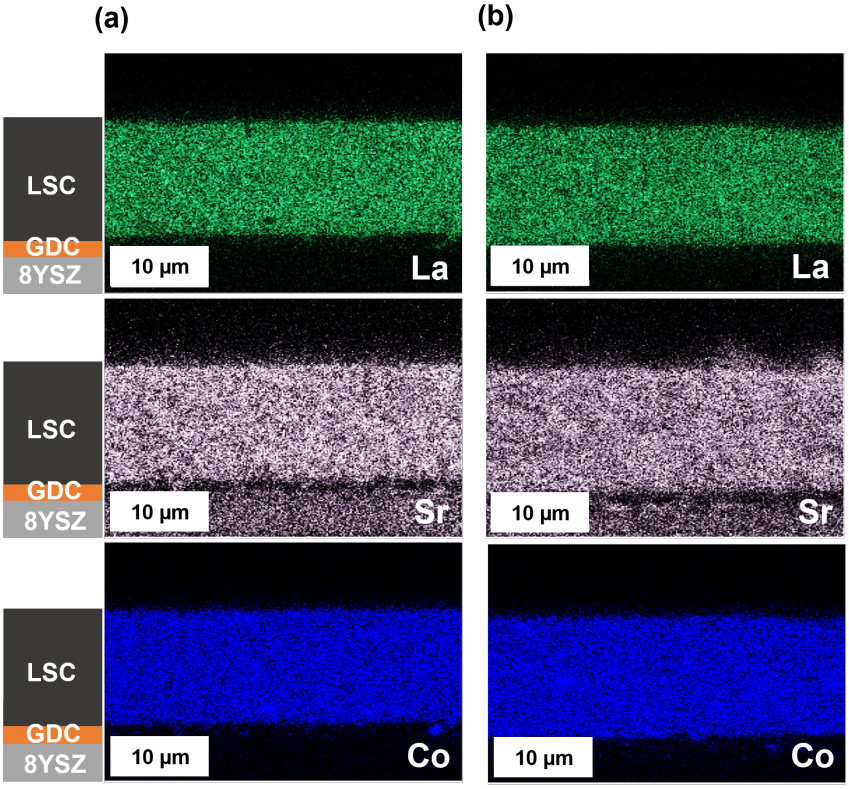

Figure 5.9: Cross-sectional SEM-EDX mapping of the oxygen electrode side for La (Kα, 4.65 keV), Co (Kα, 6.93 keV), and Sr (Lα, 13.89 keV) line (a) before and (b) after 1000 h durability test under constant current load of -1 A $\cdot$ cm^{-2} at 800 °C with 50% H_2O + 50% H_2. Reproduced from[2] published under the CC BY 4.0 (http://creativecommons.org/licenses/by/4.0/).

which impacts the charge transfer and transport reactions at the fuel electrode. The Ni-depletion is well known for the cermet based fuel electrodes[47,139,140]. Hauch et al.[46] suggested that the Ni is deposited away from the electrode/electrolyte interface by electrochemical reduction of gaseous Ni hydroxide species (Equation 5.1 and Equation 5.2).

$$Ni^{2+} + 2\ OH^- \longrightarrow Ni(OH)_{2(g)} \tag{5.1}$$

$$Ni(OH)_{2(g)} + 4\ e^- \longrightarrow Ni_{(s)} + 2\ O^{2-} + H_{2(g)} \tag{5.2}$$

The 3D reconstruction analysis of single cell by Lay-Grindler et al.[141] operated under steam electrolysis at -0.8 A $\cdot$ cm^{-2} and 800 °C for 1000 h, showed an increase in Ni particle size up to 1.704 µm and a decrease in the triple phase boundary (TPB) length. The comparison of steam and co-electrolysis in this work underlines that higher steam contributes to higher degradation.

Mogensen et al.[51] remarked that gaseous Ni migration below 800 °C is unlikely,

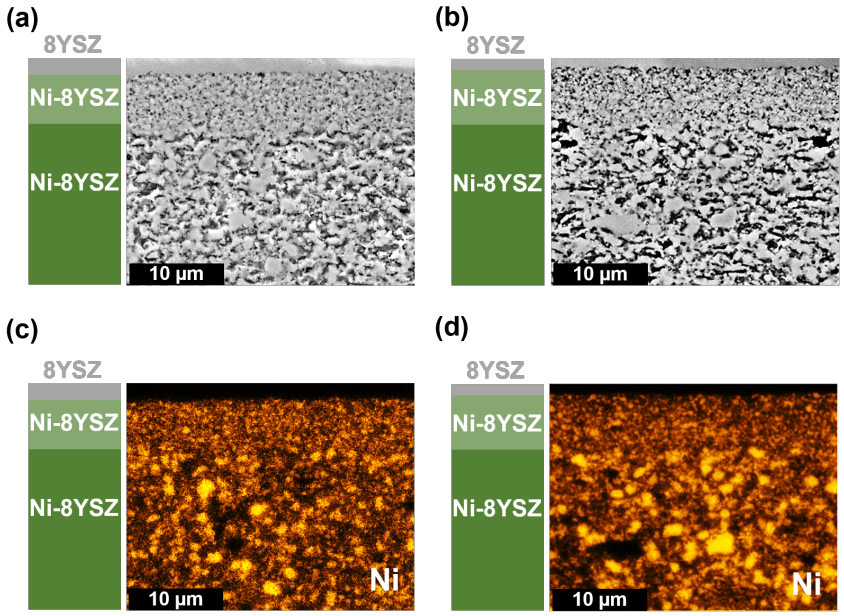

Figure 5.10: Cross-sectional SEM-EDX mapping of the fuel electrode side for the Ni (Kα, 7.47 keV) line (a, c) before and (b, d) after the long-term test for 1000 h at 800 °C with 50% H_2O + 50% H_2. Reproduced from[2] published under the CC BY 4.0 (http://creativecommons.org/licenses/by/4.0/).

because of the low reactant partial pressure. According to their hypothesis, the Ni particles migrate through the formation of gas or surface species of $Ni(OH)_x$ depending on the operating conditions. The Ni migration is described by Mogensen to be driven by the electrical potential, resulting in Ni migration along the pO_2 and/or electrochemical potential gradients from positive local potential towards relative negative potential. This results in the TPB moving from the direct electrolyte/electrode interface to the electrode microstructure.

The Ni content in the Ni-8YSZ active layer and support layer as a function of distance from the electrolyte was calculated from the EDX analysis for the as-reduced cell and the long-term operated cells. The Ni-content was obtained by performing three vertical EDX line scans at the cells' cross-section after the long-term test from the electrolyte up to a 30 µm distance from the Ni-8YSZ support layer. Afterward, the elements' intensity counts were summed up and averaged in order to get an indication of the Ni content as a function of distance away from the electrolyte. The Ni/(Y+Zr+Ni) ratio was calculated for all measured cells and compared to the as-reduced reference cell and their variation as a function of distance is shown in Figure 5.11. The averaged Ni content of a reduced cell was around 0.58 at the electrolyte/electrode interface, whereas for the long-term operated cell under steam electrolysis conditions at 800 °C, the Ni content at the electrolyte/electrode

interface was reduced to 0.4 and 0.36 at 750 °C and 800 °C, respectively. The cell measured in co-electrolysis conditions showed a slightly higher Ni content of 0.41 at the same level. The Ni content in a distance of up to 5 to 8 µm from the electrolyte is lower than the bulk content. These trend lines underline that after SOEC operation Ni migrates away from the electrolyte/electrode interface to the support layer. The largest Ni-depletion is observed for the single cell operated under steam electrolysis at 800 °C and the same cell showed the highest degradation rate.

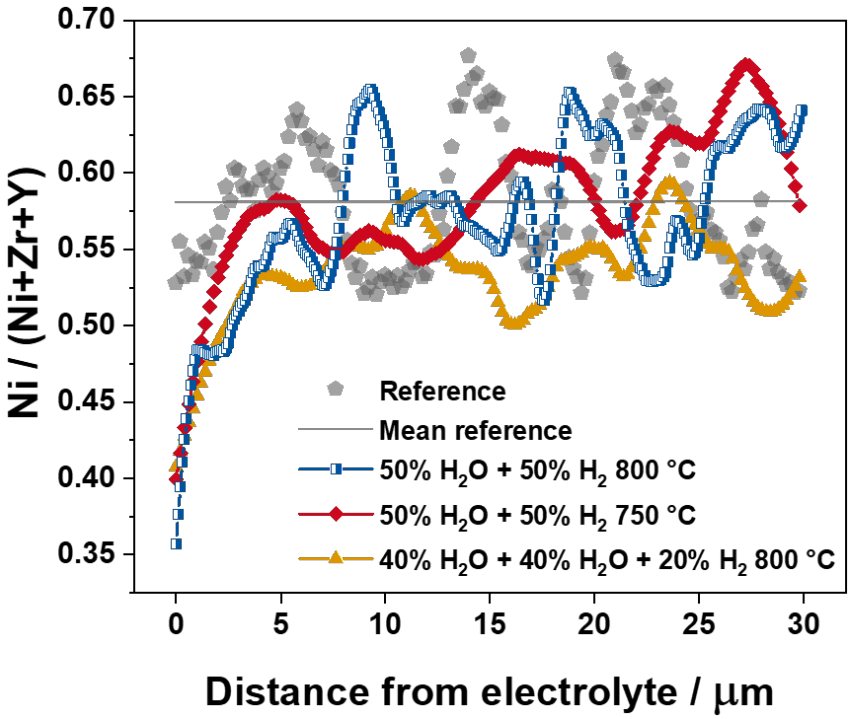

Figure 5.11: The mean atomic ratio Ni/(Zr + Y + Ni) in the active and support fuel electrode layers as a function of distance from the 8YSZ electrolyte. The average of results were computed on 30 x 4 µm^2 sized areas close to the electrode/electrolyte interface. Reproduced from[2] published under the CC BY 4.0 (http://creativecommons.org/licenses/by/4.0/).

Similar observations were also made by Trini et al.[11] by SEM-EDX horizontal line scan analysis, in which the Ni content decreased from 0.49 to 0.28 after SOEC operation due to a pronounced decrease in percolating triple phase boundaries. In addition, Sun et al. have reported the increased active electrode layer porosity within 10 µm from the electrode-electrolyte interface and densification of the neighboring support layer as a direct consequence of Ni redistribution[142]. This Ni migration was found to directly depend on the hydrogen-steam flow path. Therefore, it can be concluded that the Ni depletion and microstructural change in the fuel electrode are one of the major issues that leads to a large degradation and performance loss under steam electrolysis conditions at 800 °C.

5.2 SFM as Fuel Electrode for Steam Electrolysis

The following results show the material characterization of the Ni-free $Sr_2FeMoO_{6-\delta}$ and composite $Sr_2FeMoO_{6-\delta}$-GDC MIEC electrode materials with regard to redox-stability, and total conductivity in oxidizing and reducing atmospheres. The influence of gas atmosphere and temperature is depicted in detail through in-situ high-temperature XRD and Transmission Electron Microscopy (TEM). The electrochemical performance of the electrode materials is evaluated in steam electrolysis as well as co-electrolysis conditions and compared to state-of-the-art Ni-8YSZ and Ni-GDC fuel electrode materials. The long-term stability of electrolyte-supported single cells with $Sr_2FeMoO_{6-\delta}$ and composite $Sr_2FeMoO_{6-\delta}$-GDC fuel electrodes was assessed in steam electrolysis conditions. Post-test SEM-EDX analyses were carried out on resin-embedded cell cross-sections to determine any deteriorative microstructural changes and to determine the corresponding degradation mechanisms. Parts of the results have been measured in collaboration with Niklas Eyckeler and Carla L. Coll during their bachelor thesis[117,118]. High-temperature XRD studies were performed by and evaluated with Mirko Ziegner (IMD-2, FZJ). The XPS measurements have been commissioned from and evaluated with Dr. Heinrich Hartmann (ZEA-3, FZJ). High-resolution SEM-EDX, HAADF-STEM, and HRTEM imaging was performed by and evaluated together with Pritam K. Chakraborty, and Dr. Shibabrata Basak (IET-1, FZJ).

5.2.1 In-Situ Phase Analysis

The as-prepared $Sr_2FeMoO_{6-\delta}$ powder was characterized in an XRD study in air and after reduction in Ar-4% H_2 for 7 h at 900 °C (Figure 5.12a , Figure 5.12b). The XRD of the as-prepared SFM powder shows distinct secondary phase formation of 37 wt% $SrMoO_4$ (space group: I41/a, ICSD-99089) in addition to two phases of $Sr(Fe_{0.8}Mo_{0.2})_3$ (space group: $Pm\bar{3}m$, ICSD 191551) with 42 wt% ($\alpha = 3.929$ Å) and 21 wt% ($\alpha = 3.910$ Å). This result is consistent with previous observations on the phase stability of $Sr_2FeMoO_{6-\delta}$[69,70,143]. Phase diagram studies on the composition $Sr_2FeMoO_{6-\delta}$ showed that the solid solubility of Mo in air is limited to 17 at.% Mo, wherefore the $Sr_2FeMoO_{6-\delta}$ composition is not obtained in air and the secondary phase $SrMoO_4$ is observed[70]. After annealing the oxidized sample under reducing conditions at 900 °C for 7 h, the room temperature XRD data showed that the perovskite phases were converted into several mixed phases. The reduced sample was composed of 27 wt% Ruddlesden-Popper phase $Sr_3FeMoO_{7-\delta}$ (space group: I4/mmm, ICSD-156787), 36 wt% simple cubic perovskite $Sr(Fe_{0.8}Mo_{0.2})_3$ (space group: $Pm\bar{3}m$, ICSD 191551), 33 wt% double perovskite $Sr_2(Fe_{1.33}Mo_{0.66})O_{5.88}$

(space group: $Fm\bar{3}m$, ICSD-168704) with superstructure reflexed at 19° and 37.9°, as well as around 4 wt% exsoluted iron (Fe^0). The perovskite phase $SrFe_{1-x}Mo_xO_{3-\delta}$ (x = 0.3) has been reported to exhibit mixed oxygen ionic and electronic conducting properties[65,69,71,144]. The semiconducting and oxygen-deficient Ruddlesden-Popper phase $Sr_3FeMoO_{7-\delta}$ exhibited mixed valence states for Fe and Mo ions in X-Ray Absorption Near Edge Structure (XANES), neutron diffraction and Mössbauer data, which hints at sufficient electronic conductivity[145,146].

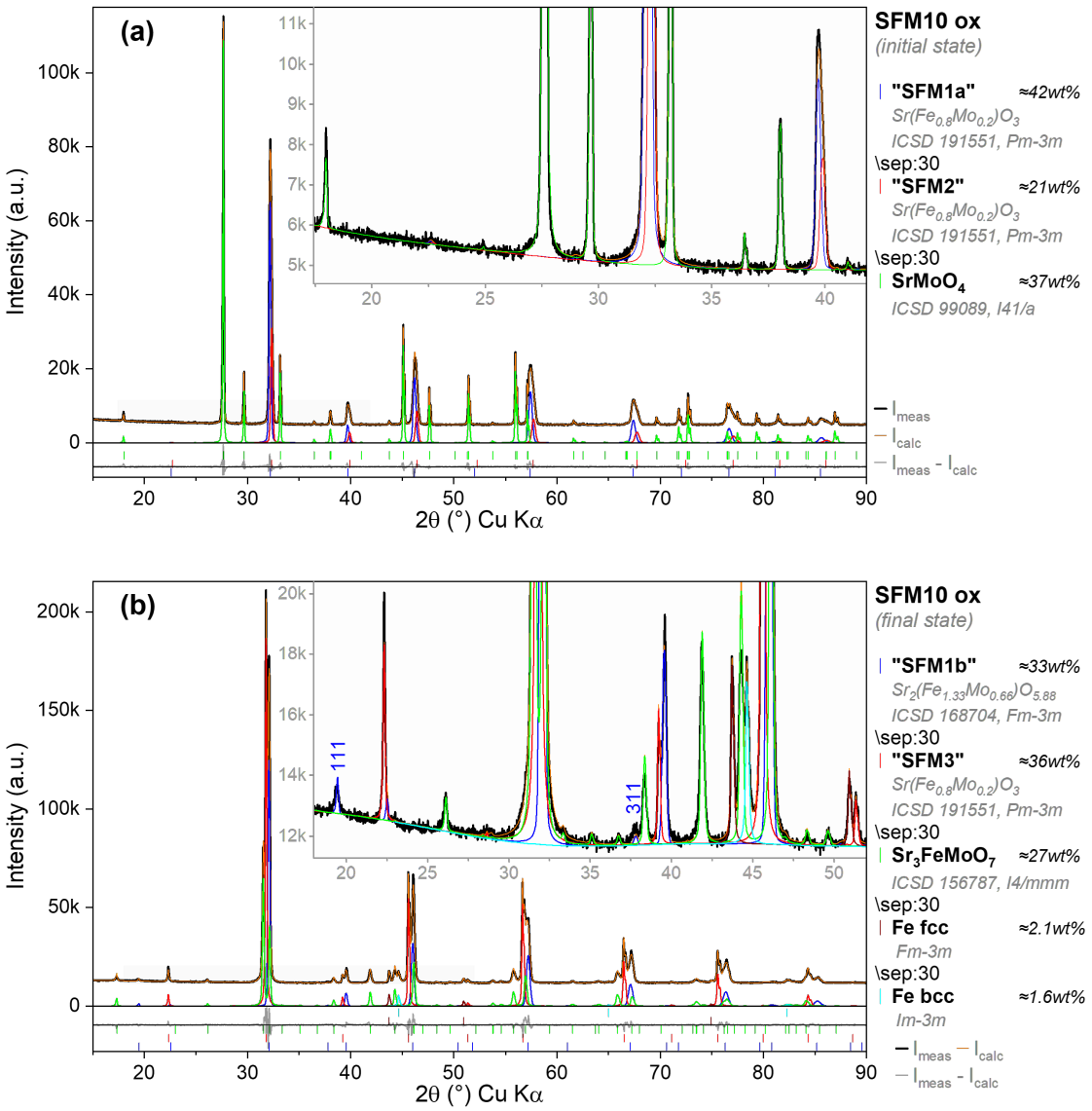

Figure 5.12: Room-temperature powder XRD pattern with Rietveld refinement analysis of the as-prepared SFM in (a) air (R_{wp} = 2.27%, R_p = 1.60%) and (b) after reduction in 100% H_2 for 7 h at 900 °C (R_{wp} = 2.44%, R_p = 1.72%).

X-Ray Photoelectron Spectroscopy (XPS) measurements were carried out on the surface of bar samples to study the oxidation states of iron and molybdenum in SFM

at room temperature for oxidized (Figure 5.13a) and reduced samples (Figure 5.13b). The data analysis of Fe 2p confirms that the majority of the iron in SFM exists as Fe^{3+} (binding energy = 710.8 eV) in the as-prepared sample. The reported mixed valence state of $Fe^{3+} \leftrightarrow Fe^{2+}$ (709.8 eV) could not be confirmed due to low measurement intensities. In comparison, the XPS scan of iron for the sample reduced for 72 h at 900 °C in 100% H_2 shows the distinct mixed oxidation states of Fe^{2+} (709.8 eV), Fe^{3+} (710.8 eV, and 720.2 eV) as well as metallic iron Fe^0 (706.8 eV). These results are consistent with previous studies of other SFM-based perovskite materials and highlight the formation of metallic iron in the sample surface (Fe particle exsolution)[147–149]. The Mo 3d XPS spectra show two broad peaks for the oxidized sample, which could be fitted with two valence states of Mo^{6+} (233.5 eV and 236.7 eV) and Mo^{5+} (232.5 eV and 235.7 eV). As anticipated from Equation 5.3, the Mo^{5+} valence is coupled with Fe^{3+} and slightly predominant compared to Mo^{6+} in the oxidized sample. After the reduction of the SFM sample, the Mo^{6+} concentration (233.1 eV and 236.2 eV) increases to 50.0%, while the concentration of Mo^{5+} (231.5 eV and 234.7 eV) decreases from 55.2% to 19.6%. These XPS results support the in-situ high-temperature XRD and suggest exsolution of Fe nanoparticles.

$$Fe^{3+} + Mo^{5+} \leftrightarrow Fe^{2+} + Mo^{6+} \tag{5.3}$$

The exsolution process of metal nanoparticles can be regarded as partial decomposition of perovskite oxides by exceeding the materials' thermodynamic stability limits due to, e.g. elevated temperatures, or chemical gradient. During the exsolution process, the metal ion migrates from the oxide lattice to the perovskite surface, where it segregates or aggregates as a highly dispersed metal nanoparticle anchored on the perovskite matrix. In contrast to other deposition methods like wet impregnation or vapor deposition, the strong metal-oxide interface of in-situ grown metal nanoparticles increases their resistance to particle coarsening and agglomeration. Additionally, charge barriers for facilitating charge-transfer processes are reduced. The regulation mechanisms behind the exsolution of nanoparticles taking places around the perovskite matrix are still discussed controversially. The Gibbs free energy difference during the reduction of the metal M^{n+} to M^0 is the main driving force for particle exsolution. Another is the energetic difference between the bulk and surface ions, called segregation energy. The exsolution of a B-site ion results in the formation of partial Schottky point defects in the perovskite lattice. Simultaneously to the exsoluted B-site metal, the lattice oxygen dissociates, which results in oxygen vacancy formation and O_2 release[150,151]. This process is described

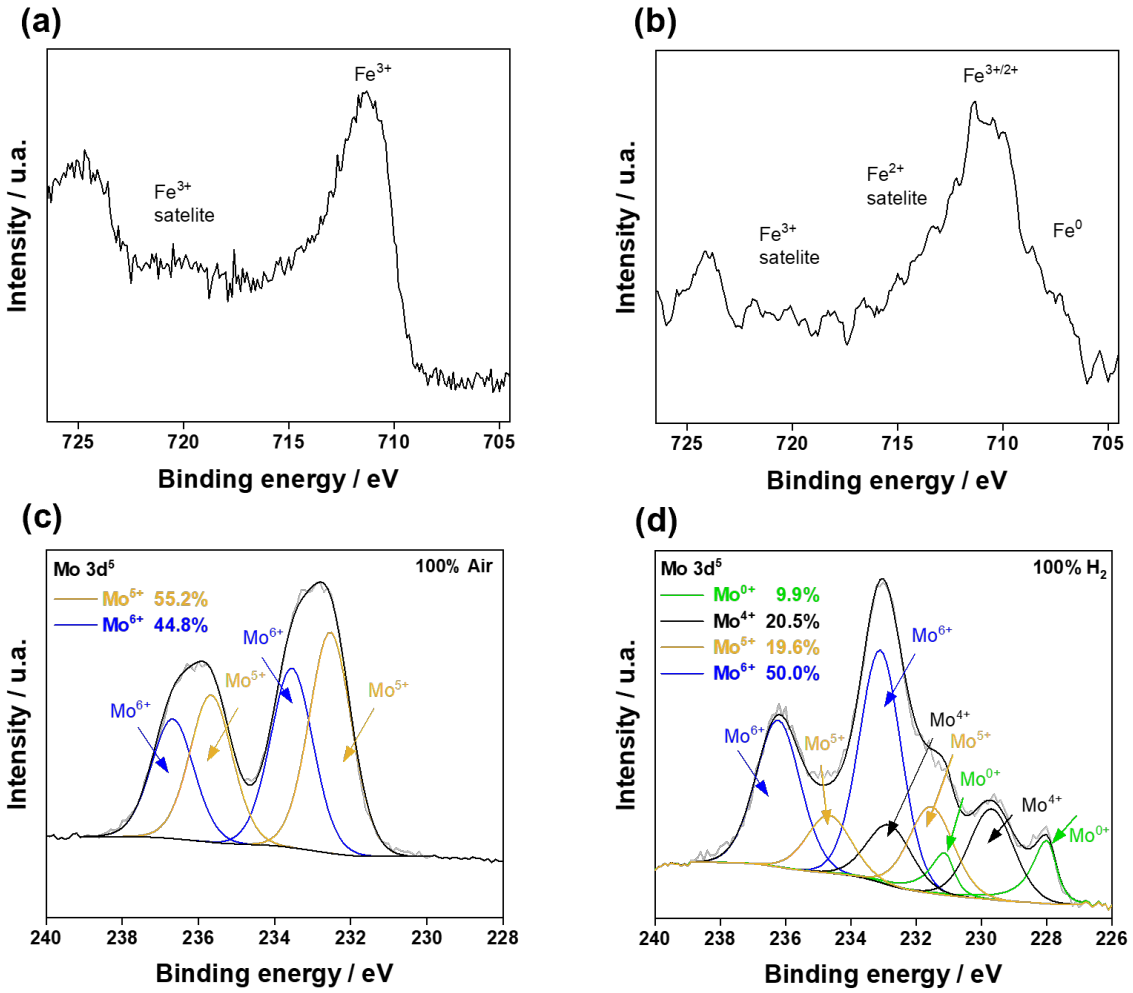

Figure 5.13: Selected XPS scans of $Sr_2FeMoO_{6-\delta}$ samples sintered in air and after reduction in 100% H_2: Fe spectrum (a) before and (b) after reduction. Mo spectrum (c) before and (d) after reduction.

by Equation 5.4, where the B-site exsoluted ions and the oxygen are given by M^{x+} and O^{y-}, with the metal and oxygen vacancies V_M and V_O and the exsoluted metal on the surface denoted by $M_{surface}$.

$$M^{x+} + \frac{n}{2}O^{y-} \leftrightarrow V_M + \frac{n}{2}V_O + M_{surface} + \frac{n}{4}O_{2(g)} \tag{5.4}$$

The driving force of B-site cation exsolution as seen for MIECs has been investigated by different groups. Irvine et al.[152–154] attributed the B-site cation exsolution to a combination of chemical and electrochemical reduction mechanisms starting generally at surface defect sites. In reducing conditions, surface defect (i.e. oxygen vacancies) formation and the reduction of B-site transition metal cations would become more favorable. Thus, the nucleation barriers are lowered through crystal defects[150,155]. Kwon et al.[156,157] derived their explanation for B-site exsolution

from density functional simulations and attributed it to thermodynamics.

The authors proposed that the exsolution energies for the B-site doped double-perovskites $PrBaMnT_2O_{5+\delta}$ are lower compared to the undoped material (T = Fe, Co and/or Ni). Xi et al.[158] associated the electrocatalytic activity to the continued exsolution of bi-metal alloy nanoparticles and the oxygen vacancies and defects formation lead to lattice expansion and increased macrostrain in the perovskite structure. A large enough lattice strain, would lead to energetically favorable dislocations in the lattice, impacting the defect formation, local bonding structure, and oxygen surface stoichiometry. In addition, ionic migration barriers are influences by oxygen vacancies and macrostrain, which can accelerate ionic conductivity and an increase the oxygen exchange rate.

To support the obtained data, high-resolution SEM and TEM images were obtained (Figure 5.14, Figure 5.15). Figure 5.14a and Figure 5.14b illustrate the secondary electron SEM images of the SFM samples before and after reduction respectively. The as-prepared SFM powder particles exhibit a smooth and homogeneous surface. In contrast, the featured surface of the reduced sample is rough and uneven likely attributed to sub-micron nanoparticle on the surface. To elucidate the nature and composition of the growth on the reduced sample surface, EDX mapping was conducted. Figure 5.14c depicts a typical high-angle annular dark-field High-Angle Annular Dark-Field Imaging (HAADF)-STEM image of the reduced SFM, accompanied by its corresponding elemental mapping in Figure 5.14d-g. The Z-contrast difference highlighted by green dotted boxes in Figure 5.14c, is attributed to thickness effects, possibly indicating the presence of internal nanopores within the particles[159,160]. Figure 5.14e shows the presence of Fe-rich exsolution measuring 10-70 nm. The elemental distribution of all other elements is relatively even throughout the particle.

The TEM image in Figure 5.15a serves to affirm the presence of Fe-rich nano-exsolutions on the SFM particle surface post-reduction. The High-Resolution Transmission Electron Microscopy (HRTEM) image additionally reveals the strong anchoring effect between the exsoluted Fe nanoparticle and the perovskite substrate (Figure 5.15c). The exsoluted nanoparticles from the perovskite matrix form various new perovskite–metal hetero-interfaces, thereby extending the Triple Phase Boundary (TPB). Exsoluted nanoparticles also exhibit higher conductivities than the bulk phase, therefore they are highly catalytically active and lead to enhanced electrochemical material performance. As a result of metal nanoparticles exsolution, oxygen vacancies are formed and aggregate near the perovskite interface[161,162]. The anchoring effect contributes significantly to the surface stability of the electrode ma-

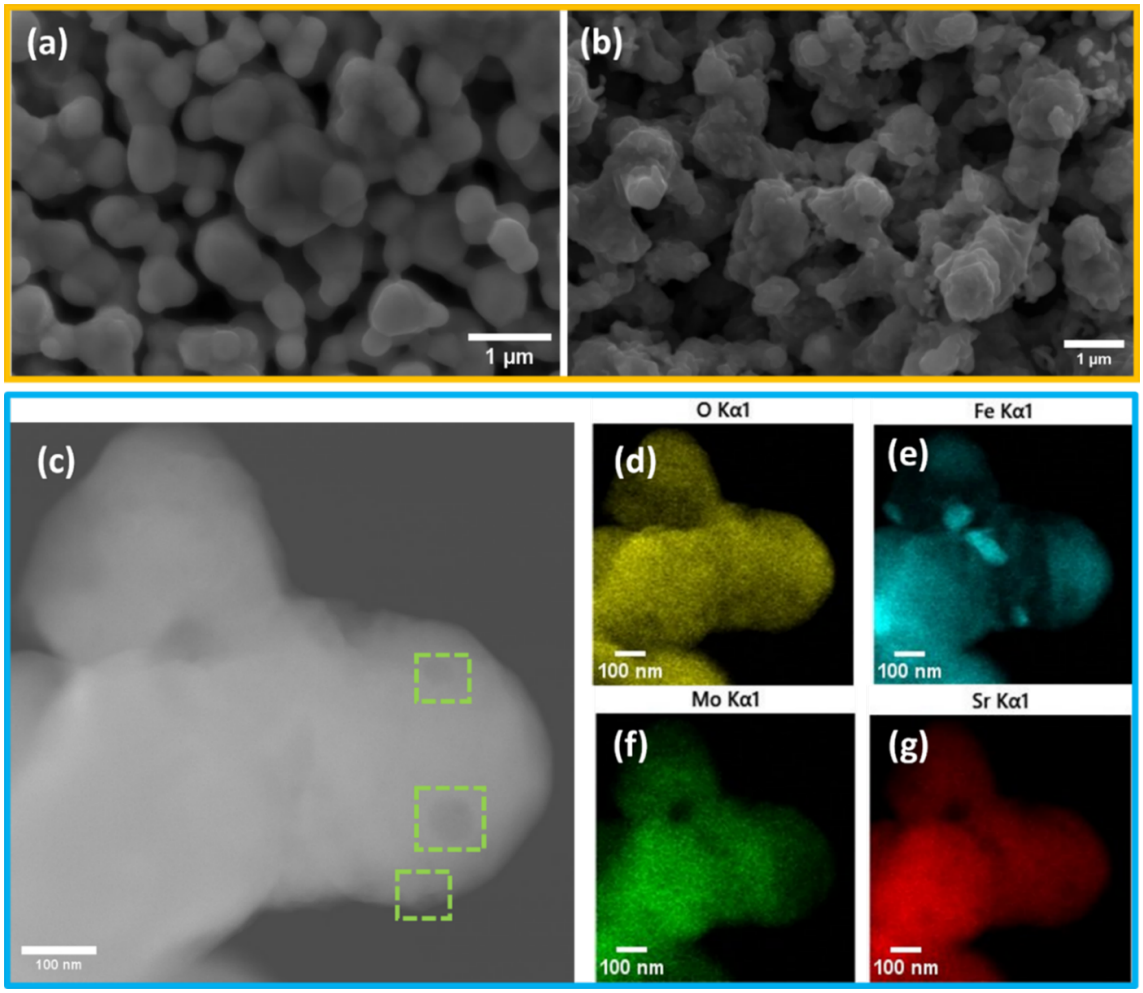

Figure 5.14: SEM image of (a) as-prepared and, (b) reduced $Sr_2FeMoO_{6-\delta}$ powders. (c) High magnification HAADF-STEM image of the reduced $Sr_2FeMoO_{6-\delta}$ particle illustrating the contrast features in green boxes and (e-g) elemental mapping of the corresponding particle.

terial during operation as they effectively prevent the sintering and agglomeration of metal nanoparticles at higher temperatures. Furthermore, this anchoring enhances the catalytic activity of the nanoparticles and imparts resistance to hydrocarbon coking, augmenting the overall performance of the system[158,163,164]. The lattice spacing information was evaluated from the HRTEM images. The TEM image in Figure 5.15a illustrates the lattice spacing of the reduced SFM matrix having a = 0.248 nm lattice gap, corresponding to the plane (3 1 0) of $Sr_2(Fe_{1.33}Mo_{0.66})O_{5.88}$ (space group: $Fm\bar{3}m$, ICSD-168704). In Figure 5.15c, the 0.358 nm lattice spacing of Fe nanoparticle exsolution matches the (1 0 0) plane of FCC-gamma-Fe (space group: $Fm\bar{3}m$, ICSD-43096). The substrate possesses a lattice spacing of 0.276 nm, which corresponds to the (1 1 0) plane of $Sr(Fe_{0.8}Mo_{0.2})O_3$ (space group: $Pm\bar{3}m$, ICSD-191551).

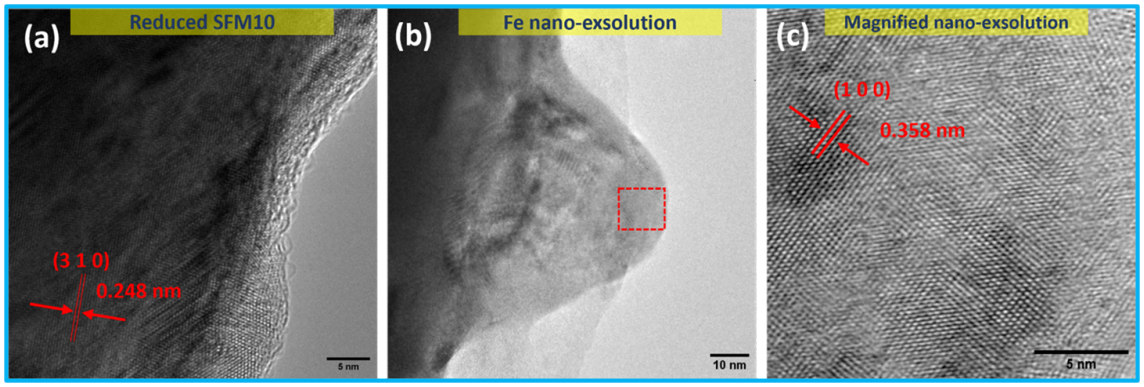

Figure 5.15: (a) HRTEM image of reduced SFM, (b) TEM image of reduced SFM with exsolution illustrating the anchoring effect of the Fe nano-exsolution with the SFM matrix, and (c) HRTEM image of Fe nano-exsolution of the inset marked with red box depicted in (b).

Further information regarding the lattice parameters of the as-prepared sample, the reduced sample and the Fe-rich exsolution has been provided in supplementary Figure A.2 and Figure A.3. The lattice spacing information from the HRTEM images provide information regarding the phases present in the as-prepared and reduced states of the SFM particles respectively and support the data obtained from the in-situ high-temperature XRD. Figure A.3a illustrates the HRTEM image of as-prepared SFM particles and exhibits lattice spacing of 0.276 nm which corresponds to the (1 1 0) plane of $SrFe(_{0.8}Mo_{0.2})O_3$ (space group: $Pm\bar{3}m$, ICSD-191551). In Figure A.3b, the lattice spacing of 0.321 nm observed for the reduced SFM particles, corresponds to the planes (1 0 3) of Sr_3FeMoO_7 (space group: I4/mmm, ICSD-156787). The results obtained from the TEM lattice parameter calculations support the data obtained from the XRD characterization of both as-prepared and reduced SFM particles. In the supplementary Figure A.4a-i, snapshots of different time stamps taken from an in-situ reduction video are provided. These figures depicting the Fe nano-exsolution growth offer insights into the underlying mechanism of their growth.

5.2.2 Material Characterization

The compatibility of the thermal expansion coefficients is a prerequisite for further use of SOC materials, otherwise, a reduction in system lifetime and cell failure may occur. The relative expansion dL/L with varied temperatures was determined in air for $Sr_2FeMoO_{6-\delta}$ and $Sr_2FeMoO_{6-\delta}$-GDC. The chemical compatibility of SFM and GDC was established through combined sintering of powder at 1150 °C for 6 h (Figure A.5). The Thermal Expansion Coefficients (TECs) calculated from the slope of dilatometry measurements are displayed in Figure

5.16. The TEC for the SFM-based electrodes are $13.8 \cdot 10^{-6}$ °C^{-1} for SFM and $12.9 \cdot 10^{-6}$ °C^{-1} for SFM-GDC. These values are in range with other perovskite materials suggested as alternative fuel electrode material like $La_{1.2}Sr_{0.8}Mn_{0.4}Fe_{0.6}O_{3-\delta}$ (LSMF), which exhibits an thermal expansion coefficient of $13.6 \cdot 10^{-6}$ °C^{-1}[165]. The oxygen electrode material $La_{0.6}Sr_{0.4}Co_{0.2}Fe_{0.8}O_{3-\delta}$ (LSCF) exhibits a noticeable higher expansion coefficient with $17.5 \cdot 10^{-6}$ °C^{-1}[79], while the TEC for the state-of-the-art fuel electrode material Ni-8YSZ (40% Ni-60% 8YSZ) is much lower with $12.5 \cdot 10^{-6}$ °C^{-1}[79]. The thermal expansion coefficients for SFM and SFM-GDC are similar to Ni-8YSZ and other electrolyte materials, which indicates their good thermo-mechanical compatibility[5,166,167].

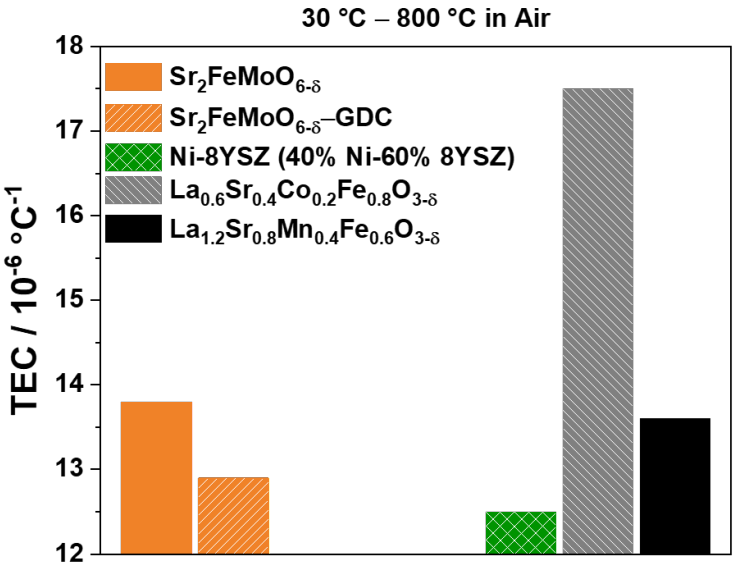

Figure 5.16: Thermal expansion coefficients of SFM-based fuel electrode materials derived from dilatometry experiments in air compared to state-of-the-art and alternative perovskite electrode materials.

The Thermo Gravimetric Analysis (TGA) of $Sr_2FeMoO_{6-\delta}$ and the $Sr_2FeMoO_{6-\delta}$-$Ce_{0.8}Gd_{0.2}O_{1.9}$ composite[58] material was determined from room temperature up to 1000 °C in air and under reducing conditions (Ar-4% H_2 atmosphere, heating rate 1 ml $\cdot$ min^{-1}). The samples were slowly heated in air two times up to 1000 °C to remove any moisture traces from the powders before the atmosphere was changed to Ar–4% H_2. The recorded data are shown in Figure 5.17a for SFM and in Figure 5.17b for SFM-GDC. In the air atmosphere, the weight loss of SFM and SFM-GDC increases with temperature, as oxygen ions are released. As the sample was cooled down from 1000 °C to 100 °C, the complete reversibility of the weight loss was observed. During heat-up under reducing conditions in Ar-4% H_2, SFM and SFM-GDC show a weight loss plateau starting around 400 °C. Moreover, SFM shows

higher weight loss under reducing atmosphere compared to SFM-GDC. At higher temperatures, non-reversible weight loss increases sharply due to oxygen vacancies formation, the release of lattice oxygen, as well as desorption of any adsorbing oxygen species such as adsorbed $H_2O_{ad.}$ or $O_{ad.}$. Additionally, above 400 °C, the reduction of Fe^{3+} and Mo^{6+} is reported, which could also induce a phase transition under a reducing atmosphere[17,168,169]. Since the oxygen vacancy concentration is directly linked to the conductivity of MIEC materials, the total conductivity of SFM and SFM-GDC was characterized under oxidizing and reducing atmospheres.

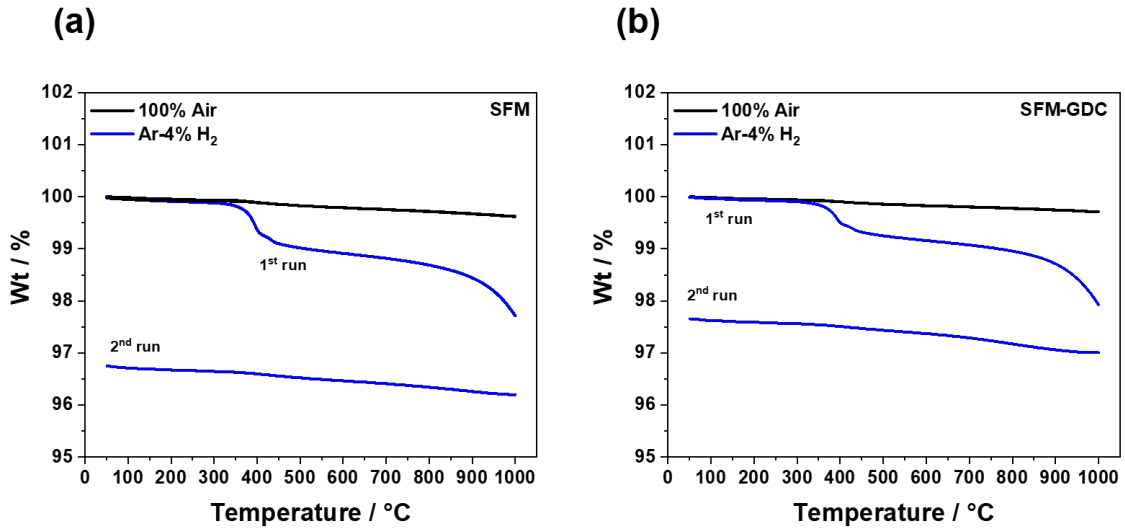

Figure 5.17: Thermal gravimetrical analysis in air and Ar-4% H_2 (50 °C $\leq$ 1000 °C) for (a) $Sr_2FeMoO_{6-\delta}$ and (b) $Sr_2FeMoO_{6-\delta}$-GDC.

The total conductivity was measured with DC measurements in air and hydrogen atmospheres at operating temperatures between 500 °C and 900 °C and is displayed as total electrical conductivity σ vs. 1000/T in Figure 5.18. The conductivity's activation energies E_A were determined according to the linearized Arrhenius relation given in Equation 5.5, where R gives the resistance, σ_0 is the conductivity, T the temperature and $\Re$ the ideal gas constant.

$$ln\ R = \sigma_0 + \frac{E_A}{\Re T} \tag{5.5}$$

In air, $Sr_2FeMoO_{6-\delta}$ and $Sr_2FeMoO_{6-\delta}$-GDC exhibit semiconducting behavior up to the maximum conductivity at 650 °C with 4.5 $S \cdot cm^{-1}$ and 2.1 $S \cdot cm^{-1}$ respectively. At higher temperatures, the conductivity behavior is pseudo-metallic and decreases up to 3.5 $S \cdot cm^{-1}$ for $Sr_2FeMoO_{6-\delta}$ and 1.7 $S \cdot cm^{-1}$ for $Sr_2FeMoO_{6-\delta}$-GDC at 900 °C. The electrical conductivity in air is lower than for SFM due to the

phase impurities observed[4].

Under reducing atmosphere, the electrical conductivity of $Sr_2FeMoO_{6-\delta}$ and $Sr_2FeMoO_{6-\delta}$-GDC increased compared to the measurements in air, although it still exhibited pseudo-metallic behavior between 900 °C to 650 °C. After 24 h in H_2, a conductivity of 13.5 $S \cdot cm^{-1}$ was achieved for $Sr_2FeMoO_{6-\delta}$ at 900 °C, which increased up to 17.1 $S \cdot cm^{-1}$ at 650 °C. The composite material $Sr_2FeMoO_{6-\delta}$-GDC showed pseudo-metallic behavior as well as higher conductivities from 48.1 $S \cdot cm^{-1}$ at 900 °C to 64.7 $S \cdot cm^{-1}$ at 650 °C. The higher conductivity increase for $Sr_2FeMoO_{6-\delta}$ after a change in atmosphere is related to the large $SrMoO_4$ secondary phase in air atmosphere, which is not present in reducing conditions. The pseudo-metallic behavior of $Sr_2FeMoO_{6-\delta}$ has been previously observed for $SrFeO_{3-\delta}$-based perovskite materials and was related to the loss of oxygen during the heating procedure and the partial delocalization of mobile electronic charge carriers[4,70].

The double perovskite $Sr_2FeMoO_{6-\delta}$ is a ferromagnetic material, which exhibits electrical conductivity and oxygen ionic conductivity in reducing atmosphere. Although the oxygen vacancy diffusion rate increases with temperature, the electrical conductivity mechanism is related to the hopping of small polarons associated with the mixed-valent redox relation as expressed in Equation 5.6 using the Kröger-Vink notation[72]. In an oxidizing atmosphere at high oxygen partial pressures (pO_2), the electronic holes are the dominant charge carriers with a valence balance between iron and molybdenum.

$$\frac{1}{2}O_2 + V_O^{\bullet\bullet} \leftrightarrow O_O^{\times} + 2h^{\bullet} \tag{5.6}$$

As described with the use of the Kröger-Vink notation in Equation 5.3 and Equations 5.7 - 5.8, oxygen vacancies are formed to maintain the electroneutrality as a result of the partial reduction of Mo^{6+} to Mo^{5+} and Fe^{3+} to Fe^{2+} in atmospheres of low oxygen partial pressures[69,170–172].

$$2Fe_{Fe}^{\times} + O_O^{\times} \leftrightarrow 2Fe_{Fe}' + V_O^{\bullet\bullet} + \frac{1}{2}O_2 \tag{5.7}$$

$$2Mo_{Mo}^{\times} + O_O^{\times} \leftrightarrow 2Mo_{Mo}' + V_O^{\bullet\bullet} + \frac{1}{2}O_2 \tag{5.8}$$

Although the ionic conductivity of ferrite-molybdates increases in the reducing atmosphere and has been observed to be higher than in air, it remains negligible compared to the predominant electrical conductivity[72]. GDC exhibits good ionic conductivity ($\sim$0.1 $S \cdot cm^{-1}$ at 800 °C) in air and develops mixed ionic and electronic conductivity due to the reduction of Ce^{4+} to Ce^{3+} in reducing conditions[35,173–175].

This mechanism additionally increases the total conductivity of SFM-GDC under reducing conditions. SFM as well as SFM-GDC exhibit higher conductivities in reducing atmosphere (σ_{SFM} = 13.5 S · cm^{-1} at 900 °C, 15.3 S · cm^{-1} at 800 °C; $\sigma_{SFM-GDC}$ = 48.1 S · cm^{-1} at 900 °C, 53.3 S · cm^{-1} at 800 °C) than other perovskite materials such as $La_{0.75}Sr_{0.25}Cr_{0.50}Mn_{0.50}O_{3-\delta}$ (1.5 S · cm^{-1} at 900 °C in 5% H_2-Ar)[176] and $Sr_2MgMoO_{6-\delta}$ (4 S · cm^{-1} in 5% H_2-Ar, 9.3 S · cm^{-1} at 800 °C in H_2)[177] have also been considered promising alternative fuel electrode materials[4]. In comparison to $Sr_2FeMoO_{6-\delta}$, conductivities for the double perovskite $Sr_2NbMoO_{6-\delta}$ were also observed to be lower at 850 °C with 0.05 S · cm^{-1} in air and 2.215 S · cm^{-1} in reducing conditions of 5% H_2 + 95% Ar[178].

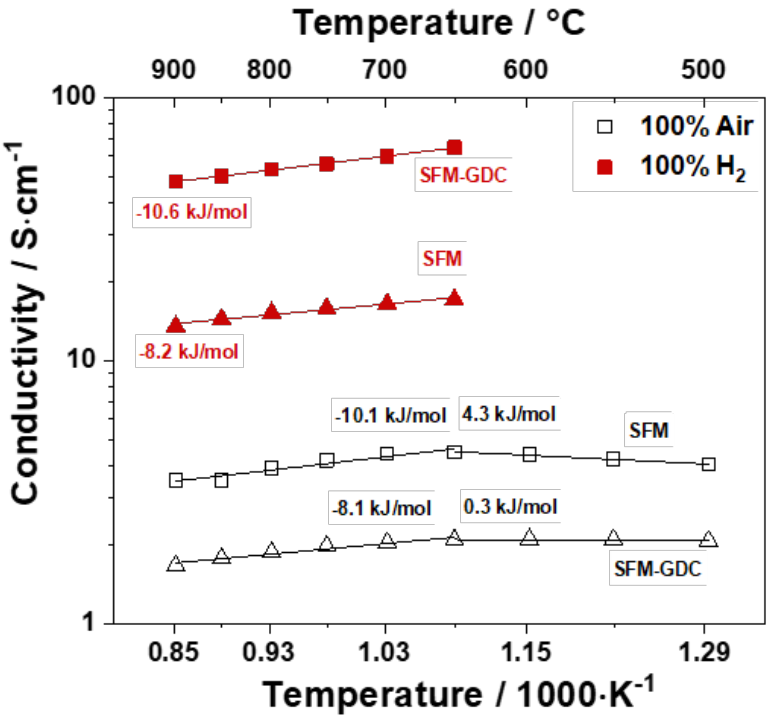

Figure 5.18: Conductivity measurements in the temperature range from 500 °C to 900 °C in air and hydrogen for $Sr_2FeMoO_{6-\delta}$ and the composite sample $Sr_2FeMoO_{6-\delta}$-GDC.

5.2.3 Electrochemical Characterization

5.2.3.1 Electrochemical Performance Analysis

The fuel electrode materials SFM and SFM-GDC were characterized in steam electrolysis and co-electrolysis conditions between 750 °C and 900 °C. The experimental OCV was compared for all operating conditions to the theoretical values derived by the Nernst equation to rule out gas leaks. The experimental deviation from the theoretical potential in steam electrolysis conditions at 900 °C amounted to

1.8 mV, which is a deviation of less than 1%. Figure 5.19a and Figure 5.19b display the respective current-voltage characteristics and Figure 5.19c as well as Figure 5.19d the impedance measurements at OCV and 900 °C for SFM and SFM-GDC respectively. The performance of SFM at 1.5 V as observed in the current-voltage characteristics is only slightly higher compared to SFM-GDC. The single cell with the SFM fuel electrode achieved $-1.26\ \mathrm{A \cdot cm^{-2}}$ and $-1.27\ \mathrm{A \cdot cm^{-2}}$ for steam and co-electrolysis conditions, respectively. The SFM-GDC fuel electrode achieved slightly lower current densities in steam and co-electrolysis with $-1.24\ \mathrm{A \cdot cm^{-2}}$ and $-1.27\ \mathrm{A \cdot cm^{-2}}$ respectively. With decreasing temperature, the performance difference between SFM and SFM-GDC increases, and at 750 °C, $-0.48\ \mathrm{A \cdot cm^{-2}}$ with SFM and $-0.37\ \mathrm{A \cdot cm^{-2}}$ with SFM-GDC were achieved in steam electrolysis (Figure 5.19a, b, Figure A.6). The state-of-the-art Ni-8YSZ fuel electrode measured in the same conditions exhibited lower performance for steam and co-electrolysis in comparison to the SFM and SFM–GDC fuel electrodes at 900 °C ($-0.91\ \mathrm{A \cdot cm^{-2}}$[179], and $-1.06\ \mathrm{A \cdot cm^{-2}}$[179]). However, electrolyte-supported Ni-GDC fuel-electrode containing single cells exhibit higher current densities at 900 °C and 1.5 V with $-1.31\ \mathrm{A \cdot cm^{-2}}$, and $-1.37\ \mathrm{A \cdot cm^{-2}}$ in steam, and co-electrolysis conditions[180]. The results obtained in this work for SFM ($-0.67\ \mathrm{A \cdot cm^{-2}}$, 850 °C and 1.3 V) and SFM-GDC ($-0.62\ \mathrm{A \cdot cm^{-2}}$, 850 °C and 1.3 V) are in the range of the values obtained for the single cell with SFM-SDC electrode (SFM SDC/LCO/LSGM/SDC-LSCF), which showed a current density of $-0.64\ \mathrm{A \cdot cm^{-2}}$ at 850 °C and 1.3 V with 42% H_2O + 58% H_2 fuel gas mixture[17]. In the Figure 5.19c and Figure 5.19d, the impedance spectra measured in steam and co-electrolysis at 900 °C are shown. For SFM, the ASR is lower compared to SFM-GDC irrespective of the measurement conditions. The ASR of the SFM-GDC composite electrode increases by $1423\ \mathrm{m\Omega \cdot cm^2}$ for steam and $3164\ \mathrm{m\Omega \cdot cm^2}$ in co-electrolysis atmosphere when decreasing the temperature from 900 °C to 750 °C. The SFM electrode exhibits a smaller increase in ASR with $747\ \mathrm{m\Omega \cdot cm^2}$ and $1352\ \mathrm{m\Omega \cdot cm^2}$ for steam and co-electrolysis respectively. The ASR is composed of the ohmic resistance R_Ω and polarization resistance R_P. The ohmic resistance R_Ω is determined by the interception of the Nyquist plot with the real impedance axis (abscissa) at higher frequencies. The activation energy for R_Ω is determined based on the slope of the Arrhenius equation and equals between $50 - 56 \pm 5\ \mathrm{kJ \cdot mol^{-1}}$. This closely aligns with values reported in the literature for the ionic conductivity in YSZ electrolyte films and suggests that the primary contribution to R_Ω is the 250 µm thick 8YSZ electrolyte[181–183].

Table 5.2: Electrochemical performance of $Sr_2FeMoO_{6-\delta}$-based fuel electrodes in comparison to state-of-the-art Ni-cermet electrodes at 900 °C.

Fuel Electrode	**Test conditions**	$\boldsymbol{R_{P,OCV}}$ **/** $\boldsymbol{\Omega \cdot cm^2}$	$\boldsymbol{i_{1.5V}}$ **/** $\boldsymbol{A \cdot cm^{-2}}$
Ni-8YSZ	H_2O electrolysis	0.17[179]	−0.91[179]
	co-electrolysis	0.20[179]	−1.06[179]
Ni-GDC	H_2O electrolysis	0.06[179]	−1.31[180]
	co-electrolysis	0.09[180]	−1.37[180]
GDC	H_2O electrolysis	0.16[181]	−0.92[181]
	co-electrolysis	0.28[181]	−0.82[181]
$Sr_2FeMoO_{6-\delta}$	H_2O electrolysis	0.07	−1.26
	co-electrolysis	0.17	−1.27
$Sr_2FeMoO_{6-\delta}$-GDC	H_2O electrolysis	0.13	−1.24
	co-electrolysis	0.27	−1.27

GDC: $Ce_{0.8}Gd_{0.2}O_{1.9}$, SFM: $Sr_2FeMoO_{6-\delta}$, 8YSZ: 8mol% YSZ

5.2.3.2 Equivalent Circuit Model Evaluation

The Nyquist plots for the single button cells with SFM and SFM-GDC composite fuel electrodes broadly show two contributions, i.e. low-frequency and high frequency contributions (Figure 5.20). To deconvolute the underlying frequency-dependent physical processes at the electrodes, impedance spectra were taken with varied temperature, fuel composition and oxygen partial pressure and subsequently evaluated by Distribution of Relaxation Times (DRT) analysis. The number of time constants observed in the DRT spectra, were used to establish an equivalent circuit model (ECM) with an appropriate number of passive elements to fit the impedance spectra. The exemplary DRT spectra (Figure 5.20b) show four underlying time constants P1, P2, P3, and P4 in the analyzed frequency range from the total cell impedance given in the experimental Nyquist plots. Therefore, the final ECM consists of four R//Q elements connected in series including an inductor (I) and a serial resistor (R_Ω). The inductance I and series resistance (R_Ω) account for the wires' inductivity and the ohmic losses contributed by the electrolyte and electrodes (Figure 5.20a). The quality analysis of the Complex Nonlinear-Least-Square (CNLS) fit with this ECM is given in Figure 5.20b-d) by comparing the DRT and Nyquist plots of experimental and fitted data and shows qualitatively good agreement. Further-

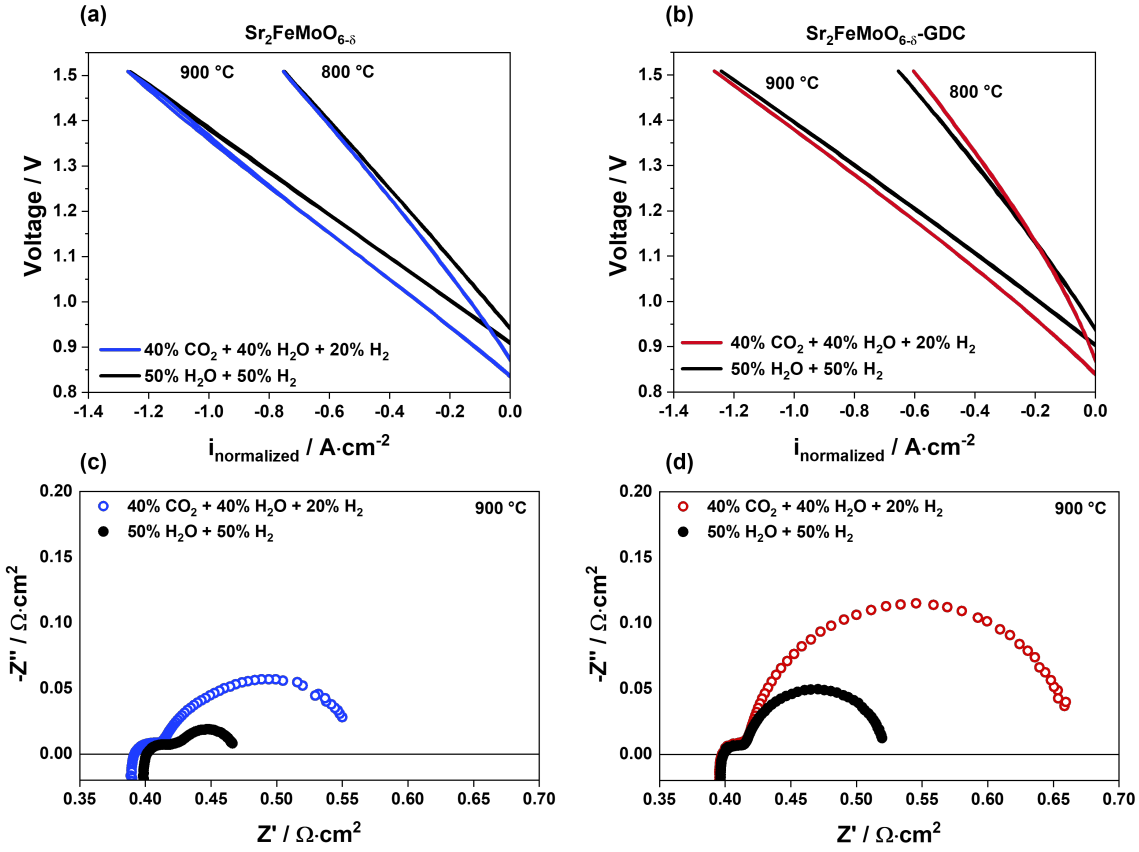

Figure 5.19: (a) I–V curves and (b) impedance spectra at OCV measured for $Sr_2FeMoO_{6-\delta}$ at 900 °C as well as 800 °C in steam electrolysis, and co-electrolysis conditions. (c) I–V curves and (d) impedance spectra at OCV measured for the composite $Sr_2FeMoO_{6-\delta}$-$Ce_{0.8}Gd_{0.2}O_{1.9}$ in steam electrolysis, and co-electrolysis conditions at 900 °C as well as 800 °C.

more, the relative residuals as well as the low X^2 (chi-square) error of 10^{-8} between the fitted and experimental data indicate a reasonable ECM.

5.2.3.3 Temperature Variation

The single cells with SFM and SFM-GDC fuel electrodes were evaluated in steam electrolysis (50% H_2O + 50% H_2) and co-electrolysis (40% H_2O + 40% H_2O + 20% H_2) atmosphere between 750 °C and 900 C in steps of 25 °C to characterize the thermally activated processes. The DRT analysis spectra with the regularization parameter $\lambda = 10^{-4}$ are given in Figure 5.21 and the corresponding Nyquist plots are listed in the supplement (Figure A.7). With decreasing temperature, the low- and high-frequency contributions increase, indicating thermally activated processes. All these impedance diagrams were fitted by four R//Q elements including I and R_Ω. The DRT spectra in Figure 5.21 depict four time constants for SFM in the investigated frequency range from 0.1 Hz to 100 kHz with an additional shoulder

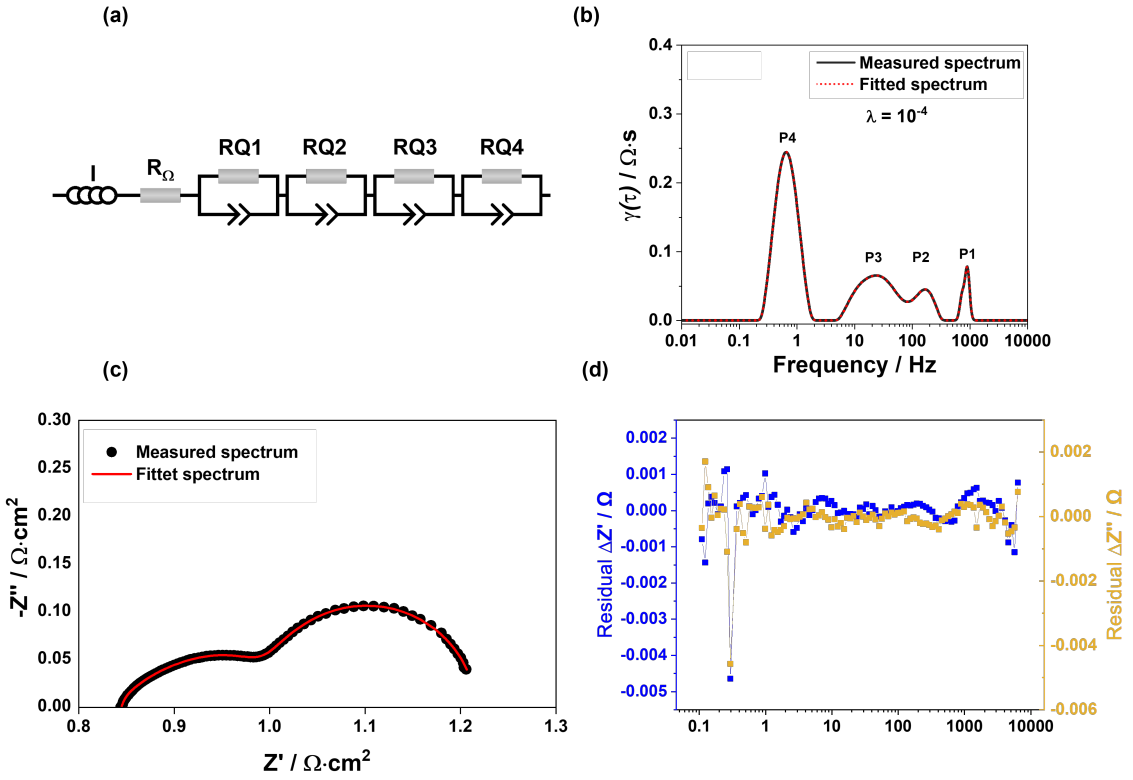

Figure 5.20: (a) Equivalent circuit model (ECM) used for the fitting of the experimental impedance data. (b) Distribution of relaxation times (DRT) of experimental and fitted impedance data for $Sr_2FeMoO_{6-\delta}$ at 750 °C in 50% H_2O + 50% H_2 recorded at OCV. (c) Nyquist plot of the experimental data and corresponding fit. (d) The corresponding residual of the fitted data to verify the quality of the CNLS fit.

peak at around 10 Hz. The peaks P1, P2, P3, and P4 correspond to the circuit elements used in the ECM with RQ1, RQ2, RQ3, and RQ4, respectively. All peaks exhibit thermal activation and a shift in frequency with the variation of operating temperature. In addition, the DRT spectra for SFM-GDC emphasize that the low-frequency process P4 is much more dominating than for SFM.

The individual resistances obtained for four different processes are shown in Figure 5.22 and are corroborated by frequency-dependent DRT spectra as a function of temperature for SFM and SFM-GDC under steam- and co-electrolysis conditions. As can be seen from the DRT spectra and the resistance analysis, the predominant physical process, which corresponds to the rate-limiting step is P4 (R_{RQ4}, 2 - 0.1 Hz) for both steam- and co-electrolysis conditions. The activation energy of this low-frequency process is between 118 ± 12 kJ · mol^{-1} to 149 ± 5 kJ · mol^{-1}. Physical processes suggested in this frequency range include gas conversion as well as diffusion processes at the fuel electrode side. These processes, however, exhibit very low thermal activation and therefore cannot be attributed to P4[1,133,184,185].

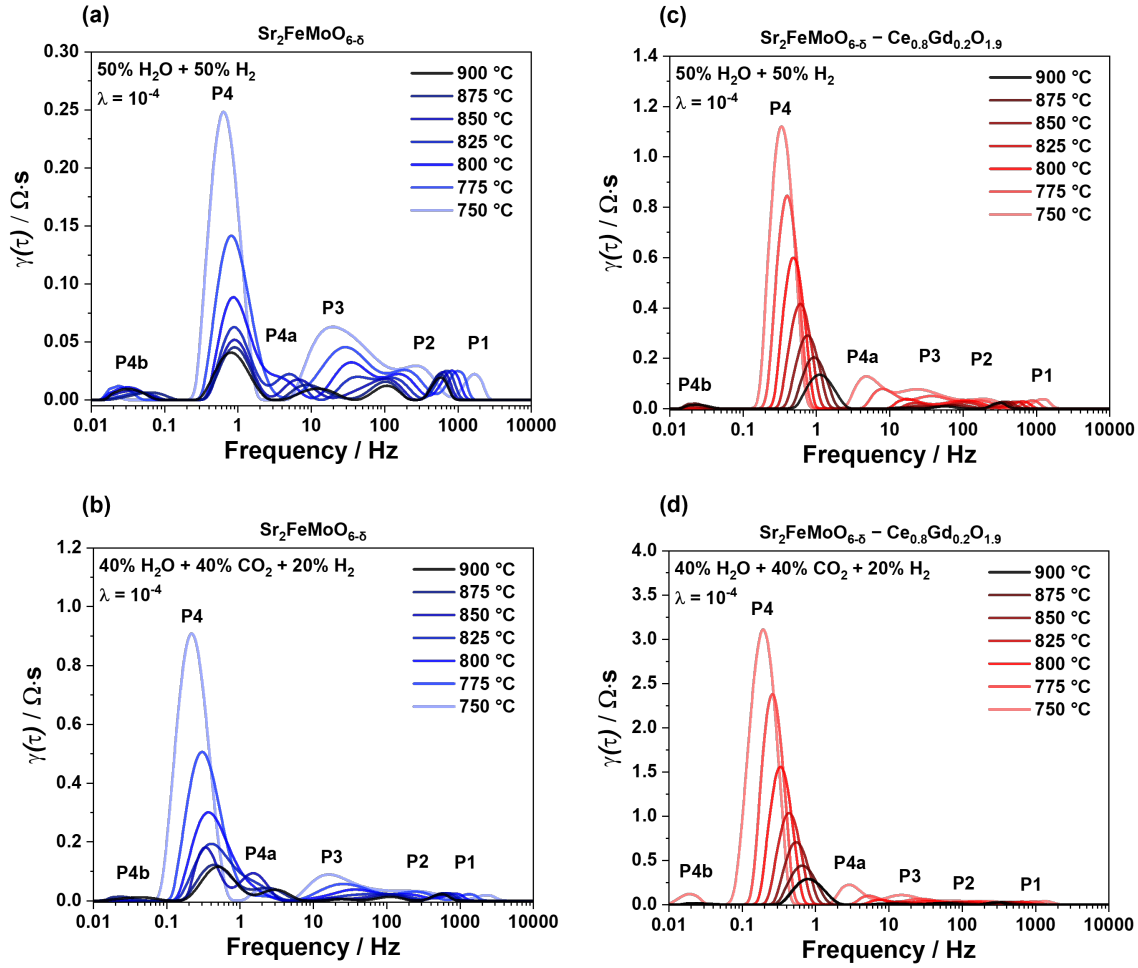

Figure 5.21: DRT spectra as a function of temperature measured at OCV between 750 °C and 900 °C for (a, c) SFM and (b, d) SFM-GDC in steam electrolysis, and co-electrolysis.

Very few studies based on perovskite fuel electrodes show individual process analysis including activation energies, suggest adsorption and/or dissociation processes at the SFM-based fuel electrode in this frequency range[58,147,158,186,187]. As shown by Figure A.8, the process that is mainly influenced by polarization is also P4[188]. This is an indication of a charge transfer process that has been observed for MIEC electrodes around 1 - 2 Hz[189] with an activation energy of approximately 107 - 126 kJ · mol^{-1}[181]. The other processes P1 (2000 - 1000 Hz), P2 (500 - 100 Hz), and P3 (100 - 10 Hz) also exhibit a temperature dependency and a frequency shift with increasing operation temperature.

The observed high-frequency contribution P1 is modeled by R_{RQ1} and shows similar activation energies of 153 kJ · mol^{-1} in steam and co-electrolysis for SFM and SFM-GDC fuel electrodes. The described frequency range (Table 5.3) and the high activation energy have been previously attributed to an electrode charge-transfer

process at the LSCF oxygen electrode[181,190–192]. The middle to high-frequency process modeled by R_{RQ2} (500 - 100 Hz) shows activation energies between 120 - 130 kJ · mol^{-1} for both steam and co-electrolysis. The thermally influenced process in this frequency range has been attributed to the surface exchange kinetics and oxygen diffusion in the bulk and at the surface of the LSCF electrode[190].

The mid to low-frequency process given by R_{RQ3} (P3, 100 - 10 Hz) shows an E_A highly influenced by the choice of fuel electrode material. For single cells with an SFM-GDC electrode, this process exhibits an activation energy of around 206 ± 5 kJ · mol^{-1} to 222 ± 8 kJ · mol^{-1}. For SFM, however, the activation energy is around (72 ± 16 kJ · mol^{-1}) for steam and (96 ± 20 kJ · mol^{-1}) for co-electrolysis. The significant deviation in activation energies indicates that the variation of fuel electrode material has an influence on the process resistance R_{RQ3} in this frequency range. Previous studies suggested an overlap of fuel electrode and oxygen electrode mechanisms e.g., transport processes[190]. The different activation energies seen for SFM and SFM-GDC with regards to the process P3 suggest a different dominant process at the SFM fuel electrode with a lower activation energy. A middle frequency process (100 Hz) has been related previously to oxide ion transport from bulk to surface as well as across the electrolyte/electrode interface with 100 kJ · mol^{-1}[185,189,193]. The decreased activation energy for the mid-frequency process could also suggest an influence of transport processes in the fuel and oxygen electrode[190].

5.2.3.4 Gas Variation at the Fuel and Oxygen Electrode

The in-depth process analysis was further corroborated by the characterization of the fuel gas influence on the impedance data. As shown in Figure 5.23, the concentration of steam and hydrogen in the operating atmosphere was varied and the impedance spectra were recorded at OCV and 900 °C. The results emphasize that an increase in H_2 has no impact on the ohmic resistance, as expected, and neither on the high-frequency arc. The main influence is observed in the mid-to low-frequency region with a decreased polarization resistance R_P with increasing pH_2O from 93 mΩ · cm^2 at 30% H_2O + 70% H_2 to 80 mΩ · cm^2 with 50% H_2O + 50% H_2. The DRT analysis of the impedance data in Figure 5.23 exhibits that the main impact of the fuel gas variation is attributed to P3 and P4 in the mid-to low-frequency regions. The peaks P1, and P2 are not dependent on a variation in fuel gas compositions.

The oxygen partial pressure on the oxygen electrode side was additionally varied at 900 °C in steam electrolysis conditions of 50% H_2O + 50% H_2 between 21% O_2 and 3% O_2 balanced with N_2. The impedance spectra measured at OCV are displayed in Figure 5.24a and were further analyzed to discern the influence of the oxygen partial pressure pO_2 on the process (resistances) P1, P2, P3, and P4. The

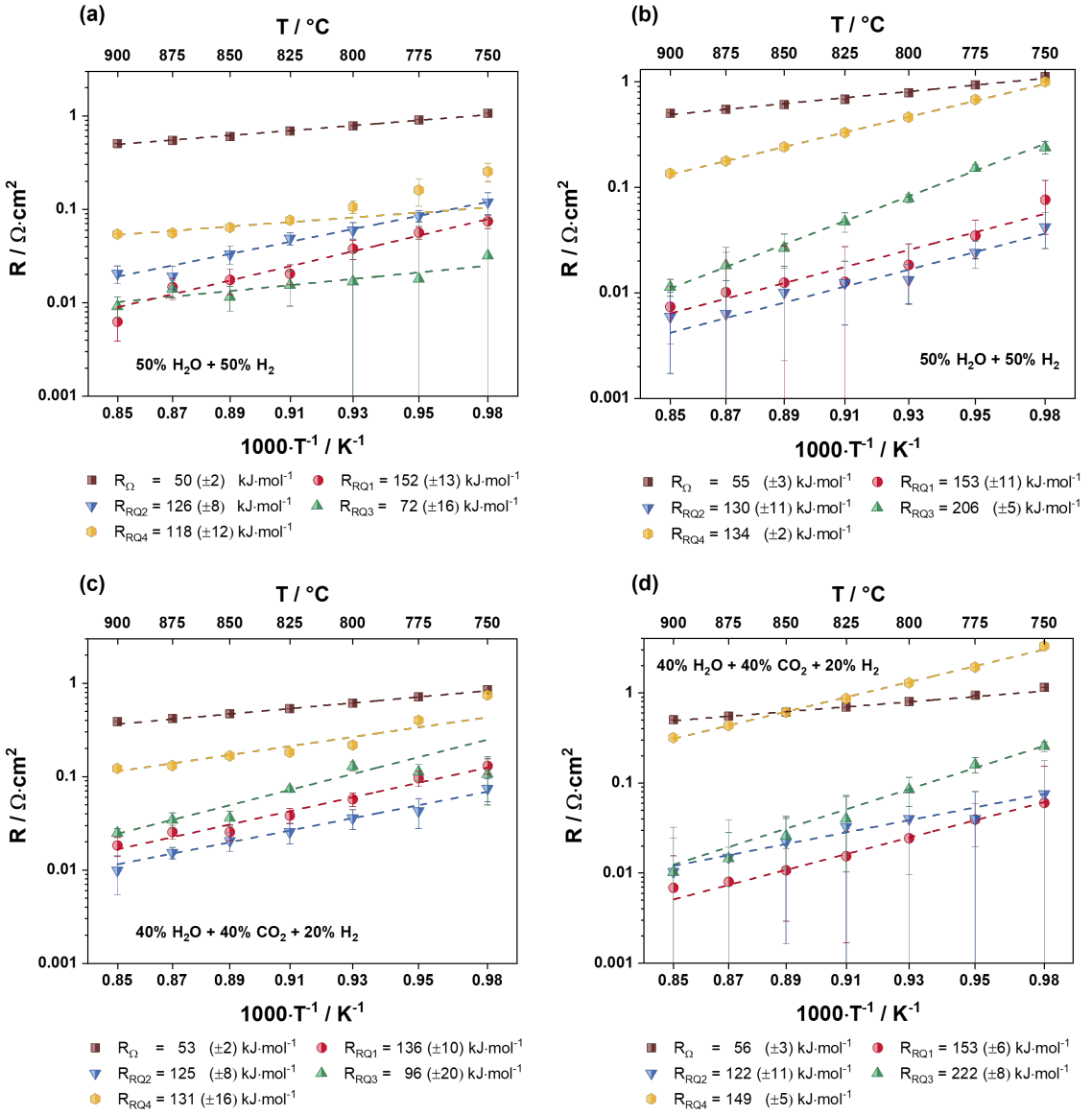

Figure 5.22: Temperature-dependent process resistance analysis measured at OCV from 900 °C to 750 °C in (a) steam electrolysis, and (b) co-electrolysis for $Sr_2FeMoO_{6-\delta}$ as well as for the composite $Sr_2FeMoO_{6-\delta}$-$Ce_{0.8}Gd_{0.2}O_{1.9}$ in (c) steam and (d) co-electrolysis.

corresponding DRT spectra in Figure 5.24b are plotted as a function of pO_2 and show negligible changes in the process peaks with varied pO_2 from 21% to 3%. For an in-depth characterization of the processes attributed to the oxygen electrode, symmetrical LSCF cells were characterized by impedance spectroscopy at an operating temperature of 900 °C with an O_2 content of 21% and 3%. Subsequently, the results were compared to the single cell measurements with an LSCF oxygen electrode in the same operating conditions[181]. The DRT data revealed that P1 and P2 of both investigated cell types overlap and are thus mainly attributed to

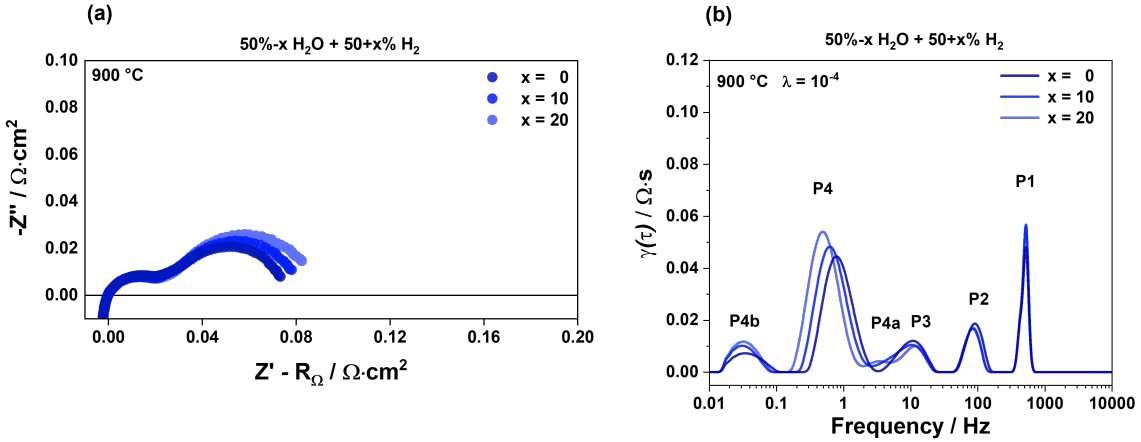

Figure 5.23: (a) The Nyquist plots and (b) the corresponding DRT spectra for the fuel gas variation of H_2 and H_2O at 900 °C.

processes at the oxygen electrode. The contribution of the physical processes in the mid-frequency range between 100 - 10 Hz is dependent on pO_2 and decreases with increasing O_2 content. A similar observation has been made for the low-frequency process at approximately 1 Hz. For the measurements at 21% O_2, the contribution of the LSCF electrode to P3 is notable, while P4 is minimally impacted.

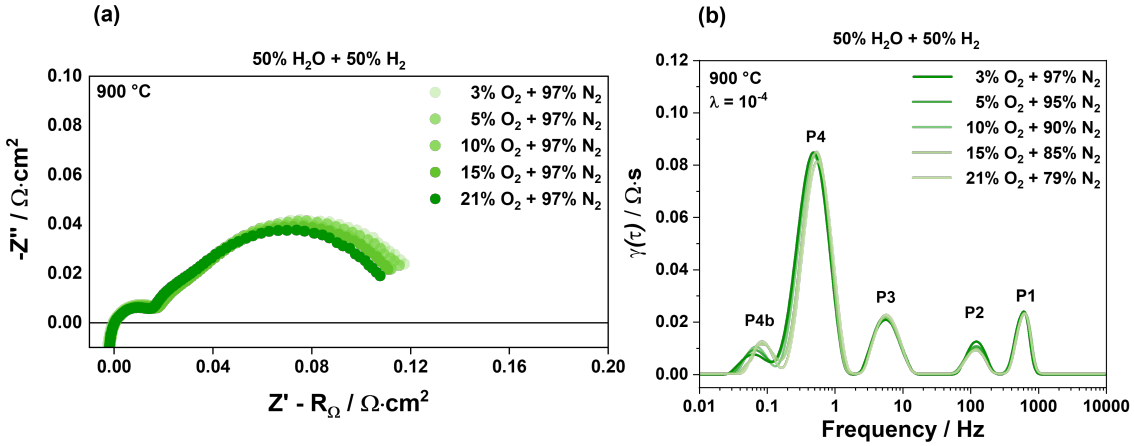

Figure 5.24: (a) The Nyquist plots and (b) the corresponding DRT spectra for the gas variation of O_2 and N_2 at the oxygen electrode at 900 °C.

To conclude, the processes P1 and P2 are thermally activated processes attributed to the LSCF oxygen electrode charge transfer (P1, 2000 - 900 Hz) and surface exchange processes (P2, 400 - 100 Hz). The mid to low-frequency process P3 (100 - 10 Hz) is related to the fuel and oxygen electrode with assigned to the adsorption and diffusion processes and transport processes of the fuel and oxygen electrode overlapping in this frequency region. The process P4 (2 - 0.1 Hz) has been identified as the rate-limiting step in steam- and co-electrolysis. The observed acti-

Table 5.3: Suggested process contribution to the polarization resistance and their equivalent frequency ranges for novel fuel electrode materials $Sr_2FeMoO_{6-\delta}$ and $Sr_2FeMoO_{6-\delta}$-$Ce_{0.8}Gd_{0.2}O_{1.9}$.

Process	***F*/Hz**	**Dependencies**	**Assignment**
P1 (R_{RQ1})	2000 - 900	Temperature	Charge transfer at the LSCF oxygen electrode
P2 (R_{RQ2})	400 - 100	Temperature	Surface exchange kinetics and O^{2-} diffusion in the bulk and at the surface of LSCF
P3 (R_{RQ3})	100 - 10	Temperature, medium pH_2O	Adsorption, Desorption, transport processes in the fuel and oxygen electrode
P4 (R_{RQ4})	2 - 0.1	Temperature, high pH_2O	Charge transfer at the SFM(-GDC) fuel electrode

vation energies and the impact of polarization on this process lead to the assignment of P4 to the fuel electrode charge transfer process.

5.2.4 Long-Term Stability

5.2.4.1 Electrochemical Analysis

The single cells composed of SFM(-GDC)/GDC/8YSZ/GDC/LSCF were electrochemically tested under a constant load of $-0.3\ A \cdot cm^{-2}$ at 900 °C in steam electrolysis conditions for up to 500 h to investigate and quantify the degradation behavior. The resulting degradation curves are displayed in Figure 5.25. As can be seen, the cell with an SFM fuel electrode is stable for up to 50 h, after which the voltage increases continuously and exhibits a degradation rate of around $765\ mV \cdot kh^{-1}$. In comparison, the cell with a composite SFM-GDC fuel electrode exhibits a linear degradation trend with a minimal increase of $15.6\ mV \cdot kh^{-1}$. Ni-GDC fuel electrode containing ESCs have shown a degradation rate of $499\ mV \cdot kh^{-1}$ in 50% H_2O + 50% H_2 at 900 °C at $-0.5\ A \cdot cm^{-2}$[180]. GDC is a mixed ionic and electronic conductor and has been used as a fuel electrode material in ESCs as well. In 50% H_2O + 50% H_2 at 900 °C, the cell composed of GDC/8YSZ/GDC/LSCF has exhibited a degradation of $112\ mV \cdot kh^{-1}$[181]. Fuel Electrode-Supported Cells (FESCs), on the

other hand, have been extensively studied in the literature regarding their degradation behavior. Degradation rates of 30 $mV \cdot kh^{-1}$[194] to 370 $mV \cdot kh^{-1}$[2] have been observed for Ni cermet-supported single cells and 24 $mV \cdot kh^{-1}$[38], 40 $mV \cdot kh^{-1}$[55] to 190 $mV \cdot kh^{-1}$[38] for FESC stacks. Previous studies have characterized SFM fuel electrode materials in humidified atmospheres of steam and co-electrolysis. However, the authors reported degradation measurements only up to 100 h measurement time. The symmetrical SFM/GDC/YbScSZ/GDC/SFM cells with $Sr_2Fe_{1.5}Mo_{0.5}O_{6-\delta}$ exhibited good stability at $-0.5\ A \cdot cm^{-2}$ for 24 h in 75% H_2O + 25% CO_2, and an ASR increase of only 0.03 $m\Omega \cdot cm^2$[16]. The data in Figure 5.25 show a voltage increase of 0.006 V during the first 24 h, which emphasizes that a degradation tests up to 24 h is not sufficient to assess the degradation behavior of SFM-based fuel electrodes. Degradation tests of SFM composite fuel electrodes in humidified conditions have been conducted for less than 500 h as well[17,73,164,195]. For instance, symmetrical SFM-SDC/LSGM/SFM-SDC ($Sr_2Fe_{1.5}Mo_{0.5}O_{6-\delta}$-$Sm_{0.2}Ce_{0.8}O_{1.9}$) cells tested at $-0.12\ A \cdot cm^{-2}$ and 800 °C for 100 h exhibited degradation of 0.0001 $V \cdot h^{-1}$. Similar results were obtained in H_2O/CO_2 co-electrolysis atmosphere at 850 °C and 1.1 V for 100 h[164]. Further characterization was conducted on Ni-doped SFM electrode containing single cells, i.e. $Sr_2Fe_{1.3}Ni_{0.2}Mo_{0.5}O_{6-\delta}$-SDC/LCO/LSGM/SDC-LSCF in 42% H_2O + 58% H_2 for 60 h under current load of $-0.3\ A \cdot cm^{-2}$. From their results, the authors concluded that in SOECs, Ni-doped SFM perovskites are stable at high temperatures and high humidity[17].

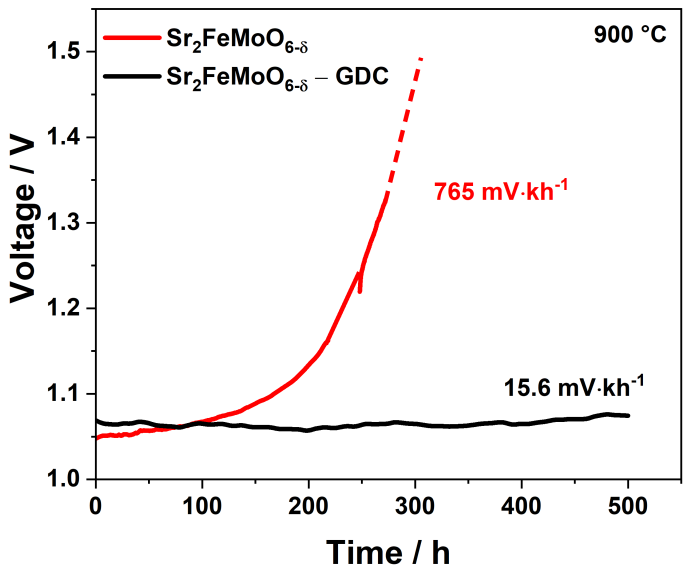

Figure 5.25: Long-term stability test of single cells with SFM and composite SFM-GDC fuel electrodes in 50% H_2O + 50% H_2 fuel gas composition under constant current load of $-0.3\ A \cdot cm^{-2}$ at 900 °C for up to 500 h.

For further detailed degradation analysis, impedance spectra were recorded before and after the degradation test. The spectra in addition to the DRT analysis are displayed in Figure 5.26 and were measured at OCV and 900 °C with a fuel gas composition of 50% H_2O + 50% H_2. The individual process resistances of the fitted spectra are given in Table 5.4. The total resistance (ASR) for the cell based on an SFM fuel electrode after around 300 h increases from 468 $m\Omega \cdot cm^2$ to 959 $m\Omega \cdot cm^2$. In comparison, over 500 h of measurement, the ASR increases only 64 $m\Omega \cdot cm^2$ from 532 $m\Omega \cdot cm^2$ to 596 $m\Omega \cdot cm^2$ for the SFM-GDC fuel electrode. It can be discerned from the fitted results and the impedance spectra, the contribution of the ohmic resistance R_Ω to the ASR increase over the measurement time is minimal in comparison to the polarization resistance R_P. For the SFM cell, the increase in ohmic resistance accounted for around 8.8% of the ASR change, which is in the range of 9.4% found for the SFM-GDC cell. On the other hand, a large increase in the R_P, i.e. 448 $m\Omega \cdot cm^2$, is observed for the severely degraded SFM cell. This is mainly due to an increase in the process resistances R_{RQ2}, R_{RQ3}, and R_{RQ4}. The resistance values for the SFM-GDC fuel electrode (Table 5.4) correspond to the lower voltage increase and smaller changes in the Nyquist plot (Figure 5.26). In addition to the small ohmic resistance increase of 6 $m\Omega \cdot cm^2$, the polarization resistance increases by 58 $m\Omega \cdot cm^2$ due to an increase in R_{RQ4}. The DRT analysis is in support of these results and shows a shift of R_{RQ1} to higher frequencies without an increase in P1. The resistances P2, P3, and P4 for SFM cell as well as P4 for SFM-GDC cell, however, display an increase. Thus, the performance loss after the degradation test can be mainly attributed to the mid- to low-frequency process P3 and P4 linked with the SFM fuel electrode as well as to a lesser part to the oxygen electrodes associated with the high- to mid-frequency processes. The degradation observed for SFM-GDC is attributed to the process P4 as well, while P1, P2, and P3 remain relatively constant.

5.2.4.2 Microstructural Post-Test Analysis

After the long-term stability measurements under constant current load, the tested cells as well as as-prepared single cells were investigated through SEM-EDX. The samples were embedded in epoxy resin, polished and Au sputtered before analysis. The SEM-EDX analyses of as-prepared and degraded cell cross-sections for SFM and SFM-GDC electrodes are shown in Figure 5.27. For all cells, the electrolyte is crack-free, and no delamination of the electrodes is observed. The composite SFM-GDC electrode exhibits an even distribution of GDC particles in the SFM electrode microstructure before and after the 500 h long-term stability test in 50% H_2O + 50% H_2 at 900 °C and under constant current of -0.3 $A \cdot cm^{-2}$. Very slight Sr

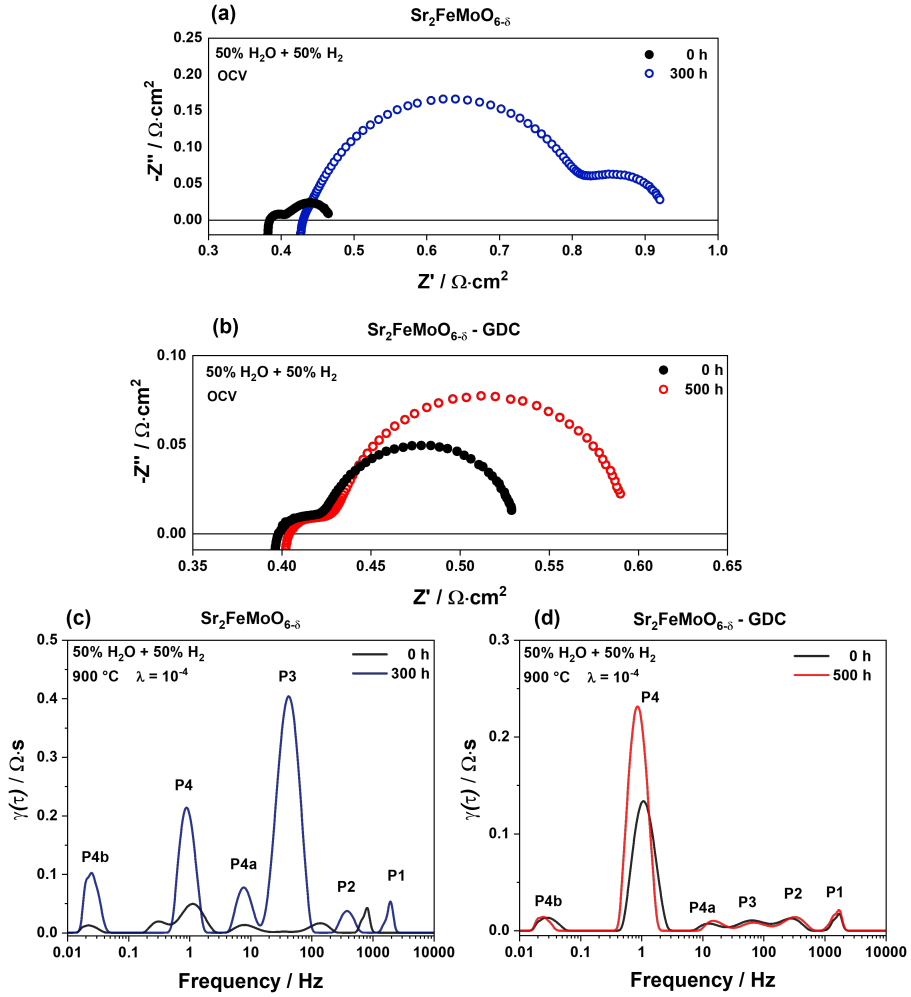

Figure 5.26: Comparison of Nyquist plots and DRT plots for (a, c) SFM and (b, d) SFM-GDC fuel electrodes in the single cell composition SFM(-GDC)/GDC/8YSZ/ GDC/LSCF before and after the long-term degradation measurement under constant $-0.3\ \mathrm{A \cdot cm^{-2}}$ current load in 50% H_2O + 50% H_2 atmosphere at 900 °C.

segregation of the SFM-GDC composite structure through the GDC barrier layer to the GDC/8YSZ interface is observed. This can be connected to an insufficiently dense GDC layer. A striking structural instability of the SFM fuel electrode is observed through the evolution of a dense layer at the SFM/GDC interface. The EDX analysis reveals that the formed phase consists pre-dominantly of Sr and Fe. To the author's knowledge, this phase formation at the GDC barrier layer/SFM fuel electrode interface after long-term operation in steam electrolysis has not been reported in the literature up to now. Sr segregation has been mainly reported for Sr-containing oxygen electrodes after degradation testing and has been linked to the materials stoichiometry, the ion mobility as well as operating conditions (temperature, polarization). Strontium-doped lanthanum manganite (LSM) exhibits high cation mobility and inter-diffusion under a high anodic current ($-1.5\ \mathrm{A \cdot cm^{-2}}$ at

Table 5.4: Resistance evolution of SFM-based fuel electrodes as a function of operation time in H_2O electrolysis.

Time	R_Ω	R_{RQ1}	R_{RQ2}	R_{RQ3}	R_{RQ4}	R_P	**ASR**
h	$\Omega \cdot cm^2$	$\Omega \cdot cm^2$	$\Omega \cdot cm^2$	$\Omega \cdot cm^2$	$\Omega \cdot cm^2$	$\Omega \cdot cm^2$	$\Omega \cdot cm^2$
$Sr_2FeMoO_{6-\delta}$							
0	0.382	0.006	0.019	0.009	0.052	0.086	0.468
300	0.425	0.055	0.207	0.125	0.147	0.534	0.959
SFM: $Sr_2FeMoO_{6-\delta}$-GDC							
0	0.395	0.003	0.010	0.018	0.106	0.137	0.532
500	0.401	0.005	0.011	0.017	0.162	0.193	0.596

750 °C)[136]. Similar observations have been made for Sr-perovskite materials like $SrTiO_3$ (STO)[196], $SrTi_{1-x}FexO_3$ (STF)[197], and $Sr_2Fe_{1.5}Mo_{0.5}O_{6-\delta}$ (SFM)[198]. The origin of the segregation mechanism in Sr-containing fuel electrode perovskite materials will have to be further investigated in the future. A starting point could be the structural instability of the perovskite material under operating conditions as described above. This could in turn lead to higher cation mobility in addition to a change in stoichiometry and oxygen vacancies. The SEM-EDX of SFM-GDC also shown in Figure 5.27 displays no interphase formation at electrode/GDC interface after 500 h in steam electrolysis conditions. The composite SFM-GDC fuel electrode exhibits, therefore, superior chemical stability in humidified conditions as also shown in the cell voltage vs time curve (Figure 5.25).

Further SEM-EDX analyses for the LSCF oxygen electrode are displayed in Figure 5.28 for the as-prepared and operated cells. Although a GDC barrier layer was deposited on the 8YSZ electrolyte, the volatile SrO diffused through the pores or along the grain boundaries of the GDC layer to the GDC/8YSZ interface and formed electronically insulating $SrZrO_3$ phase. The amount of formed $SrZrO_3$ indicates the degree of Sr segregation at GDC/YSZ interface and it can be seen from Figure 5.28 that the extent of Sr segregation increases after the long-term test. This mechanism of Sr-segregation in LSCF electrode has been widely discussed[36,85,138,140,142,199–204]. The formation of the insulating $SrZrO_3$ phase already occurs during the sintering process of the LSCF electrode and deteriorates during the electrolysis operation of the cell[55,205]. The Sr-loss from the electrode leads to reduced ionic and electronic

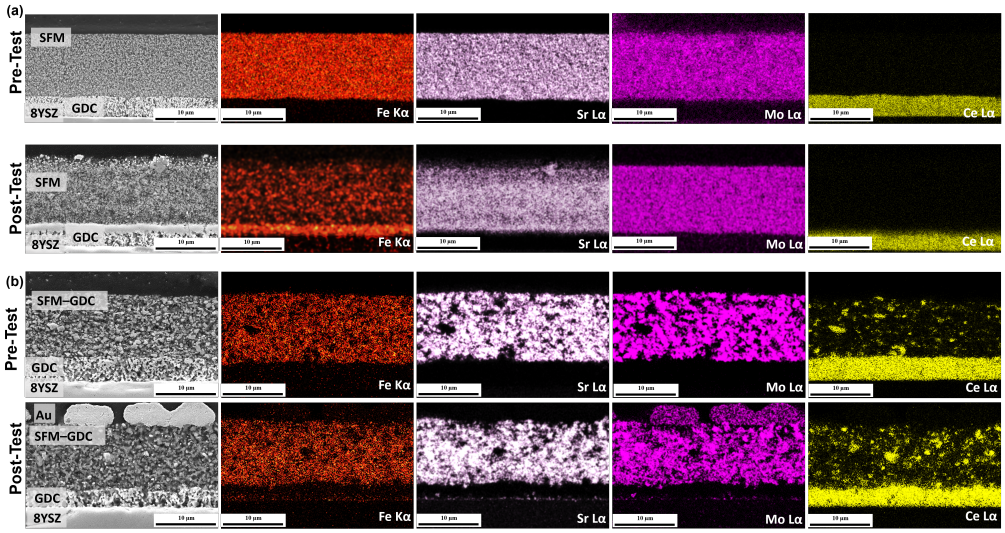

Figure 5.27: Cross-sectional SEM-EDX mapping of the fuel electrode side for Sr (Lα, 13.89 keV), Fe (Kα, 6.40 keV), Mo (Lα, 17.14 keV), Ce (Lα, 33.90 keV) lines for (a) SFM and (b) for SFM-GDC before and after the long-term test up to 500 h in 50% H_2O + 50% H_2 at -0.3 A $\cdot$ cm^{-2} and 900 °C.

conductivity, hindered O^- ion flux, loss of active TPB length of the electrode and consequently cell performance loss[138] as indicated by increased polarization resistance (R_P)[85,206] as well as ohmic resistance[199].

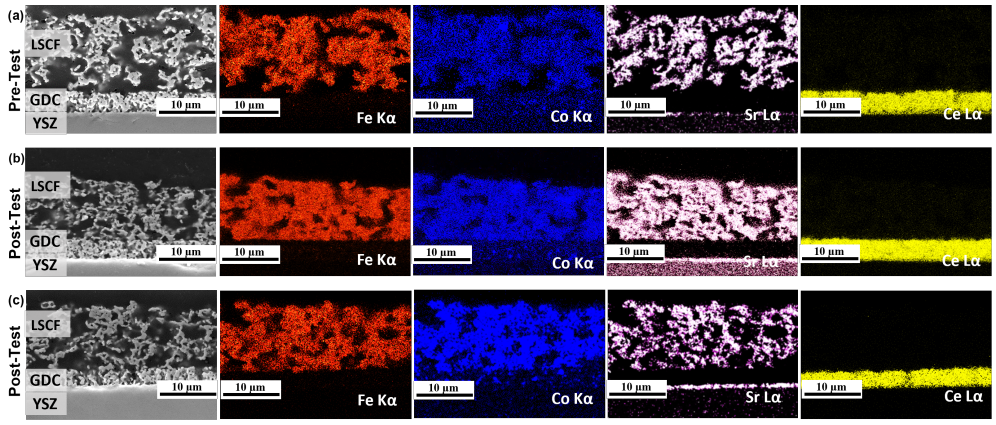

Figure 5.28: Cross-sectional SEM-EDX mapping of the oxygen electrode side for Fe (Kα, 6.40 keV), Ce (Lα, 33.90 keV), Co (Kα, 6.93 keV), Sr (Lα, 13.89 keV) lines (a) before and after the long-term test for (b) SFM and (c) SFM-GDC up to 500 h in 50% H_2O + 50% H_2 at -0.3 A $\cdot$ cm^{-2} and 900 °C .

5.3 Characterization of Metal-Doped SFM

As a result of aliovalently doped perovskites $Sr_2FeMo_{0.65}M_{0.35}O_{6-\delta}$ with the dopant metals M = Ni, Co, Cu, Ti, and Mn, defect configurations are observed as charge compensation.These defects can enhance the catalytic activity of the ceramic materials and facilitate oxygen ion diffusion (ionic conductivity). The following results show the material characterization of doped MIEC electrode materials based on $Sr_2FeMo_{0.65}M_{0.35}O_{6-\delta}$ with regard to redox-stability, total conductivity in oxidizing and reducing atmospheres as well as electrochemical performance. The oxidation states of the dopant ions' are investigated through XPS measurements, indicating the impact of oxidizing and reducing atmospheres. The electrochemical performance of the electrode materials is evaluated in steam electrolysis as well as co-electrolysis conditions and compared to state-of-the-art Ni-8YSZ and Ni-GDC. The long-term stability of $Sr_2FeMo_{0.65}Ni_{0.35}O_{6-\delta}$ was assessed in steam electrolysis conditions. Microstructural changes after the durability testing were characterized using post-test SEM-EDX analyses of resin-embedded cell cross-sections. Parts of the following results have been measured in collaboration with Finn Dröge during his bachelor thesis[207]. The XPS measurements have been commissioned from and evaluated with Dr. Heinrich Hartmann (ZEA-3, FZJ). High-resolution SEM imaging was performed by and evaluated together with Pritam K. Chakraborty, and Dr. Shibabrata Basak (IET-1, FZJ). Parts of the results have been published under the CC BY 4.0 (http://creativecommons.org/licenses/by/4.0/)[6].

5.3.1 Dopant Influence on Material Properties

The XRD pattern of the as-prepared $Sr_2FeMo_{0.65}M_{0.35}O_{6-\delta}$ (M = Ni, Cu, Co, Mn, and Ti) powders are depicted in Figure 5.29. The patterns show that the varied ion doping affected the phase stability after sintering in air. The $Sr_2FeMo_{0.65}Ni_{0.35}O_{6-\delta}$ (SFMNi) and $Sr_2FeMo_{0.65}Co_{0.35}O_{6-\delta}$ (SFMCo) powders entail secondary $SrMoO_4$ after sintering at 1100 °C for 8 h. With an increased sintering temperature of 1250 °C, the diffraction patterns of both materials show phase pure SFM-based powders. In contrast, the measured diffraction pattern of $Sr_2FeMo_{0.65}Cu_{0.35}O_{6-\delta}$ (SFMCu) shows phase pure powder after sintering in air at 1100 °C. Pure phases were not achieved for $Sr_2FeMo_{0.65}Ti_{0.35}O_{6-\delta}$ (SFMTi) and $Sr_2FeMo_{0.65}Mn_{0.35}O_{6-\delta}$ (SFMMn) after sintering in air, however, the XRD data shows phase purity after subsequent sintering in 100% H_2 for 8 h at 900 °C. The reduction of the other materials SFMCo, SFMNi, and SFMCu leads to the formation of additional phases as previously observed for SFM (c.f. Figure 5.13). The formation of different perovskite phases and oxidation state change of the dopant ions in conjunction with iron exsolution have an impact

on the catalytic activity of the material. Therefore, XPS measurements were carried out on the surface of bar samples to study the oxidation states of the different materials in dependence of the atmosphere.

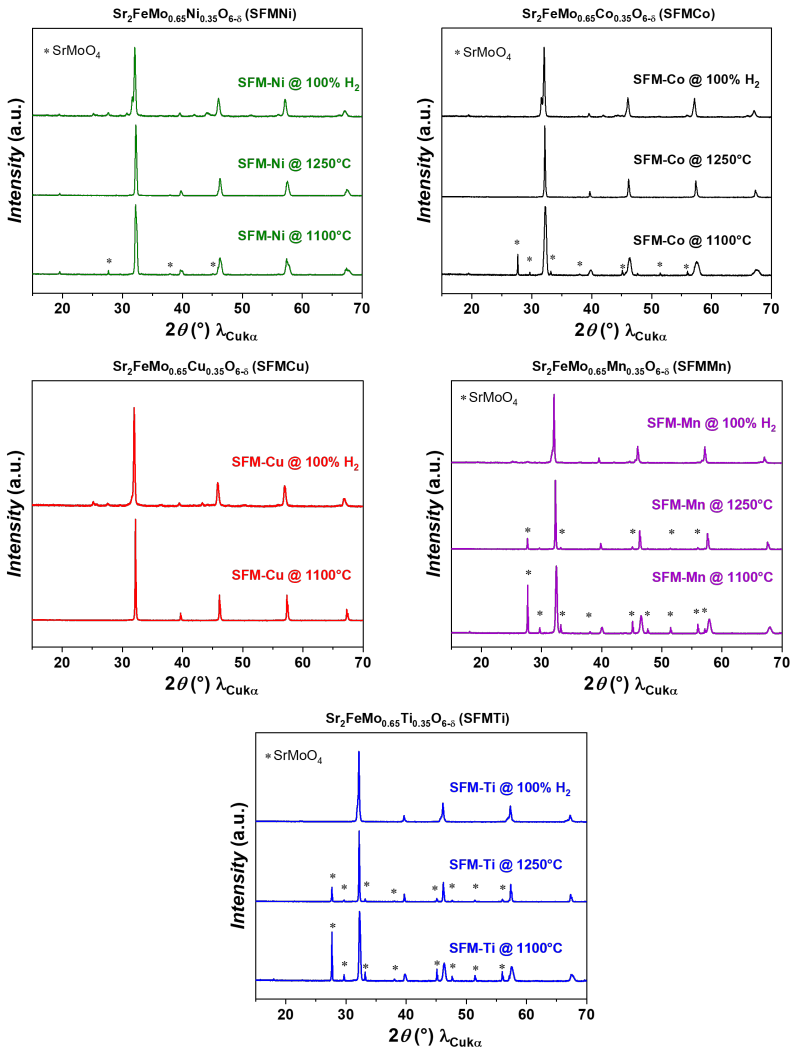

Figure 5.29: Room-temperature XRD of the as-prepared doped SFM-based powders after different sintering temperatures in air and after reduction in 100% H_2 for 8 h at 900 °C. Partially reproduced from[6] published under the CC BY 4.0 (http://creativecommons.org/licenses/by/4.0/).

The results in Figure 5.30 and Figure 5.31 depict the selected XPS scans of $Sr_2FeMo_{0.65}M_{0.35}O_{6-\delta}$ samples with M = Ni, Co, Cu, Ti, and Mn sintered in air and after reduction in 100% H_2. A change in the oxidation state of the dopant ion is evident for SFMNi, SFMCo, and SFMCu with atmospheric change from air (Figure 5.30a) to 100% H_2 (Figure 5.30b), Cu^{1+} (932.7 eV) is reduced to Cu^0 (932.6 eV), Co^{2+} (787.2 eV, 782.9 eV, 780.6 eV) is partially reduced to Co^0 (778.3 eV) and Ni^{2+} (867.2 eV, 864.9 eV, 861.7 eV, 856.3 eV, 854.8 eV) to Ni^0 (852.7 eV)[208]. As

previously discussed, the exsoluted nanoparticles exhibit higher conductivities, and improved catalytic activity compared to the bulk phase, which leads to enhanced electrochemical material performance.[161,162]. In the case of B-site doped double perovskite structures like SFMx, the formation of catalytically active bimetallic alloy nanoparticles, e.g. Fe-Co and Fe-Ni, have been observed under reducing conditions and at elevated temperatures[151,158,209]. Treatment time plays a role specifically for the Ni^{2+} exsolution processes including ion migration to the perovskite surface, reduction to Ni^0 and assembly into nanoparticles. CoFe alloy nanoparticles exsolution has also been reported in H_2 atmosphere above 700 °C[151].

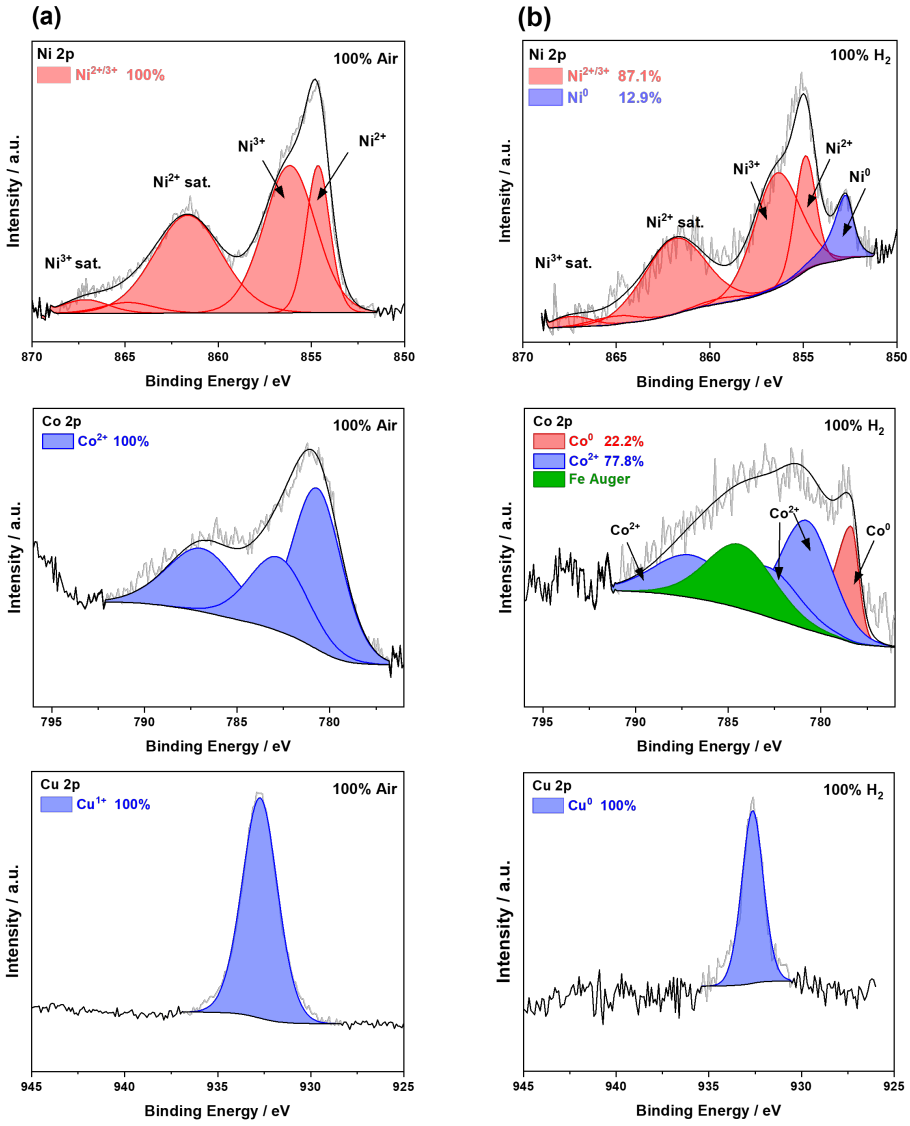

Figure 5.30: Selected XPS scans of $Sr_2FeMo_{0.65}M_{0.35}O_{6-\delta}$ samples with M = Ni, Co, and Cu to determine the changes in oxidation state after sintering in (a) air and (b) after reduction in 100% H_2. Reproduced from[6] published under the CC BY 4.0 (http://creativecommons.org/licenses/by/4.0/).

For the doped perovskite samples SFMMn and SFMTi depicted in Figure 5.31, no change in oxidation state is observed after reducing in 100 % H_2. The binding energy of Ti^{4+} is given by 464.1 eV and 458.4 eV as well as 641.1 eV for Mn^{2+}[208]. These results indicate that no bimetallic alloy particles are exsoluted from the perovskite matrix during the reduction process in 100% H_2. Previous studies have observed that the reduction of Ni^{2+} to Ni^0 is easier than that of Ti^{4+} to Ti^{3+}[210,211].

The explanation is the thermodynamic redox-stability between metal and oxide state of the dopant metals as given in the Ellingham diagram[212,213]. It shows the negative Gibbs free energy change (ΔG) for exothermic oxidation reactions as a function of temperature with the corresponding oxygen partial pressure at equilibrium. Oxides with higher Gibbs free change energy are more easily reduced to metals, i.e. Fe and Ni. With decreased Gibbs free change energy, the metals become progressively more reactive towards oxidation and harder to reduce, i.e. Ti and Mn.

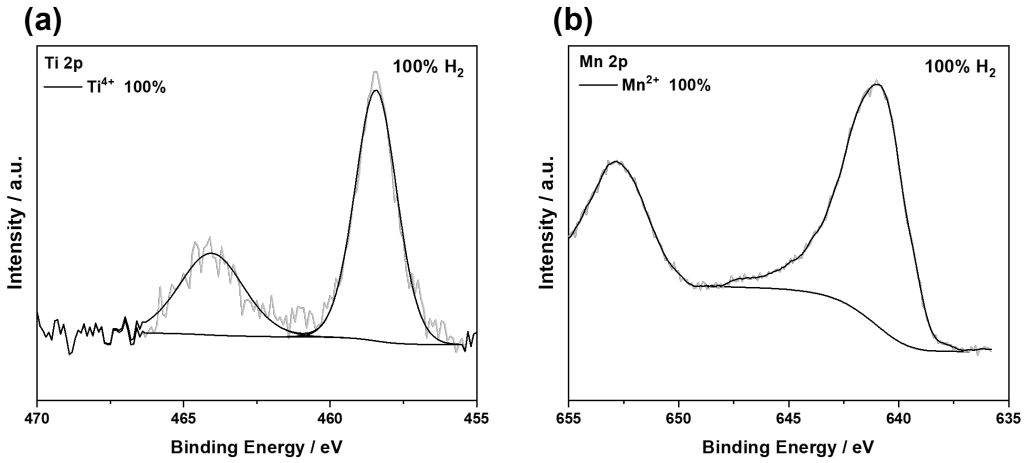

Figure 5.31: X-Ray Photoelectron Spectroscopy scan evaluations of (a) $Sr_2FeMo_{0.65}Ti_{0.35}O_{6-\delta}$ and (b) $Sr_2FeMo_{0.65}Mn_{0.35}O_{6-\delta}$ after reduction in 100% H_2.

To support the obtained data, high-resolution SEM images were obtained (Figure 5.32a-i). Figure 5.32a and Figure 5.32b illustrate the secondary electron SEM images of the $Sr_2FeMo_{0.65}Ni_{0.35}O_{6-\delta}$ (SFMNi) samples before and after reduction in 100% H_2 respectively. The as-prepared SFMNi powder particles exhibit a smooth and homogeneous surface. In contrast, the featured surface of the reduced sample is rough due to spherical sub-micron nanoparticles observed on the surface. To elucidate the nature and composition of the growth on the reduced sample surface, EDX mapping was conducted. Figure 5.32c depicts a SEM image of the reduced SFM, accompanied by its corresponding elemental mapping in Figure 5.32d-i. The elemental mapping of Figure 5.32d-f shows the presence of Fe-rich, Ni-rich and Mo-rich ex-

solution measuring 10 - 50 nm. The elemental distribution of all other elements is relatively even throughout the particle.

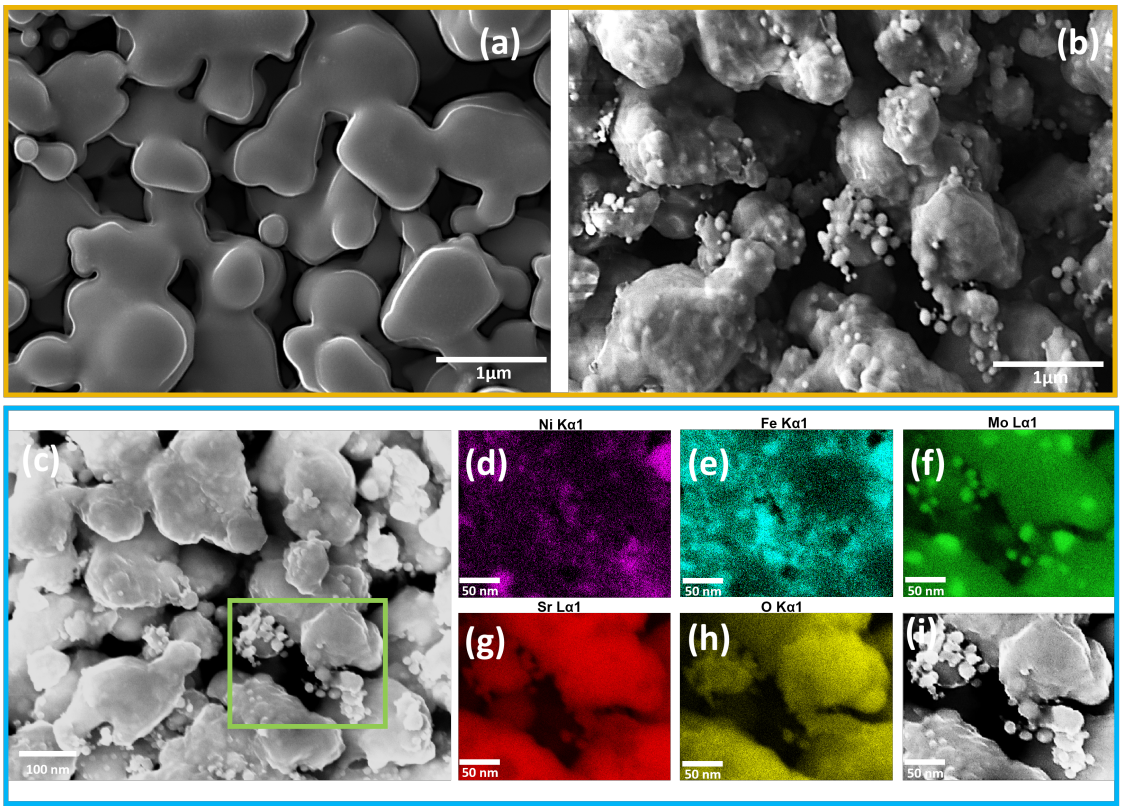

Figure 5.32: SEM image of (a) as-prepared and, (b) reduced $Sr_2FeMo_{0.65}Ni_{0.35}O_{6-\delta}$ cell surface. (c) High magnification SEM-EDX image of the reduced $Sr_2FeMo_{0.65}Ni_{0.35}O_{6-\delta}$ particles illustrating the contrast features in green boxes and (d-h) elemental mapping of the corresponding particles in (i). Reproduced from[6] published under the CC BY 4.0 (http://creativecommons.org/licenses/by/4.0/).

In the previous chapter, the influence of oxidizing and reducing atmosphere on the perovskite structure and the cell performance has been analyzed (cf. Figure 5.12 and Figure 5.27). The influence of doping the SFM perovskite structure on the total conductivity is shown in Figure 5.33. Under reducing conditions, the characterized materials $Sr_2FeMoO_{6-\delta}$, $Sr_2FeMoO_{6-\delta}$-GDC, $Sr_2FeMo_{0.65}Cu_{0.35}O_{6-\delta}$ (SFMCu), and SFMCu-GDC exhibit pseudo-metallic behavior with a maximum total conductivity at 650 °C. The B-site doping with Cu shows an increase of the total conductivity at 650 °C from 17 $S \cdot cm^{-1}$ for SFM to 21 $S \cdot cm^{-1}$ for SFMCu. The addition of GDC in reducing conditions contributes to an increased total conductivity of 152 $S \cdot cm^{-1}$ at 650 °C due do its MIEC properties for $Sr_2FeMo_{0.65}Cu_{0.35}O_{6-\delta}$-GDC.

It has been proposed that electrons move through percolation paths made of Fe-O-Fe bonds (σ- or π-bond). In reducing conditions, the loss of oxygen leads to an increase in these bonds and electron delocalization[71]. In contrast, the Mo-O-Fe

and Mo-O-Mo bonds are less favored for electron or electron hole transport, as the Mo-O metal oxygen bond is much stronger compared to the Fe-O bonds. Mid-to-late transition metals form much weaker bonds, which break more easily upon removal of oxygen from the lattice structure to form a vacancy[69,71,214,215]. The exchange of strongly bonded Mo-O on the B-site with Cu-O and the subsequent increase of total conductivity may be related to this phenomena as well. Cu is reduced to Cu^0 and forms exsoluted, highly catalytically active nanoparticles. In addition, Cu^{1+} weakly bonds to oxygen and thereby increases the possibility of vacancy formation[216]. Similar results have been observed for an increase in Fe contents, which led to an increased electronic conductivity through progressive charge delocalization[214].

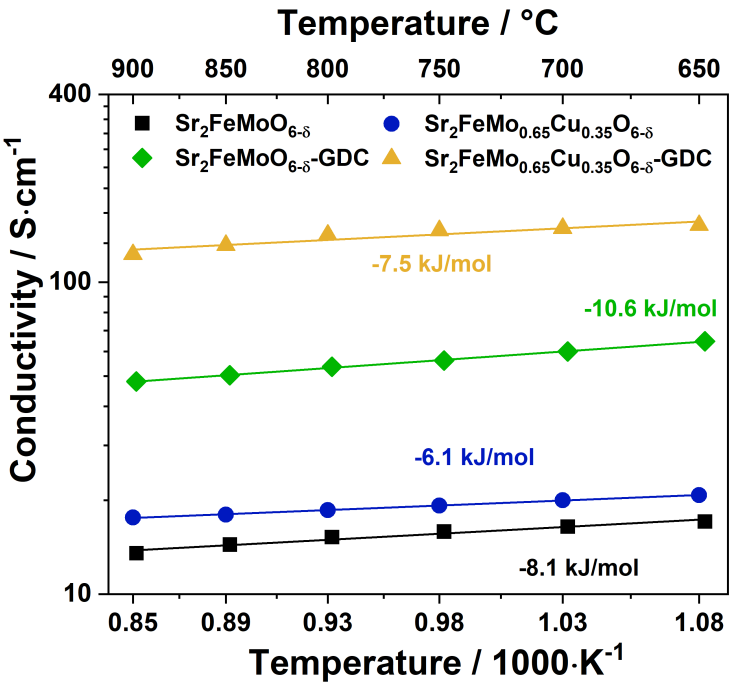

Figure 5.33: Conductivity measurements in the temperature range from 650 °C to 900 °C in 100% H_2 for SFM-based perovskite materials. The measurements in hydrogen were conducted down to 650 °C for safety reasons[4].

The influence of doping the $Sr_2FeMoO_{6-\delta}$ perovskite matrix on the thermal expansion behavior is detailed in Table 5.5 calculated from dilatometry measurements in air. The corresponding relative expansion dL/L as a function of temperature is displayed in the appendix (Figure A.9). To avoid thermomechanical stress and ensures long-term cell stability, the electrodes' TEC should be in range of other cell components. The typical value for common electrolyte materials such as yttrium-stabilized zirconia (YSZ), gadolinium-doped ceria (GDC), strontium-, and magnesium-doped lanthanum gallium oxide (LSGM) is around 10 - $13 \cdot 10^{-6}$ $°C^{-1}$[5,217]. The measured TEC for a NiO-GDC (50:50 wt%) composite

electrode in air was $13.5 \cdot 10^{-6}$ °C^{-1} in a temperature range of 25 - 1000 °C[218]. Increasing the Ni content from 15 vol% to 30 vol% resulted also in a TEC from $10.4 \cdot 10^{-6}$ °C^{-1} to $13.2 \cdot 10^{-6}$ °C^{-1} at 900 °C[43]. Similar results can be discerned from Table 5.5. In the temperature range from 30 - 1000 °C, the TEC for $Sr_2FeMoO_{6-\delta}$ is $14.1 \cdot 10^{-6}$ °C^{-1} and increases to $16.3 \cdot 10^{-6}$ °C^{-1} for $Sr_2FeMo_{0.65}Ni_{0.35}O_{6-\delta}$. The other doped SFM-perovskites are in range of these values and comparable to other alternative perovskite-based fuel electrode materials. $La_{0.4}Sr_{0.6}Ti_{1-x}Mn_xO_{3-\delta}$ (LST) has been categorized as a redox-stable perovskite with great potential as an electrode material in SOECs[13]. The material exhibits TEC values of 11 - $13 \cdot 10^{-6}$ °C^{-1} between 30 °C and 1000 °C[219,220]. The thermal expansion coefficients obtained for pure $Sr_2NbO_{6-\delta}$ (SFN) and Mo-doped SFN in the temperature range of 30 - 1000 °C were $11.3 \cdot 10^{-6}$ °C^{-1} and $12.5 \cdot 10^{-6}$ °C^{-1} in air respectively. The Mo doping into the SFN double perovskite lattice led to an increase in thermal expansion in air as well as in a reducing atmosphere[5,221].

Table 5.5: Comparison of different Thermal Expansion Coefficients (TECs) for doped SFM-perovskite materials.

Material	**TEC from Dilatometry / 10^{-6} řC^{-1}**	
	30 – 800 °C	**30 – 1000 °C**
Ni-8YSZ (40% Ni-60% 8YSZ)	12.5[166]	12.6[166]
$Sr_2FeMoO_{6-\delta}$	13.8	14.1
$Sr_2Fe_{1.5}Mo_{0.5}O_{6-\delta}$	13.3	15.1
$Sr_2FeMo_{0.65}Ni_{0.35}O_{6-\delta}$	15.3	16.3
$Sr_2FeMo_{0.65}Co_{0.35}O_{6-\delta}$	14.0	14.6
$Sr_2FeMo_{0.65}Cu_{0.35}O_{6-\delta}$	14.2	14.5
$Sr_2FeMo_{0.65}Ti_{0.35}O_{6-\delta}$	13.0	13.4
$Sr_2FeMo_{0.65}Mn_{0.35}O_{6-\delta}$	13.7	14.1

5.3.2 Electrochemical Characterization

5.3.2.1 Electrochemical Performance Analysis

The electrochemical performance of $Sr_2FeMo_{0.65}Ni_{0.35}O_{6-\delta}$ as fuel electrode was characterized with current-voltage characteristics and electrochemical impedance spectroscopy for steam and co-electrolysis depicted in Figure 5.34 and listed in Ta-

ble 5.6. Current densities of $-1.62\ \mathrm{A \cdot cm^{-2}}$ and $-1.74\ \mathrm{A \cdot cm^{-2}}$ were obtained in steam and co-electrolysis respectively at 1.5 V and 900 °C. In comparison to the $Sr_2FeMoO_{6-\delta}$ fuel electrode, these values are higher by 28% and 39% respectively. The SFMNi fuel electrode also exhibits an improved performance in comparison to Ni-8YSZ and Ni-GDC by 79% and 24% in steam (Figure 5.34b) and 65% and 28% in co-electrolysis at 1.5 V(Figure 5.34a). These results indicate that the addition of electrochemically active Ni especially improves the catalytic reduction of H_2O in electrolysis operation. Similar observations were made for the doped fuel electrode material $Sr_2Fe_{1.3}Ni_{0.2}Mo_{0.5}O_{6-\delta}$ mixed with $Sm_{0.2}Ce_{0.8}O_{1.9}$ (SDC) compared to $Sr_2Fe_{1.5}Mo_{0.5}O_{6-\delta}$-SDC in humidified conditions. The polarization resistance was reduced from $0.44\ \mathrm{m\Omega \cdot cm^2}$ to $0.21\ \mathrm{m\Omega \cdot cm^2}$ with the addition of Ni[17].

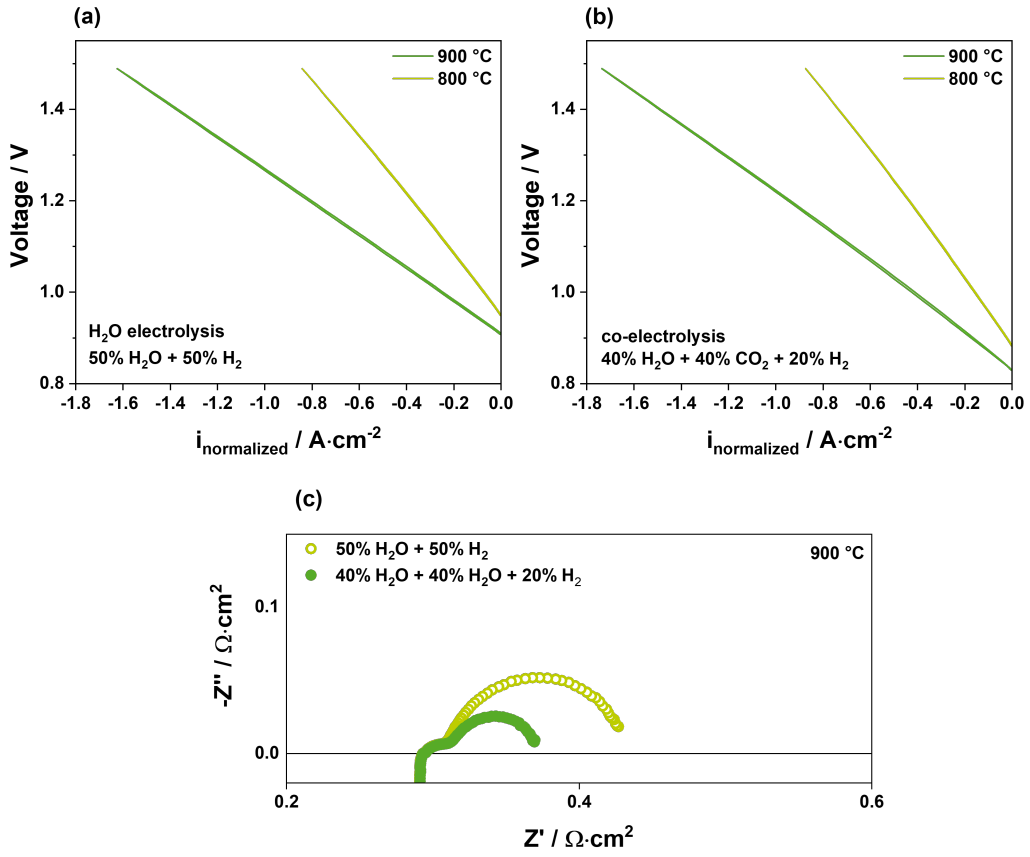

Figure 5.34: I–V curves measured at 900 °C for $Sr_2FeMo_{0.65}Ni_{0.35}O_{6-\delta}$ in (a) steam electrolysis, and (b) co-electrolysis conditions. (c) The impedance spectra were measured in steam electrolysis and co-electrolysis atmospheres at 900 °C and OCV. Reproduced from[6] published under the CC BY 4.0 (http://creativecommons.org/licenses/by/4.0/).

Table 5.6: Electrochemical performance of the $Sr_2FeMo_{0.65}Ni_{0.35}O_{6-\delta}$ fuel electrode in comparison to state-of-the-art Ni-cermet electrodes with varied atmospheres at 900 °C. Reproduced from[6] published under the CC BY 4.0 (http://creativecommons.org/licenses/by/4.0/).

Fuel Electrode	**Test conditions**	$R_{P,OCV}$ / $\Omega \cdot cm^2$	$i_{1.5V}$ / $A \cdot cm^{-2}$
Ni-8YSZ	H_2O electrolysis	0.17[180]	−0.91[180]
	co-electrolysis	0.20[180]	−1.06[180]
Ni-GDC	H_2O electrolysis	0.06[180]	−1.31[180]
	co-electrolysis	0.09[180]	−1.37[180]
GDC	H_2O electrolysis	0.16[181]	−0.92[181]
	co-electrolysis	0.28[181]	−0.82[181]
$Sr_2FeMo_{0.65}Ni_{0.35}O_{6-\delta}$	H_2O electrolysis	0.10	−1.62
	co-electrolysis	0.14	−1.74

GDC: $Ce_{0.8}Gd_{0.2}O_{1.9}$, 8YSZ: 8mol% YSZ

5.3.2.2 Equivalent Circuit Model Evaluation

Impedance spectra were taken under different measurement conditions such as variation of temperature and gas composition. To evaluate the experimental data, the number of time constants was analyzed by the DRT method resulting in an ECM with an inductor, a serial resistor followed by four RQ elements connected in series as used for $Sr_2FeMoO_{6-\delta}$ and $Sr_2FeMoO_{6-\delta}$-GDC (Figure 5.35a). In Figure 5.35b, the DRT spectra for $Sr_2FeMo_{0.65}Ni_{0.35}O_{6-\delta}$ measured at 750 °C in 50% H_2O + 50% H_2 at OCV is depicted as an example. In comparison to Figure 5.20b (c.f. chapter 5.2.3.2), the low-frequency process P4 is much more pronounced. The signal intensity of P4 is much higher compared to P1, P2, and P3, which might lead to higher fitting uncertainties of the impedance data. The experimental impedance data and the fit shown in Figure 5.20c agree qualitatively well. The relative residuals are given in Figure 5.20d and the low X^2 error of 10^{-7} between the fitted and experimental data indicate a reasonable ECM.

5.3.2.3 Temperature Variation

The performance of single cells with an SFMNi fuel electrode was characterized in steam electrolysis (50% H_2O + 50% H_2) and co-electrolysis (40% H_2O + 40% CO_2 + 20% H_2) conditions between 750 °C and 900 °C in steps of 25 °C to determine

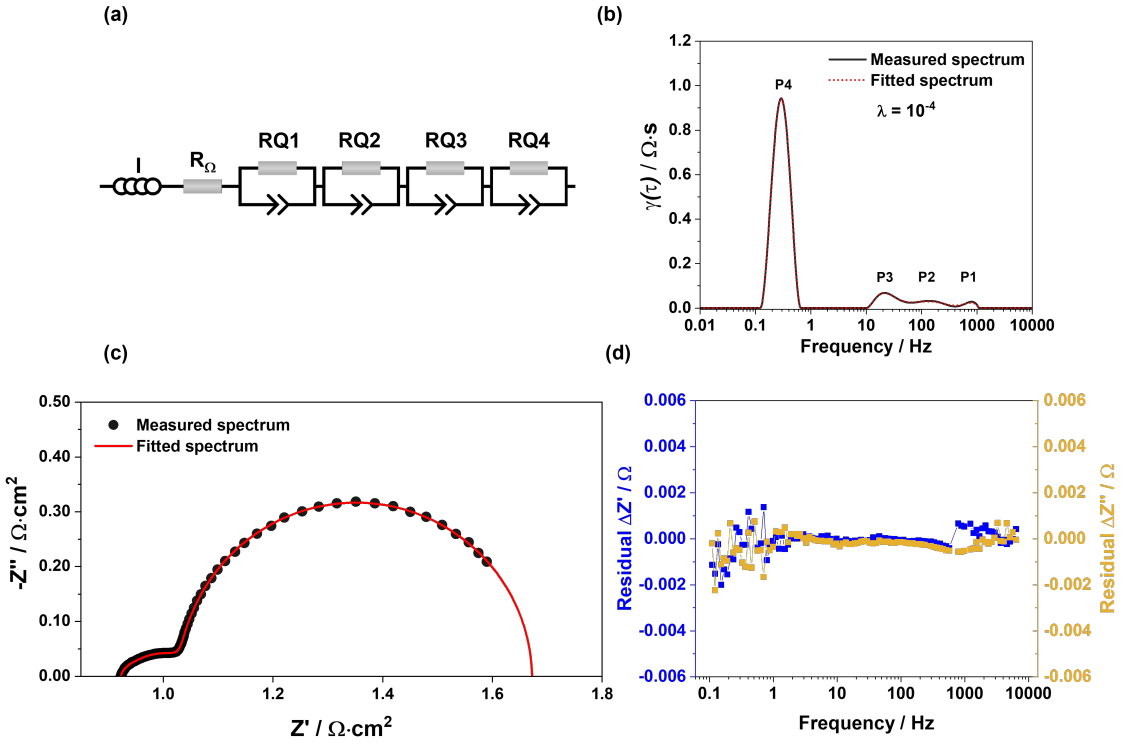

Figure 5.35: (a) Equivalent circuit model (ECM) of the experimental impedance data used for complex non-linear curve fit. (b) Distribution of relaxation times (DRT) of the experimental and fitted impedance data for $Sr_2FeMo_{0.65}Ni_{0.35}O_{6-\delta}$ at 750 °C in 50% H_2O + 50% H_2 recorded at OCV. (c) Nyquist plots of the exemplary experimental data and the corresponding fit. (d) The residual of fitted data to verify the quality of the CNLS fit. Reproduced from[6] published under the CC BY 4.0 (http://creativecommons.org/licenses/by/4.0/).

the thermally activated processes. Within the Figures 5.36c-d, in the given Nyquist plots, two distinct arcs can be discerned with one at lower and the other one at higher frequencies. Throughout all temperature ranges, the dominance of the low-frequency arc over its high-frequency counterpart is evident. Both arcs exhibit an increase in magnitude as the operational temperature decreases, indicating thermally activated processes. The ASR increases consequently from 0.37 $\Omega \cdot cm^2$ to 1.25 $\Omega \cdot cm^2$ in steam electrolysis and from 0.54 $\Omega \cdot cm^2$ 1.52 $\Omega \cdot cm^2$ in co-electrolysis conditions when decreasing the operation temperature from 900 °C to 750 °C. In addition, the temperature variation has a discernible impact on the ohmic resistance R_Ω and polarization resistance R_P. The activation energy for R_Ω is determined based on the slope of the Arrhenius equation and equals between 56 $\pm$ 2 $kJ \cdot mol^{-1}$. This closely aligns with values reported in literature for the ionic conductivity in YSZ electrolyte films and suggests that the primary contribution to R_Ω is the thick 8YSZ electrolyte[180,181,183].

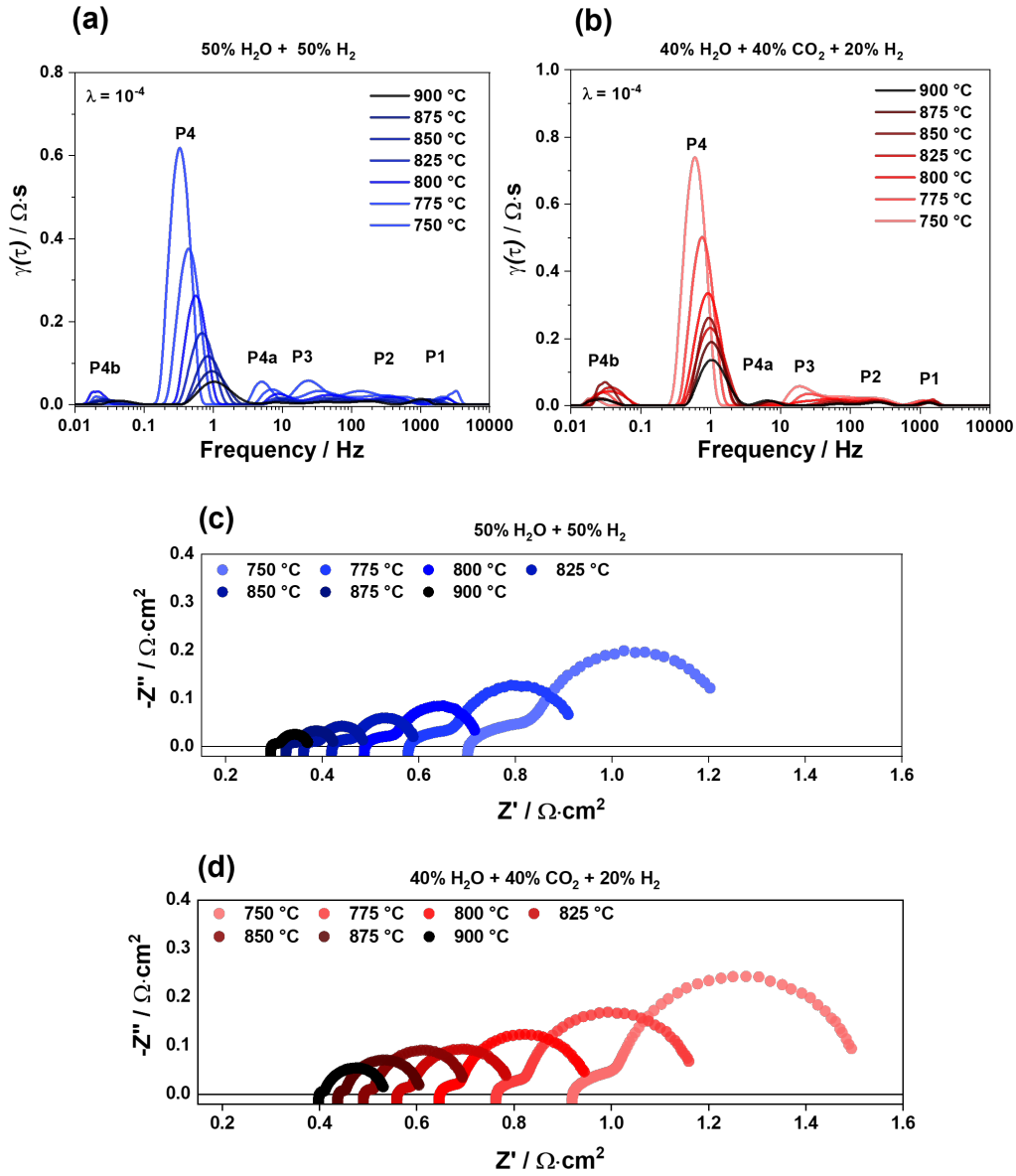

Figure 5.36: DRT spectra from 900 °C to 750 °C in (a) steam electrolysis, and (b) co-electrolysis for $Sr_2FeMo_{0.65}Ni_{0.35}O_{6-\delta}$. The corresponding Nyquist plots measured at OCV from 900 °C to 750 °C in (c) steam electrolysis, and (c) co-electrolysis for $Sr_2FeMo_{0.65}Ni_{0.35}O_{6-\delta}$. Reproduced from[6] published under the CC BY 4.0 (http://creativecommons.org/licenses/by/4.0/).

The impact of the thermally activated processes independent of the experimental gas composition, can also be observed in the DRT spectra in Figure 5.36a and Figure 5.36b. For steam and co-electrolysis, the DRT spectra exhibit four distinct time constants P1, P2, P3, and P4 that increase in magnitude with decreasing operating temperature. The process associated with P4 (1.1 - 0.33 Hz) dominates the DRT spectra over the whole temperature range under steam as well as co-electrolysis conditions in comparison to P1, P2, and P3. This makes P4 the major

contributing process to the cell resistance irrespective of operating conditions, called the rate-limiting process. Similar observations were made for $Sr_2FeMoO_{6-\delta}$ and $Sr_2FeMoO_{6-\delta}$-GDC previously (c.f. chapter 5.2.3.3, Figure 5.22). The peaks P1 (2655 - 1115 Hz), P2 (200 - 100 Hz), and P3 (25 - 12 Hz) increase less pronounced with temperature and shift to slightly higher frequencies in the case of P1 and P2 as well as to slightly lower frequencies for P3. This trend was also observed for SFM and the composite fuel electrode SFM-GDC. In the subsequent discussion of individual process resistances, the circuit elements R_{RQ1}, R_{RQ2}, R_{RQ3}, and R_{RQ4} correspond to the peaks P1, P2, P3, and P4. The detailed Arrhenius analysis is shown in Figure 5.37. In comparison to SFM and SFM-GDC (c.f. Figure A.7), the fuel electrode made of $Sr_2FeMo_{0.65}Ni_{0.35}O_{6-\delta}$ exhibits an ASR of 371 $m\Omega \cdot cm^2$ at 900 °C under steam electrolysis conditions, which is slightly lower than the ASR for SFM (469 $m\Omega \cdot cm^2$) and much lower than for SFM-GDC (532 $m\Omega \cdot cm^2$). The activation energy of the rate-limiting process P4 was observed to be 112 ± 16 $kJ \cdot mol^{-1}$ and 120 ± 11 $kJ \cdot mol^{-1}$ for steam and co-electrolysis respectively, which is in range of the activation energy of 118 ± 12 $kJ \cdot mol^{-1}$ observed for $Sr_2FeMoO_{6-\delta}$. Within this frequency range, the suggested processes include the conversion of gases and diffusion phenomena taking place at the fuel electrode side. However, these processes exhibit only minimal thermal activation, so it is not appropriate to attribute them to the P4.[1,58,133,184–187]. The process P4 shows a distinct impact by polarization variation. This suggests a Butler-Volmer type behavior and indicates that P4 is related to the charge transfer process at the fuel electrode side, observed in MIECs within the frequency range of 1 - 2 Hz, accompanied by an activation energy of approximately 107-126 $kJ \cdot mol^{-1}$[181]. In the mid to low-frequency range, R_{RQ3} (P3, 25 - 12 Hz) unveils a distinctive activation energy closely tied to the selection of the gas stream at the fuel and oxygen electrode side. Additionally, it is impacted by the fuel electrode material. For $Sr_2FeMo_{0.65}Ni_{0.35}O_{6-\delta}$, the determined activation energy of 80 - 89 ± 11 $kJ \cdot mol^{-1}$ is close to the value for $Sr_2FeMoO_{6-\delta}$ of around 72 - 96 ± 20 $kJ \cdot mol^{-1}$ for steam and co-electrolysis.

5.3.2.4 Gas Variation at the Fuel and Oxygen Electrode

The in-depth process analysis was further corroborated by variation of gas composition at the fuel and oxygen electrode side to identify the distinct impedance contributions from the two electrodes. The recorded impedance data as well as the corresponding DRT spectra are shown in Figure 5.38. In steam electrolysis, the steam content was kept constant, while the H_2 content was systematically reduced from 50% to 10% H_2 balanced with N_2. The corresponding Nyquist plot and DRT spectra for the fuel gas variation at 900 °C are illustrated in Figure 5.38a. With

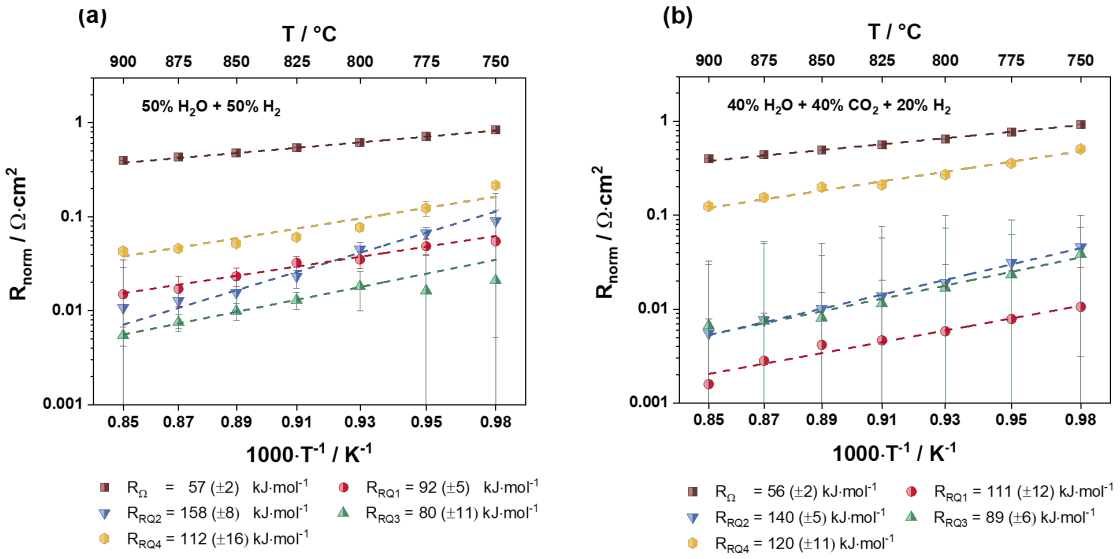

Figure 5.37: Temperature-dependent process resistance analysis measured at OCV from 900 °C to 750 °C in (a) steam electrolysis, and (b) co-electrolysis for $Sr_2FeMo_{0.65}Ni_{0.35}O_{6-\delta}$. Reproduced from[6] published under the CC BY 4.0 (http://creativecommons.org/licenses/by/4.0/).

reducing H_2 content at the fuel electrode, the polarization resistance increases from 88 $m\Omega \cdot cm^2$ with 50% H_2O + 50% H_2 to 230 $m\Omega \cdot cm^2$ measured in an atmosphere of 50% H_2O +10% H_2 + 40% N_2. In co-electrolysis, the CO_2 was varied from 40% to 10%, which led to an RP increase of 13 $m\Omega \cdot cm^2$ from 146 $m\Omega \cdot cm^2$ to 159 $m\Omega \cdot cm^2$. The results in both electrolysis modes emphasize that the gas variation is mainly influencing the low-frequency arc in the Nyquist plots, while the high-frequency arc and the ohmic resistance are not impacted. The DRT analysis in Figure 5.38b shows that P4 is severely increasing with decreasing H_2 gas at the fuel electrode. The processes P1, P2, and P3 are less impacted by the variation of the gas atmosphere. P3 slightly decreases and shifts to higher frequencies. P2 increases slightly while P1 decreases slightly with decreasing H_2 content in addition to a shift to higher frequencies.

To explore the role of the oxygen electrode in the impedance spectra, the oxygen partial pressure was systematically varied from 0.03 to 1 atm balanced with N_2. In Figure 5.39, the Nyquist plots and the corresponding DRT plots illustrate the dependency on the oxygen partial pressure at 900 °C with a constant fuel gas composition of 50% H_2O + 50% H_2. The Nyquist plots and the corresponding DRT spectra in Figure 5.39a and Figure 5.39b illustrate negligible changes for P1, P2, and P3, while P4 increases slightly with decreasing pO_2. Data from previous studies of symmetrical LSCF cells measured in varied N_2-O_2 mixtures identified P1 as the charge transfer process in the oxygen electrode and attributed P2 and P3 to

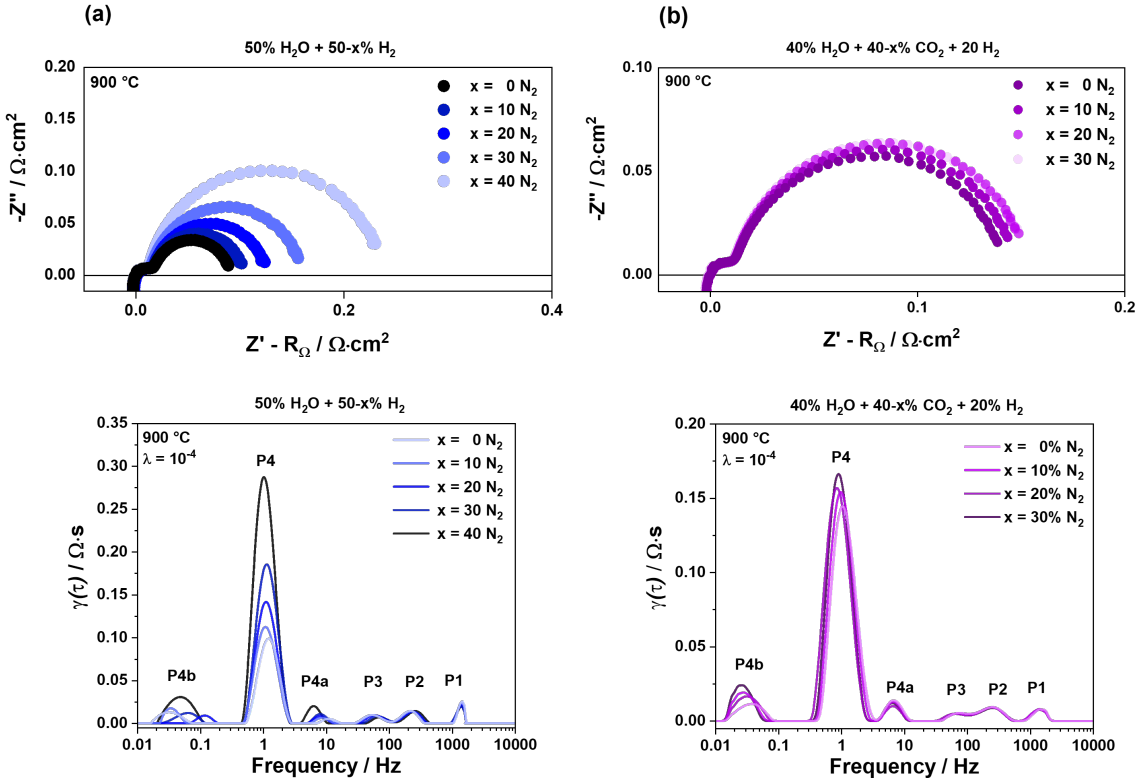

Figure 5.38: (a) Nyquist plot and (c) the corresponding DRT plots for the fuel gas variation of H_2O-H_2 at 900 °C. (b) Nyquist plot and (d) DRT plots for the fuel gas variation of H_2O-CO_2-H_2 at 900 °C. Reproduced from[6] published under the CC BY 4.0 (http://creativecommons.org/licenses/by/4.0/).

oxygen surface exchange kinetics as well as the oxygen bulk diffusion[180,181]. The low-frequency peak P4 has been observed for symmetrical LSCF cells as well, and related to the gas diffusion processes specially at low pO_2. Despite the Ni-doping of SFM, the trends observed for $Sr_2FeMo_{0.65}Ni_{0.35}O_{6-\delta}$ corroborate with those seen previously for $Sr_2FeMoO_{6-\delta}$ and $Sr_2FeMoO_{6-\delta}$-GDC (c.f. Table 5.3).

5.3.3 Long-Term Stability

5.3.3.1 Electrochemical Analysis

The alternative SFMNi fuel electrode was tested at 900 °C for 500 h under constant current density of $-0.5\ A \cdot cm^{-2}$. The measured cell voltage curve is shown in Figure 5.40 and depicts a stable linear trend for the first 100 h in the fuel gas atmosphere of 50% H_2O + 50% H_2. Thereafter, the cell voltage increases continuously up to 193 mV ($326\ mV \cdot kh^{-1}$). The voltage increase for the $Sr_2FeMoO_{6-\delta}$-based fuel electrode is much higher in comparison with 452 mV (c.f. Figure 5.25). Ni-GDC fuel electrodes, on the other hand, have shown a degradation rate of $499\ mV \cdot kh^{-1}$ in 50% H_2O + 50% H_2 at 900 °C at $-0.5\ A \cdot cm^{-2}$[180]. The state-of-the-art Ni-YSZ fuel

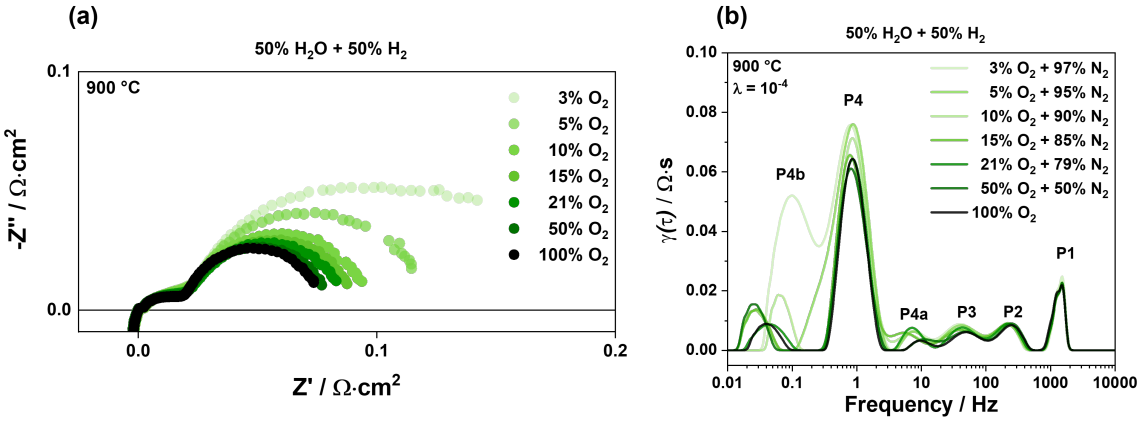

Figure 5.39: (a) Nyquist plot and (b) the corresponding DRT plots for the variation of O_2-N_2 content on the oxygen electrode side at 900 °C. Reproduced from[6] published under the CC BY 4.0 (http://creativecommons.org/licenses/by/4.0/).

electrode exhibits a much higher degradation rate than Ni-GDC with 760 mV · kh^{-1} within the first 100 h[179]. The composite $Sr_2FeMoO_{6-\delta}$-GDC based single cells exhibit a lower degradation of 15.6 mV · kh^{-1}. Although the SFMNi fuel electrode has shown good catalytic capacities, it is less stable than $Sr_2FeMoO_{6-\delta}$-GDC in humidified conditions. Impedance spectra and current-voltage characteristics were

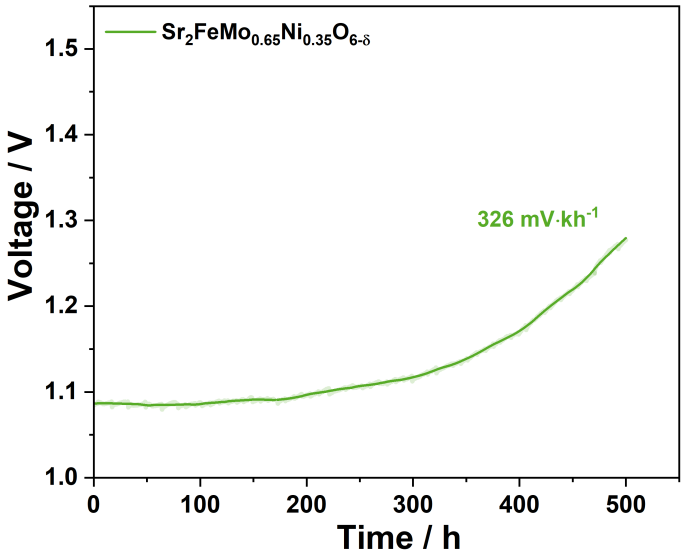

Figure 5.40: Long-term stability test of single cells with a cell composition of $Sr_2FeMo_{0.65}Ni_{0.35}O_{6-\delta}$ /GDC/8YSZ/GDC/LSCF in 50% H_2O + 50% H_2 fuel gas composition under constant current load of -0.5 A · cm^{-2} at 900 °C for up to 500 h. Reproduced from[6] published under the CC BY 4.0 (http://creativecommons.org/licenses/by/4.0/).

recorded before and after the degradation test to analyze the degradation impact on the individual process resistances. The results are given in Figure 5.41a-d. The

maximum current density decreases from $-1.41\ \mathrm{A \cdot cm^{-2}}$ to $-0.58\ \mathrm{A \cdot cm^{-2}}$, i.e. by 59%, after the durability test at 900 °C for 500 h in 50% H_2O + 50% H_2 as shown by the current-voltage characteristics in Figure 5.41a. The increase in ASR during steam electrolysis in dependence on the fuel electrode is depicted in Figure 5.41b for SFM, SFM-GDC, and SFMNi. The comparison underlines that despite the high performance of SFMNi, the ASR increase of 572 $\mathrm{m\Omega \cdot cm^2}$ is the highest observed for all three tested electrodes and is comparable to SFM (491 $\mathrm{m\Omega \cdot cm^2}$). The slight difference of less than 100 $\mathrm{m\Omega \cdot cm^2}$ can be related to the different current load that was applied during the durability test. The results for the composite SFM-GDC electrode highlight that the addition of GDC increases the fuel electrode stability, which leads to an ASR increase of 63 $\mathrm{m\Omega \cdot cm^2}$ over 500 h of measurement time. The Nyquist plots in Figure 5.41c show the measured impedance spectra before and after the degradation test. As can be seen, the ohmic and polarization resistances both increase over the course of the measurement. The fitted impedance results are listed in Table 5.7 and illustrate the contribution of R_Ω and R_P to the ASR increase over time. R_Ω accounts for around 12% of the ASR increase, which is in range with 9.4% found for SFM-GDC and 8.8% for SFM. This means R_P contributes mainly with a share of 88% to the ASR increase. As seen from Table 5.7 and the DRT analysis in Figure 5.41d, the individual resistances increase over time. The process resistance R_{RQ3} contributes mainly to the R_P increase with 219 $\mathrm{m\Omega \cdot cm^2}$, followed by R_{RQ1} (180 $\mathrm{m\Omega \cdot cm^2}$). The process resistances R_{RQ2}, and R_{RQ4} show only a small increase of 68 $\mathrm{m\Omega \cdot cm^2}$ and 39 $\mathrm{m\Omega \cdot cm^2}$ respectively. The DRT analysis depicts as well, a frequency shift of R_{RQ1}, R_{RQ2} and R_{RQ3} to higher frequencies.

Table 5.7: Resistance evolution of SFMNi fuel electrode as a function of operation time in steam electrolysis during 500 h durability testing at 900 °C under constant load of $-0.5\ \mathrm{A \cdot cm^{-2}}$. Reproduced from[6] published under the CC BY 4.0 (http://creativecommons.org/licenses/by/4.0/).

Time	$\boldsymbol{R_\Omega}$	$\boldsymbol{R_{RQ1}}$	$\boldsymbol{R_{RQ2}}$	$\boldsymbol{R_{RQ3}}$	$\boldsymbol{R_{RQ4}}$	$\boldsymbol{R_P}$	**ASR**
h	$\boldsymbol{\Omega \cdot cm^2}$	$\boldsymbol{\Omega \cdot cm^2}$	$\boldsymbol{\Omega \cdot cm^2}$	$\boldsymbol{\Omega \cdot cm^2}$	$\boldsymbol{\Omega \cdot cm^2}$	$\boldsymbol{\Omega \cdot cm^2}$	$\boldsymbol{\Omega \cdot cm^2}$
$Sr_2FeMo_{0.65}Ni_{0.35}O_{6-\delta}$							
0	0.375	0.005	0.006	0.005	0.054	0.070	0.445
500	0.442	0.185	0.074	0.224	0.093	0.576	1.017

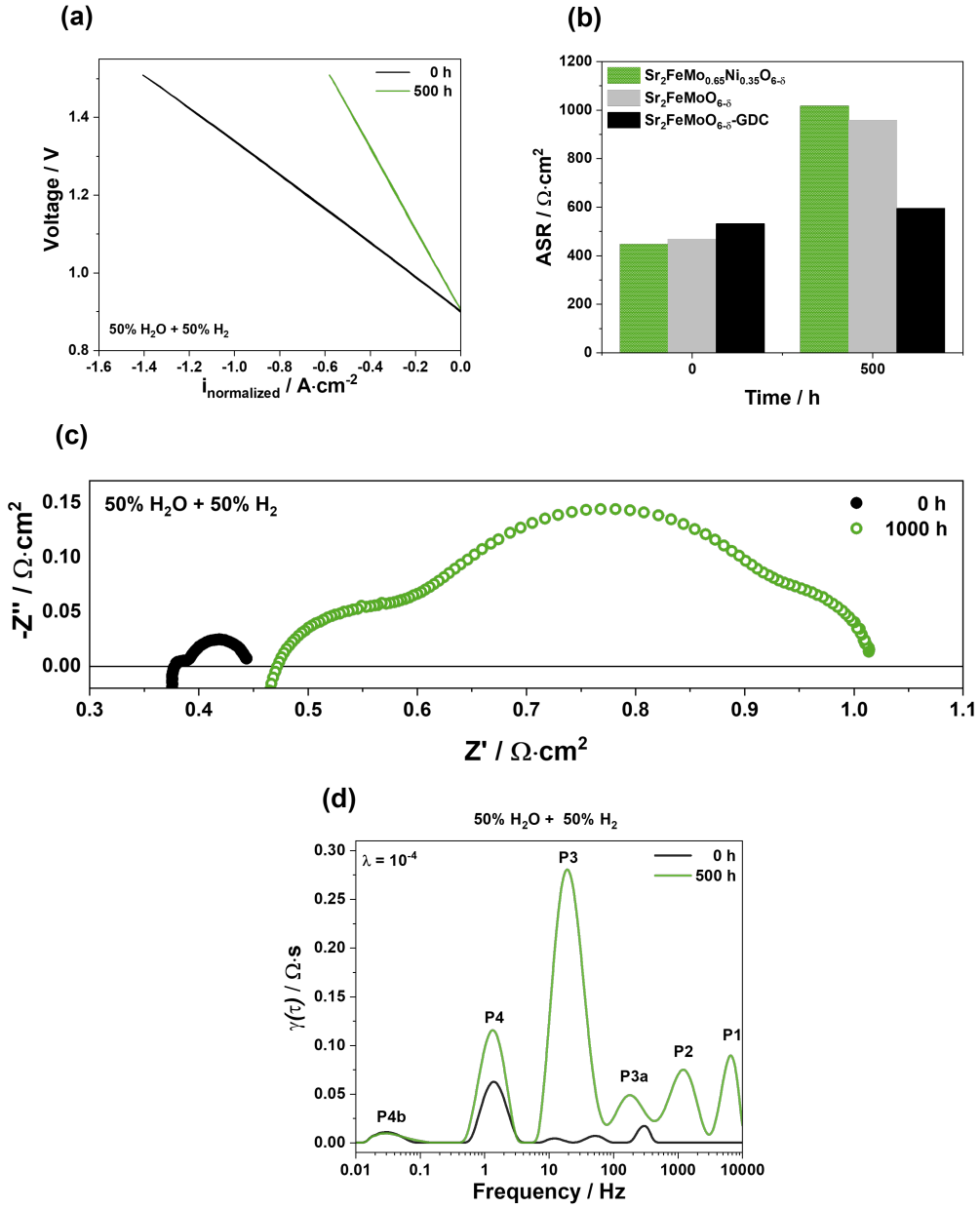

Figure 5.41: (a) Current-voltage characteristics, (b) ASR, (c) the Nyquist plots and (d) the corresponding DRT plots for a single cell with $Sr_2FeMo_{0.65}Ni_{0.35}O_{6-\delta}$ as fuel electrode before and after the long-term degradation measurement at constant $-0.5\ A \cdot cm^{-2}$ current load in 50% H_2O + 50% H_2 atmosphere at 900 °C. Reproduced from[6] published under the CC BY 4.0 (http://creativecommons.org/licenses/by/4.0/).

5.3.3.2 Microstructural Post-Test Analysis

As shown previously in Figure 5.15 (c.f. chapter 5.2.1), the exsoluted Fe particles are partially embedded in the parent oxide surface and have been shown to be more resilient to particle agglomeration compared to the deposited analogs, thus

improving the electrode stability at high temperatures. The microstructure of as-prepared and tested SFMNi fuel electrodes were characterized with SEM-EDX to determine structural changes. The samples were encased in epoxy resin, polished, and sputtered with gold before undergoing analysis. Figure 5.42 illustrates the cross-section of the as-prepared and tested SFMNi fuel electrode. For both cells, the electrolyte remains unchanged, and no electrode delamination is observed. Notably, the electrode microstructure shows increased pore formation and particle growth after the long-term test in humidified atmosphere. This result corresponds to the high degradation rate and striking increase in ASR for the single cells with SFMNi fuel electrode shown in the Figures 5.40 and 5.41.

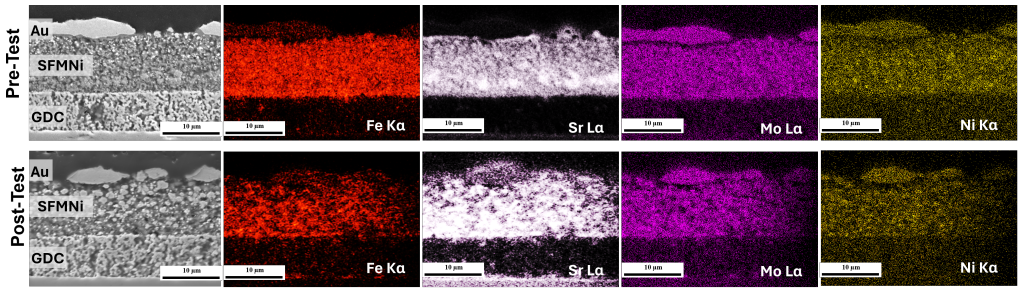

Figure 5.42: Cross-sectional SEM-EDX mapping of the fuel electrode side for Sr (Lα, 13.89 keV), Fe (Kα, 6.40 keV), Mo (Lα, 17.14 keV), Ni (Kα, 7.47 keV) lines (a) before and (b) after the long-term test up to 500 h in 50% H_2O + 50% H_2 at -0.5 A $\cdot$ cm^{-2} and 900 °C. Reproduced from[6] published under the CC BY 4.0 (http://creativecommons.org/licenses/by/4.0/).

The cross-sectional SEM-EDX analysis the LSCF oxygen electrode for the as-prepared and operated cells is displayed in Figure 5.43. Similar to the previous results, a slight Sr segregation through the pores of the GDC barrier layer and subsequent formation of an insulating $SrZrO_3$ layer is observed, which may have led to the increase in ohmic resistance throughout the degradation test.

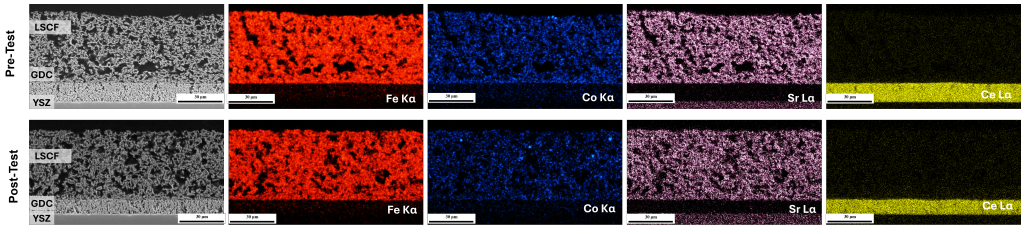

Figure 5.43: Cross-sectional SEM-EDX mapping of the oxygen electrode side for Ce (Lα, 33.90 keV), Fe (Kα, 6.40 keV), Co (Kα, 6.93 keV), Sr (Lα, 13.89 keV) lines (a) before and (b) after the long-term test up to 500 h in 50% H_2O + 50% H_2 at -0.5 A $\cdot$ cm^{-2} and 900 °C. Reproduced from[6] published under the CC BY 4.0 (http://creativecommons.org/licenses/by/4.0/).

5.4 SFM-based Fuel Electrodes for CO_2 Electrolysis

High-temperature CO_2 electrolysis can valorizes industrial CO_2 emissions by electrochemical reduction to carbon monoxide (CO). CO is an important building block in the chemical industry to derive essential chemical intermediates, which include synthetic natural gas, methane produced through methanation, liquid hydrocarbons, e.g. synthetic fuels, and chemical lubricants through Fischer-Tropsch synthesis. Additionally, the production of aldehydes via the "oxo process" hydroformylation necessitates CO to give way to bulk chemicals such as esters, alcohols, and amines[5]. The state-of-the-art fuel electrode material Ni-YSZ as well as the alternative Ni-GDC have both been shown to be impacted by continuous exposure to CO_2 containing gas mixtures. The analysis of Ni-YSZ fuel electrodes in CO_2/CO gas atmosphere was investigated under constant current load of $-1\ \mathrm{A \cdot cm^{-2}}$ as well as at OCV up to 1000 h. The 3D electrode microstructural reconstruction showed that the cell operated at zero current exhibited Ni coarsening and no Ni migration as observed for steam electrolysis. In comparison, the cell operated at $-1\ \mathrm{A \cdot cm^{-2}}$ showed an increase in Ni particle size, i.e. Ni coarsening and significant Ni particle loss in the active electrode layer in addition to an increased Ni fraction in the support layer. The severity of Ni migration was comparable to previous result for Ni-YSZ operated in steam electrolysis conditions[222]. The investigation of Ni-GDC as fuel electrode in CO_2 electrolysis conditions of 80% CO_2 + 20% CO at 900 °C showed microstructural changes of the fuel electrode after the degradation test. An increase in Ni particle size, Ni depletion and pore formation at the electrolyte/-electrode interface were observed, which impact the number of catalytically active TPB sites[182]. Therefore, in this chapter, the SFM-based MIEC electrode materials were characterized in CO_2 electrolysis condition with regard to their performance and long-term microstructural stability. A comparison is drawn to the state-of-the-art Ni-8YSZ and Ni-GDC cermet electrodes. Parts of the following results have been measured in collaboration with Niklas Eyckeler, Carla L. Coll, and Finn Dröge during their bachelor thesis[117,118,207].

5.4.1 Electrochemical Performance

The electrochemical performance of SFM-based fuel electrode materials was characterized with current-voltage characteristics and electrochemical impedance spectroscopy for CO_2 electrolysis with 80% CO_2 + 20% CO fuel gas mixture in the temperature range of 750 °C to 900 °C.

The results are displayed in Figure 5.44 and listed in Table 5.8. The maximum current density of $-1.28\ A \cdot cm^{-2}$ at 1.5 V, as shown in Figure 5.44a, illustrates that $Sr_2FeMo_{0.65}Ni_{0.35}O_{6-\delta}$ is the highest performing fuel electrode in CO_2 electrolysis conditions at 900 °C. In comparison, the Ni cermet electrodes achieved a lower current density with $-0.63\ A \cdot cm^{-2}$ for Ni-8YSZ and $-1.16\ A \cdot cm^{-2}$ for Ni-GDC[182]. The Ni-GDC cermet electrode is shown to have a higher performance as GDC exhibits MIEC properties under reducing conditions due to the partial reduction of Ce^{4+} to Ce^{3+}. The use of an GDC fuel electrodes without Ni exhibited decreased current density ($-0.79\ A \cdot cm^{-2}$)[223].

The single cells with Ni-free SFM fuel electrodes show higher performance than Ni-8YSZ at 900 °C (Table 5.8). Single cells with the $Sr_2Fe_{1.5}Mo_{0.5}O_{6-\delta}$ fuel electrode achieved $-1.17\ A \cdot cm^{-2}$ current density compared to $-1.03\ A \cdot cm^{-2}$ observed for the $Sr_2FeMoO_{6-\delta}$ fuel electrode. The composite $Sr_2Fe_{1.5}Mo_{0.5}O_{6-\delta}$-GDC fuel electrode exhibits enhanced performance with $-1.23\ A \cdot cm^{-2}$, while $Sr_2FeMoO_{6-\delta}$-GDC reached $-1.11\ A \cdot cm^{-2}$. Similar results are shown in Figure 5.44b in the comparison of the polarization resistance at OCV. $Sr_2FeMoO_{6-\delta}$, $Sr_2FeMoO_{6-\delta}$-GDC and $Sr_2Fe_{1.5}Mo_{0.5}O_{6-\delta}$ exhibit an R_P of 36 $m\Omega \cdot cm^2$, 33 $m\Omega \cdot cm^2$, and 34 $m\Omega \cdot cm^2$ respectively. These values are higher than the polarization resistance of Ni-GDC with 23 $m\Omega \cdot cm^2$, but significantly lower than 44 $m\Omega \cdot cm^2$ observed for Ni-8YSZ. $Sr_2Fe_{1.5}Mo_{0.5}O_{6-\delta}$-GDC and $Sr_2FeMo_{0.65}Ni_{0.35}O_{6-\delta}$ reach polarization resistances of 24 $m\Omega \cdot cm^2$ and 22 $m\Omega \cdot cm^2$, which are in range of the Ni-GDC fuel electrode resistance (23 $m\Omega \cdot cm^2$). The SFM-based fuel electrodes exhibit higher perfor-

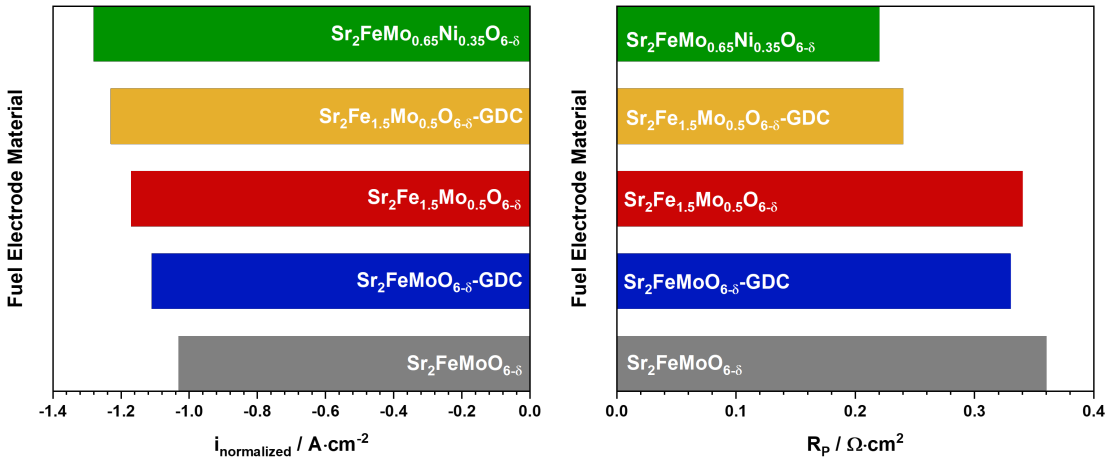

Figure 5.44: Current density observed at 1.5 V and polarization resistance measured at open circuit voltage for different SFM-based fuel electrode materials in CO_2 electrolysis conditions of 80% CO_2 + 20% CO at 900 °C.

mance compared to other mixed-ionic and electronic conducting perovskites consid-

ered as alternative fuel electrode material. Current densities of $-0.67\ \mathrm{A \cdot cm^{-2}}$ for $Sr_2Fe_{1.5}Mo_{0.5}O_{6-\delta}$ up to $-0.74\ \mathrm{A \cdot cm^{-2}}$ for $Sr_2FeMo_{0.65}Ni_{0.35}O_{6-\delta}$ were achieved in dry CO_2 electrolysis conditions at 800 °C. The perovskite electrode $La_{0.2}Sr_{0.8}TiO_{3+\delta}$ shows in comparison a current density of $-0.105\ \mathrm{A \cdot cm^{-2}}$ at 800 °C and 1.5 V. By doping at the B-site and creating A-site cation deficiency, the electrochemical conversion of CO_2 to CO for $(La_{0.2}Sr_{0.8})_{0.95}Ti_{0.9}Mn_{0.1}O_{3+\delta}$ electrode was enhanced to $-0.22\ \mathrm{A \cdot cm^{-2}}$ and to $-0.45\ \mathrm{A \cdot cm^{-2}}$ for $(La_{0.2}Sr_{0.8})_{0.95}Ti_{0.85}Mn_{0.1}Ni_{0.05}O_{3+\delta}$[224].

Table 5.8: Electrochemical performance of $Sr_2FeMoO_{6-\delta}$–based fuel electrodes in comparison to state-of-the-art Ni-cermet electrodes under CO_2 electrolysis conditions of 80% CO_2 + 20% CO at 900 °C.

Fuel Electrode	$\boldsymbol{R_{P,OCV}}$ **/** $\boldsymbol{\Omega \cdot cm^2}$	$\boldsymbol{i_{1.5V}}$ **/** $\boldsymbol{A \cdot cm^{-2}}$
Ni-8YSZ	0.44[182]	−0.63[182]
Ni-GDC	0.23[182]	−1.16[182]
GDC	0.51[223]	−0.79[223]
$Sr_2FeMoO_{6-\delta}$	0.36	−1.03
$Sr_2FeMoO_{6-\delta}$-GDC	0.33	−1.11
$Sr_2Fe_{1.5}Mo_{0.5}O_{6-\delta}$	0.34	−1.17
$Sr_2Fe_{1.5}Mo_{0.5}O_{6-\delta}$-GDC	0.24	−1.23
$Sr_2FeMo_{0.65}Ni_{0.35}O_{6-\delta}$	0.22	−1.28

GDC: $Ce_{0.8}Gd_{0.2}O_{1.9}$, 8YSZ: 8mol% YSZ

5.4.1.1 Equivalent Circuit Model Evaluation

Impedance spectra were taken under different measurement conditions such as variation of temperature and gas composition. To evaluate the experimental data, the number of time constants was analyzed by the DRT method resulting in an ECM with an inductor, a serial resistor followed by four RQ elements connected in series as used for $Sr_2FeMoO_{6-\delta}$ and $Sr_2FeMoO_{6-\delta}$-GDC (Figure 5.35a). In Figure 5.35b, the DRT spectra for $Sr_2FeMo_{0.65}Ni_{0.35}O_{6-\delta}$ measured at 750 °C in 80% CO_2 + 20% CO at OCV is depicted as an example. In comparison to Figure 5.20b (c.f. chapter 5.2.3.2), the low-frequency process P4 is much more pronounced. The signal intensity of P4 is much higher compared to P1, P2, and P3, which might lead to higher fitting uncertainties of the impedance data. The experimental impedance data and the fit shown in Figure 5.20c agree qualitatively well. The relative residuals are given

in Figure 5.20d and the low X^2 error of 10^{-7} between the fitted and experimental data indicate a reasonable ECM.

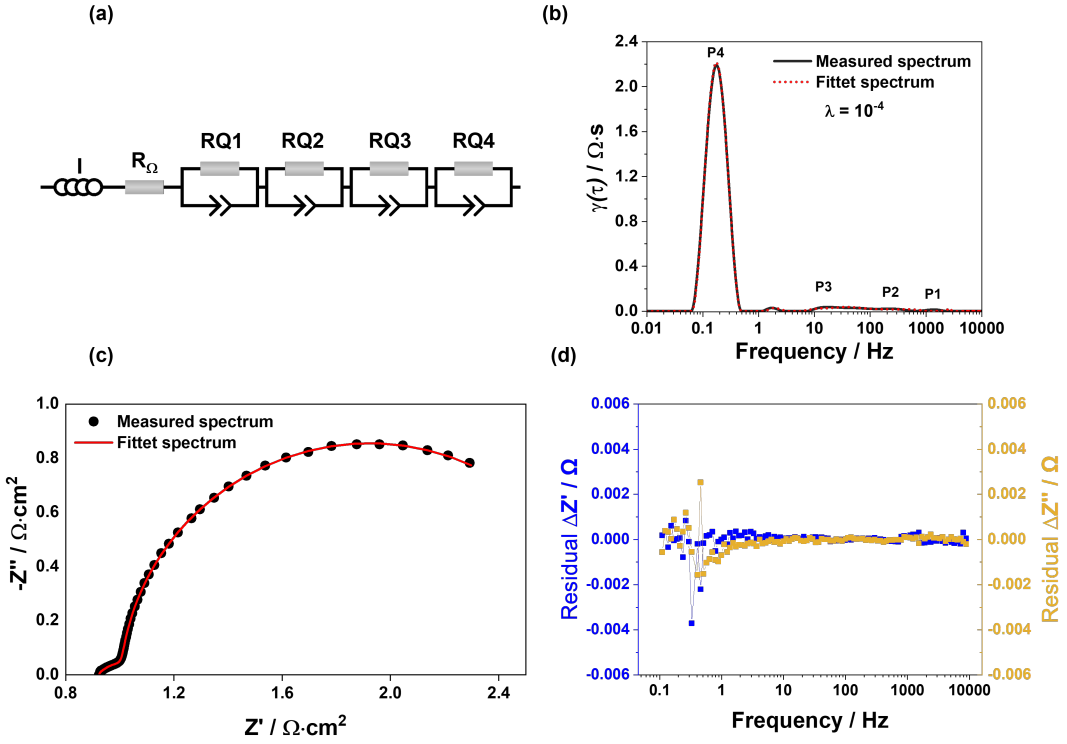

Figure 5.45: (a) Equivalent circuit model (ECM) of the experimental impedance data used for complex non-linear curve fit. (b) Distribution of relaxation times (DRT) of the experimental and fitted impedance data for $Sr_2FeMo_{0.65}Ni_{0.35}O_{6-\delta}$ at 750 °C in 80% CO_2 + 20% CO recorded at OCV. (c) Nyquist plots of the experimental data and the corresponding fit. (d) The residual of fitted data to verify the quality of the CNLS fit.

5.4.1.2 Temperature Variation

The impact of operating temperature was investigated between 750 °C up to 900 °C in dry CO_2 electrolysis condition of 80% CO_2 + 20% CO through impedance analysis at OCV. $Sr_2FeMo_{0.65}Ni_{0.35}O_{6-\delta}$ and $Sr_2FeMoO_{6-\delta}$-GDC were selected as examples. The Nyquist plots and corresponding DRT spectra as a function of temperature are displayed in Figure 5.46. Two distinct arcs are identified in the impedance spectra similar to the previously observation in steam and co-electrolysis with a low- and high-frequency arc (c.f. chapters 5.2.3.3 and 5.3.2.3). Throughout the varied temperature range, both arcs increase, although the low-frequency arc shows a much more pronounced increase in magnitude. The RP increases from 0.22 $\Omega \cdot cm^2$ to 1.91 $\Omega \cdot cm^2$ for SFMNi in CO_2 electrolysis and from 0.33 $\Omega \cdot cm^2$ to 2.71 $\Omega \cdot cm^2$ for SFM-GDC when decreasing the operation temperature from 900 °C to at 750 °C.

Further analysis of the impedance data as shown in the DRT spectra show five to six peaks in the different spectra. In the low-frequency range below 1 Hz, however, artifacts can occur in case the last impedance data point is not completely on the x-axis and is made-up, therefore, partially of imaginary impedance[98]. This causes an additional peak P4b at around 0.03 Hz in the DRT of $Sr_2FeMo_{0.65}Ni_{0.35}O_{6-\delta}$ in Figure 5.46, although the spectra was only recorded up to 0.11 Hz. To define the process peaks, the variation of the λ parameter between 10^{-3} and 10^{-5} is an additional criterion. The variation results show that both peaks have no linear trend with temperature, which hints that peak P4b below 0.1 Hz as well as P4a around 2.5 Hz are artifacts. The impedance spectra were therefore modeled with same equivalent circuit used for humidified conditions consisting of four time constants in series to a resistor and an inductor as shown in Figure 5.35. The peaks P1, P2, P3 and P4 in the DRT correspond to the circuit elements R_{RQ1}, R_{RQ2}, R_{RQ3} and R_{RQ4}, respectively.

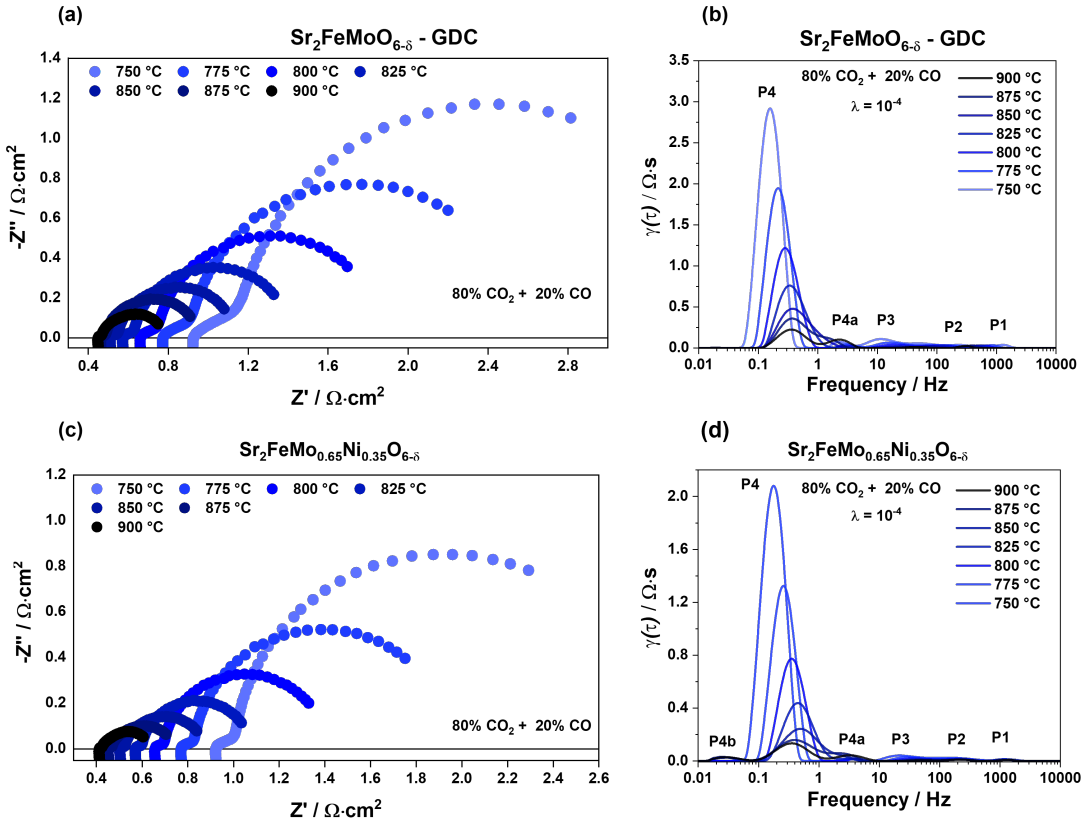

Figure 5.46: (a) Nyquist plots and (b) the corresponding DRT spectra measured for SFM-GDC at OCV in 80% CO_2 + 20% CO as a function of temperature between 750 °C and 900 °C. (c) Nyquist plots and (d) the corresponding DRT spectra measured for SFMNi at OCV in 80% CO_2 + 20% CO as a function of temperature between 750 °C and 900 °C.

The resistance analysis as a function of temperature is depicted for the SFM-GDC fuel electrode in Figure 5.47a and for SFMNi in in Figure 5.47b. As for all SFM-based fuel electrodes, the process P4 exhibits the highest resistance values among the investigated temperatures and is therefore assigned as rate-limiting step in agreement with the DRT analysis. This thermally activated process is observed in the frequency range of 1 - 0.1 Hz with an activation energy of 144 ± 5 kJ · mol^{-1} for the single cell containing the SFM-GDC fuel electrode (Figure 5.47a). This value is in range of the activation energy observed for SFM-GDC in steam and co-electrolyis of around 134 - 149 ± 5 kJ · mol^{-1}. Several studies report diffusion processes in this frequency range, however, the obtained activation energy in this work is much higher[1,58,133,184–187]. The impact of temperature variation and the previous assignment of P4 to the fuel electrode side give the conclusion that the physical process in this work might be related to the charge transfer reaction at the fuel electrode. Previous studies of the GDC fuel electrode have shown an activation energy of 166 ± 7 kJ · mol^{-1} observed for a thermally activated processes in the same frequency range, which was associated with the charge transfer during the reduction of CO_2 on ceria (doped) materials[181,225]. The process P3 was observed around 100 - 10 Hz and exhibits an activation energy of 173 ± 5 kJ · mol^{-1} in the analyzed temperature range for CO_2 electrolysis (Figure 5.47a). In comparison, the activation energies shown for steam and co-electrolysis with 206 ± 5 kJ · mol^{-1} to 222 ± 8 kJ · mol^{-1} are slightly higher for this process as seen in Figure 5.22. Process P3 has been related to adsorption, desorption and transport processes on the LSCF electrode surface, which have shown an activation energy of 192 ± 12 kJ · mol^{-1}[181,226]. A deviation from this activation energy could be explained due to an overlap of different processes at the fuel and oxygen electrode sides in this frequency range, which has been observed in previous studies[190]. The other processes P1 (15000 - 1000 Hz) and P2 (300 - 100 Hz) show temperature dependency and a shift to lower frequency with decreasing operation temperature in case of the process P2. The observed high-frequency contribution P1 is modeled by R_{RQ1} and shows similar activation energies of 157 ± 10 kJ · mol^{-1} in CO_2 electrolysis compared to steam and co-electrolysis for the SFM-GDC fuel electrode. The described frequency range and the high activation energy have been previously attributed to an electrode charge-transfer process at the LSCF oxygen electrode[181,190–192]. In comparison, the middle to high-frequency process modeled by R_{RQ2} for P2 shows an activation energy of 116 ± 4 kJ · mol^{-1}, which is in range of the values obtained for steam and co-electrolyis (120 - 130 kJ · mol^{-1}) as well. Previously, this process was attributed to surface exchange kinetics at the LSCF surface[190]. The activation energies for the processes P1, P2, and P4 for

SFMNi modeled by the resistances R_{RQ1}, R_{RQ2}, and R_{RQ4} in Figure 5.47 are in range with the values observed for SFM-GDC. However, as shown in the previous chapters 5.2.3.3 and 5.3.2.3, the activation energies for the process P3 given by R_{RQ3} for SFM-based electrodes without GDC are lower than observed for SFM-GDC (Figure 5.47b). It has been suggested that an additional mechanism with lower activation energy like transport processes, adsorption and desorption or the oxide ion transport across the electrolyte/electrode interface influence the mid-frequency process P3.

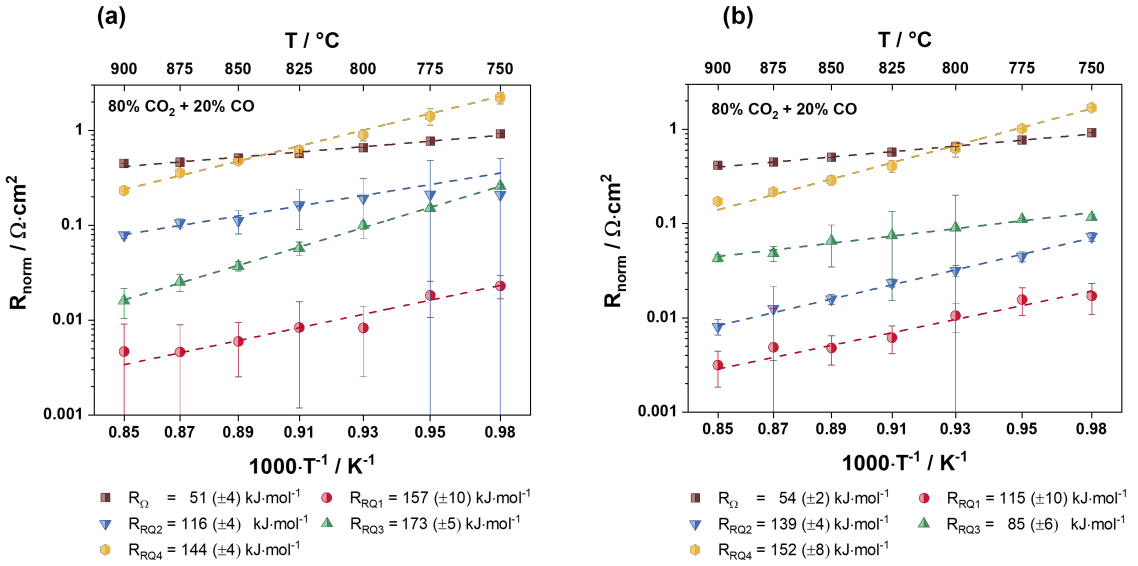

Figure 5.47: Temperature variation between 750 °C and 900 °C measured at OCV for (a) $Sr_2FeMoO_{6-\delta}$-GDC and (b) $Sr_2FeMo_{0.65}Ni_{0.35}O_{6-\delta}$ in 80% CO_2 + 20% CO.

5.4.1.3 Gas Variation

With the intention of further investigations and validation of fuel electrode processes, impedance measurements were conducted under various CO_2:CO compositions from 90% CO_2 down to 50% CO_2. These measurements were subsequently analyzed using DRT analysis and ECM fitting. Figure 5.48a illustrates the Nyquist plots with the variation of CO_2 content at 900 °C under OCV conditions. An increase in CO_2 concentration resulted in a higher polarization resistance R_P value, while the ohmic resistances R_Ω remained relatively unaffected. Notably, the low-frequency arc exhibited a significant increase in magnitude, with negligible changes in the intermediate and high-frequency regions. In Figure 5.48b, the DRT spectra corresponding to variations in the CO_2:CO ratio are depicted. Peaks P1, P2 and P3 in the high to intermediate frequency range displayed no significant dependence on changes in fuel gas composition. In contrast, Peak P4 demonstrated a notable dependence on CO_2 variation, with an increase in magnitude corresponding to higher CO_2 content. In previous studies of state-of-the-art Ni-8YSZ and Ni-GDC cermet fuel electrodes,

similar behavior was observed. the trend was linked to a favored adsorption process and attributed to more favorable thermodynamics of the CO oxidation reaction. The electrochemical activity towards CO oxidation is higher than for the CO_2 reduction reaction at OCV conditions, thus the reaction barrier for the CO oxidation is lower, which results subsequently in an higher activation energy associated with CO_2 desorption from the active catalyst sites[182,227,228].

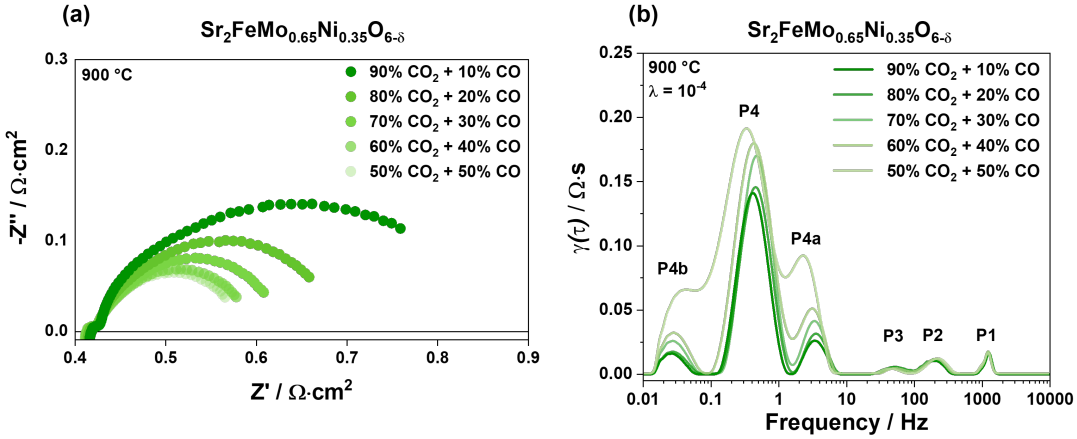

Figure 5.48: (a) Nyquist plots and (b) the corresponding DRT spectra for the gas variation of CO_2 and CO measured at OCV and 900 °C.

5.4.2 Long-Term Stability

5.4.2.1 Electrochemical Analysis

Long term stability tests were performed with single cells under constant current load of $-0.3\ \mathrm{A \cdot cm^{-2}}$ for the SFM-GDC and $-0.5\ \mathrm{A \cdot cm^{-2}}$ for the SFMNi fuel electrode material up to 1000 h in 80% CO_2 + 20% CO at 900 °C . The variation of cell potential with time for SFM-GDC and SFMNi is shown in Figure 5.49. The single cell with the SFM-GDC fuel electrode exhibited a stable cell potential of 1.01 V at $-0.3\ \mathrm{A \cdot cm^{-2}}$ for around 300 h. Thereafter, the cell potential increased slightly, which led to an overall degradation rate of $7\ \mathrm{mV \cdot kh^{-1}}$. As seen in Figure 5.49, the single cell containing the SFMNi fuel electrode showed decreasing potential in the first 200 h by 17 mV from 1090 mV to 1073 mV and then a stable degradation rate in the following 800 h. In comparison, the Ni-GDC cermet and the MIEC GDC fuel electrodes tested in the same gas mixture of 80% CO_2 + 20% CO under constant current load of $-0.5\ \mathrm{A \cdot cm^{-2}}$ exhibited no activation period, however, they showed an increase in R_Ω, R_P and the measured cell potential. A total degradation rate of $31\ \mathrm{mV \cdot kh^{-1}}$ was observed for Ni-GDC after 1200 h[179,182], while the GDC fuel electrode exhibited a degradation rate of $62\ \mathrm{mV \cdot kh^{-1}}$[223]. The evolution of the ohmic resistance R_Ω and the polarization resistance R_P was investigated

for SFMNi by performing impedance measurements at OCV before and after the 1000 h cell test (Figure A.10b). R_Ω decreased from 376 $m\Omega \cdot cm^2$ to 323 $m\Omega \cdot cm^2$ by 53 $m\Omega \cdot cm^2$ and R_P decreased marginally by 5 $m\Omega \cdot cm^2$ from 274 $m\Omega \cdot cm^2$ to 269 $m\Omega \cdot cm^2$. The current-voltage characteristics underline a performance increase of 13 $mA \cdot cm^{-2}$ with operation time, which led to a higher maximum current density of -1.36 $A \cdot cm^{-2}$ after 1000 h. The DRT analysis in Figure A.10c shows a decrease in the peaks P1 and P2, which both shift to lower frequencies as well. The peak P3 remains unchanged while the peak P4 exhibits an increase. The cell potential decrease in the beginning of the durability tests have been observed for other $Sr_2FeMoO_{6-\delta}$-based fuel electrodes as well as other MIEC fuel electrode materials under dry CO_2 electrolysis conditions. The authors observed a decreasing cell potential and ohmic resistance corresponding with an increased maximum current density during the durability test, which points to an activation process of the fuel electrode during the electrolysis reaction[229,230].

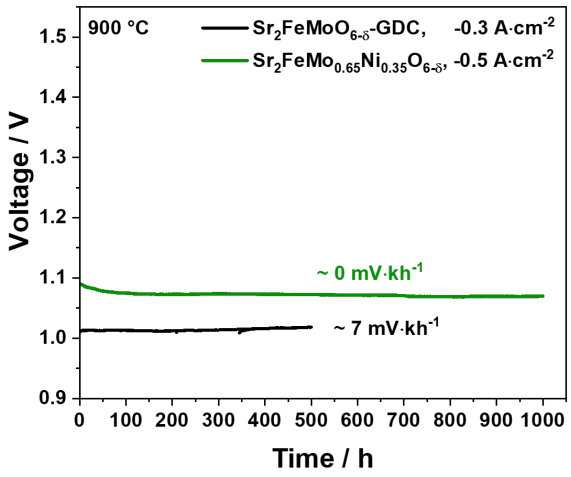

Figure 5.49: Long-term stability test of single cells win an atmosphere of 80% CO_2 + 20% CO at 900 °C with $Sr_2FeMo_{0.65}Ni_{0.35}O_{6-\delta}$ and $Sr_2FeMoO_{6-\delta}$-GDC fuel electrode materials under constant current load of -0.3 $A \cdot cm^{-2}$ and -0.5 $A \cdot cm^{-2}$ for up to 1000 h.

5.4.2.2 Microstructural Post-Test Analysis

To elucidate any microstructural changes compared to cells tested in steam electrolysis (Figure 5.27), the microstructure of as-prepared and tested cells containing SFM-GDC fuel electrodes were characterized with SEM-EDX. The samples were encased in epoxy resin, polished, and sputtered with gold before undergoing analysis. In Figure 5.50, the cross-sectional SEM-EDX mapping of the $Sr_2FeMoO_{6-\delta}$-GDC microstructure is shown after 500 h of long-term testing. Compared to the durability tests in humidified conditions of steam electrolysis with 50% H_2O and 50% H_2,

the operated cell looks similar to the as-prepared cell in Figure 5.50a. However, the SFM-GDC electrode showed slight Sr segregation at the GDC/8YSZ interface after the 500 h in steam electrolysis conditions (Figure 5.27b). In contrast, after 500 h CO_2 electrolysis, no segregation is observed. This indicates a much higher stability in addition to the good performance of $Sr_2FeMoO_{6-\delta}$-based fuel electrode materials for CO_2 to CO conversion.

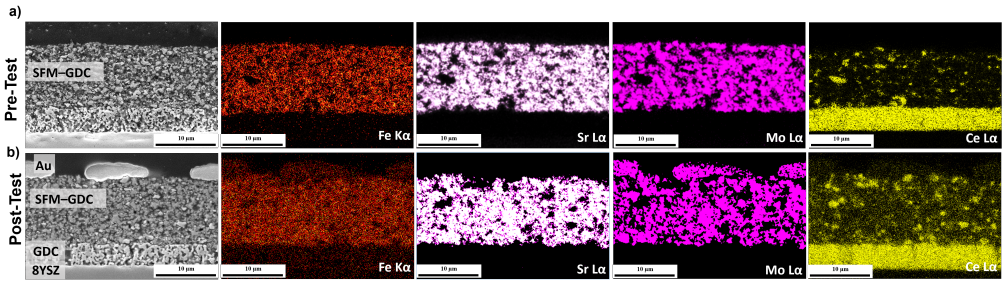

Figure 5.50: Cross-sectional SEM-EDX mapping of the SFM-GDC fuel electrode side for Sr (Lα, 13.89 keV), Fe (Kα, 6.40 keV), Mo (Lα, 17.14 keV), Ce (Lα, 33.90 keV) lines (a) before and (b) after 500 h durability testing in 80% CO_2 + 20% CO at 900 °C under constant current load of -0.3 A $\cdot$ cm^{-2}.

The cross-sectional SEM-EDX analysis the LSCF oxygen electrode for the as-prepared and operated cells is displayed in Figure 5.51. Similar to the previous results in steam electrolysis, a slight Sr segregation through the pores of the GDC barrier layer and subsequent formation of an insulating $SrZrO_3$ layer is observed.

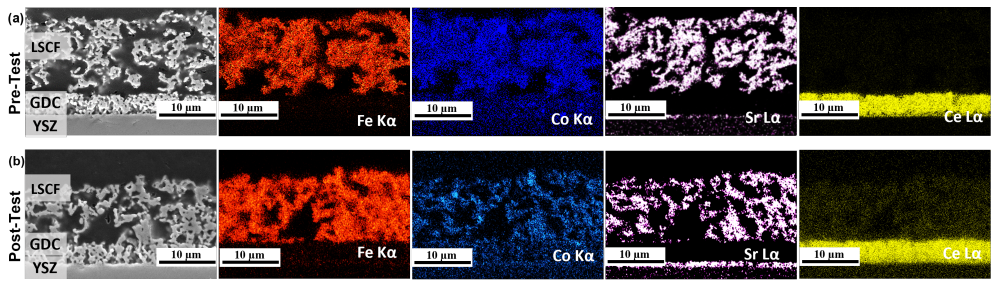

Figure 5.51: Cross-sectional SEM-EDX mapping of the SFM-GDC fuel electrode side for Sr (Lα, 13.89 keV), Fe (Kα, 6.40 keV), Mo (Lα, 17.14 keV), Ce (Lα, 33.90 keV) lines (a) before and (b) after 500 h durability testing in 80% CO_2 + 20% CO at 900 °C under constant current load of -0.3 A $\cdot$ cm^{-2}.

6. Conclusion and Outlook

The focus of this thesis was the performance and degradation mechanism analysis of Ni cermet and Ni-free perovskite electrode materials in steam, dry CO_2 and co-electrolysis conditions. Commercial button cells with an Ni-YSZ fuel electrode were galvanostatically tested in steam and co-electrolysis conditions at 800 °C and 750 °C under constant current load of $-1\ \mathrm{A \cdot cm^{-2}}$. Electrochemical impedance spectra were taken at OCV after every four days to analyze the impedance and cell performance as a function of time. The investigation of the ASR elucidated that an increased ASR over time mainly originates in the progressively higher R_P increase. Additionally, the results showed that the operating temperature and gas humidity are directly impacting the cell degradation over time. The as-prepared and operated single cells were investigated through in-depth SEM-EDX imaging, which showed Ni particle migration from the active fuel electrode layer to the support layer as well as subsequent Ni particle agglomeration. These major microstructural changes led to higher pore size and fraction close to the electrolyte/electrode interface and a subsequent decrease of the active TPB sites.

As the major degradation process for Ni cermet electrodes was identified to be the Ni depletion in the active layer, Ni-free $Sr_2Fe_{2-x}Mo_xO_{6-\delta}$-based fuel electrode materials were synthesized. The $Sr_2FeMoO_{6-\delta}$ powder was reduced in 100% H_2 at 900 °C and XRD and TEM analyses were performed to analyze structural changes in reducing operation conditions. The phase analysis obtained from the TEM lattice parameter calculations as well as the X-Ray Diffraction pattern verify that reduced $Sr_2FeMoO_{6-\delta}$ powder is composed of $Sr_2(Fe_{1.33}Mo_{0.66})O_{5.88}$ (space group: $Fm\bar{3}m$, ICSD-168704), $Sr(Fe_{0.8}Mo_{0.2})O_3$ (space group: $Pm\bar{3}m$, ICSD-191551), Sr_3FeMoO_7 (space group: I4/mmm, ICSD-156787) as well as FCC-gamma-Fe (space group: $Fm\bar{3}m$, ICSD-43096) for exsoluted Fe nanoparticles. These particles enhances the catalytic reactivity through increased catalytic active sites. A strong anchoring was observed between the exsoluted Fe nanoparticles and the perovskite substrate, which could improved the material stability in operation. The investigation of the total conductivity revealed that $Sr_2FeMoO_{6-\delta}$ as well as $Sr_2FeMoO_{6-\delta}$-GDC exhibit higher conductivities in reducing atmosphere than other perovskite-based materials. Both materials were electrochemically tested and exhibited better performance than Ni-YSZ in steam and co-electrolysis, however, lower performance than Ni-GDC.

The impedance spectra recorded at OCV as a function of temperature were analyzed with an ECM composed of an inductor, a serial resistance and four RQ elements, which were attributed to the four processes P1, P2, P3, and P4. The pro-

cesses P1 and P2 are thermally activated processes attributed to the LSCF oxygen electrode charge transfer (P1, 2000 - 900 Hz) and surface exchange processes (P2, 400 - 100 Hz). The mid to low-frequency process P3 (100 - 10 Hz) is related to the fuel and oxygen electrode with assigned to the adsorption and diffusion processes and transport processes of the fuel and oxygen electrode overlapping in this frequency region. The process P4 (2 - 0.1 Hz) has been identified as the rate-limiting step in steam- and co-electrolysis. The observed activation energies and the impact of polarization on this process lead to the assignment of P4 to the fuel electrode charge transfer process. A long-term degradation test was carried out in the gas mixtures 50% H_2O and 50% H_2 at -0.3 A $\cdot$ cm^{-2} and 900 °C for 500 h. The post-test microstructural analysis showed destabilization of the SFM fuel electrode in comparison to the stable SFM-GDC phase.

The influence of doping was investigated through synthesis of the double perovskite $Sr_2FeMo_{0.65}M_{0.65}O_{6-\delta}$ with M = Ti, Co, Cu, Mn, and Ni. B-site doping showed an increased conductivity in oxidizing and reducing atmospheres up to, e.g. 152 S $\cdot$ cm^{-1} at 650 °C for $Sr_2FeMo_{0.65}Cu_{0.65}O_{6-\delta}$-GDC, which is explained by the exsolution of e.g. bimetallic Fe-Cu alloy nanoparticles as seen in XPS measurements. The exsoluted particles were also observed in the SEM and TEM for $Sr_2FeMo_{0.65}Ni_{0.65}O_{6-\delta}$. Current densities of -1.62 A $\cdot$ cm^{-2} and -1.74 A $\cdot$ cm^{-2} were obtained for $Sr_2FeMo_{0.65}Ni_{0.65}O_{6-\delta}$ in steam and co-electrolysis conditions, which are higher than observed for Ni-GDC (up to 21%) and Ni-YSZ (up to 44%). However, the durability test at -0.5 A $\cdot$ cm^{-2} revealed an high degradation rate after 200 h with significant performance loss after 500 h of around 59%. The origin of degradation was shown to be an unstable SFM microstructure in humidified conditions, which led to particle agglomeration and electrode densification.

To investigate the impact of fuel gas, the SFM-based fuel electrode materials were tested in CO_2 electrolysis conditions with an atmosphere of 80% CO_2 + 20% CO at 900 °C between current densities of -0.3 A $\cdot$ cm^{-2} and -0.5 A $\cdot$ cm^{-2} for up to 1000 h. The obtained current densities in CO_2 electrolysis at 1.5 V underlined that $Sr_2FeMoO_{6-\delta}$ and $Sr_2FeMoO_{6-\delta}$-GDC perform better than Ni-YSZ by around 63 - 76%. The performance of $Sr_2Fe_{1.5}Mo_{0.5}O_{6-\delta}$ and $Sr_2Fe_{1.5}Mo_{0.5}O_{6-\delta}$-GDC was comparable to Ni-GDC and up to 95% higher than for Ni-YSZ. The highest current density with -1.28 A $\cdot$ cm^{-2} was exhibited by $Sr_2FeMo_{0.65}Ni_{0.65}O_{6-\delta}$ at 900 °C, which is around 10% higher than current densities of Ni-GDC and 103% higher than observed for Ni-YSZ.

Long-term stability tests were performed for up to 1000 h in 80% CO_2 + 20% CO atmosphere at 900 °C to investigate the performance stability of the cells in non-

humidified conditions. The variation of cell potential with time for $Sr_2FeMoO_{6-\delta}$-GDC remained stable up to 300 h, after which the potential increased slightly and a total degradation rate of 7 $mV \cdot kh^{-1}$ was observed.

The long-term stability of the high performing $Sr_2FeMo_{0.65}Ni_{0.65}O_{6-\delta}$ fuel electrode material was investigated at -0.5 $A \cdot cm^{-2}$ and exhibited decreasing cell potential in the first 200 h. Thereafter, the degradation rate remained stable until 1000 h measurement time. The observed decreasing cell potential corresponds to a minimal increased current density during the durability test, which points to an activation process of the fuel electrode during the electrolysis reaction. The origin of this activation could be due to the microstructural changes at the fuel electrode or the SFM/GDC interface. The microstructural analysis showed that after CO_2 electrolysis, no Sr segregation was observed in contrast to the durability test in steam electrolysis. Future investigations should focus specifically on the long-term performance of the B-site doped $Sr_2FeMo_{0.65}M_{0.65}O_{6-\delta}$ with M = Cu, Co, Ti, and Mn fuel electrode materials in CO_2 electrolysis to analyze the best performing and highest durable material. An additional research interest could be to introduce A-site deficiency in the $Sr_2Fe_{2-x}Mo_xO_{6-\delta}$ materials. It has been observed that this could significantly advance in-situ nanoparticle formation at the perovskite surface.

Bibliography

[1] S. E. Wolf, L. Dittrich, M. Nohl, S. Foit, I. Vinke, L. G. J. de Haart, R.-A. Eichel, *ECS Trans.* **2021**, *103*, 493–500.

[2] S. E. Wolf, V. Vibhu, E. Tröster, I. C. Vinke, R.-A. Eichel, L. G. J. de Haart, *Energies* **2022**, *15*, 5449.

[3] S. E. Wolf, L. Dittrich, M. Nohl, T. Duyster, I. C. Vinke, R.-A. Eichel, L. G. J. de Haart, *J. Electrochem. Soc.* **2022**, *169*, 034531.

[4] S. E. Wolf, V. Vibhu, C. L. Coll, N. Eyckeler, I. C. Vinke, R.-A. Eichel, L. G. J. de Haart, *ECS Trans.* **2023**, *111*, 2119–2130.

[5] S. E. Wolf, F. E. Winterhalder, V. Vibhu, L. G. J. de Haart, O. Guillon, R.-A. Eichel, N. H. Menzler, *J. Mater. Chem. A* **2023**, *11*, 17977–18028.

[6] S. E. Wolf, V. Vibhu, P. K. Chakraborty, S. Basak, I. C. Vinke, L. de Haart, R.-A. Eichel, *Electrochem. Commun.* **2024**, *167*, 107799.

[7] S. R. Foit, I. C. Vinke, L. G. J. de Haart, R.-A. Eichel, *Angew. Chem. Int. Ed.* **2017**, *56*, 5402–5411.

[8] C. Graves, S. D. Ebbesen, M. Mogensen, K. S. Lackner, *Renewable Sustainable Energy Rev.* **2011**, *15*, 1–23.

[9] M. P. Hoerlein, M. Riegraf, R. Costa, G. Schiller, K. A. Friedrich, *Electrochim. Acta* **2018**, *276*, 162–175.

[10] F. Monaco, M. Hubert, J. Vulliet, J. P. Ouweltjes, D. Montinaro, P. Cloetens, P. Piccardo, F. Lefebvre-Joud, J. Laurencin, *J. Electrochem. Soc.* **2019**, *166*, F1229–F1242.

[11] M. Trini, A. Hauch, S. de Angelis, X. Tong, P. V. Hendriksen, M. Chen, *J. Power Sources* **2020**, *450*, 227599.

[12] X. Sun, Y. Liu, P. V. Hendriksen, M. Chen, *J. Power Sources* **2021**, *506*, 230136.

[13] Q. Qin, K. Xie, H. Wei, W. Qi, J. Cui, Y. Wu, *RSC Adv.* **2014**, *4*, 38474–38483.

[14] R. Xing, Y. Wang, S. Liu, C. Jin, *J. Power Sources* **2012**, *208*, 276–281.

[15] B. Ge, J. Sheng, Y. Zhuang, J. Ma, Z. Yang, C. Li, S. Peng, *Mater. Res. Express* **2020**, *7*.

[16] L. Bernadet, C. Moncasi, M. Torrell, A. Tarancón, *Int. J. Hydrog. Energy* **2020**, *45*, 14208–14217.

[17] Y. Wang, T. Liu, M. Li, C. Xia, B. Zhou, F. Chen, *J. Mater. Chem. A* **2016**, *4*, 14163–14169.

[18] G. Xiao, Q. Liu, F. Zhao, L. Zhang, C. Xia, F. Chen, *J. Electrochem. Soc.* **2011**, *158*, B455.

[19] Y. Guo, T. Guo, S. Zhou, Y. Wu, H. Chen, X. Ou, Y. Ling, *Ceram. Int.* **2019**, *45*, 10969–10975.

[20] J. Gao, X. Meng, T. Luo, H. Wu, Z. Zhan, *Int. J. Hydrogen Energy* **2017**, *42*, 18499–18503.

[21] Q. Liu, D. E. Bugaris, G. Xiao, M. Chmara, S. Ma, H.-C. zur Loye, M. D. Amiridis, F. Chen, *J. Power Sources* **2011**, *196*, 9148–9153.

[22] J. Artz, T. E. Müller, K. Thenert, J. Kleinekorte, R. Meys, A. Sternberg, A. Bardow, W. Leitner, *Chem. Rev.* **2018**, *118*, 434–504.

[23] R. Schlögl, *ChemSusChem* **2010**, *3*, 209–222.

[24] R. Franke, D. Selent, A. Börner, *Chem. Rev.* **2012**, *112*, 5675–5732.

[25] W. Doenitz, R. Schmidberger, E. Steinheil, R. Streicher, *Int. J. Hydrog. Energy* **1980**, *5*, 55–63.

[26] S. Badwal, *Solid State Ionics* **2001**, *143*, 39–46.

[27] C. Lenser, D. Udomsilp, N. H. Menzler, P. Holtappels, T. Fujisaki, L. Kwati, H. Matsumoto, A. G. Sabato, F. Smeacetto, A. Chrysanthou, S. Molin in *Advanced Ceramics for Energy Conversion and Storage*, Elsevier, **2020**, pp. 387–547.

[28] L. Wehrle, D. Schmider, J. Dailly, A. Banerjee, O. Deutschmann, *Appl. Energy* **2022**, *317*, 119143.

[29] D. Sarantaridis, A. Atkinson, *Fuel Cells* **2007**, *7*, 246–258.

[30] N. Q. Minh in *High-Temperature Solid Oxide Fuel Cells for the 21st Century*, Elsevier, **2016**, pp. 255–282.

[31] Christian Walter, Oliver Posdziech, Matthias Boltze in EFCF 2022 Proceedings of the Conference, (Eds.: Olivier Bucheli, Gabriela Geisser, Fiona Moore, Dr. Michael Spirig), **2022**, A0501.

[32] M. C. Tucker, *J. Power Sources* **2010**, *195*, 4570–4582.

[33] B. Zhu, I. Albinsson, C. Andersson, K. Borsand, M. Nilsson, B.-E. Mellander, *Electrochem. Commun.* **2006**, *8*, 495–498.

[34] N. Mahato, A. Banerjee, A. Gupta, S. Omar, K. Balani, *Prog. Mater Sci.* **2015**, *72*, 141–337.

[35] A. J. Jacobson, *Chem. Mater.* **2010**, *22*, 660–674.

[36] Q. Fang, L. Blum, N. H. Menzler, *J. Electrochem. Soc.* **2015**, *162*, F907–F912.

[37] R. Peters, M. Frank, W. Tiedemann, I. Hoven, R. Deja, N. Kruse, Q. Fang, L. Blum, R. Peters, *J. Electrochem. Soc.* **2021**, *168*, 014508.

[38] S. D. Ebbesen, J. Høgh, K. A. Nielsen, J. U. Nielsen, M. Mogensen, *Int. J. Hydrogen Energy* **2011**, *36*, 7363–7373.

[39] M. Riedel, M. P. Heddrich, K. A. Friedrich, *Fuel Cells* **2020**, *20*, 592–607.

[40] N. Q. Minh, *J. American Ceramic Society* **1993**, *76*, 563–588.

[41] V. V. Kharton, A. P. Viskup, A. V. Kovalevsky, E. N. Naumovich, F. Marques, *Solid State Ionics* **2001**, *143*, 337–353.

[42] J. Zhang, C. Lenser, N. Russner, A. Weber, N. H. Menzler, O. Guillon, *J. Am. Chem. Soc.* **2023**, *106*, 93–99.

[43] S. Aruna, M. Muthuraman, K. Patil, *Solid State Ionics* **1998**, *111*, 45–51.

[44] D. W. Dees, T. D. Claar, T. E. Easler, D. C. Fee, F. C. Mrazek, *J. Electrochem. Soc.* **1987**, *134*, 2141.

[45] V. N. Nguyen, Q. Fang, U. Packbier, L. Blum, *Int. J. Hydrog. Energy* **2013**, *38*, 4281–4290.

[46] A. Hauch, S. D. Ebbesen, S. H. Jensen, M. Mogensen, *J. Electrochem. Soc.* **2008**, *155*, B1184.

[47] M. Trini, P. S. Jørgensen, A. Hauch, J. J. Bentzen, P. V. Hendriksen, M. Chen, *J. Electrochem. Soc.* **2019**, *166*, F158–F167.

[48] S. D. Ebbesen, X. Sun, M. B. Mogensen, *Faraday Discuss.* **2015**, *182*, 393–422.

[49] Y. Wang, W. Li, L. Ma, W. Li, X. Liu, *J. Mater. Sci. Technol.* **2020**, *55*, 35–55.

[50] P. Moçoteguy, A. Brisse, *Int. J. Hydrogen Energy* **2013**, *38*, 15887–15902.

[51] M. B. Mogensen, M. Chen, H. L. Frandsen, C. Graves, A. Hauch, P. V. Hendriksen, T. Jacobsen, S. H. Jensen, T. L. Skafte, X. Sun, *Fuel Cells* **2021**, *21*, 415–429.

[52] S. He, S. P. Jiang, *Prog. Nat. Sci.: Mater. Int.* **2021**, *31*, 341–372.

[53] M. H. Pihlatie, A. Kaiser, M. Mogensen, M. Chen, *Solid State Ionics* **2011**, *189*, 82–90.

[54] C. E. Frey, Q. Fang, D. Sebold, L. Blum, N. H. Menzler, *J. Electrochem. Soc.* **2018**, *165*, F357–F364.

[55] F. Tietz, D. Sebold, A. Brisse, J. Schefold, *J. Power Sources* **2013**, *223*, 129–135.

[56] J. Zhou, L. Xu, C. Ding, C. Wei, Z. Tao, *Mater. Lett.* **2019**, *257*, 126758.

[57] P. Qiu, S. Sun, J. Li, L. Jia, *Sep. Purif. Technol.* **2022**, *298*, 121581.

[58] C. Li, Y. Deng, L. Yang, B. Liu, D. Yan, L. Fan, J. Li, L. Jia, *Adv. Powder Mater.* **2023**, *2*, 100133.

[59] R. Das, R. Choudhary, D. Pradhan, *Mater. Sci. Eng. B* **2022**, *281*, 115715.

[60] D. A. Osinkin, A. A. Kolchugin, N. M. Bogdanovich, S. M. Beresnev, *Electrochim. Acta* **2020**, *361*, 137058.

[61] G. King, P. M. Woodward, *J. Mater. Chem.* **2010**, *20*, 5785.

[62] C. Meneghini, S. Ray, F. Liscio, F. Bardelli, S. Mobilio, D. D. Sarma, *Phys. Rev. Lett.* **2009**, *103*, 046403.

[63] D. Serrate, J. M. de Teresa, M. R. Ibarra, *J. Phys.: Condens. Matter* **2007**, *19*, 023201.

[64] A. A. Markov, I. A. Leonidov, M. V. Patrakeev, V. L. Kozhevnikov, O. A. Savinskaya, U. V. Ancharova, A. P. Nemudry, *Solid State Ionics* **2008**, *179*, 1050–1053.

[65] O. Savinskaya, A. P. Nemudry, *J. Solid State Electrochem.* **2011**, *15*, 269–275.

[66] G. Y. Liu, G. H. Rao, X. M. Feng, H. F. Yang, Z. W. Ouyang, W. F. Liu, J. K. Liang, *J. Alloys Compd.* **2003**, *353*, 42–47.

[67] G. Xiao, Q. Liu, X. Dong, K. Huang, F. Chen, *J. Power Sources* **2010**, *195*, 8071–8074.

[68] L. Zhang, Q. Zhou, Q. He, T. He, *J. Power Sources* **2010**, *195*, 6356–6366.

[69] Q. Liu, X. Dong, G. Xiao, F. Zhao, F. Chen, *Adv. Mater.* **2010**, *22*, 5478–5482.

[70] J. Rager, M. Zipperle, A. Sharma, J. L. MacManus-Driscoll, *J. Am. Ceram. Soc.* **2004**, *87*, 1330–1335.

[71] A. B. Muñoz-García, D. E. Bugaris, M. Pavone, J. P. Hodges, A. Huq, F. Chen, H.-C. zur Loye, E. A. Carter, *J. Am. Chem. Soc.* **2012**, *134*, 6826–6833.

[72] B. He, L. Zhao, S. Song, T. Liu, F. Chen, C. Xia, *J. Electrochem. Soc.* **2012**, *159*, B619–B626.

[73] Y. Wang, T. Liu, S. Fang, F. Chen, *J. Power Sources* **2016**, *305*, 240–248.

[74] K. Momma, F. Izumi, *J. Appl. Crystallogr.* **2011**, *44*, 1272–1276.

[75] S. Jiang, *Solid State Ionics* **2002**, *146*, 1–22.

[76] S. T. Aruna, M. Muthuraman, K. C. Patil, *J. Mater. Chem.* **1997**, *7*, 2499–2503.

[77] F. Tietz, I. Arulraj, M. Zahid, D. Stover, *Solid State Ionics* **2006**, *177*, 1753–1756.

[78] I. Yasuda, K. Ogasawara, M. Hishinuma, T. Kawada, M. Dokiya, *Solid State Ionics* **1996**, *86-88*, 1197–1201.

[79] A. Petric, *Solid State Ionics* **2000**, *135*, 719–725.

[80] H. Ullmann, N. Trofimenko, F. Tietz, D. Stöver, A. Ahmad-Khanlou, *Solid State Ionics* **2000**, *138*, 79–90.

[81] T. Jacobsen, M. Mogensen, *ECS Trans.* **2008**, *13*, 259–273.

[82] S. P. Jiang, *Int. J. Hydrogen Energy* **2019**, *44*, 7448–7493.

[83] H. Wang, S. A. Barnett, *J. Electrochem. Soc.* **2018**, *165*, F564–F570.

[84] V. Vibhu, I. C. Vinke, F. Zaravelis, S. G. Neophytides, D. K. Niakolas, R.-A. Eichel, L. G. J. de Haart, *Energies* **2022**, *15*, 2726.

[85] P. Hjalmarsson, M. Søgaard, M. Mogensen, *Solid State Ionics* **2008**, *179*, 1422–1426.

[86] Z. Lu, S. Darvish, J. Hardy, J. Templeton, J. Stevenson, Y. Zhong, *J. Electrochem. Soc.* **2017**, *164*, F3097–F3103.

[87] S. P. Simner, M. D. Anderson, M. H. Engelhard, J. W. Stevenson, *Electrochem. Solid-State Lett.* **2006**, *9*, A478.

[88] V. M. Janardhanan, O. Deutschmann, *Z. Phys. Chem.* **2007**, *221*, 443–478.

[89] H. Vogt, *J. Electrochem. Soc.* **1990**, *137*, 1179–1184.

[90] T. Kuwabara, P. Kurzweil in *Encyclopedia of electrochemical power sources*, (Ed.: J. Garche), Elsevier, Amsterdam, **2009**, pp. 548–556.

[91] R. P. O'Hayre, F. B. Prinz, S.-W. Cha, W. G. Colella, *Fuel cell fundamentals*, Third edition, Wiley, Hoboken, **2016**.

[92] *Impedance spectroscopy: Theory, experiment, and applications*, Third edition, (Eds.: E. Barsoukov, J. R. Macdonald), Wiley, Hoboken, NJ, **2018**.

[93] M. E. Orazem, B. Tribollet, *Electrochemical impedance spectroscopy*, Second edition, Wiley, Hoboken, New Jersey, **2017**.

[94] S. Wang, J. Zhang, O. Gharbi, V. Vivier, M. Gao, M. E. Orazem, *Nat. Rev. Methods Primers* **2021**, *1*.

[95] A. C. Lazanas, M. I. Prodromidis, *ACS Meas. Sci. Au* **2023**, *3*, 162–193.

[96] T. H. Wan, M. Saccoccio, C. Chen, F. Ciucci, *Electrochim. Acta* **2015**, *184*, 483–499.

[97] M. A. Danzer, *Batteries* **2019**, *5*, 53.

[98] M. Nohl, G. Raut, S. E. Wolf, T. Duyster, L. Dittrich, I. C. Vinke, R.-A. Eichel, L. G. J. de Haart, *ECS Trans.* **2021**, *103*, 1403–1412.

[99] J. Weese, *Comput. Phys. Commun.* **1992**, *69*, 99–111.

[100] A. N. Tichonov, V. J. Arsenin, *Solutions of ill-posed problems*, Winston and Wiley, Washington, D.C. and New York, NY, **1977**.

[101] N. Schlüter, S. Ernst, U. Schröder, *ChemElectroChem.* **2019**, *6*, 6027–6037.

[102] A. Lasia, *Electrochemical Impedance Spectroscopy and its Applications*, Springer New York, New York, NY, **2014**.

[103] L. Nyikos, T. Pajkossy, *Electrochim. Acta* **1985**, *30*, 1533–1540.

[104] Z. Kerner, T. Pajkossy, *J. Electroanal. Chem.* **1998**, *448*, 139–142.

[105] R. E. White, *Modern Aspects of Electrochemistry*, Springer, New York, NY, **2002**.

[106] A. Lasia, *J. Electroanal. Chem.* **1995**, *397*, 27–33.

[107] C. Hitz, A. Lasia, *J. Electroanal. Chem.* **2001**, *500*, 213–222.

[108] C. A. Schiller, W. Strunz, *Electrochim. Acta* **2001**, *46*, 3619–3625.

[109] J. Newman, *J. Electrochem. Soc.* **1970**, *117*, 198.

[110] K. Nisanciolu, J. Newman, *J. Electrochem. Soc.* **1974**, *121*, 523.

[111] M. Durbha, M. E. Orazem, B. Tribollet, *J. Electrochem. Soc.* **1999**, *146*, 2199–2208.

[112] M. N. Kakaei, J. Neshati, A. R. Rezaierod, *Prot. Met. Phys. Chem.* **2018**, *54*, 548–556.

[113] J.-B. Jorcin, M. E. Orazem, N. Pébère, B. Tribollet, *Electrochim. Acta* **2006**, *51*, 1473–1479.

[114] P. Zoltowski, *J. Electroanal. Chem.* **1998**, *443*, 149–154.

[115] J. R. Macdonald, *Ann. Biomed. Eng.* **1992**, *20*, 289–305.

[116] P. Courty, H. Ajot, C. Marcilly, B. Delmon, *Powder Technol.* **1973**, *7*, 21–38.

[117] N. Eyckeler, Bachelor Thesis, RWTH Aachen University, **2022**.

[118] C. L. Coll, Bachelor Thesis, Technical University of Berlin, **2023**.

[119] M. Hahn, S. Schindler, L.-C. Triebs, M. A. Danzer, *Batteries* **2019**, *5*, 43.

[120] E. Tröster, Bachelor Thesis, Reutlingen University, **2021**.

[121] J. Schefold, A. Brisse, H. Poepke, *Int. J. Hydrogen Energy* **2017**, *42*, 13415–13426.

[122] J. Schefold, H. Poepke, A. Brisse, *ECS Trans.* **2020**, *97*, 553–563.

[123] K. Chen, S. P. Jiang, *J. Electrochem. Soc.* **2016**, *163*, F3070–F3083.

[124] M. Rao, X. Sun, A. Hagen, *J. Electrochem. Soc.* **2018**, *165*, F748–F755.

[125] Jerôme Aicart, PhD Thesis, Université de Grenoble, **2014**.

[126] K. Lillmaa, M. Maide, R. Kanarbik, G. Nurk, E. Lust, *J. Electrochem. Soc.* **2016**, *163*, F3190–F3196.

[127] Y. Tao, S. D. Ebbesen, M. B. Mogensen, *J. Power Sources* **2016**, *328*, 452–462.

[128] A. Leonide, Doktorarbeit, Universität Karlsruhe, **10.02.2010**.

[129] V. Sonn, A. Leonide, E. Ivers-Tiffée, *J. Electrochem. Soc.* **2008**, *155*, B675.

[130] A. Momma, T. Kato, Y. Kaga, S. Nagata, *J. Ceram. Soc. Japan* **1997**, *105*, 369–373.

[131] V. Brichzin, *Solid State Ionics* **2002**, *152-153*, 499–507.

[132] R. Knibbe, M. L. Traulsen, A. Hauch, S. D. Ebbesen, M. Mogensen, *J. Electrochem. Soc.* **2010**, *157*, B1209.

[133] A. Leonide, V. Sonn, A. Weber, E. Ivers-Tiffée, *J. Electrochem. Soc.* **2008**, *155*, B36.

[134] C. Graves, S. D. Ebbesen, M. Mogensen, *Solid State Ion.* **2011**, *192*, 398–403.

[135] K. Chen, S. P. Jiang, *Int. J. Hydrogen Energy* **2011**, *36*, 10541–10549.

[136] J. Kim, H.-I. Ji, H. P. Dasari, D. Shin, H. Song, J.-H. Lee, B.-K. Kim, H.-J. Je, H.-W. Lee, K. J. Yoon, *Int. J. Hydrogen Energy* **2013**, *38*, 1225–1235.

[137] J. R. Mawdsley, J. David Carter, A. Jeremy Kropf, B. Yildiz, V. A. Maroni, *Int. J. Hydrogen Energy* **2009**, *34*, 4198–4207.

[138] S. J. Kim, G. M. Choi, *Solid State Ionics* **2014**, *262*, 303–306.

[139] X. Sun, P. V. Hendriksen, M. B. Mogensen, M. Chen, *Fuel Cells* **2019**, *19*, 740–747.

[140] P. Hjalmarsson, X. Sun, Y.-L. Liu, M. Chen, *J. Power Sources* **2014**, *262*, 316–322.

[141] E. Lay-Grindler, J. Laurencin, J. Villanova, P. Cloetens, P. Bleuet, A. Mansuy, J. Mougin, G. Delette, *J. Power Sources* **2014**, *269*, 927–936.

[142] D. The, S. Grieshammer, M. Schroeder, M. Martin, M. Al Daroukh, F. Tietz, J. Schefold, A. Brisse, *J. Power Sources* **2015**, *275*, 901–911.

[143] G. Miao, C. Yuan, T. Chen, Y. Zhou, W. Zhan, S. Wang, *Int. J. Hydrogen Energy* **2016**, *41*, 1104–1111.

[144] O. A. Savinskaya, A. P. Nemudry, A. N. Nadeev, S. V. Tsybulya, N. Z. Lyakhov, *Bull. Russ. Acad. Sci. Phys.* **2010**, *74*, 1053–1054.

[145] G. M. Veith, M. Greenblatt, M. Croft, K. V. Ramanujachary, J. Hattrick-Simpers, S. E. Lofland, I. Nowik, *Chem. Mater.* **2005**, *17*, 2562–2567.

[146] F. Sher, A. J. Williams, A. Venimadhev, M. G. Blamire, J. P. Attfield, *Chem. Mater.* **2005**, *17*, 1792–1796.

[147] Y. Jiang, Y. Yang, C. Xia, H. J. M. Bouwmeester, *J. Mater. Chem. A* **2019**, *7*, 22939–22949.

[148] Z. Du, H. Zhao, S. Yi, Q. Xia, Y. Gong, Y. Zhang, X. Cheng, Y. Li, L. Gu, K. Świerczek, *ACS nano* **2016**, *10*, 8660–8669.

[149] X. Xi, Y. Fan, J. Zhang, J.-L. Luo, X.-Z. Fu, *J. Mater. Chem. A* **2022**, *10*, 2509–2518.

[150] Z. Sun, C. Hao, S. Toan, R. Zhang, H. Li, Y. Wu, H. Liu, Z. Sun, *J. Mater. Chem. A* **2023**, *11*, 17961–17976.

[151] J. Mei, T. Liao, Z. Sun, *Mater. Today Energy* **2023**, *31*, 101216.

[152] J. Irvine, D. Neagu, M. C. Verbraeken, C. Chatzichristodoulou, C. Graves, M. B. Mogensen, *Nat. Energy* **2016**, *1*, 15014.

[153] D. Neagu, G. Tsekouras, D. N. Miller, H. Ménard, J. T. S. Irvine, *Nat. Chem.* **2013**, *5*, 916–923.

[154] D. Neagu, T. S. Oh, D. N. Miller, H. Menard, S. M. Bukhari, S. R. Gamble, R. J. Gorte, J. M. Vohs, J. T. S. Irvine, *Nat. Commun.* **2015**, *6*, 8120.

[155] Y. Li, W. Zhang, Y. Zheng, J. Chen, B. Yu, Y. Chen, M. Liu, *Chem. Soc. Rev.* **2017**, *46*, 6345–6378.

[156] O. Kwon, S. Sengodan, K. Kim, G. Kim, H. Y. Jeong, J. Shin, Y.-W. Ju, J. W. Han, G. Kim, *Nat. Commun.* **2017**, *8*, 15967.

[157] O. Kwon, K. Kim, S. Joo, H. Y. Jeong, J. Shin, J. W. Han, S. Sengodan, G. Kim, *J. Mater. Chem. A* **2018**, *6*, 15947–15953.

[158] X. Xi, X.-W. Wang, Y. Fan, Q. Wang, Y. Lu, J. Li, L. Shao, J.-L. Luo, X.-Z. Fu, *J. Power Sources* **2021**, *482*, 228981.

[159] F. Song, K. Schenk, X. Hu, *Energy Environ. Sci.* **2016**, *9*, 473–477.

[160] M. Shao, B. H. Smith, S. Guerrero, L. Protsailo, D. Su, K. Kaneko, J. H. Odell, M. P. Humbert, K. Sasaki, J. Marzullo, R. M. Darling, *Phys. Chem. Chem. Phys.* **2013**, *15*, 15078–15090.

[161] C. Zhao, Y. Li, W. Zhang, Y. Zheng, X. Lou, B. Yu, J. Chen, Y. Chen, M. Liu, J. Wang, *Energy Environ. Sci.* **2020**, *13*, 53–85.

[162] M. L. Weber, M. Wilhelm, L. Jin, U. Breuer, R. Dittmann, R. Waser, O. Guillon, C. Lenser, F. Gunkel, *ACS nano* **2021**, *15*, 4546–4560.

[163] Y. Li, B. Hu, C. Xia, W. Q. Xu, J. P. Lemmon, F. Chen, *J. Mater. Chem. A* **2017**, *5*, 20833–20842.

[164] S. Hou, K. Xie, *Electrochim. Acta* **2019**, *301*, 63–68.

[165] Y. S. Chung, T. Kim, T. H. Shin, H. Yoon, S. Park, N. M. Sammes, W. B. Kim, J. S. Chung, *J. Mater. Chem. A* **2017**, *5*, 6437–6446.

[166] F. Tietz, *Ionics* **1999**, *5*, 129–139.

[167] F. Tietz, I. A. Raj, M. Zahid, A. Mai, D. Stöver, *Prog. Solid State Chem.* **2007**, *35*, 539–543.

[168] J. Feng, G. Yang, N. Dai, Z. Wang, W. Sun, D. Rooney, J. Qiao, K. Sun, *J. Mater. Chem. A* **2014**, *2*, 17628–17634.

[169] G. Xiao, C. Jin, Q. Liu, A. Heyden, F. Chen, *J. Power Sources* **2012**, *201*, 43–48.

[170] Y. Li, X. Chen, Y. Yang, Y. Jiang, C. Xia, *ACS Sustainable Chem. Eng.* **2017**, *5*, 11403–11412.

[171] M. Patrakeev, I. Leonidov, V. Kozhevnikov, V. Kharton, *Solid State Sci.* **2004**, *6*, 907–913.

[172] M. Retuerto, F. Jiménez-Villacorta, M. J. Martínez-Lope, Y. Huttel, E. Roman, M. T. Fernández-Díaz, J. A. Alonso, *Phys. Chem. Chem. Phys.* **2010**, *12*, 13616.

[173] B. Steele, *Solid State Ionics* **2000**, *129*, 95–110.

[174] A. Nenning, M. Holzmann, J. Fleig, A. K. Opitz, *Mater. Adv.* **2021**, *2*, 5422–5431.

[175] J. Paier, C. Penschke, J. Sauer, *Chem. Rev.* **2013**, *113*, 3949–3985.

[176] G. Kim, G. Corre, J. T. S. Irvine, J. M. Vohs, R. J. Gorte, *Electrochem. Solid-State Lett.* **2008**, *11*, B16.

[177] Y.-H. Huang, R. I. Dass, J. C. Denyszyn, J. B. Goodenough, *J. Electrochem. Soc.* **2006**, *153*, A1266.

[178] B. Ge, J. T. Ma, D. Ai, C. Deng, X. Lin, J. Xu, *Electrochim. Acta* **2015**, *151*, 437–446.

[179] I. D. Unachukwu, V. Vibhu, J. Uecker, I. C. Vinke, R.-A. Eichel, L. G. J. de Haart, *ECS Trans.* **2023**, *111*, 1445–1452.

[180] I. D. Unachukwu, V. Vibhu, I. C. Vinke, R.-A. Eichel, L. G. J. de Haart, *J. Power Sources* **2023**, *556*, 232436.

[181] J. Uecker, I. D. Unachukwu, V. Vibhu, I. C. Vinke, R.-A. Eichel, L. G. J. de Haart, *Electrochim. Acta* **2023**, *452*, 142320.

[182] I. D. Unachukwu, V. Vibhu, J. Uecker, I. C. Vinke, R.-A. Eichel, L. G. J. de Haart, *J. CO2 Util.* **2023**, *69*, 102423.

[183] F. Kundracik, M. Hartmanová, J. Müllerová, M. Jergel, I. Kostič, R. Tucoulou, *Mater. Sci. Eng. B* **2001**, *84*, 167–175.

[184] S. D. Ebbesen, M. Mogensen, *J. Power Sources* **2009**, *193*, 349–358.

[185] S. Primdahl, *Solid State Ionics* **2002**, *152-153*, 597–608.

[186] H. Lv, Le Lin, X. Zhang, D. Gao, Y. Song, Y. Zhou, Q. Liu, G. Wang, X. Bao, *J. Mater. Chem. A* **2019**, *7*, 11967–11975.

[187] X. Xi, J. Liu, W. Luo, Y. Fan, J. Zhang, J.-L. Luo, X.-Z. Fu, *Adv. Energy Mater.* **2021**, *11*, 2102845.

[188] Z. A. Feng, F. El Gabaly, X. Ye, Z.-X. Shen, W. C. Chueh, *Nat. Commun.* **2014**, *5*, 4374.

[189] M. Riegraf, R. Costa, G. Schiller, K. A. Friedrich, S. Dierickx, A. Weber, *J. Electrochem. Soc.* **2019**, *166*, F865–F872.

[190] P. Caliandro, A. Nakajo, S. Diethelm, J. van Herle, *J. Power Sources* **2019**, *436*, 226838.

[191] D. Papurello, D. Menichini, A. Lanzini, *Electrochim. Acta* **2017**, *258*, 98–109.

[192] D. G. Goodwin, H. Zhu, A. M. Colclasure, R. J. Kee, *J. Electrochem. Soc.* **2009**, *156*, B1004.

[193] S. Primdahl, Y. L. Liu, *J. Electrochem. Soc.* **2002**, *149*, A1466.

[194] A. Padinjarethil, A. Hagen, *ECS Adv.* **2023**, *2*, 024503.

[195] Y. Yang, Z. Yang, Y. Chen, F. Chen, S. Peng, *J. Electrochem. Soc.* **2019**, *166*, F109–F113.

[196] K. Szot, M. Pawelczyk, J. Herion, C. Freiburg, J. Albers, R. Waser, J. Hulliger, J. Kwapulinski, J. Dec, *Appl. Phys. A* **1996**, *62*, 335–343.

[197] Y. Chen, W. Jung, Z. Cai, J. J. Kim, H. L. Tuller, B. Yildiz, *Energy Environ. Sci.* **2012**, *5*, 7979.

[198] H.-Y. Li, P.-C. Su, *Appl. Mater. Today* **2023**, *31*, 101769.

[199] F. Monaco, D. Ferreira-Sanchez, M. Hubert, B. Morel, D. Montinaro, D. Grolimund, J. Laurencin, *Int. J. Hydrogen Energy* **2021**, *46*, 31533–31549.

[200] H. Tu, Y. Takeda, N. Imanishi, O. Yamamoto, *Solid State Ionics* **1999**, *117*, 277–281.

[201] M. Keane, M. K. Mahapatra, A. Verma, P. Singh, *Int. J. Hydrogen Energy* **2012**, *37*, 16776–16785.

[202] Z. Pan, Q. Liu, M. Ni, R. Lyu, P. Li, S. H. Chan, *Int. J. Hydrogen Energy* **2018**, *43*, 5437–5450.

[203] H. Wang, K. J. Yakal-Kremski, T. Yeh, G. M. Rupp, A. Limbeck, J. Fleig, S. A. Barnett, *J. Electrochem. Soc.* **2016**, *163*, F581–F585.

[204] E. Lay-Grindler, J. Laurencin, J. Villanova, I. Kieffer, F. Usseglio-Viretta, T. Le Bihan, P. Bleuet, A. Mansuy, G. Delette, *ECS Trans.* **2013**, *57*, 3177–3187.

[205] *Proc. 13th Symposium on Modeling & Validation of Fuel cells*, (Eds.: G. Rinaldi, A. Nakajo, M. Hubert, D. F. Sanchez, J. Laurencin, P. Burdet, J. van Herle), ausanne, Switzer-land, **2016**.

[206] T. Matsui, M. Komoto, H. Muroyama, K. Kishida, H. Inui, K. Eguchi, *J. Power Sources* **2016**, *312*, 80–85.

[207] F. Dröge, Bachelor Thesis, RWTH Aachen University, **2023**.

[208] C. J. Powell, X-ray Photoelectron Spectroscopy Database XPS,Version 4.1, NIST Standard Reference Database 20, **1989**.

[209] A. J. Carrillo, J. M. Serra, *Catalysts* **2021**, *11*, 741.

[210] C. Arrivé, T. Delahaye, O. Joubert, G. Gauthier, *J. Power Sources* **2013**, *223*, 341–348.

[211] K. Takehira, *Catal. Surv. Asia* **2002**, *6*, 19–32.

[212] M. Hasegawa in *Treatise on Process Metallurgy*, Elsevier, **2014**, pp. 507–516.

[213] D. R. Gaskell in *Encyclopedia of Materials: Science and Technology*, Elsevier, **2001**, pp. 5481–5486.

[214] V. V. Kharton, A. V. Kovalevsky, A. P. Viskup, J. R. Jurado, F. M. Figueiredo, E. N. Naumovich, J. R. Frade, *J. Solid State Chem.* **2001**, *156*, 437–444.

[215] V. Kharton, A. Kovalevsky, E. Tsipis, A. Viskup, E. Naumovich, J. Jurado, J. Frade, *J. Electrochem. Soc.* **2002**, *7*, 30–36.

[216] R. D. Shannon, *Acta Crystallogr. Sect. A* **1976**, *32*, 751–767.

[217] E. V. Tsipis, V. V. Kharton, *J. Solid State Electrochem.* **2008**, *12*, 1039–1060.

[218] V. Gil, J. Tartaj, C. Moure, *Ceram. Int.* **2009**, *35*, 839–846.

[219] Q. X. Fu, F. Tietz, D. Stöver, *J. Electrochem. Soc.* **2006**, *153*, D74.

[220] D. Neagu, J. T. S. Irvine, *Chem. Mater.* **2010**, *22*, 5042–5053.

[221] R. Fu, P. Jiang, H. Xu, B. Niu, F. Jiang, L. Yang, T. Feng, T. He, *Int. J. Hydrogen Energy* **2019**, *44*, 31394–31405.

[222] Y. Shang, A. L. Smitshuysen, M. Yu, Y. Liu, X. Tong, P. S. Jørgensen, L. Rorato, J. Laurencin, M. Chen, *J. Mater. Chem. A* **2023**, *11*, 12245–12257.

[223] J. Uecker, I. D. Unachukwu, V. Vibhu, I. C. Vinke, L. G. J. de Haart, R.-A. Eichel, *ChemElectroChem* **2024**, DOI 10.1002/celc.202300617.

[224] L. Ye, M. Zhang, P. Huang, G. Guo, M. Hong, C. Li, J. T. S. Irvine, K. Xie, *Nat. Commun.* **2017**, *8*, 14785.

[225] Z. Zhao, M. Uddi, N. Tsvetkov, B. Yildiz, A. F. Ghoniem, *Phys. Chem. Chem. Phys.* **2017**, *19*, 25774–25785.

[226] C. Grosselindemann, N. Russner, S. Dierickx, F. Wankmüller, A. Weber, *J. Electrochem. Soc.* **2021**, *168*, 124506.

[227] S. Foit, L. Dittrich, T. Duyster, I. Vinke, R.-A. Eichel, L. G. J. de Haart, *Processes* **2020**, *8*, 1390.

[228] R. Green, C. Liu, S. Adler, *Solid State Ionics* **2008**, *179*, 647–660.

[229] A. Pandiyan, V. Kyriakou, D. Neagu, S. Welzel, A. Goede, M. C. van de Sanden, M. N. Tsampas, *J. CO2 Util.* **2022**, *57*, 101904.

[230] W. Wu, H. Ding, Y. Zhang, Y. Ding, P. Katiyar, P. K. Majumdar, T. He, D. Ding, *Adv. Sci.* **2018**, *5*, 1800360.

A. Appendix

A.1 Publications

- **Internal Biogas Reforming in Solid Oxide and Proton Conducting Fuel Cells: Progress, Challenges and Perspectives**,
  S. E. Wolf, J. Uecker, N. Eyckeler, L. Schley, L.G.J. (Bert) de Haart, V. Vibhu, and R.-A. Eichel, under review in *Journal of Physics: Energy*.
  Contribution: Conceptualization, Investigation, Writing—original draft, Writing—review & editing.

- **Electrochemical and durability characterization of novel high- temperature solid oxide electrolysis cells with SFM and SFM-GDC for hydrogen and carbon monoxide (synthesis gas) production**
  S. E. Wolf, V. Vibhu, P. K. Chakraborty, C. L. Coll, S. Basak, I.C. Vinke, L.G.J. (Bert) de Haart, and R.-A. Eichel, under review in *Journal of Materials Chemistry A*.
  Contribution: Conceptualization, Formal analysis, Investigation, Methodology, Software, Validation, Writing—original draft, Writing—review & editing.

- **Unveiling the Exsolution Mechanism and Catalytic Behavior of $Sr_2FeMo_{0.65}Ni_{0.35}O_{6-\delta}$ through In Situ Transmission Electron Microscopy**,
  P. K. Chakraborty, S. E. Wolf, S. Basak, V. Vibhu, L.G.J. (Bert) de Haart, and R.-A. Eichel, accepted in *Nano Today*.
  Contribution: Formal analysis, Investigation, Methodology, Software, Validation, Writing—original chapter draft, Writing—review & editing.

- **Alternative Elektrodenmaterialien für reversible Hochtemperatur-Festoxidelektrolysezellen**, patent application, submitted September 2023.

- **Long-Term Electrochemical Characterization of Novel $Sr_2FeMo_{0.65}Ni_{0.35}O_{6-\delta}$ Fuel Electrode for High-Temperature Steam Electrolysis in Solid Oxide Cells**,
  S. E. Wolf, V. Vibhu, P. K. Chakraborty, S. Basak, I.C. Vinke, L.G.J. (Bert) de Haart, and R.-A. Eichel
  Electrochemistry Communications, **2024**, *167*, 107799.
  Contribution: Conceptualization, Formal analysis, Investigation, Methodology, Software, Validation, Writing—original draft, Writing—review & editing.

- **Solid oxide electrolysis cells – current material development and industrial application**
  S. E. Wolf, F. E. Winterhalder, V. Vibhu, L.G.J. (Bert) de Haart, O. Guillon, R.-A. Eichel, and N. H. Menzler
  Journal of Materials Chemistry A, **2023**, *11*(34), 17977–18028.
  Contribution: Conceptualization, Investigation, Writing—original draft, Writing—review & editing.

- **Long-Term Stability of Perovskite-Based Fuel Electrode Material $Sr_2Fe_{2-x}Mo_xO_{6-\delta}$–GDC for Enhanced High- Temperature Steam- and CO_2-electrolysis**
  S. E. Wolf, V. Vibhu, C. L. Coll, N. Eyckeler, I.C. Vinke, R.-A. Eichel, and L.G.J. (Bert) de Haart
  ECS Transactions, **2023**, *111*(6), 2119–2130.
  Contribution: Conceptualization, Formal analysis, Investigation, Methodology, Software, Validation, Writing—original draft, Writing—review & editing.

- **Steam Electrolysis vs. Co-Electrolysis: Mechanistic Studies of Long-Term Solid Oxide Electrolysis Cells**
  S. E. Wolf, V. Vibhu, E. Tröster, I. C. Vinke, R.-A. Eichel, and L. G. J. (Bert) de Haart
  Energies, **2022**, *15*(15), 5449.
  Contribution: Conceptualization, Formal analysis, Investigation, Methodology, Software, Validation, Writing—original draft, Writing—review & editing.

- **Boundary Investigation of High Temperature Co-Electrolysis Towards Direct CO_2 Electrolysis**
  S. E. Wolf, L. Dittrich, M. Nohl, T. Duyster, I. C. Vinke, R.-A. Eichel, and L. G. J. (Bert) de Haart
  Journal of The Electrochemical Society, **2022**, *169*, 034531.
  Contribution: Formal analysis, Investigation, Methodology, Software, Validation, Writing—original draft, Writing—review & editing.

- **Analysis of the DRT as Evaluation Tool for EIS Data Analysis**
  M. Nohl, G. Raut, S. E. Wolf, T. Duyster, L. Dittrich, I. C. Vinke, R.-A. Eichel, and L. G. J. (Bert) de Haart
  ECS Transactions, **2021**, *103*, 1403–1412.
  Contribution: Experimental data were contributed.

- **Boundaries of High-Temperature Co-Electrolysis Towards Direct CO_2-Electrolysis**
  S. E. Wolf, L. Dittrich, M. Nohl, S.Foit, I. C. Vinke, R.-A. Eichel, and L. G. J. (Bert) de Haart
  ECS Transactions, **2021**, *103*, 493–500.
  Contribution: Formal analysis, Investigation, Methodology, Software, Validation, Writing—original draft, Writing—review & editing.

- **Forschungszentrum Jülich – Current Activities in SOC Development**
  L.G.J. (Bert) de Haart, S.B. Beale, R. Deja, L. Dittrich, T. Duyster, Q. Fang, S. Foit, S.-M. Groß-Barsnick, U. de Haart, I. Hoven, N. Kruse, C. Lenser, Q. Ma, N. Margaritis, N.H. Menzler, D. Naumenko, M. Nohl, R. Peters, D. Sebold, F Thaler, W. Tiedemann, I.D. Unachukwu, B. Varghese, V. Vibhu, I.C. Vinke, S. E. Wolf, S. Zhang, J. Zurek, and L. Blum
  ECS Transactions, **2021**, *103*, 299–305.
  Contribution: Results were contributed.

Planned Publications

- **Highly Stable $Sr_2FeMoO_{6-\delta}$-Based Fuel Electrodes for High Temperature CO_2 electrolysis in Solid Oxide Electrolysis Cells**,
  S. E. Wolf, V. Vibhu, J.-M. Bassat, L.G.J. (Bert) de Haart and R.-A. Eichel

- **Oxygen Diffusion and Surface Exchange Coefficient Measurements of Cobalt Substituted Layered Ruddlesden-Popper Nickelates $Ln_2Ni_{1-x}Co_xO_4$ (Ln = Nd, La, Pr)**,
  S. E. Wolf, V. Vibhu, J. Gamon, L.G.J. (Bert) de Haart, J.-M. Bassat, and R.-A. Eichel

A.2 Conference Contributions

- ***Presentation*** **SOC Degradation 2.0**
  S. E. Wolf, and L.G.J. (Bert) de Haart
  3. H2Giga Statustreffen, 17 September 2024, Berlin, Germany.

- ***Presentation*** **Electrochemical and Degradation Behavior of Novel Mixed $Sr_2Fe_{2-x}Mo_{x-y}M_yO_{6-\delta}$ Electrode Materials Under High-Temperature Electrolysis Conditions**

S. E. Wolf, V. Vibhu, I.C. Vinke, L.G.J. (Bert) de Haart, and R.-A. Eichel
16th European SOFC & SOE Forum, 2−5 July 2024, Lucerne, Switzerland.

- ***Poster*** **Oxygen Diffusion and Surface Exchange Coefficient Measurements of Layered Perovskite Materials**
  S. E. Wolf, V. Vibhu, J. Gamon, I.C. Vinke, L.G.J. (Bert) de Haart, J.-M. Bassat, and R.-A. Eichel
  16th European SOFC & SOE Forum, 2−5 July 2024, Lucerne, Switzerland.

- ***Presentation*** **Long-Term Stability of Perovskite-Based Fuel Electrode Material $Sr_2Fe_{2-x}Mo_xO_{6-\delta}$ – GDC for Enhanced High- Temperature Steam- and CO_2-electrolysis**
  S. E. Wolf, V. Vibhu, C. L. Coll, N. Eyckeler, I.C. Vinke, L.G.J. (Bert) de Haart, and R.-A. Eichel
  18th International Symposium on Solid Oxide Fuel Cells (SOFC-XVIII), 28 May−2 June 2023, Boston, USA.

- ***Poster*** **Time-Dependent Degradation Process Identification of Solid Oxide Electrolysis Cells**
  S. E. Wolf, E. Tröster, V. Vibhu, I. C. Vinke, R.-A. Eichel, and L.G.J. (Bert) de Haart
  15th European SOFC & SOE Forum, 5−8 July 2022, Lucerne, Switzerland.

- ***Poster*** **Process Analysis and Material Engineering for SOEC**
  S. E. Wolf, L. Dittrich, V. Vibhu, I. C. Vinke, L.G.J. (Bert) de Haart, and R.-A. Eichel
  Helmholtz Energy Young Scientists Workshop 2022, 30−31 May 2022, Frankfurt, Germany.

- ***Presentation*** **SOC Degradation 2.0 - Prolonging Reliability and Lifetime of SOCs**
  S. E. Wolf, and L.G.J. (Bert) de Haart
  5th International Workshop on Degradation Issues of Fuel Cells and Electrolysers, 3−4 May 2022, Corfu, Greece.

- ***Presentation*** **Boundaries of High-Temperature Co-Electrolysis Towards Direct CO_2-Electrolysis** S. E. Wolf, L. Dittrich, M. Nohl, S. Foit, I.C. Vinke, L.G.J. (Bert) de Haart, and R.-A. Eichel
  17th International Symposium on Solid Oxide Fuel Cells (SOFC-XVII), 18−23 July 2021, Digital Meeting.

A.3 Supplementary Results

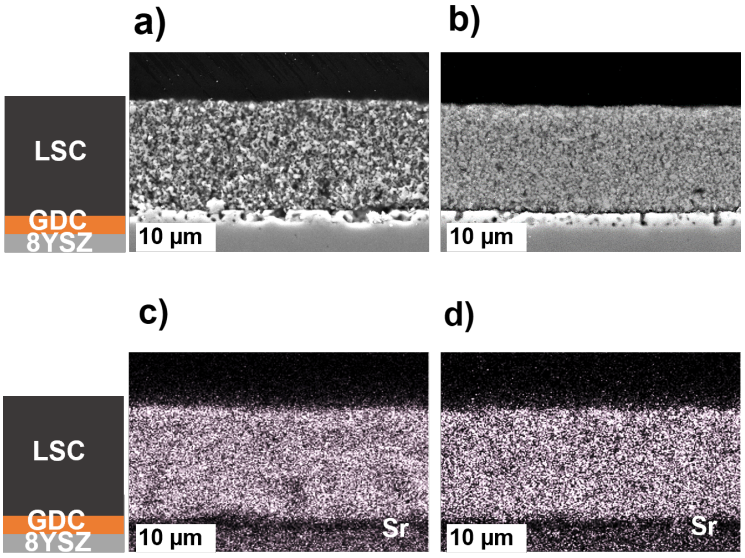

Figure A.1: SEM-EDX mapping of single cells towards oxygen electrode side for Sr (Lα, 1.81 keV) after the durability test (a, c) at 750 °C and 50% H_2O + 50% H_2 and (b, d) at 800 °C with 40% H_2O + 40% CO_2 + 20% H_2 at for 1000 h. Reproduced from[2] published under the CC BY 4.0 (http://creativecommons.org/licenses/by/4.0/).

Table A.1: Total increase of ohmic and polarization resistance after 1000 h under constant load of $-1\ A \cdot cm^{-2}$. Reproduced from[2] published under the CC BY 4.0 (http://creativecommons.org/licenses/by/4.0/).

Conditions /%	T/ °C	ΔR_Ω / $m\Omega \cdot cm^2$	ΔE / $\% \cdot h^{-1}$
50% H_2O + 50% H_2	800	370	33
50% H_2O + 50% H_2	750	259	22
40% H_2O + 40% CO_2 + 20% H_2	800	179	16

Table A.2: Relaxation processes frequency obtained by impedance spectroscopy after 1000 h with 9 $l \cdot h^{-1}$ inlet fuel consisting of 50% H_2O + 50% H_2, and 40% H_2O + 40% CO_2 + 20% H_2 at 800 °C. Reproduced from[2] published under the CC BY 4.0 (http://creativecommons.org/licenses/by/4.0/).

Process	H_2O Electrolysis / Hz	co-Electrolysis / Hz
RQ1	18600	5105
RQ2	2950	1100
RQ3	457	85
RQ4	7.9	1.9

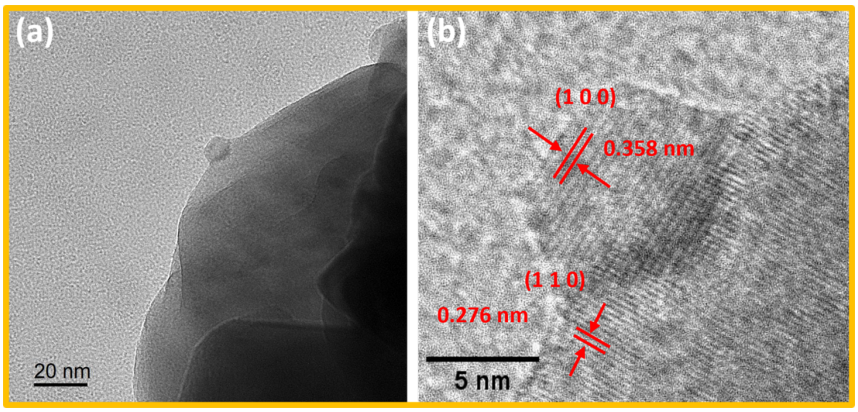

Figure A.2: (a) TEM image of reduced SFM with exsolution, (b) HRTEM lattice parameter calculations of Fe nano-exsolution and the reduced SFM substrate at higher magnification.

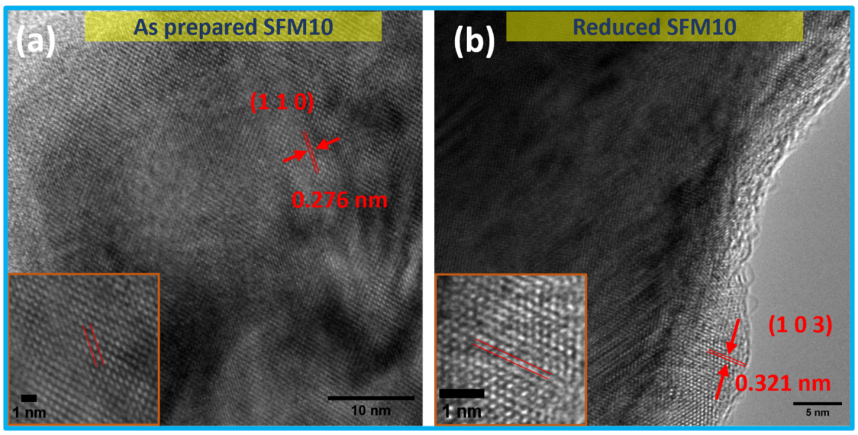

Figure A.3: HRTEM images of (a) as-prepared SFM particle with inset for lattice parameter calculations and, (b) reduced SFM particle with inset lattice parameter calculations.

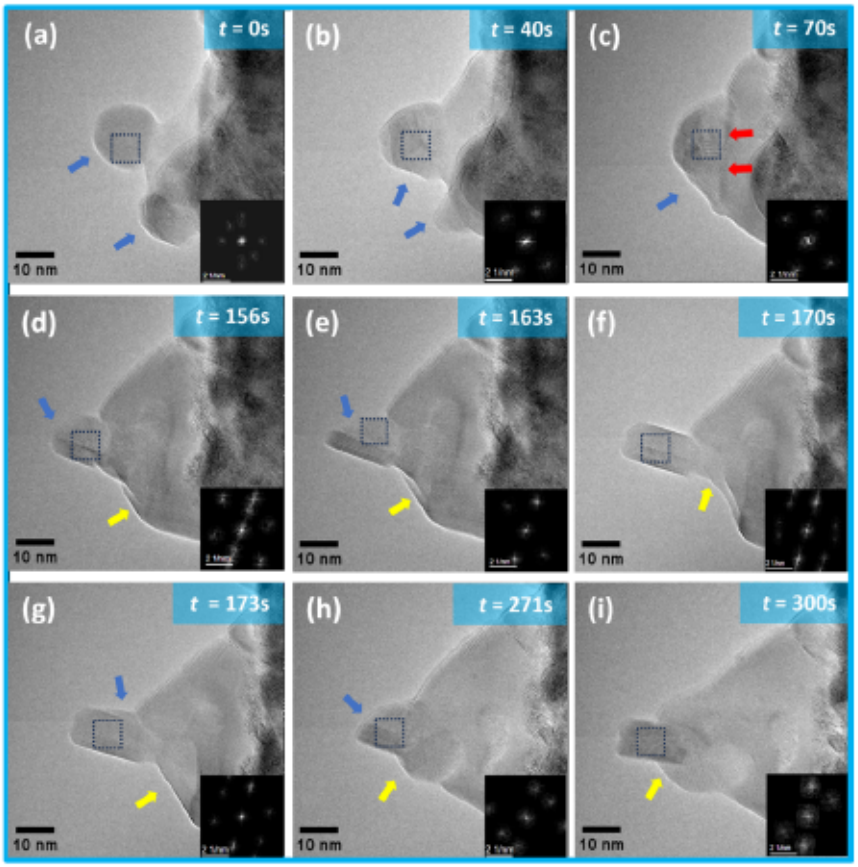

Figure A.4: (a-i) Stages of exsolution growth of an as-prepared SFM particle under reducing conditions as seen through in-situ TEM.

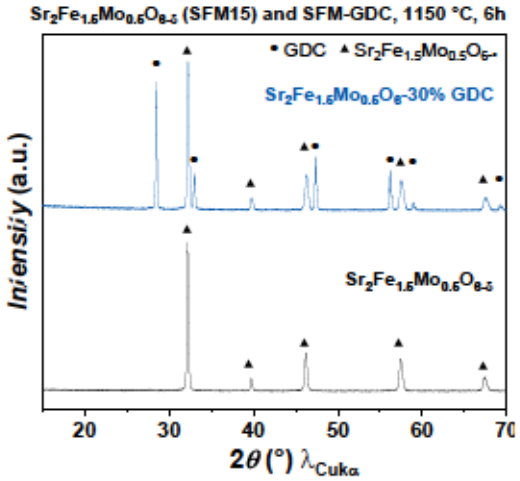

Figure A.5: X-Ray Diffraction pattern of SFM and SFM-GDC after sintering in air for 6 h at 1150 °C.

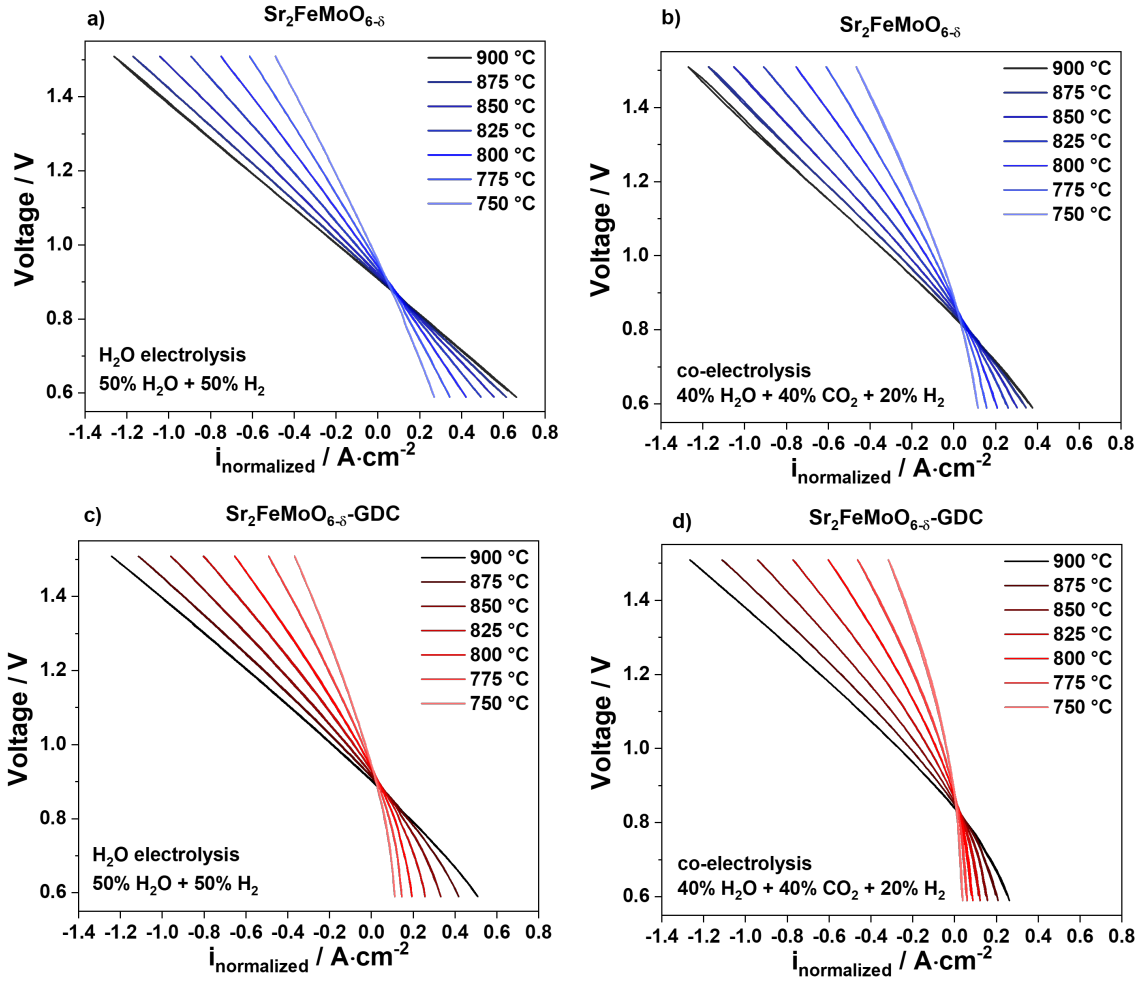

Figure A.6: I–V curves at different temperatures for $Sr_2FeMoO_{6-\delta}$ in (a) steam electrolysis, and (b) co-electrolysis. In comparison, I–V curves of $Sr_2FeMoO_{6-\delta}$-$Ce_{0.8}Gd_{0.2}O_{1.9}$ for (c) steam electrolysis, and (d) co-electrolysis are shown.

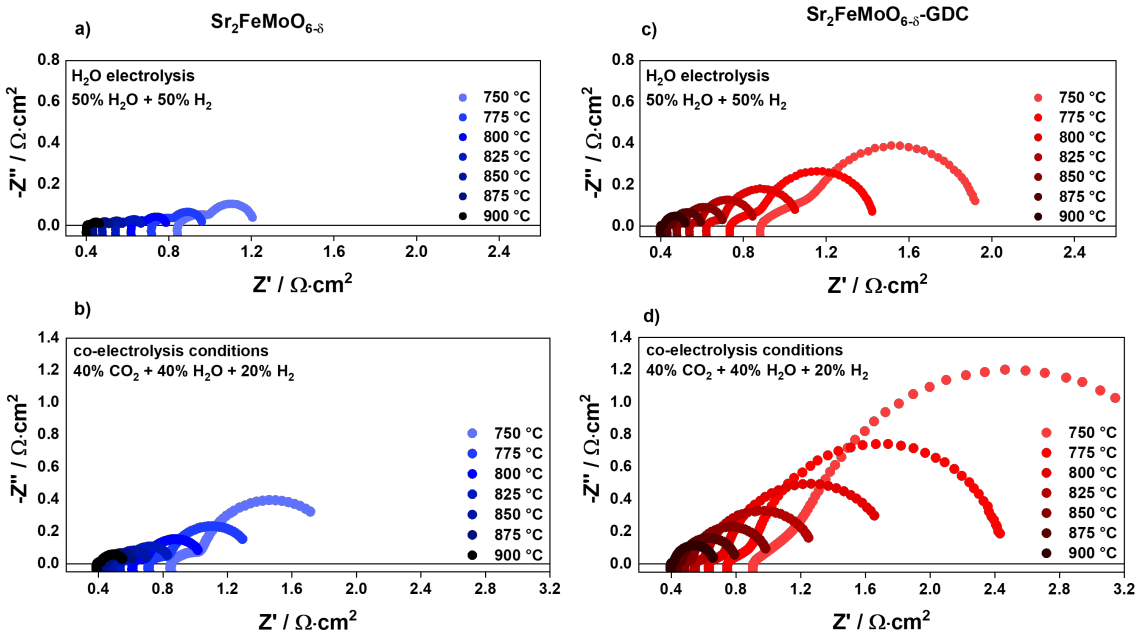

Figure A.7: Impedance spectra with a variation of temperature measured at OCV between 750 °C and 900 °C for $Sr_2FeMoO_{6-\delta}$ in (a) steam electrolysis, and (b) co-electrolysis. The spectra for $Sr_2FeMoO_{6-\delta}$-$Ce_{0.8}Gd_{0.2}O_{1.9}$ are shown in (c) for steam electrolysis, and (d) co-electrolysis.

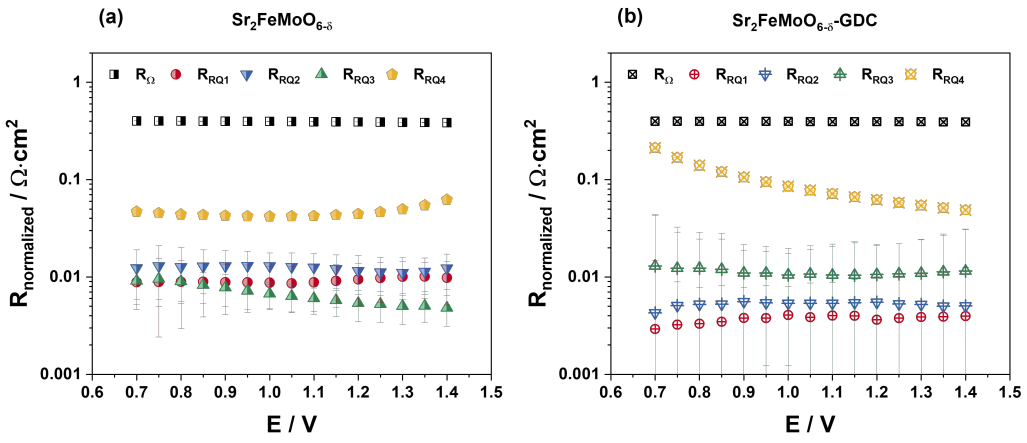

Figure A.8: Polarization variation at 900 °C in 50% H_2O + 50% H_2 measured with single cells containing (a) SFM and (b) SFM-GDC fuel electrodes.

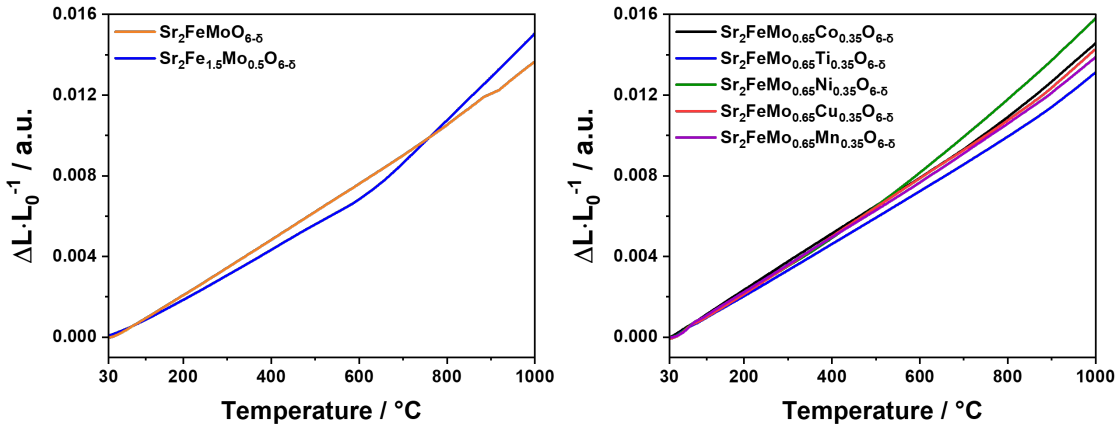

Figure A.9: Longitudinal expansion for SFM fuel electrode materials as a function of temperature between 30 °C and 1000 °C.

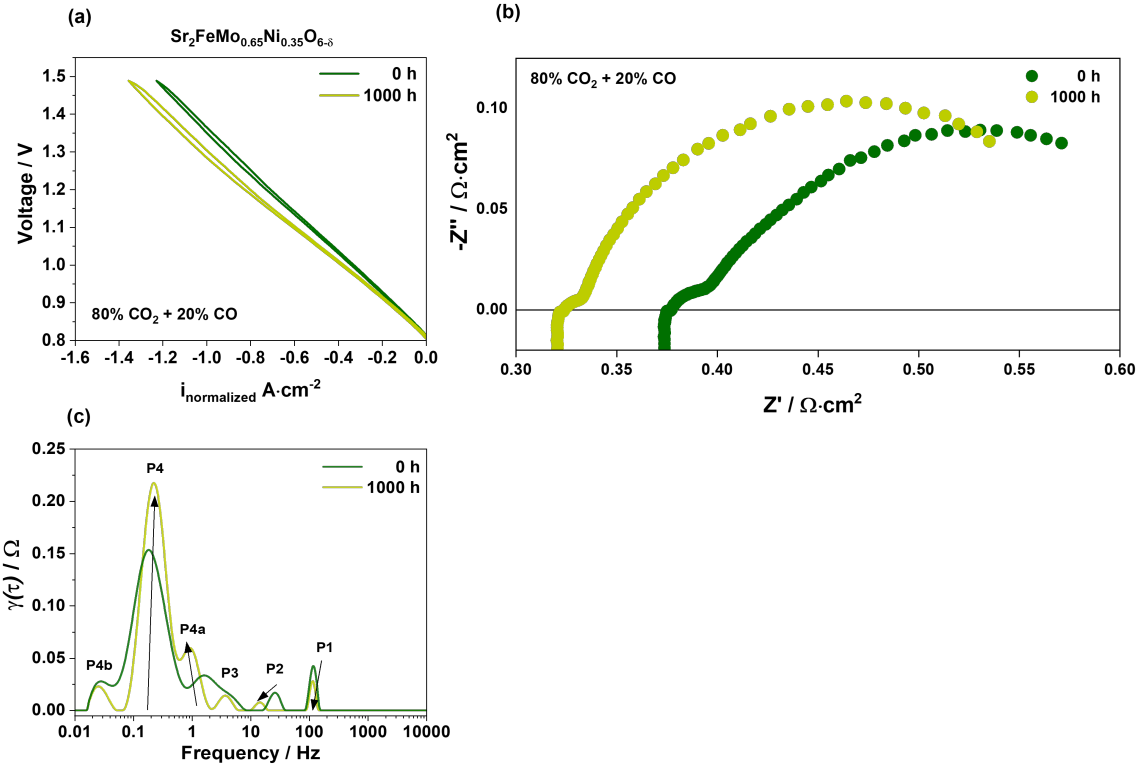

Figure A.10: Single cells tested in an atmosphere of 80% CO_2 + 20% CO at 900 °C with a $Sr_2FeMo_{0.65}Ni_{0.35}O_{6-\delta}$ fuel electrode under constant current load of $-0.5\ A \cdot cm^{-2}$ for 1000 h. Depicted are (a) current-voltage characteristics, (b) Nyquist plots, and (c) the corresponding DRT spectra before and after the durability test.

List of Figures

List of Tables